

**ELUCIDATION OF THE NEEDLE-TIP AND TIP-TRANSLOCON  
INTERACTIONS OF THE *SALMONELLA* SPI-1 TYPE III SECRETION  
SYSTEM AND IDENTIFICATION OF SMALL MOLECULE BINDERS OF THE  
TIP AND TRANSLOCON PROTEINS**

By

©2016  
Andrew C. McShan

Submitted to the Department of Molecular Biosciences  
and the Graduate Faculty of the University of Kansas  
in partial fulfillment of the requirements for the degree of  
Doctor of Philosophy.

Chairperson: 

---

Roberto N. De Guzman, Ph.D.

Committee Members: 

---

Justin Blumenstiel, Ph.D.

---

Yoshiaki Azuma, Ph.D.

---

Mark Richter, Ph.D.

---

Liang Tang, Ph.D.

---

Eric Deeds, Ph.D.

Date Defended: 5/11/2016

The Dissertation Committee for Andrew C. McShan certifies that this is the approved version of the following dissertation:

**ELUCIDATION OF THE NEEDLE-TIP AND TIP-TRANSLOCON  
INTERACTIONS OF THE *SALMONELLA* TYPE III SECRETION SYSTEM AND  
IDENTIFICATION OF SMALL MOLECULE BINDERS OF THE TIP AND  
TRANSLOCON**

Chairperson: \_\_\_\_\_ Roberto N. De Guzman, Ph.D.

Committee Members: \_\_\_\_\_ Justin Blumenstiel, Ph.D.

\_\_\_\_\_ Yoshiaki Azuma, Ph.D.

\_\_\_\_\_ Mark Richter, Ph.D.

\_\_\_\_\_ Liang Tang, Ph.D.

\_\_\_\_\_ Eric Deeds, Ph.D.

Date Approved: 5/11/2016

## Abstract

The type III secretion system (T3SS) is required by many pathogenic Gram-negative bacteria for the initiation and maintenance of infections within eukaryotic host cells. T3SS harboring bacteria include the causative agents of food poisoning/typhoid fever (*Salmonella* Typhimurium/Typhi), dysentery (*Shigella flexneri/dysenteriae*), nosocomial pneumonia (*Pseudomonas aeruginosa*), bubonic plague (*Yersinia pestis*), melioidosis (*Burkholderia pseudomallei*), and trachoma (*Chlamydia trachomatis*). Together, these bacteria are estimated to result in millions of deaths worldwide each year. Therefore, it is of great interest to elucidate the mechanisms of T3SS-mediated virulence utilized by pathogenic Gram-negative bacteria. *Salmonella* is the focus of this dissertation because it is an excellent model organism for T3SS research due to the ease of genetic manipulation and the availability of biological assays.

The T3SS is utilized to inject bacterial virulence factors (also known as effectors) into the host cell cytoplasm, where they manipulate host cell signaling pathways to promote bacterial engulfment, maintenance of infection, and evasion of the host immune system. T3SS effectors are translocated across both bacterial and host cell membranes by the structural component of the T3SS, the needle apparatus. The needle apparatus contains a bacterial membrane embedded base structure, an extracellular needle with a 25Å wide channel, a tip complex that regulates secretion and serves as an environmental sensor, and translocon proteins that assemble a pore in the host cell membrane. How the needle, tip and translocon proteins interact with each other to assemble a functional T3SS needle apparatus and coordinate the secretion of T3SS effectors is poorly understood. Because the needle, tip and translocon proteins are essential for the pathogenesis of T3SS

harboring bacteria, are exposed to the extracellular environment during infection, and are conserved in structure and function, they are attractive targets for the development of novel virulence based anti-bacterial therapeutics. Hence, the importance of elucidating the structure, function and molecular interactions of the T3SS needle, tip and translocon proteins.

This dissertation is focused on two major themes. The first theme is the elucidation of essential protein-protein interactions of the *Salmonella* T3SS needle apparatus through a combination of solution nuclear magnetic resonance (NMR) and fluorescence spectroscopy. To this end, I used amide ( $^{15}\text{N}$ ) and isoleucine, leucine and valine methyl (ILV  $^{13}\text{C}$ -methyl) probes in NMR titrations to map the interaction of T3SS proteins. I additionally labeled T3SS proteins with fluorescent probes to perform fluorescence polarization (FP) and Förster resonance energy transfer (FRET) protein-protein binding assays to complement the NMR studies. Using these methods, the interaction between the *Salmonella* SP-1 T3SS needle protein PrgI and the tip protein SipD, as well as between SipD and the major translocon protein SipB, are described in detail and validated using bacterial invasion assays. The results of NMR and FP/FRET experiments allowed for the proposal of a model for the needle/tip/translocon protein-protein interaction interface where the proximal end of SipD (the bottom of the coiled-coil) is used for interaction with PrgI, while the distal end of SipD (the top of the coiled-coil and the mixed  $\alpha/\beta$  domain) is the surface used for interaction with SipB. The second theme is focused on the T3SS needle apparatus as an attractive target for the development of inhibitors. A review of the current T3SS inhibitor literature is described. In addition, I identified small molecules binders of the tip and translocon proteins from a surface

plasmon resonance (SPR) screen and subsequently validated and mapped the protein-small molecule interactions using titration and saturation transfer different (STD) NMR spectroscopy.

### **Acknowledgements**

First and foremost, I graciously thank my mentor Dr. Roberto N. De Guzman for his excellent leadership, guidance, unyielding support and stringent scientific critiques. Roberto more often than not took the time to sit with me one-on-one and help analyze complex data or figure out why a hypothesis didn't measure up. He also exposed me to the wonderful world of structural biochemistry, particularly solution NMR. Although NMR is an extremely versatile technique, it can be quite complex, both theoretically and experimentally. Ultimately, Roberto was essential in my ability to successfully utilize NMR to answer important questions in this dissertation. Furthermore, Roberto helped improve my manuscripts writing skills, allowed me to travel to out of state for scientific conferences, was kind enough to allow me to take three months off for an out of state internship at Genentech, and helped me achieve the ability to present experimental results in a simple yet convincing manner. I am forever grateful to Roberto.

I thank all the current and former members of the De Guzman lab that have provided me with experimental and intellectual guidance, as well as making sure the atmosphere in the lab was always fun and collaborative. I graciously thank Kawaljit Kaur, who has always been a great friend and support system in the lab. I additionally thank Supratim Dey, Sikta Patnaik, Pallavi Guha Biswas, Amritangshu Chakravarty, Sanjay Yadava, Sukanya Chaudhury, Srirupa Chatterjee, Thenmalar Rathinavelan, Fernando Estrada and Bryce Nordhues. I would also like to thank the talented

undergraduates who aided me with experiments, especially Mason Wilkinson, James Fields, Kevin Knight, and Shoichi Tachiyama.

I additionally thank members of KU who aided me with experiments: Dr. Asokan Anbanandam for technical assistance with NMR spectroscopy and Dr. Carey Johnson/Dr. Mark Richter for technical assistance with fluorescence spectroscopy. I would like to graciously thank Dr. Teruna Siahaan for providing me with guidance throughout my period on the NIGSM Biotechnology Training Grant, as well as to Dr. Y. John Wang and Pervina Kei from Genentech for allowing me to do an extremely rewarding internship with them in beautiful South San Francisco, California. I thank the other members of my graduate class for support and friendship, including Hikmat Al Hashimi, Smita Paranjape, Amber Smith, Denny Swartzlander and Makoto Yoshida. I thank the members of my dissertation committee. Dr. Justin Blumenstiel provided me with an excellent undergraduate research experience that was essential to my ability to be successful in graduate school. Dr. Yoshiaki Azuma and Dr. Eric Deeds allowed me to have extremely rewarding rotations during my first year and always provided helpful suggestions. Dr. Mark Richter and Dr. Liang Tang allowed me to help teach biochemistry, where I discovered my love for teaching. All members of my dissertation committee provided experimental and intellectual guidance throughout my graduate career. I would also like to thank members of the MB staff that helped with day-to-day operations, especially Judi Harris, John Connolly and Linda Wiley.

I thank Paul W., Petra L., Eve R., Fallon L., Alaina B., Danni F., Enya Q., Sarah C., Philipp R., Chelsea T., Cassandra M., Scott R., Gillian D., Chelsie P., Jacob G., Jerry M., Spencer W., Diana D. and all my friends outside of the lab for keeping me sane,

cheering me on when experiments were not successful and (sometimes literally) providing me with a shoulder to cry on.

Last, I thank my amazing family for always supporting and believing in me. I thank my father for allowing me to endlessly play with dinosaur toys and providing me with books about the cosmos. From him I learned that from the age of 10 that I wanted to become a research scientist to discover all the mysteries that the world had to offer. It would be those scientists that I read about, primarily Carl Sagan, which ultimately drove me to become a research scientist and think intellectually. I thank my mother who always told me that I could be whatever I wanted to be, so much so that I was just crazy enough to believe her. She spent hours upon hours helping me with homework as a youth and cheering me on throughout both my undergraduate and graduate career. From her I acquired persistence and resilience, which were absolutely essential traits to my success as a scientist. Finally, I thank my wonderful sister and brother.

Rock Chalk Jayhawk, KU. Beak 'em.

## Table of Contents

	<b>Page</b>
Abstract.....	iii
Acknowledgements.....	v
Table of Contents.....	viii
List of Figures.....	xiii
List of Tables.....	xv
List of Abbreviations.....	xvi
<b>Chapter 1. Introduction</b>	
1.1. Introduction to the Type III Secretion System (T3SS).....	1
1.2. The <i>Salmonella</i> Typhimurium T3SS.....	8
1.2.1. Overview of <i>Salmonella</i> as a Pathogen.....	8
1.2.2. Genetic Organization of the <i>S. Typhimurium</i> T3SS.....	10
1.3. Structural Components of the T3SS Apparatus.....	12
1.3.1. The Base.....	17
1.3.2. The Needle.....	20
1.3.3. The Tip Complex.....	26
1.3.4. The Translocon.....	31
1.3.5. Assembly of the T3SS Apparatus.....	34
1.4. Functional Components of the T3SS.....	35
1.4.1. The Export Apparatus, Sorting Platform and Associated Proteins.....	35
1.4.2. T3SS Chaperones.....	36
1.4.3. <i>Salmonella</i> Typhimurium T3SS Effectors.....	40
1.5. Future Directions of T3SS Research.....	41
1.6. References.....	43
<b>Chapter 2. Assignment of ILV Methyl Resonances of SipD<sup>Δ38</sup></b>	
2.1. Introduction.....	58
2.2. Materials and Methods.....	59
2.2.1. Expression and Purification of Perdeuterated SipD <sup>Δ38</sup> .....	59
2.2.2. <sup>1</sup> H- <sup>13</sup> C HSQC of Perdeuterated SipD <sup>Δ38</sup> .....	62
2.2.3. 3D <sup>13</sup> C- <sup>1</sup> H- <sup>13</sup> C HMQC-NOESY-HMQC of Perdeuterated SipD <sup>Δ38</sup> .....	62
2.2.4. Assignment Strategy and Data Analysis.....	62
2.3. Results.....	63
2.3.1. SipD <sup>Δ38</sup> Purification and Ile Methyl Assignments.....	63
2.3.2. SipD <sup>Δ38</sup> Leu and Val Methyl Assignments by 3D NMR.....	67
2.4. Discussion.....	70
2.5. Accession Codes.....	70
2.6. References.....	71
<b>Chapter 3. NMR Characterization of SipD<sup>Δ132</sup></b>	
3.1. Introduction.....	73
3.2. Materials and Methods.....	73
3.2.1. Expression and Purification of SipD <sup>Δ132</sup> .....	73

3.2.2. Circular Dichroism of SipD <sup>Δ38</sup> and SipD <sup>Δ132</sup> .....	74
3.2.3. <sup>1</sup> H- <sup>15</sup> N TROSY of SipD <sup>Δ38</sup> and SipD <sup>Δ132</sup> and Transfer of Assignments.....	74
3.2.4. <sup>1</sup> H- <sup>13</sup> C HSQC of SipD <sup>Δ38</sup> and SipD <sup>Δ132</sup> and Transfer of Assignments.....	75
3.3. Results.....	75
3.3.1. Circular Dichroism of SipD <sup>Δ38</sup> and SipD <sup>Δ132</sup> .....	75
3.3.2. <sup>1</sup> H- <sup>15</sup> N TROSY of SipD <sup>Δ38</sup> and SipD <sup>Δ132</sup> and Transfer of Assignments.....	76
3.3.3. <sup>1</sup> H- <sup>13</sup> C HSQC of SipD <sup>Δ38</sup> and SipD <sup>Δ132</sup> and Transfer of Assignments.....	80
3.4. Discussion.....	86
3.5. References.....	87

## **Chapter 4. NMR Characterization of the Protein-Protein Interaction of the Tip SipD and Needle PrgI of *Salmonella***

4.1. Introduction.....	88
4.2. Materials and Methods.....	88
4.2.1. Protein Expression and Purification.....	88
4.2.2. <sup>1</sup> H- <sup>15</sup> N TROSY of SipD and <sup>1</sup> H- <sup>15</sup> N HSQC of PrgI*.....	90
4.2.3. <sup>1</sup> H- <sup>13</sup> C HSQC of SipD and PrgI*.....	90
4.2.4. NMR Titrations Between PrgI* and SipD <sup>Δ38</sup> or SipD <sup>Δ132</sup> .....	91
4.3. Results.....	91
4.3.1. Titration of SipD <sup>Δ38</sup> and SipD <sup>Δ132</sup> with PrgI*.....	91
4.3.2. Titration of PrgI* with SipD <sup>Δ132</sup> .....	99
4.4. Discussion.....	102
4.5. References.....	103

## **Chapter 5. Characterization of the SipD and PrgI Interaction by Fluorescence Spectroscopy**

5.1. Introduction.....	105
5.2. Materials and Methods.....	106
5.2.1. Site-Directed Mutagenesis, Protein Expression and Purification.....	106
5.2.2. Fluorophore Conjugation of Proteins.....	107
5.2.3. Fluorescence Polarization (FP).....	108
5.2.4. Förster Resonance Energy Transfer (FRET).....	108
5.2.5. <i>Salmonella</i> Invasion Assay.....	109
5.3. Results.....	110
5.3.1. Fluorophore Conjugation to PrgI* and SipD <sup>Δ38</sup> /SipD <sup>Δ100</sup> .....	110
5.3.2. Fluorescence Polarization of PrgI* and SipD <sup>Δ38</sup> /SipD <sup>Δ100</sup> .....	111
5.3.3. FRET of PrgI* and SipD <sup>Δ38</sup> /SipD <sup>Δ100</sup> .....	112
5.3.4. <i>Salmonella</i> Invasion Assay.....	113
5.4. Discussion.....	118
5.5. References.....	119

## **Chapter 6. CD and NMR Characterization of SipB N-Terminal Domain Constructs**

6.1. Introduction.....	121
6.2. Materials and Methods.....	122
6.2.1. Protein Expression and Purification.....	122
6.2.2. Size Exclusion Chromatography (SEC).....	123

6.2.3. Circular Dichroism (CD).....	124
6.2.4. NMR Spectroscopy.....	124
6.3. Results.....	125
6.3.1. Purification of SipB <sup>11-232</sup> , SipB <sup>11-312</sup> and SipB <sup>82-240</sup> .....	125
6.3.2. SEC of SipB <sup>11-232</sup> and SipB <sup>11-312</sup> .....	126
6.3.3. CD of SipB <sup>11-232</sup> and SipB <sup>11-312</sup> .....	126
6.3.4. NMR Spectroscopy of SipB <sup>11-232</sup> , SipB <sup>11-312</sup> and SipB <sup>82-240</sup> .....	127
6.4. Discussion.....	133
6.5. References.....	134

## **Chapter 7. Identification of the Binding Surfaces Involved in the *Salmonella* Tip-Translocon Protein-Protein Interaction**

7.1. Introduction.....	136
7.2. Materials and Methods.....	137
7.2.1. Protein Expression and Purification.....	137
7.2.2. <sup>1</sup> H- <sup>15</sup> N TROSY of SipD <sup>Δ38</sup> and SipD <sup>Δ132</sup> .....	137
7.2.3. <sup>1</sup> H- <sup>13</sup> C HSQC of SipD <sup>Δ38</sup> and SipD <sup>Δ132</sup> .....	137
7.2.4. NMR Titrations and Data Analysis.....	138
7.3. Results.....	138
7.3.1. Titration of <sup>15</sup> N/ILV SipD <sup>Δ38</sup> with SipB <sup>11-232</sup> .....	138
7.3.2. Titration of <sup>15</sup> N/ILV SipD <sup>Δ38</sup> with SipB <sup>11-312</sup> .....	145
7.3.3. Titration of <sup>15</sup> N/ILV SipD <sup>Δ132</sup> with SipB <sup>11-232</sup> and SipB <sup>11-312</sup> .....	145
7.4. Discussion.....	153
7.5. References.....	155

## **Chapter 8. Characterization of the Interaction Between SipD and the SipB N-Terminal Domain by Fluorescence Spectroscopy**

8.1. Introduction.....	156
8.2. Materials and Methods.....	156
8.2.1. Site-Directed Mutagenesis, Protein Expression and Purification.....	156
8.2.2. Fluorophore Conjugation of Proteins.....	157
8.2.3. Circular Dichroism (CD).....	158
8.2.4. Fluorescence Polarization (FP).....	158
8.2.5. Förster Resonance Energy Transfer (FRET).....	159
8.2.6. <i>Salmonella</i> Invasion Assay.....	160
8.2.7. Western Immunoblot Analysis.....	160
8.3. Results.....	161
8.3.1. Fluorophore Conjugation to Proteins.....	161
8.3.2. FP of SipB <sup>82-312</sup> and SipD <sup>Δ38</sup> /SipD <sup>Δ100</sup> .....	162
8.3.3. FRET of SipB <sup>82-312</sup> and SipD <sup>Δ38</sup> /SipD <sup>Δ100</sup> .....	163
8.3.4. FP and FRET of SipB <sup>82-312</sup> and PrgI*.....	167
8.3.5. Invasion Assay with SipD Mixed α/β Domain Mutants.....	168
8.4. Discussion.....	169
8.5. References.....	172

## **Chapter 9. The Bacterial Type III Secretion System as a Target for Developing New Antibiotics**

9.1. Introduction.....	174
9.2. The Type III Secretion System - Multiple Targeting Opportunities.....	175
9.2.1. Overview of the T3SS.....	175
9.2.2. The T3SS Needle Apparatus.....	176
9.2.3. Chaperones and Effectors.....	177
9.2.4. T3SS Gene Transcription.....	178
9.3. Literature of T3SS Inhibitors.....	178
9.3.1. Salicylidene Acylhydrazides.....	178
9.3.2. Thiazolidinones.....	180
9.3.3. Other Classes of T3SS Inhibitors.....	181
9.3.4. Non-Small Molecule Inhibitors of T3SS.....	182
9.3.5. Small Molecules That Bind T3SS Proteins.....	184
9.4. Future Directions.....	185
9.4.1. Identification of T3SS Targets.....	185
9.4.2. SAR Design.....	186
9.4.3. Animal Models, Pharmacokinetics and Formulation.....	187
9.5. Conclusion.....	188
9.6. References.....	192

## **Chapter 10. Characterization of the Binding of Hydroxyindole, Indoleacetic Acid and Morpholinoaniline to the Salmonella Type III Secretion System Proteins SipD and SipB**

10.1. Introduction.....	202
10.2. Materials and Methods.....	203
10.2.1. Protein Expression and Purification.....	203
10.2.2. Surface Plasmon Resonance (SPR) Screening.....	203
10.2.3. NMR Spectroscopy and Data Analysis.....	205
10.3. Results.....	206
10.3.1. SPR Screening.....	206
10.3.2. NMR Titrations of SipD <sup>Δ38</sup> with 5-hydroxyindole.....	207
10.3.3. STD NMR of 5-hydroxyindole with SipD <sup>Δ38</sup> .....	209
10.3.4. SipD <sup>Δ38</sup> binds to 4-morpholinoaniline.....	217
10.3.5. SipB <sup>82-240</sup> binds to 5-hydroxyindole and 3-indoleacetic acid.....	218
10.4. Discussion.....	219
10.5. References.....	225

## **Chapter 11. CD and NMR Characterization of Chaperone/Translocon Complexes**

11.1. Introduction.....	228
11.2. Materials and Methods.....	228
11.2.1. Subcloning, Protein Expression and Purification.....	228
11.2.2. Size Exclusion Chromatography (SEC).....	230
11.2.3. Circular Dichroism (CD).....	231
11.2.4. NMR Spectroscopy.....	231
11.3. Results.....	232

11.3.1. Purification of hisSicA/SipC.....	232
11.3.2. NMR Spectroscopy of hisSicA/SipC.....	233
11.3.3. Purification of hisPcrH/PopD and hisPcrH/PopB.....	237
11.3.4. NMR of Free hisPcrH, hisPcrH/PopD and hisPcrH/PopB.....	237
11.4. Discussion.....	243
11.5. References.....	244

## **Chapter 12. Overall Discussion Future Directions**

12.1. Overall Discussion and Future Directions.....	246
12.1.1. Isotopic Labeling of ILV Side-Chain Methyls in T3SS Proteins.....	247
12.1.2. Comparison of SipD <sup>Δ38</sup> and SipD <sup>Δ132</sup> .....	248
12.1.3. Summary of the needle-tip and tip-translocon interactions.....	249
12.1.4. Model of the T3SS Needle/Tip/Translocon Interface.....	251
12.1.5. Fluorescence based binding assays of T3SS proteins.....	252
12.1.6. Comparison of SipB <sup>82-240</sup> , SipB <sup>11-232</sup> and SipB <sup>11-312</sup> Constructs.....	253
12.1.7. Small molecule binders of SipD <sup>Δ38</sup> and SipB <sup>82-240</sup> .....	254
12.1.8. Characterization of Chaperone/Translocon Complexes.....	257
12.2. References.....	258

## **Addendum. Interaction of PcrV and PcrG by Fluorescence Spectroscopy**

A1.1. Introduction.....	260
A1.2. Materials and Methods.....	261
A1.2.1. Protein Expression and Purification.....	261
A1.2.2. Secondary Structure Prediction.....	262
A1.2.3. Circular Dichroism (CD).....	263
A1.2.4. Fluorophore Conjugation.....	263
A1.2.5. Fluorescence Polarization (FP).....	264
A1.2.6. Förster Resonance Energy Transfer (FRET).....	264
A1.3. Results.....	265
A1.3.1. CD of Fluorophore Labeled PcrG <sup>9-76</sup> E28C and PcrV <sup>25-294</sup> D133C.....	265
A1.3.2. FP of PcrG <sup>9-76</sup> E28C-FM and Unlabeled PcrV <sup>25-294</sup> .....	266
A1.3.3. FRET of PcrG <sup>9-76</sup> E28C-FM and PcrV <sup>25-294</sup> D133C-AF647.....	266
A1.4. Discussion.....	271
A1.5. References.....	272

## List of Figures

1-1 – Visualization of T3SS Needle Complexes by Electron Microscopy.....	4
1-2 – Organization of T3SS Genes.....	11
1-3 – Organization of the <i>Salmonella</i> T3SS SPI-1 Apparatus.....	14
1-4 – Organization of the <i>Salmonella</i> T3SS SPI-1 Base.....	19
1-5 – Needle Monomer Structures.....	24
1-6 – Atomic Models of Polymerized T3SS SPI-1 Needles.....	25
1-7 – Tip Monomer Structures.....	29
1-8 – Atomic Model of the <i>Shigella flexneri</i> T3SS SPI-1 Tip Complex.....	30
1-9 – Partial Structures of T3SS Translocon Proteins.....	33
2-1 – ILV Side-Chain Methyl Isotope Labeling Strategy.....	61
2-2 – Position of ILV Residues on SipD <sup>Δ38</sup> .....	64
2-3 – SDS-PAGE Gel of SipD <sup>Δ38</sup> Purification.....	65
2-4 – Examples of SipD <sup>Δ38</sup> Assignment Strategy Using Ile-to-Leu Point Mutants.....	66
2-5 – Representative Example of SipD <sup>Δ38</sup> Leu/Val Assignment From 3D Data.....	68
2-6 – Complete Assignment of ILV Methyl Resonances of SipD <sup>Δ38</sup> .....	69
3-1 – Circular Dichroism of SipD <sup>Δ38</sup> and SipD <sup>Δ132</sup> .....	77
3-2 – Testing Trosyef3gpsi vs. Trosy3gppsi19.2 with SipD <sup>Δ38</sup> .....	78
3-3 – Comparison of Trosy3gppsi19.2 and Trosyef3gpsi Bruker Pulse Programs.....	79
3-4 – Comparison of the Amide Resonances of SipD <sup>Δ38</sup> and SipD <sup>Δ132</sup> .....	81
3-5 – Backbone and Side-Chain Amide Resonance Assignments of SipD <sup>Δ132</sup> .....	82
3-6 – Ile-to-Leu Point Mutation Allows for Assignment of SipD <sup>Δ132</sup> Ile Methyls.....	83
3-7 – Comparison of ILV Methyl Resonances of SipD <sup>Δ38</sup> and SipD <sup>Δ132</sup> .....	84
3-8 – ILV Methyl Assignments of SipD <sup>Δ132</sup> .....	85
4-1 – <sup>15</sup> N Titration of SipD <sup>Δ38</sup> with PrgI*.....	93
4-2 – ILV Titration of SipD <sup>Δ38</sup> with PrgI*.....	94
4-3 – <sup>15</sup> N Titration of SipD <sup>Δ132</sup> with PrgI*.....	95
4-4 – ILV Titration of SipD <sup>Δ132</sup> with PrgI*.....	96
4-5 – New Peaks from ILV Titration of SipD <sup>Δ132</sup> with PrgI*.....	97
4-6 – Peak Intensity Analysis of <sup>15</sup> N and ILV Titrations of SipD <sup>Δ132</sup> with PrgI*.....	98
4-7 – <sup>15</sup> N Titration of PrgI* with SipD <sup>Δ132</sup> .....	100
4-8 – ILV Titration of PrgI* with SipD <sup>Δ132</sup> .....	101
5-1 – UV-Vis Absorption Spectra of Fluorophore Labeled PrgI* and SipD <sup>Δ38</sup> .....	114
5-2 – Circular Dichroism of Fluorophore Labeled PrgI* and SipD <sup>Δ38</sup> .....	114
5-3 – Fluorescence Polarization of PrgI*-AF488 and SipD <sup>Δ38</sup> /SipD <sup>Δ100</sup> .....	115
5-4 – FRET of PrgI*-AF488 and SipD <sup>Δ38</sup> /SipD <sup>Δ100</sup> -AF647.....	116
5-5 – Circular Dichroism of SipD <sup>Δ100</sup> Mutants.....	117
5-6 – <i>Salmonella</i> Invasion Assay of SipD Coiled-Coil Mutants.....	118
6-1 – Purification of SipB N-Terminal Domain Constructs.....	128
6-2 – SEC of SipB N-Terminal Domain Constructs.....	129
6-3 – CD of SipB N-Terminal Domain Constructs.....	130
6-4 – <sup>1</sup> H- <sup>15</sup> N TROSY of SipB N-Terminal Domain Constructs.....	131
6-5 – <sup>1</sup> H- <sup>13</sup> C HSQC of SipB N-Terminal Domain Constructs.....	132
6-6 – Positions of ILV residues on SipB <sup>82-226</sup> .....	133
7-1 – <sup>15</sup> N Titration of SipD <sup>Δ38</sup> with SipB <sup>11-232</sup> .....	141

7-2 – ILV Titration of SipD <sup>Δ38</sup> with SipB <sup>11-232</sup> .....	142
7-3 – New SipD <sup>Δ38</sup> ILV Methyl Peaks Appear Upon Titration with SipB <sup>11-232</sup> .....	143
7-4 – Effect of Temperature on the <sup>1</sup> H- <sup>13</sup> C HSQC of the SipD <sup>Δ38</sup> :SipB <sup>11-232</sup> Complex..	144
7-5 – <sup>15</sup> N/ILV Titration of SipD <sup>Δ38</sup> with SipB <sup>11-312</sup> .....	148
7-6 – <sup>15</sup> N Titration of SipD <sup>Δ132</sup> with SipB <sup>11-232</sup> .....	149
7-7 – <sup>15</sup> N Titration of SipD <sup>Δ132</sup> with SipB <sup>11-312</sup> .....	150
7-8 – ILV Titration of SipD <sup>Δ132</sup> with SipB <sup>11-232</sup> .....	151
7-9 – ILV Titration of SipD <sup>Δ132</sup> with SipB <sup>11-312</sup> .....	152
7-10 – Comparison of results from the <sup>15</sup> N and ILV Titrations of SipD with SipB.....	154
8-1 – UV-Vis Absorption Spectra of Fluorophore Labeled SipB <sup>82-312</sup> .....	164
8-2 – Circular Dichroism of Fluorophore Labeled SipB <sup>82-312</sup> .....	164
8-3 – Fluorescence Polarization of SipB <sup>82-312</sup> -AF647 and SipD <sup>Δ38</sup> /SipD <sup>Δ100</sup> .....	165
8-4 – FRET of SipB <sup>82-312</sup> -AF647 and SipD <sup>Δ38</sup> /SipD <sup>Δ100</sup> -AF488/FM.....	166
8-5 – FP and FRET of SipB <sup>82-312</sup> and PrgI* .....	170
8-6 – <i>Salmonella</i> Invasion Assay with SipD Mixed α/β Domain Mutants.....	171
8-7 – Western Immunoblot Analysis of SipD Mixed α/β Domain Mutants .....	172
9-1 – Strategies for Inhibiting the T3SS.....	190
9-2 – T3SS Inhibitor Structures.....	191
10-1 – Structure of Small Molecule Scaffolds.....	210
10-2 – SPR Screening of SipD <sup>Δ38</sup> and SipB <sup>82-240</sup> .....	211
10-3 – Further SPR Screening of SipD <sup>Δ38</sup> and SipB <sup>82-240</sup> .....	212
10-4 – <sup>15</sup> N NMR Titration of SipD <sup>Δ38</sup> with 5-hydroxyindole.....	213
10-5 – ILV Methyl Titration of SipD <sup>Δ38</sup> with 5-hydroxyindole.....	214
10-6 – Plots of Chemical Shift Deviations of SipD <sup>Δ38</sup> with 5-hydroxyindole.....	214
10-7 – SipD Surfaces Affected by Binding with 5-hydroxyindole.....	215
10-8 – STD NMR of 5-hydroxyindole with SipD <sup>Δ38</sup> .....	216
10-9 – <sup>15</sup> N Titration of SipD <sup>Δ38</sup> with 4-morpholinoaniline.....	221
10-10 – ILV Titration of SipD <sup>Δ38</sup> with 4-morpholinoaniline.....	222
10-11 – NMR Titration Analysis of SipD <sup>Δ38</sup> with 4-morpholinoaniline.....	222
10-12 – SipD Surfaces Affected by Binding with 4-morpholinoaniline.....	223
10-13 – <sup>15</sup> N Titration of SipB <sup>82-240</sup> with 5-hydroxyindole and 3-indoleacetic Acid.....	224
10-14 – ILV Titration of SipB <sup>82-240</sup> with 5-hydroxyindole and 3-indoleacetic Acid.....	224
10-15 – STD NMR of SipB <sup>82-240</sup> with 3-indoleacetic acid and 5-hydroxyindole.....	225
11-1 – Purification of hisSicA/SipC.....	234
11-2 – Circular Dichroism of hisSicA/SipC.....	235
11-3 – NMR Spectroscopy of hisSicA/SipC.....	236
11-4 – Purification of hisPcrH/PopD.....	239
11-5 – Purification of Free hisPcrH and hisPcrH/PopB.....	239
11-6 – Circular Dichroism of hisPcrH/PopD and hisPcrH/PopB.....	240
11-7 – NMR Spectroscopy of hisPcrH/PopD.....	241
11-8 – NMR Spectroscopy of Free hisPcrH and hisPcrH/PopB.....	242
12-1 – Proposed Model of the PrgI, SipD and SipB Interface.....	255
12-2 – Comparison of the SipD Surface Affected by Small Molecules.....	256
A1-1 – Positions of Cysteine Mutation of PcrG and PcrV.....	267
A1-2 – CD of Fluorophore Labeled PcrG <sup>9-76</sup> E28C and PcrV <sup>25-294</sup> D133C.....	268
A1-3 – Fluorescence Polarization of PcrG <sup>9-76</sup> E28C-FM with PcrV <sup>25-294</sup> .....	269

A1-4 – FRET of PcrG <sup>9-76</sup> E28C-FM and PcrV <sup>25-294</sup> D133C-AF647.....	270
A1-5 – Possible Model of the PcrG <sup>9-76</sup> and PcrV <sup>25-294</sup> Interaction.....	272

### List of Tables

<b>Table</b>	<b>Title</b>	<b>Page</b>
Table 1-1 – Classification of T3SS Families.....		7
Table 1-2 – List of T3SS Apparatus Homologs.....		15
Table 1-3 – Structural Proteins of the T3SS Needle Apparatus.....		16
Table 1-4 – Atomic Structures of T3SS Chaperones.....		38
Table 1-5 – Atomic Structures of <i>Salmonella</i> Typhimurium T3SS Effectors.....		39
Table 8-1 – Calculations of SipB/SipD FRET Efficiency.....		167
Table 9-1 – T3SS Inhibitors and Their Putative Targets.....		189

## List of Abbreviations

AF488/AF647 – Alexa Fluor Dye 488/647  
CD – Circular Dichroism  
CSD – Chemical Shift Deviation  
DMEM – Dulbecco's modified Eagle's Medium  
DMSO – Dimethyl Sulfoxide  
DTT – Dithiothreitol  
EM – Electron Microscopy  
FM – Fluorescein Maleimide  
FP – Fluorescence Polarization  
FRET – Förster Resonance Energy Transfer  
GB1 –  $\beta$ 1 Domain of Streptococcal Protein G  
HMQC – Heteronuclear Multiple-Quantum Correlation  
HSQC – Heteronuclear Single Quantum Coherence  
ILV – Isoleucine, Leucine and Valine Side-Chain Methyls  
Ipa – Invasion Plasmid Antigen  
IPTG – Isopropyl- $\beta$ -D-thiogalactopyranoside  
Kd – Dissociation Constant  
LB – Luria-Bertani Medium  
NMR – Nuclear Magnetic Resonance  
NOE – Nuclear Overhauser Effect  
NOESY – Nuclear Overhauser Effect Spectroscopy  
PBS – Phosphate Buffered Saline  
PDB ID – Protein Data Bank Identification Number  
Pcr/Lcr – *Pseudomonas* calcium response/Low calcium response  
PCR – Polymerase Chain Reaction  
Prg – PhoP-Repressed Gene  
RMSD – Root Mean Square Deviation  
SEC – Size Exclusion Chromatography  
Sip – *Salmonella* Invasion Protein  
SPI-1/2 – *Salmonella* Pathogenicity Island 1/2  
SPR – Surface Plasmon Resonance  
STD – Saturation Transfer Difference  
T3SS – Type III Secretion System  
TCEP – Tris(2-carboxyethyl)phosphine  
TEV – Tobacco Etch Virus  
Tm – Thermal Melt  
TROSY – Transverse Relaxation Optimized Spectroscopy  
UV/vis – Ultraviolet/Visible

## Chapter 1. Introduction

*“Biological systems, through evolution, have achieved levels of intricacy and subtlety that dwarf the complexity of the 20th century’s most sophisticated engineering feats.”*

- Department of Energy’s “Genomes to Life”

### 1.1. Introduction to the Type III Secretion System (T3SS)

The development and popularization of novel genetic and molecular biology tools in the 1970s, especially recombinant DNA techniques and sequencing, resulted in a wealth of scientific discoveries, one being the elucidation and characterization of protein secretion systems. The secretion of proteins across cellular membranes is now recognized as a fundamental requirement for the survival of many organisms, including plants<sup>1</sup>, animals<sup>2</sup>, Gram-positive bacteria<sup>3</sup> and Gram-negative bacteria<sup>4</sup>. Secreted proteins perform a vast array of functions, including biogenesis of extracellular constituents, nutrient acquisition from the environment, intercellular communication, and regulation of motility<sup>5</sup>. The general secretory pathway (i.e. *sec*-dependent protein secretion) and twin-arginine translocation pathway are sufficient for transport of proteins by Gram-positive bacteria due to their single membrane composition<sup>3;6</sup>. However, Gram-negative bacteria have evolved additional specialized secretory systems to secrete proteins across both inner and outer membranes<sup>5</sup>. Gram-negative bacteria encode at least six distinct secretion machineries (types I through VI), which are classified based on their structure, function and substrate specificities<sup>7</sup>. Importantly, because secretion systems are fundamental to the virulence of pathogenic bacteria, secretion systems have recently become targets for the development of novel antibacterial therapeutics<sup>8</sup>. One such virulence machinery utilized by many Gram-negative bacteria is the type III secretion system (also denoted in the

literature as type 3 secretion system or type three secretion system; abbreviated herein as T3SS). Because the majority of pathogenic Gram-negative bacteria that are linked to significant public health threats and infectious disease in humans harbor one or more T3SSs, it is arguably one of the most well characterized bacterial secretion systems to date. Although a bulk of the initial T3SS discoveries were made in the late 1980s and early 1990s, it wasn't until two 1993 reviews on Gram-negative bacterial secretion systems that the term 'type III secretion system' was popularized<sup>4; 9</sup>.

During the 1980s and 1990s, the laboratories of Guy Cornelis and Hans Wolf-Watz were simultaneously attempting to determine the mechanism of  $\text{Ca}^{2+}$  dependency and the mechanism of virulence for *Yersinia pestis*, the causative agent of bubonic plague. Several virulent *Yersinia* species were found to harbor a ~70 kb plasmid (whose name varies between species) that expressed virulence determinants and  $\text{Ca}^{2+}$  response regulators<sup>10; 11</sup>. The virulence-associated proteins, or effectors, that were secreted were called Yops for *Yersinia* outer proteins<sup>12; 13</sup> and were secreted independently of the classical *sec* secretion pathway signals<sup>13; 14</sup>. In *Yersinia pestis*, the newly identified plasmid encoded protein secretion machinery, which had not yet been visualized, was called the Ysc, or *Yersinia* secretion component, secretion apparatus. Likewise, Jorge Galán and Roy Curtiss were characterizing the molecular determinants of virulence in *Salmonella* Typhimurium. A key unknown that they wanted to address was the molecular mechanism that allowed *Salmonella* to invade intestinal epithelial cells. Previous results had shown that invasion was correlated with a gene locus called *inv* for invasion in *Yersinia*<sup>15</sup> (independent of the plasmid associated virulence Ysc mentioned above). Therefore, Galán and Curtiss isolated the chromosomal genetic locus, which they also

called *inv*, that conferred to the ability of *Salmonella* to invade epithelial cells<sup>16</sup>. The distribution of the *inv* genes was evaluated in other *Salmonella* serovars and found to be present in most virulent serovars<sup>17</sup>. Interestingly, these results were quite different observations from the plasmid encoded *Yersinia* T3SS results in that the *Salmonella* T3SS genes were laid out into operons (called *Salmonella* pathogenicity islands or SPI) on the bacterial chromosome instead of on a plasmid. History would later show that *Yersinia* contains two distinct T3SS apparatuses, one encoded by a plasmid (Ysc) and one encoded by the chromosome (Ysa, SPI-like). The next few years, Galán and colleagues continued to characterize genetic and biochemical aspects of the T3SS. It wasn't until 1998 that the supramolecular structure of the T3SS was visualized by electron microscopy<sup>18</sup>. Galán and coworkers described the apparatus as resembling a syringe or needle with a basal structure that was anchored into the bacterial cell surface<sup>18</sup>. This discovery led to others later referring to the T3SS as a bacterial nanoinjector or injectisome.<sup>19; 20</sup> Since, the T3SS apparatus has been visualized in other bacteria, including *Yersinia*<sup>20</sup>, enteropathogenic *E. coli*<sup>21</sup>, *Shigella*<sup>21</sup> and *Pseudomonas*<sup>22</sup> (**Fig. 1-1**). During this time, experiments that would also elucidate the presence of the T3SS in Gram-negative bacterial pathogens of plants and insects were identified. In 1986, hypersensitive response genes, *hrp*, that are required for bacteria to trigger a plant defense response were identified in *Pseudomonas syringae*<sup>23</sup>. Later, *hrp* genes would be shown to be essential in the secretion of bacterial proteins into plant cells in a T3SS-like manner<sup>24; 25</sup>. In rare cases the *hrp* T3SS has also been documented to be essential for symbiosis, for example between *Burkholderia rhizoxinica* and the fungus *Rhizopus microsporus*<sup>26</sup>.

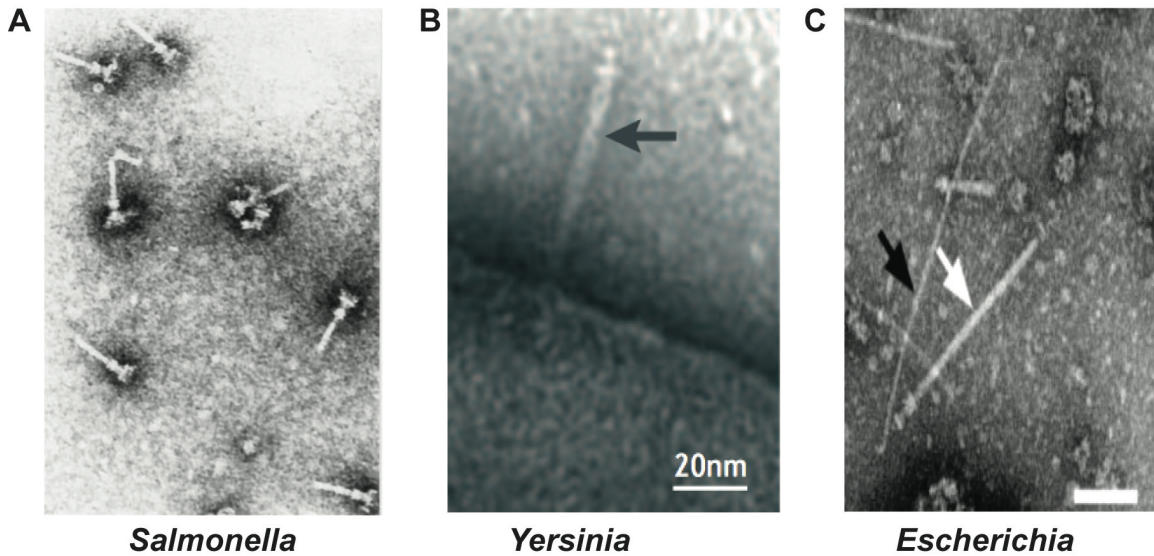


**Fig. 1-1 – Visualization of T3SS Needle Complexes by Electron Microscopy**  
**(A)** *S. Typhimurium* needle complexes purified using a CsCl density gradient (Adapted by permission from the American Association from the Advancement of Science from Figure 2A by Kubori et al.<sup>18</sup>) **(B)** *Y. enterocolitica* needle complex on the bacterial membrane negatively stained with 2% uranyl acetate (Adapted by permission from Macmillan Publishers Ltd from Figure 2A by Cornelis<sup>20</sup>) **(C)** EPEC *E. coli* needle complexes purified using a CsCl density gradient (Adapted by permission from Figure 1B by Sekiya et al.<sup>21</sup>)

Initially, the diversity of Gram-negative bacterial pathogens and the vast array of distinct diseases they cause led to the thinking that their molecular virulence mechanism must be distinct as well. Furthermore, many T3SS harboring bacteria can infect a wide range of organisms, including mammals, plants, fungi and insects<sup>27</sup>. However, over the years it has become clear that T3SS apparatus is conserved, especially the basal components, while each bacterium has evolved a unique flavor of host infection niche adapted T3SS effector proteins<sup>28</sup>. The prevalence of the T3SS is partially explained by the observation that T3SS genes can be transferred between bacteria through horizontal acquisition<sup>29</sup>. The major function of the T3SS is to deliver bacterial effectors into the cytoplasm of target eukaryotic cells. The end goal of the T3SS is to manipulate host cellular signaling pathways for the benefit of bacteria, such as promoting engulfment of the bacteria, evasion of the host innate immune system, and the establishment of a systematic infection. To this end, the T3SS is highly regulated, both at the transcriptional and post-transcriptional level<sup>30</sup>. Although the T3SS is usually defined as being host cell contact dependent for the induction of translocation, secretion can be artificially induced (for example by Congo Red in *Shigella*, calcium depletion in *Yersinia*, changes in osmolarity in *Salmonella*)<sup>31</sup> and extracellular leakage of effector proteins has been observed<sup>32</sup>. The T3SS is hypothesized to share a common evolutionary ancestor with the well-studied homologous flagellar secretion system (confusingly, also the called type III secretion system)<sup>33; 34</sup>. Therefore, the T3SS that translocates effector proteins into eukaryotic cells, which is a distinct protein apparatus from the flagellar T3SS, is sometimes referred to as the non-flagellar type III secretion system (NF-T3SS). However, in this dissertation I will refer to the NF-T3SS system simply as the T3SS and make note

whenever the flagellar T3SS system is of interest. The type III secretion system has been classified into a few different families based on phylogenetic analysis between eight homologous core proteins present in both the flagellar and non-flagellar T3SS<sup>34</sup> (**Table 1-1**). Distinguishable T3SS families include the following: *i*) SPI-1 (homology to Inv-Mxi-Spa), *ii*) SPI-2 (homology to Ssa-Esc), *iii*) Ysc (homology to Psc), *iv*) Chlamy, *v*) Rhizo, and *vi*) Hrp1 (homology to Hcr1) and Hrp2 (homology to Hrc2). Desulfovibrionales and myxococcales have also been identified as potentially unique T3SS families<sup>34</sup>.

Interestingly, some bacteria harbor two or more distinct T3SSs that are used for specific stages of infection. For example, *Salmonella enterica* utilizes the SPI-1 apparatus for initial invasion of the intestinal epithelium, but additionally utilizes the SPI-2 apparatus, which has its own set of effectors, to facilitate bacterial replication in *Salmonella*-containing vacuoles and establish a systematic infection<sup>35</sup>. The observation that T3SSs are ubiquitous in nature and utilized in both pathogenic and symbiotic bacteria-host interactions suggests a need to understand T3SS structure and function. Some of the scientific goals in this T3SS field include the following: *i*) solving atomic structures of T3SS apparatus components, chaperones and effectors, *ii*) elucidating protein-protein interactions involved in the assembly of the T3SS, *iii*) building an atomic model of the entire T3SS apparatus, *iv*) determining structures of the T3SS effectors, *v*) determining genetic regulation of secretion, and *vi*) determining how effectors influence the host cell. Structural characterization and protein-protein interaction information will aid the development of new therapeutics targeting the T3SS. For these reasons, this dissertation is written with an emphasis on biochemical and biophysical characterization of essential T3SS protein-protein interactions.

<b>T3SS Family</b>	<b>Type</b>	<b>Bacterium</b>	<b>Disease</b>
SPI-1 (Inv-Mxi-Spa)	Chromosomal	<i>Burkholderia mallei</i>	Glanders
	Chromosomal	<i>Burkholderia pseudomallei</i>	Melioidosis
	Chromosomal	<i>Chromobacterium violaceum</i>	Septicemia
	Chromosomal	Enteroinvasive <i>E. coli</i> , EIEC	Gastroenteritis
	Chromosomal	<i>Salmonella enterica</i>	Salmonellosis
	Plasmid	<i>Shigella flexneri</i>	Shigellosis
	Chromosomal	<i>Sodalis glossinidius</i>	Tsetse fly symbiont
	Chromosomal	<i>Yersinia enterocolitica</i>	Gastroenteritis
SPI-2 (Ssa-Esc)	Chromosomal	<i>Citrobacter rodentium</i>	Mouse pathogen
	Chromosomal	<i>Chromobacterium violaceum</i>	Septicemia
	Chromosomal	<i>Edwardsiella tarda</i>	Gastroenteritis
	Chromosomal	Enterohaemorrhagic <i>E. coli</i> , EHEC	Uremia and hemolysis
	Chromosomal	Enteropathogenic <i>E. coli</i> , EPEC	Gastroenteritis
	Chromosomal	<i>Salmonella enterica</i>	Salmonellosis
	Chromosomal	<i>Sodalis glossinidius</i>	Tsetse fly infection
	Chromosomal	<i>Yersinia pestis</i>	Bubonic plague
Ysc (Psc)	Chromosomal	<i>Yersinia pseudotuberculosis</i>	Far Eastern scarlatina-like fever
	Plasmid	<i>Aeromonas salmonicida</i>	Fish pathogen
	Chromosomal	<i>Bordetella pertussis</i>	Pertussis (whooping cough)
	Chromosomal	<i>Photobacterium damela</i>	Skin infection
	Chromosomal	<i>Pseudomonas aeruginosa</i>	Nosocomial infections/pneumonia
	Chromosomal	<i>Vibrio parahaemolyticus</i>	Gastroenteritis
	Plasmid	<i>Yersinia enterocolitica</i>	Gastroenteritis
	Plasmid	<i>Yersinia pestis</i>	Bubonic plague
Chlamy	Chromosomal	<i>Chlamydia trachomatis</i>	Trachoma, genital infections
	Chromosomal	<i>Chlamydophila pneumoniae</i>	Pneumonia
Rhizo	Chromosomal	<i>Mesorhizobium loti</i>	Plant symbiont
	Plasmid	<i>Rhizobium sp.</i>	Plant infection
Hrp1 (Hcr1)	Chromosomal	<i>Erwinia amylovora</i>	Plant infection
	Chromosomal	<i>Pseudomonas syringae</i>	Plant infection
	Chromosomal	<i>Vibrio parahaemolyticus</i>	Gastroenteritis
Hrp2 (Hrc2)	Chromosomal	<i>Burkholderia mallei</i>	Glanders
	Chromosomal	<i>Burkholderia pseudomallei</i>	Melioidosis
	Plasmid	<i>Ralstonia solanacearum</i>	Plant infection
	Chromosomal	<i>Xanthomonas campestris</i>	Plant infection

**Table 1-1 – Classification of T3SS Families**

A list of the seven different T3SS families and examples in different bacteria. An exhaustive list of T3SS containing genomes can be found in dataset S2 from Abby *et al.*<sup>34</sup>

## 1.2. The *Salmonella* Typhimurium T3SS

### 1.2.1. Overview of *Salmonella* as a Pathogen

This dissertation is focused on the T3SS proteins from the bacterium *Salmonella*. These are a few reasons for this. First, there exists a large body of knowledge on the *Salmonella* T3SS in the literature to serve as a framework for the studies performed here. Second, biological invasion assays are well established and *Salmonella* is easily genetically manipulated, unlike other systems, such as *Chlamydia*. Third, *Salmonella* T3SS proteins are soluble and stable, which allows for ease of recombinant protein expression and characterization by techniques that may require long experiment times, such as solution NMR spectroscopy. Fourth, *Salmonella* infections are extremely common in both the US and worldwide. Therefore, a cheap drug therapy or preventative treatment for *Salmonella* would significantly reduce the public health burden of Gram-negative bacteria, especially in children or immunocompromised individuals.

*Salmonella* are non-spore forming motile rod-shaped Gram-negative bacterium belonging to the gammaproteobacteria class and the enterobacteriaceae family. They range in size from 2 to 5  $\mu\text{m}$  in length and 0.7 to 1.5  $\mu\text{m}$  in diameter. The genus of *Salmonella* contains two species, *S. bongori* and *S. enterica*. Disease associated infections by *S. bongori* are very rare in humans because their natural reservoir is primarily cold-blooded animals, such as reptiles<sup>36</sup>. While *S. enterica* contains two competent type III secretion systems, called SPI-1 and SPI-2, *S. bongori* only contains the SPI-1 system<sup>36, 37</sup>. *S. enterica* is divided into 6 subspecies: *arizonae*, *diarizonae*, *enterica*, *houtenae*, *indica* and *salamae*. The subspecies are further divided into >2500 serovars. Human disease is primarily linked to infection by *Salmonella enterica* subsp.

*enterica*. The natural reservoir for other subspecies is primarily cold-blooded animals. However, although rare, human disease has also been reported due to infections by other *Salmonella enterica* subspecies<sup>38</sup>. The most well studied serovars of *Salmonella enterica* subsp. *enterica* are Choleraesuis, Enteritidis, Paratyphi, Typhi and Typhimurium. Serovars are distinguished by their surface antigens, such as the flagellar ‘H’ antigen, the oligosaccharide ‘O’ antigen and the polysaccharide ‘Vi’ antigen. Although the full name of a serovar might be, for example, *Salmonella enterica* subsp. *enterica* serovar Typhimurium, it is often simply referred to as *Salmonella* Typhimurium, which is the nomenclature that will be used herein. Diseases caused by the *Salmonella enterica* subsp. *enterica* serovars are dependent on the serovar and the host, but primarily include gastroenteritis, bacteremia (septicemia) and enteric fever (typhoid fever). Gastroenteritis and bacteremia are often linked to Choleraesuis, Enteritidis and Typhimurium, while enteric fever is linked to Typhi and Paratyphi<sup>39</sup>. Non-typhoidal *Salmonella* infections in healthy individuals are often resolved without treatment in less than two weeks by the host natural immune system<sup>40</sup>. In contrast, infections in children below the age of five, elderly and immunocompromised individuals are often severe and treated with antibiotics, such as ciprofloxacin or ceftriaxone<sup>40</sup>. A vaccine against typhoid fever is currently available, though limited in treatment, and vaccines against non-typhoidal *Salmonella* are currently under development<sup>41</sup>. The global burden of non-typhoidal *Samonella* has been estimated to be 94 million illnesses and 155,000 deaths yearly<sup>42</sup>, while the global burden of typhoidal *Salmonella* has been estimated to be 22 million illnesses and 220,000 deaths yearly<sup>43</sup>.

*Salmonella* are zoonotic pathogens, which means they are naturally transmissible from non-human hosts to humans. Transmission typically occurs by an oral-fecal route through contaminated food or water sources, or by physical interaction with infected organisms. After transmission, *Salmonella* activates an acid-tolerance response mechanism to survive the acidic environment of the host stomach<sup>44</sup>. The bacterium then moves to the small intestines, through the intestinal mucus layer and encounters intestinal epithelial cells, where it primarily infects apical M cells in Peyer's patches using the SPI-1 T3SS<sup>44</sup>. During infection, injected T3SS effectors induce host cell membrane ruffling by modulating the host cell cytoskeletal system leading to the engulfment of bacteria into large membrane vesicles and resulting in the formation of the *Salmonella*-containing vacuole (SCV)<sup>44</sup>. The bacterium may also migrate to the basolateral space, for example by disrupting host cell tight junctions, where they are taken up by phagocytes and disseminate into the blood stream. Other target cells include B cell, T cells, gut epithelial cells, neutrophils, macrophages, monocytes, granulocytes and dendritic cells<sup>39</sup>.

### 1.2.2. Genetic Organization of the *S. Typhimurium* T3SS

The T3SS is an essential virulence determinant in *Salmonella* and is located within two *Salmonella* pathogenicity islands, SPI-1 and SPI-2. SPI-1 and SPI-2 each encode a distinct T3SS apparatus. SPI-1 is a 40 kb segment located at centisome 63 on the *Salmonella* chromosome and contains multiple operons for proteins that assemble the SPI-1 structural apparatus (*org*, *prg*, *sip*, *spa* and *inv*), chaperones (*sicA*, *invB*, *sicP*), effectors (*avrA*, *sptP*) and transcriptional regulators (*sprB*, *hilADC*) (**Fig. 1-2**). The primary function of the SPI-1 T3SS is to promote initial invasion of intestinal epithelial

cells and modulate the host immune system. SPI-2 is a 40 kb segment located at centisome 30 on the *Salmonella* chromosome and contains the genes for proteins that assemble the SPI-2 apparatus (**Fig. 1-2**). The primary function of the SPI-2 T3SS is to promote intercellular bacterial survival within SCVs, macrophages death and the establishment of a systematic infection. In addition to the SPI-1 and SPI-2, there are other virulence determinants in *Salmonella*. *S. Typhimurium* contains at least 10 additional pathogenicity islands: SPI-3, SPI-4, SPI-5, SPI-6, SPI-9, SPI-11, SPI-12, SPI-13, SPI-14 and SPI-16. SPI-3 encodes a magnesium uptake system and the adhesion MisL<sup>45</sup>. SPI-4 encodes the T1SS and the non-fimbrial adhesin SiiE<sup>45</sup>. SPI-5 encodes T3SS effectors, such as SopB and PipB<sup>45</sup>. SPI-6 encodes the T6SS<sup>45</sup>. SPI-9 encodes components of the T1SS and biofilm formation<sup>45</sup>. SPI-11 encodes proteins important for bacterial survival in host macrophages, such as PagC, PagD and MsgA<sup>45</sup>. SPI-12 encodes T3SS effectors, such as SspH2<sup>45</sup>. The function of the other SPIs have yet to be extensively characterized.

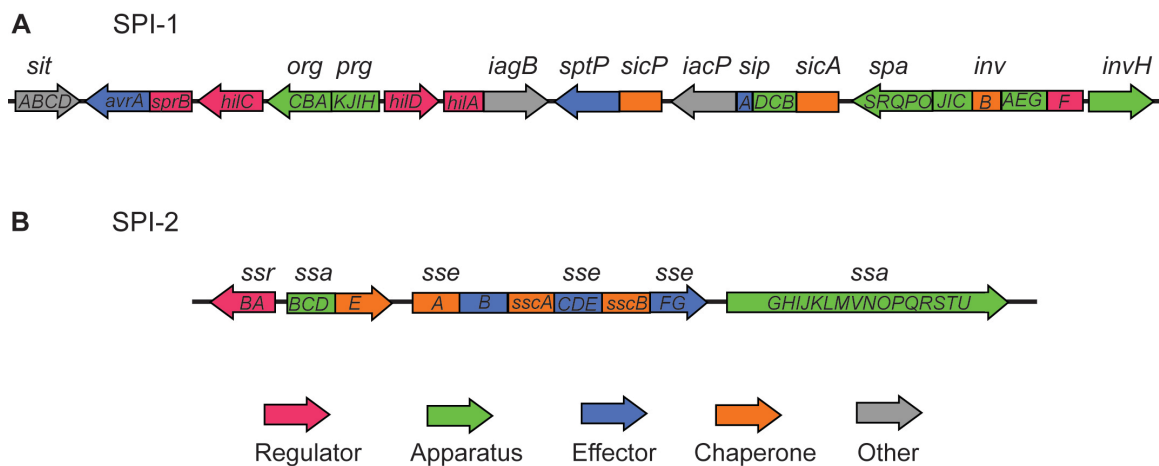


**Fig. 1-2 – Organization of T3SS Genes**

The genetic organization of (A) SPI-1 and (B) SPI-2 from *Salmonella* Typhimurium. Genes are color-coded based on their known or hypothesized function. Gene sizes are not drawn to scale. This figure was adapted from a reference by Fàbrega et al.<sup>44</sup> There are additional T3SS genes that are encoded by other SPIs.

### 1.3. Structural Components of the T3SS Apparatus

The T3SS apparatus is a 3.5 MDa nanomachine comprised of more than a dozen structural proteins. The primary constituents of the apparatus are the following: *i)* a bacterial inner and outer membrane spanning structure called the base, *ii)* a needle-like structure that protrudes into the extracellular space, *iii)* a tip complex at the distal end of the needle, and *iv)* translocon proteins that assemble a pore in the host cell membrane (**Fig. 1-3**). The term ‘needle complex’ is often used in reference to the base and the needle, while the term ‘needle apparatus’ is often used in reference to the complete T3SS apparatus, which includes the base, the needle, the tip and the translocon<sup>46</sup>. The supramolecular structure of the SPI-1 T3SS needle complex was first visualized by electron microscopy (EM) in *Salmonella* Typhimurium<sup>18</sup> following its isolation using a CsCl density gradient. Non-SPI-1 apparatuses have also been visualized, such as *S. Typhimurium* SPI-2 apparatus<sup>47</sup>, *Y. pestis* Ysc apparatus<sup>20</sup>, *C. trachomatis* apparatus<sup>48; 49</sup>, *Rhizobium* sp. apparatus<sup>50</sup> and the *P. syringae* Hrp apparatus<sup>51</sup>. Unfortunately, the tip complex is often lost or falls off the needle during purification of needle complexes, especially in preparations of *Salmonella* needles<sup>46</sup>. Hence, the needle complex being defined as the base plus the needle. However, the appearance of the tip complex is likely dependent on the purification method or bacterial species, because visualization of the T3SS needle complexes has sometimes resulted in density corresponding to the tip, such as with *Y. enterocolitica*<sup>52</sup>. The number of needle complexes per cell ranges from as low as 10 to as many as 100<sup>53; 54</sup>.

The dimensions of the needle complex are on average 25 nm wide and 80 nm long (30 nm base plus a 50 nm needle)<sup>18</sup>. The needle channel is 2.5 nm in diameter,

which is large enough to accommodate two well-packed  $\alpha$ -helices. Therefore, most T3SS substrates require unfolding for efficient secretion<sup>55</sup>. Structural elucidation of many protein components of the needle apparatus has been achieved by X-ray crystallography, NMR spectroscopy, circular dichroism, EM, structure prediction or a combination of techniques (**Table 1-3**). Cryoelectron tomography coupled with molecular docking of atomic structures has begun to form a partial atomic model of the needle apparatus (**Fig. 1-3**). The following sections will describe in detail what is known about the structure and function for each T3SS component with an emphasis on the *Salmonella* Typhimurium SPI-1 T3SS system. Primary amino acid sequences of T3SS proteins vary in sequence homology. *Salmonella* and *Shigella* translocon and tip proteins share ~30 to 40% sequence homology, whereas the needle proteins share ~60% sequence homology. Protein structures are often fairly homologous as well: *Salmonella* SipD and *Shigella* IpaD have a root mean square-deviation (RMSD) of 1.8Å. Similarly, *Yersinia* and *Pseudomonas* translocon and tip proteins share 40% sequence homology, whereas the needle proteins share ~60% sequence homology. The primary sequence homology between the *Salmonella/Shigella* and *Yersinia/Pseudomonas* systems is ~15 to 30% for the needle, tip and translocon proteins. *Salmonella* SipD and *Yersinia* LcrV have an RMSD of 2.5Å. Constituents of the base apparatus have slightly higher primary sequence homology. *Salmonella* PrgK/PrgH/InvG and *Shigella* MxiJ/MxiG/MxiD have ~40 to 50% sequence homology. *Yersinia* YscJ/YscD/YscC and *Pseudomonas* PscJ/PscD/PscC have ~60 to 70% sequence homology.

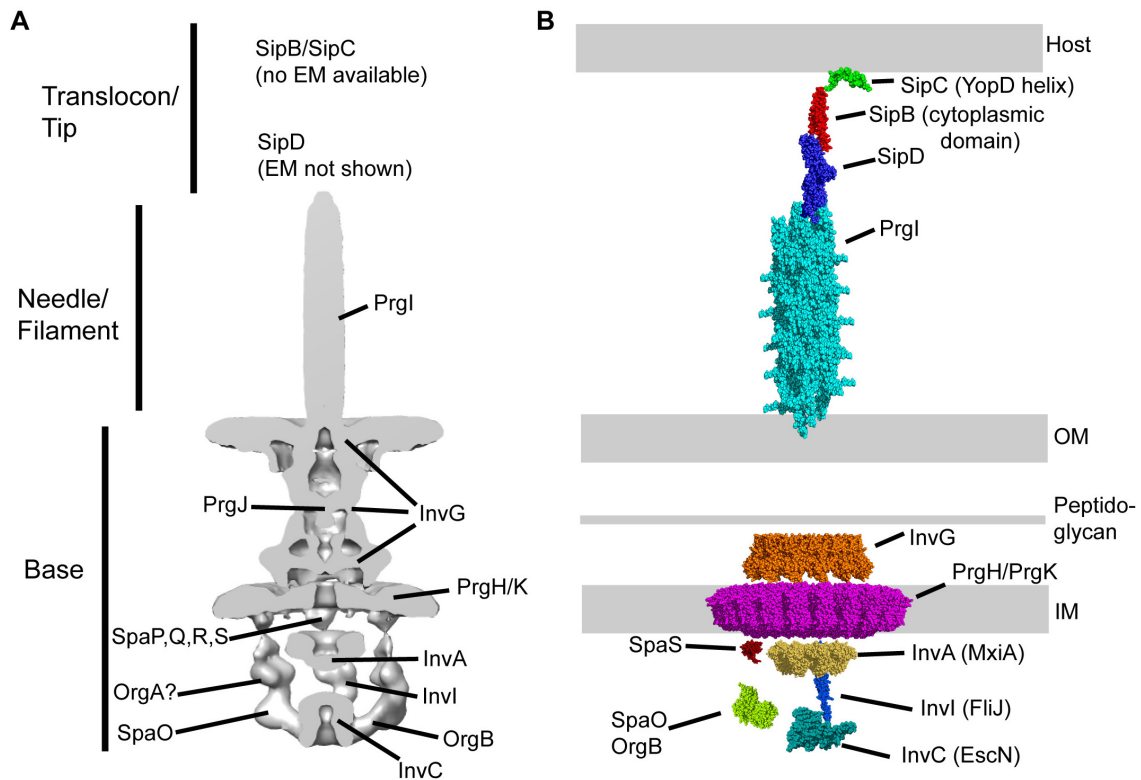


**Fig. 1-3 – Organization of the *Salmonella* T3SS SPI-1 Apparatus**

(A) Cryoelectron tomography of an *in situ* injectisome from *S. flexneri* by Hu et al<sup>56</sup>. EMDDB accession code is 2667. The map was processed with UCSF Chimera<sup>57</sup>. Known or suspected localization of each T3SS apparatus constituent is labeled. (B) Known structures of T3SS apparatus components (see: Table 1-3) are shown as spherical models. This figure is meant to show the overall organization/localization of T3SS components and known structures, as well as the current gap in knowledge. PDB accession codes are 1KDL (YopD amphipathic helix, SipC homolog), 3TUL (SipB N-terminal domain), 3NZZ (SipD), 2LPZ (PrgI needle), 3J1V (InvG), 3J6D (PrgH/PrgK), 3C01 (SpaS), 4A5P (MixA, InvA homolog), 4YX7 (SpaO-OrganB fusion), 3AJW (flagellar FliJ, InvI homolog), 2OBM (EscN, InvC homolog).

Role	<i>S. Typhimurium</i> (SPI-1)	<i>S. Typhimurium</i> (SPI-2)	<i>S. flexneri</i> (SPI-1)	<i>Y. pestis</i> (Ysc)	<i>Y. pestis</i> (Ysa/SPI-2)
Translocon	SipB/SipC	SseC/SseD	IpaB/IpaC	YopB/YopD	YspB/YspC
Tip	SipD	SseB	IpaD	LcrV	YspD
Needle	PrgI	SsaG	MxiH	YscF	?
OM ring	InvG	SsaC	MxiD	YscC	YsaC
Inner rod	PrgJ	SsaI	MxiI	YscI	YsaI
IM ring	PrgK/PrgH	SsaJ/SsaD	MxiJ/MxiG	YscJ/YscD	YsaJ/YsaD
Export apparatus	SpaP	SsaR	Spa24	YscR	YsaR
	SpaQ	SsaS	Spa9	YscS	YsaS
	SpaR	SsaT	Spa29	YscT	YsaT
	SpaS	SsaU	Spa40	YscU	YsaU
	InvA	SsaV	MxiA	YscV [LcrD]	YsaV
ATPase	InvC	SsaN	Spa47	YscN	YsaN
Gatekeeper	InvE	SsaL	MxiC	YopN	YsaW
Sorting platform	OrgA	?	MxiK	YscK	?
Sorting platform	OrgB	SsaK	MxiN	YscL	?
Sorting platform	SpaO	SsaQ	Spa33	YscQ	YsaQ
Regulator/Ruler	InvJ	SsaP	Spa32	YscP	?
Pilotin	InvH	?	MxiM	YscW	YsaP

Role	Enteropathogenic <i>E. coli</i> (Esc/SPI-2)	<i>B. pseudomallei</i> (SPI-1)	<i>P. aeruginosa</i> (Ysc)	<i>Chlamydia</i>
Translocon	EspD/EspB	BipB/BipC	PopB/PopD	CopB/CopD
Tip	EspA	BipD	PerV	CT584
Needle	EscF	BsaL	PscF	CdsF
OM ring	EscC	BsaO	PscC	CdsC
Inner rod	EscI	BsaK	PscI	?
IM ring	EscJ/EscD	BsaJ/BsaM	PscJ/PscD	CdsJ/CdsD
Export apparatus	EscR	BsaW	PscR	CdsR
	EscS	BsaX	PscS	CdsS
	EscT	BsaY	PscT	CdsT
	EscU	BsaZ	PscU	CdsU
	EscV	BsaQ	PscV [PcrD]	CdsV
ATPase	EscN	BsaS	PscN	CdsN
Gatekeeper	SepL	BsaP	PopN	CopN
Sorting platform	EscK	OrgA	PscK	CT560
Sorting platform	EscL	OrgB	PscL	CdsL
Sorting platform	EscQ	BsaV	PscQ	CdsQ
Regulator/Ruler	EscP	BsaU	PscP	?
Pilotin	?	?	ExsB	?

**Table 1-2: List of T3SS Apparatus Homologs**

Compiled from a vast number of references<sup>32; 34; 46; 58; 59; 60; 61</sup>

Unknown or unidentified homologs are marked with a ‘?’

Role	Protein	Organism	EMBD/PDB ID	Type
Translocon	SipB <sup>82-226</sup> (N-term.)	<i>S. Typhimurium</i>	3TUL	X-Ray
	IpaB <sup>74-224</sup> (N-term.)	<i>S. flexneri</i>	3U0C	X-Ray
	IpaB <sup>16-72</sup> + IpgC	<i>S. flexneri</i>	3GZ1/3GZ2	X-Ray
	YopD <sup>278-300</sup> (amphipathic $\alpha$ -helix)	<i>Y. pseudotuberculosis</i>	1KDL	sNMR
	YopD <sup>56-65</sup> + SycD	<i>Y. enterocolitica</i>	4AM9	X-Ray
	PopB <sup>51-59</sup> + PcrH	<i>P. aeruginosa</i>	4JL0	X-Ray
	PopD <sup>47-56</sup> + PcrH	<i>P. aeruginosa</i>	2XCB	X-Ray
Tip	AopB <sup>40-264</sup> + AcrH	<i>A. hydrophila</i>	3WXX	X-Ray
	SipD <sup>39-343</sup>	<i>S. Typhimurium</i>	3NZZ	X-Ray
	SipD <sup>127-343</sup> /PrgI fusion	<i>S. Typhimurium</i>	3ZQB	X-Ray
	SipD <sup>39-343</sup> + Deoxycholate	<i>S. Typhimurium</i>	3O01	X-Ray
	IpaD <sup>15-332</sup>	<i>S. flexneri</i>	2J00	X-Ray
	IpaD (tetramer)	<i>S. flexneri</i>	4D3E	EM/X-Ray
	IpaD <sup>39-322</sup> + Deoxycholate	<i>S. flexneri</i>	3R9V	X-Ray
	LcrV <sup>28-322</sup>	<i>Y. pestis</i>	4JBU	X-Ray
	EspA + Cesa	<i>E. coli</i>	1XOU	X-Ray
	BipD <sup>8-310</sup>	<i>B. pseudomallei</i>	3NFT	X-Ray
Needle	CT584	<i>C. trachomatis</i>	4MLK	X-Ray
	CV2617	<i>C. violaceum</i>	2P7N	X-Ray
	PrgI (monomer)	<i>S. Typhimurium</i>	2JOW/2X9C	sNMR/X-Ray
	PrgI (needle)	<i>S. Typhimurium</i>	2LPZ	EM/ssNMR
	MxiH (monomer)	<i>S. flexneri</i>	2CA5	X-Ray
	MxiH (needle)	<i>S. flexneri</i>	2MME	EM/ssNMR
	YscF <sup>50-87</sup> + YscE/YscG	<i>Y. pestis</i>	2P58	X-Ray
	PscF <sup>54-85</sup> + PscE/PscG	<i>P. aeruginosa</i>	2UWJ	X-Ray
	BsaL <sup>1-84</sup>	<i>B. pseudomallei</i>	2G0U	sNMR
	OM ring	InvG	<i>S. Typhimurium</i>	1871
InvG <sup>22-178</sup> (periplasmic)		<i>S. Typhimurium</i>	4G08/3J1V	X-Ray
YscC		<i>Y. enterocolitica</i>	5720-5722	-
IM ring	EscC <sup>21-174</sup> (periplasmic)	<i>E. coli</i>	3GR5	X-Ray
	EscJ <sup>21-190</sup>	<i>E. coli</i>	1YJ7	X-Ray
	PrgH/K	<i>S. Typhimurium</i>	3J6D	EM/X-Ray
	PrgH <sup>170-392</sup> (periplasmic)	<i>S. Typhimurium</i>	4G1I	X-Ray
	PrgH <sup>11-119</sup> (cytoplasmic)	<i>S. Typhimurium</i>	4G2S	X-Ray
	MxiG <sup>1-126</sup>	<i>S. flexneri</i>	2XXS/4A4Y	sNMR/X-Ray
	CdsD	<i>C. trachomatis</i>	4QQ0/4QO6	X-Ray
Export apparatus	YscD <sup>150-347</sup> (periplasmic)	<i>Y. enterocolitica</i>	4ALZ	X-Ray
	YscD <sup>2-121</sup> (cytoplasmic)	<i>Y. pestis</i>	4A0E	X-Ray
	SpaS <sup>211-258</sup>	<i>S. Typhimurium</i>	3C01	X-Ray
	Spa40 <sup>207-342</sup>	<i>S. flexneri</i>	2VT1	X-Ray
	EscU <sup>215-262</sup>	<i>E. coli</i>	3BZL	X-Ray
ATPase	YscU <sup>220-342</sup>	<i>Y. pestis</i>	2JLI	X-Ray
	CdsU <sup>249-345</sup>	<i>C. trachomatis</i>	3T7Y	X-Ray
Gate/Gatekeeper	EscN <sup>103-446</sup>	<i>E. coli</i>	2OBL/2OBM	X-Ray
	SsaN	<i>S. Typhimurium</i>	4NPH	X-Ray
	CopN	<i>C. pneumoniae</i>	4P40	X-Ray
	InvA	<i>S. Typhimurium</i>	2X49/3LW9	X-Ray
	MxiA <sup>318-686</sup>	<i>S. flexneri</i>	4A5P	X-Ray
Sorting platform	MxiC <sup>74-355</sup>	<i>S. flexneri</i>	2VJ5	X-Ray
	YopN <sup>76-293</sup>	<i>Y. pestis</i>	1XKP/1XL3	X-Ray
	SpaO <sup>145-297</sup> /OrgB <sup>1-30</sup> fusion	<i>S. Typhimurium</i>	4YX7	X-Ray
Pilotin	Spa33 (C-term)	<i>S. flexneri</i>	4TT9	X-Ray
	YscQ <sup>220-307</sup> (C-term)	<i>Y. pseudotuberculosis</i>	3UEP	X-Ray
	MxiM	<i>S. flexneri</i>	1Y9T	X-Ray
T3SS Needle Complex	MxiM + MxiD	<i>S. flexneri</i>	2JW1	sNMR
	ExsB <sup>17-141</sup>	<i>P. aeruginosa</i>	2YJL	X-Ray
	<i>In situ</i> injectisome	<i>S. flexneri</i>	2667	-
	<i>In situ</i> injectisome	<i>Y. enterocolitica</i>	5694	-
	<i>In situ</i> injectisome	<i>S. Typhimurium</i>	1100	-
	<i>In situ</i> injectisome w/ substrate	<i>S. Typhimurium</i>	2480	-

**Table 1-3: Structural Proteins of the T3SS Needle Apparatus**

Note: for the corresponding literature reference please visit the PDB entry.

Adapted from a review by Burkhinshaw et al.<sup>62</sup>

### 1.3.1. The Base

The T3SS base anchors the needle complex into the bacterial membranes. The base transverses the inner membrane (IM) through the periplasm and peptidoglycan layer to the outer membrane (OM). The base is composed of inner membrane rings, the neck and outer membrane rings. The *Salmonella* SPI-1 base contains a three-fold symmetry, where the 15-mer outer ring/neck connects to the 24-mer inner ring<sup>63</sup>. Interestingly, differences have been reported in the *Shigella* SPI-1 base, which is reported to have twelve-fold symmetry where the 12-mer outer ring/neck connects to a 24-mer inner ring<sup>64</sup>.

The inner membrane ring (IR) consists of two stacked oligomeric ring structures comprised of the proteins PrgK (28.2 kDa) and PrgH (44.4 kDa) in the *S. Typhimurium* SPI-1 T3SS base<sup>65</sup>. The two concentric rings are 27 nm wide (PrgH ring) and 18 nm wide (PrgK)<sup>65</sup>. IR1 (PrgK + PrgH) is localized in the bacterial periplasm/IM, while IR2 (PrgH) is localized in the bacterial cytoplasm below the IM. PrgK contains a lipidated N-terminal domain that is anchored into the bacterial IM and a C-terminal transmembrane domain<sup>18</sup>. The atomic structure of the PrgK monomer was solved independently for its two globular domains: PrgK<sup>19-76</sup> (N-terminal domain) by solution NMR spectroscopy and PrgK<sup>98-200</sup> (C-terminal domain) by X-ray crystallography<sup>66</sup>. PrgH contains a cytoplasmic N-terminal domain and a C-terminal transmembrane/periplasmic domain. Crystal structures of PrgH<sup>11-119</sup> (cytoplasmic domain) and PrgH<sup>170-392</sup> (periplasmic domain) have been reported<sup>63</sup>. The cytoplasmic domain of PrgH and its *Shigella* homolog MixG contain a forkhead-associated domain that is commonly reported to bind phosphothreonine and is hypothesized to mediate protein-protein interactions of the base<sup>63; 67; 68</sup>. Nanogold

labeling of needle complexes has shown that PrgH and PrgK are topologically inverted with respect to each other<sup>65</sup>. Together, the atomic structures of the PrgK and PrgH monomers docked into EM maps of *in situ* needle complexes has led to an atomic model of the SPI-1 inner ring<sup>63; 66</sup> (**Fig. 1-4**).

The outer membrane rings and the neck are comprised of InvG (61.7 kDa), which is a member of the secretin family of outer membrane proteins<sup>65; 69</sup>. The N-terminus of InvG forms the neck of the base and extends downwards making contacts with the inner membrane ring (PrgH/PrgK), while the C-terminus extends upwards to form the outer membrane ring and neck<sup>63</sup>. The assembly and stability of InvG are aided by the lipoprotein pilotin InvH (16.4 kDa)<sup>69</sup>. The structure of the *Shigella* pilotin MxiM (InvH homolog) has been solved<sup>70</sup>. In addition, the periplasmic domain of InvG<sup>22-178</sup> has been solved by X-crystallography and allowed for an atomic model of the periplasmic ring of InvG that interacts with the inner membrane rings<sup>63</sup> (**Fig. 1-4**). The diameter of the 12-mer InvG is 15 nm<sup>71</sup>. Elucidation of the structure of the C-terminal region of InvG in the future will allow for an atomic model of the neck and outer membrane ring.

The mechanism of ring formation by PrgH, PrgK and InvG has been a topic of discussion for sometime. It has been suggested that electrostatic forces at the interface of a conserved protein domain with an  $\alpha\beta\alpha\beta$  configuration called the ring-building motif drive the oligomerization<sup>63; 72</sup>. However, this domain was not required for ring formation of the *Shigella* protein MixA (InvA homolog)<sup>73</sup>. It has also been suggested, at least with PrgK, that oligomerization is driven by domain-swapped interaction facilitated by a linker region<sup>66</sup>. For now there is no single mechanism of ring formation proposed and the mechanism of ring formation may be unique for each protein.

Enclosed in the neck of the base and linked to the needle is the ‘inner rod’ formed by the protein PrgJ (10.9 kDa). Direct binding has been observed by yeast two-hybrid mating analysis and GST pull-down assays between the inner rod YscI (PrgJ homolog) and the needle YscF (PrgI homolog) of *Y. pestis*<sup>74</sup>. The hypothesized role of the inner rod is to aid the regulator protein InvJ (36.4 kDa) in substrate switching and regulating needle length<sup>75; 76; 77; 78</sup>. Although the atomic structure of PrgJ is currently unknown, circular dichroism and solution NMR studies indicate that it is most likely a partially folded  $\alpha$ -helical protein (at least in monomer form) that is partially similar to the needle protein PrgI<sup>79</sup>. Currently, no structural information exists concerning the regulator protein InvJ or its homologs.

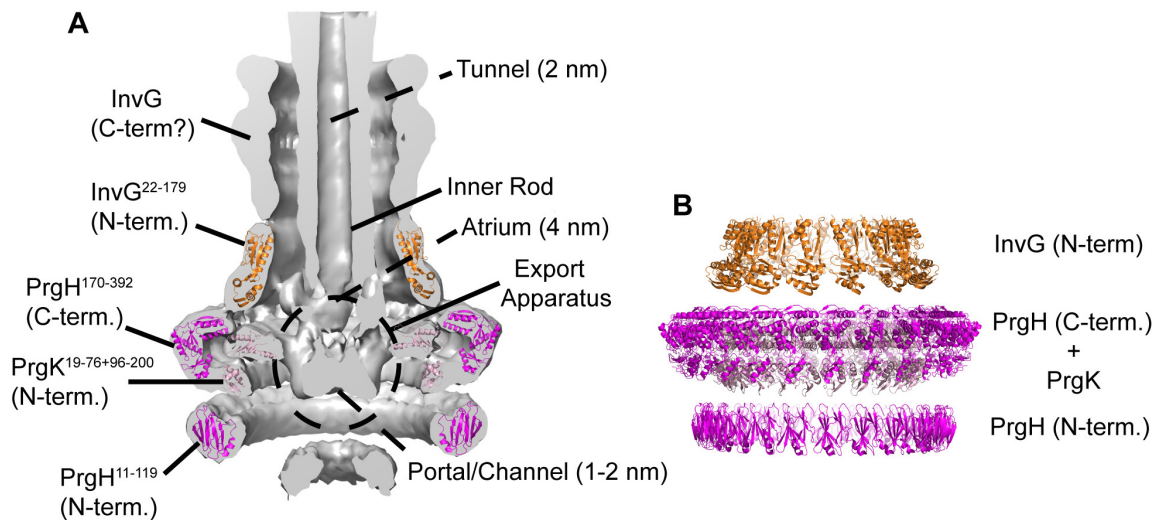


**Fig. 1-4 – Organization of the *Salmonella* T3SS SPI-1 Base**

(A) Cryoelectron tomography of an *in situ* injectisome from *S. Typhimurium* by Radics et al.<sup>80</sup> EMDB accession code is 2481. The map was processed with UCSF Chimera<sup>57</sup> and fitted with PyMol structures of the ring monomers. PDB accession codes are 3J6D (PrgK N-terminal domain), 4G1I (PrgH periplasmic C-terminal domain), 4G2S (PrgH cytoplasmic N-terminal domain) and 4G08 (InvG N-terminal domain). Adapted from Figure 1 in a reference by Galán et al.<sup>46</sup> (B) Modeled structures of InvG periplasmic ring (PDB 3J1V), PrgK+PrgH inner membrane ring (3J6D) and PrgH cytoplasmic ring (PDB 3J1W).

### 1.3.2. The Needle

The T3SS needle protrudes from the distal end of the base at the bacterial surface into the extracellular space. The role of the needle is to serve as a conduit for the translocation of bacterial effector proteins into the host cell. The needle is assembled from the polymerization of ~100 copies of PrgI (8.8 kDa) arranged in a helical manner<sup>81</sup>. The needle contains a channel that is 2.5 nm in diameter, which is large enough to accommodate two well-packed  $\alpha$ -helices. Therefore, most T3SS substrates must be unfolded to travel through the needle channel. EM studies show the wild-type *S. Typhimurium* SPI-1 T3SS needle displays a phenotype of Gaussian distribution of sizes between 30-70 nm (length) and 10-13 nm (width)<sup>77; 78</sup>. Interestingly, the length of the T3SS flagellar hook is regulated in a similar manner to the NF-T3SS needle<sup>82</sup>. The length of the NF-T3SS needle is hypothesized to be important in regulating efficiency of translocation, likely dependent on the ability to penetrate the host cell in the presence of elongated bacterial cell surface molecules, such as lipopolysaccharide and adhesins<sup>82; 83</sup>.

Initially, structural elucidation of recombinant forms of the needle monomers was not possible due to their tendency to spontaneously polymerize in solution<sup>84</sup>. However, it was found that deletion of five residues from the C-terminus (C $\Delta$ 5) decreased the ability of the needle monomer to polymerize<sup>85</sup>, which allowed for structure determination of the needle monomers of *Salmonella* PrgI<sup>86</sup>, *Shigella* MxiH<sup>85</sup>, and *Burkholderia* BsaL<sup>87</sup>. Unfortunately, the C $\Delta$ 5 mutation also decreased the ability of bacteria to invade intestinal epithelial cells *in vitro*<sup>88</sup>. Therefore, a soluble and functional PrgI V65A,V67A mutant was designed and its structure was determined<sup>88</sup>. In general, the structure of the needle monomers are conserved and consist of an  $\alpha$ -helical hairpin, where two helices are linked

by a short sequence, often containing a PXXP motif, where P is proline and X is any amino acid (**Fig. 1-5**). The N-terminus and C-terminus that flank the hairpin are flexible and disordered. Atomic structures of the needle monomers from *Pseudomonas* PscF<sup>89</sup> and *Yersinia* YscF<sup>90</sup> have also been solved. However, these needle monomer structures were solved in complex with their cognate chaperones, which have been hypothesized to prevent premature needle polymerization prior to secretion<sup>91</sup>. Chaperones have also been identified for other T3SS needle proteins. For example, EscE and EscG are chaperones to the *E. coli* needle filament protein EscF<sup>92</sup>. To date no chaperones have been reported for PrgI, MxiH or BsaL.

Elucidation of the structure of the polymerized needle began with cryo-EM/X-ray diffraction studies coupled with docking of atomic structures of the needle monomers. At first, these experiments generated low-resolution models of the *Salmonella* T3SS needle at 18Å<sup>93</sup> and *Shigella* needle at 16Å<sup>85</sup>. Currently, atomic models of the *Salmonella* needle at a precision of 0.5Å<sup>94</sup> and *Shigella* needle at a precision of 0.4Å<sup>95</sup> are available (**Fig. 1-6**). These high-resolution models were achieved through a combination of solid-state NMR spectroscopy, EM and Rosetta modeling. Results show that the structure of the polymerized *Salmonella* needle<sup>94</sup> and *Shigella* needle<sup>95</sup>, like the structure of the needle monomers, are extremely conserved. The needle is 8 nm wide with a 2.5 nm diameter channel lumen. Needle subunits are oriented in a right-handed 11-start helical manner with ~5.7 subunits per turn and a helical pitch of ~2.4 nm. Subunits stabilized by both intersubunit and intrasubunit contacts. The N-terminus is surface exposed, the PXXP motif containing linker is oriented upwards distal from the base and the C-terminus is facing towards the needle channel lumen. Residues that face towards the lumen are

highly conserved and polar. In contrast, residues facing the surface are weakly or non-conserved hydrophilic residues. The extreme C-terminal residue (Arg80 in PrgI and Arg83 in MxiH) places a positive charge into the channel. The electrostatic potential of the needle channel is hypothesized to aid in substrate progression through the channel<sup>96</sup>.

The needle proteins are also hypothesized to have additional functions. For example, they have been identified as ligands that elicit a host cell immune response through Toll-like receptor dependent cytokine release and inflammasome activation<sup>97; 98</sup>. The phenomenon of needle protein dependent host cellular signaling and cytokine release has been suggested to occur through an unknown mechanism involving the non-conserved N-terminus of T3SS needle proteins<sup>99</sup>. The needle is additionally hypothesized to serve as a potential mechanism where contact with the host cell is relayed down to the T3SS base by conformational changes in the needle<sup>100</sup>. In these models, the needle is not as rigid as previously thought, and instead is a semi-flexible filament. However, further experiments are needed to validate these hypotheses.

Regulation of the needle length is related to substrate switching. Because the needle protein is considered an early effector protein (PrgI itself is secreted to polymerize the needle), at some point the T3SS machinery undergoes a substrate switch from the needle protein to the tip/translocon and this process is connected to regulating the needle length. The regulator protein is known to play an essential role in substrate switching. In the absence of InvJ, the inner rod PrgJ cannot form, but abnormally long needles can assemble<sup>75</sup>. One hypothesis is InvJ measures length by being in an extended conformation in T3SS channel lumen. When the terminus of the protein reaches the end of the export apparatus/sorting platform it leads to substrate switching by an unknown

mechanism. This theory is partially supported by the observation that varying the length of *Yersinia* YscP (InvJ homolog) results in a different average distribution of needle lengths (for example, longer YscP led to longer needles)<sup>101</sup>. This ‘molecular ruler’ model is further supported by structural and functional studies of the *Pseudomonas* proteins PscP and PscU<sup>102</sup>. In addition, an alternative model has been proposed where InvJ aids in the formation of the socket of the base that allows for efficient inner rod formation and proper anchoring to the base. In this model, once PrgJ is properly assembled substrate switching occurs by an unknown mechanism. This ‘timer model’ is supported by the observation that mutations in PrgJ also lead to abnormally long needles, but substrate switching occurs and allows for a functional needle complex, unlike InvJ deletions<sup>75</sup>. More experimental evidence is required to determine which model of needle length regulation and substrate switching is correct.

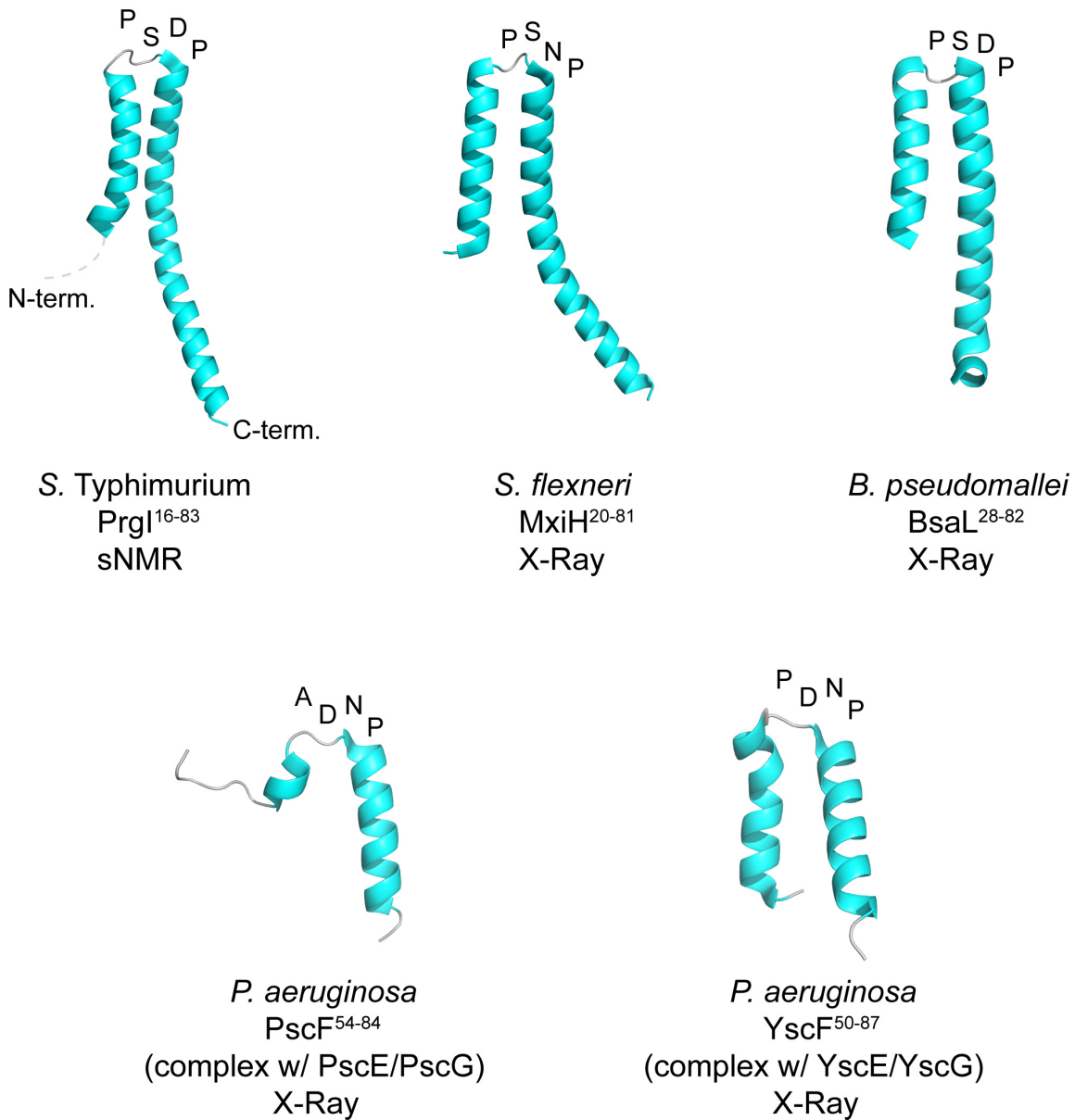


**Fig. 1-5 – Needle Monomer Structures**

Atomic structures of needle monomers are shown. Proteins are oriented with the N-terminus to the left and C-terminus to the right with  $\alpha$ -helix 1 and 2 colored in cyan. The termini are removed because they are highly flexible and/or disordered. The linker region is colored in grey and shows specific sequence for the PXXP motif for each protein. PDB accession codes are 2JOW (PrgI), 2CA5 (MxiH), 2G0U (BsaL), 2UWJ (PscF) and 2P58 (YscF).

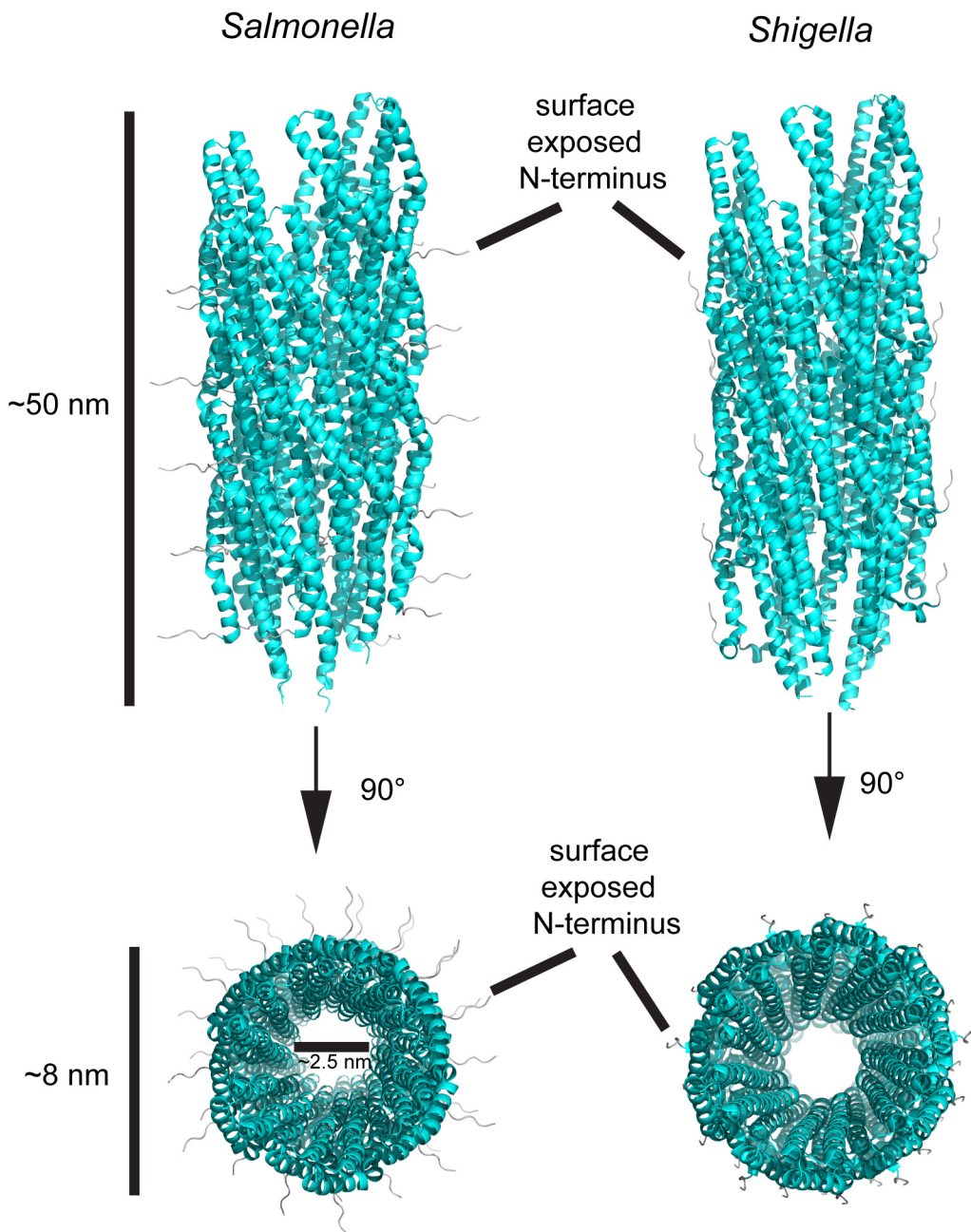


**Fig. 1-6 – Atomic Models of Polymerized T3SS SPI-1 Needles**

Atomic models of the polymerized *Salmonella*<sup>94</sup> and *Shigella*<sup>95</sup> needles are shown. Needles are oriented with the N-terminus (colored in cyan) as surface exposed, while the C-terminus faces the lumen. PDB accession codes are 2LPZ (*Salmonella* PrgI needle) and 2MME (*Shigella* MxiH needle).

### 1.3.3. The Tip Complex

At the distal end of the needle is the tip complex, comprised by the non-filamentous oligomerization of the protein SipD (36.5 kDa) in the *Salmonella* SPI-1 T3SS<sup>103</sup>. In other systems, such as the EspA (20.5 kDa) containing *E. coli* system<sup>104</sup>, the tip is an extended helical filament similar to the needle. The role of the tip complex is to sense contact with host cells<sup>105; 106</sup>, regulate effector protein secretion<sup>105; 107</sup> and act as a platform for the insertion of the translocon into the host membrane<sup>108; 109</sup>.

Tip monomers with known structures include *S. Typhimurium* SipD<sup>110</sup>, *S. flexneri* IpaD<sup>111</sup>, *B. pseudomallei* BipD<sup>111</sup>, *Y. pestis* LcrV<sup>112</sup>, *E. coli* EspA<sup>113</sup> and *C. trachomatis* CT584<sup>114</sup> (**Fig. 1-7**). SipD, IpaD and BipD contain a similar ‘dumb-bell’-like configuration. Each protein contains an N-terminal  $\alpha$ -helical hairpin, a central coiled-coil and a mixed  $\alpha/\beta$  domain (**Fig. 1-7**). LcrV (also called the V-antigen) contains the central coiled-coil domain and mixed  $\alpha/\beta$  domain, but contains a globular N-terminal domain in place of the N-terminal  $\alpha$ -helical hairpin<sup>112</sup> (**Fig. 1-7**). CT584 and EspA have even more divergent structures (**Fig. 1-7**). CT584 contains an N-terminal four  $\alpha$ -helix bundle, a three-stranded anti-parallel  $\beta$ -sheet and a C-terminal kinked  $\alpha$ -helical hairpin<sup>114</sup>. The structure of monomeric EspA (in complex with its chaperone CesA) is an extended two  $\alpha$ -helix bundle; similar to the central coiled-coil domains of other T3SS tips<sup>113</sup>. Each domain has been shown to have specific function. For SipD/IpaD/BipD, the N-terminal domain functions as a self-chaperone that prevents oligomerization within the bacterial cytoplasm and regulates interaction with other T3SS proteins<sup>111</sup>. The structure of the tip N-terminal hairpin domain is similar of the needle monomer structure and the needle is hypothesized to replace the tip N-terminal domain in the needle/tip complex during

effector translocation<sup>115; 116</sup>. In contrast, in the bacterial cytoplasm LcrV and EspA are in complexes with their cognate chaperones, LcrG<sup>117; 118</sup> and CesA, respectively<sup>119</sup>. The central coiled-coil of tip proteins have been shown to be essential for interactions with the needle protein<sup>115</sup>, as well as promoting self-oligomerization<sup>111</sup>.

Multiple models of the tip complex (oligomerized tip monomers) have been proposed. EM, cross-linking and docking of the crystal structure of IpaD (SipD homolog) led to a model of the *Shigella flexneri* SPI-1 T3SS tip complex<sup>120</sup>. The model proposed by Cheung and co-workers suggests four or five copies of IpaD form the tip complex, which has a 1 nm pore (slightly smaller than the 2.5 nm needle channel)<sup>121</sup>. This may represent a ‘closed’ translocation deficient conformation. The C-terminus of IpaD faces the channel lumen and the mixed  $\alpha/\beta$  domain is surface exposed (**Fig. 1-8**). It should be mentioned that their model lacks docking of the N-terminal domain of IpaD, although they argue there is EM density to fit the domain<sup>121</sup>. Interestingly, some of their tip complexes contained IpaB (the major translocon protein), though a significant proportion did not<sup>121</sup>. One hypothesis is that IpaB is unstable in the tip complex in the absence of necessary stabilizing factors, such as host membrane lipids. Whether IpaB is a true constituent of the tip complex remains to be shown. In agreement, low resolution EM of *Y. pestis* shows a pentameric LcrV tip complex<sup>122</sup>. The *E. coli* SPI-2 T3SS system is unique and contains a filamentous tip structure that is divergent from the more flat globular tip complex models of *Shigella* and *Yersinia*<sup>21</sup>. EspA has a similar coiled-coil  $\alpha$ -helical structure to the flagellin protein FliC and is hypothesized to assemble into a helical filamentous structure, though no model for the *E. coli* tip filament is currently available<sup>113</sup>.

Bile salts are present in high concentrations in the host intestines and have been shown to interact with some tip proteins. Examples of such bile salts are deoxycholate, taurodeoxycholate, and chenodeoxycholate. Interestingly, the binding of bile salts to *Salmonella* SipD and *Shigella* IpaD have opposite effects: invasiveness is increased in *Shigella*<sup>123; 124; 125</sup>, but repressed in *Salmonella*<sup>126</sup>. X-ray structures have been reported with deoxycholate interacting with SipD<sup>110; 116</sup> or IpaD<sup>127</sup>. Furthermore, solution NMR titrations between deoxycholate and SipD<sup>128</sup> or IpaD<sup>129</sup> have been reported. Results from NMR show that deoxycholate binds SipD under the mixed  $\alpha/\beta$  domain using a surface at the bottom of the coiled-coiled<sup>128</sup>. Although exact interacting residues are different, deoxycholate also binds at the bottom of the coiled-coil of SipD by crystallography<sup>110</sup> and with a SipD-PrgI fusion protein<sup>116</sup>. In contrast, NMR shows deoxycholate binds IpaD between N-terminal hairpin and the coiled-coiled<sup>129</sup>, while crystallography shows under the mixed  $\alpha/\beta$  domain at the bottom of the coiled-coiled<sup>127</sup>. Together, these data are inconclusive, but may suggest a difference in binding mode of deoxycholate with tip proteins that could potentially explain the difference invasiveness of *Salmonella* and *Shigella* in the presence of bile salts. Binding of bile salts to the tip protein is hypothesized to induce a conformational change that relays a signal back down to the T3SS apparatus that, by an unknown mechanism, promotes or inhibits effector secretion<sup>105</sup>.

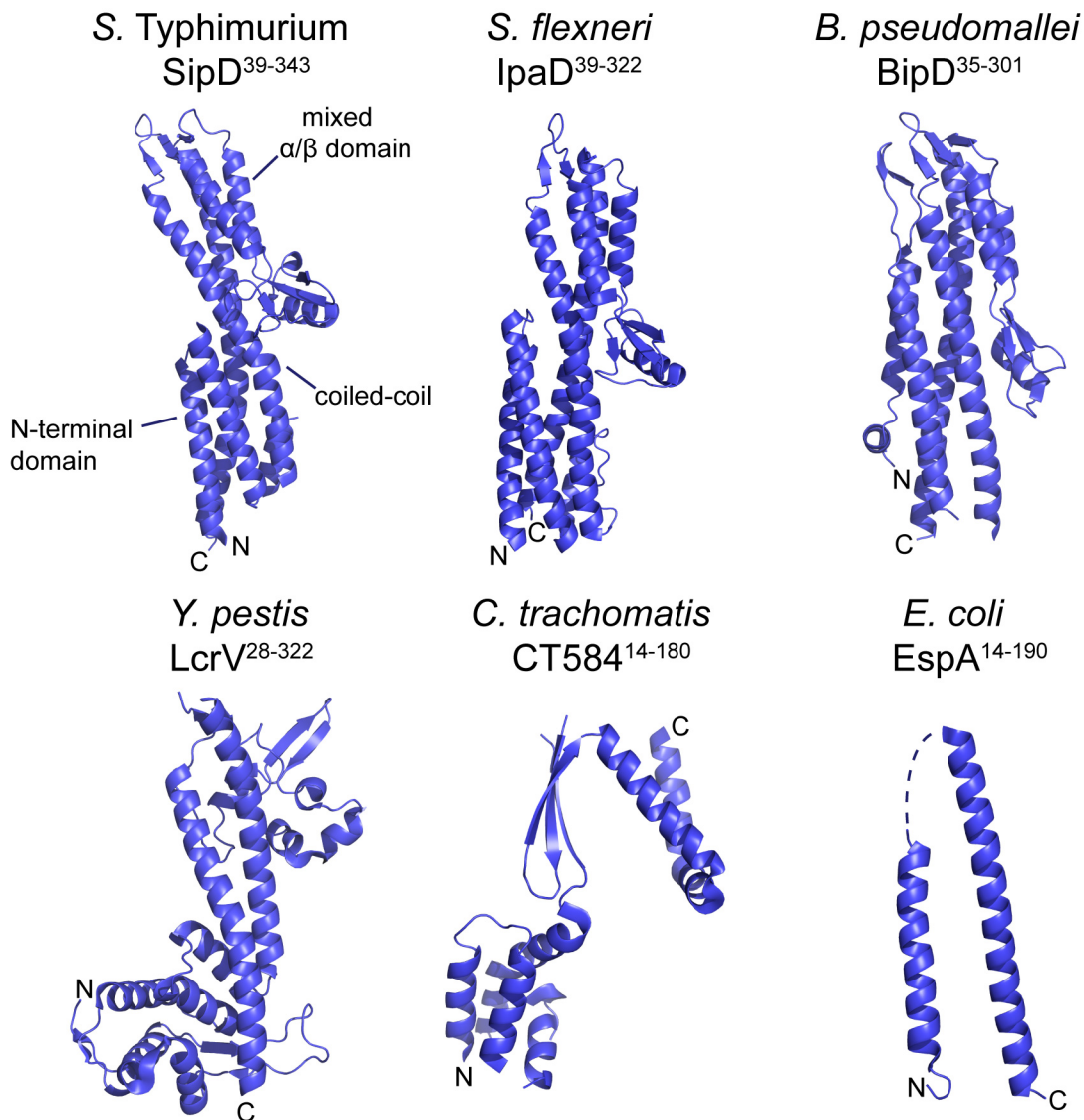


**Fig. 1-7 – Tip Monomer Structures**

Atomic structures of tip complex monomers are shown. Proteins are oriented with their N-terminal domain to the left. The N-terminus and C-terminus are labeled. PDB accession codes are 3NZZ (SipD), 2J0O (IpaD), 2J9T (BipD), 4JBU (LcrV), 4MLK (CT584) and 1XOU (EspA). SipD, IpaD and BipD are self-chaperoning proteins and have conserved structure that includes an N-terminal  $\alpha$ -helical hairpin, a central coiled-coil and a mixed  $\alpha/\beta$  domain. LcrV, CT584 and EspA have non-conserved structures. The chaperones for LcrV (LcrG) and EspA (CesA) are not shown. The chaperoning nature of CT584 is yet to be defined fully, but it is suggested to have some chaperoning capabilities<sup>130</sup>. Not shown is the structure of the tip protein from *Chromobacterium violaceum* (PDB ID 2P7N), which has a structure most resembling SipD/IpaD/BipD.

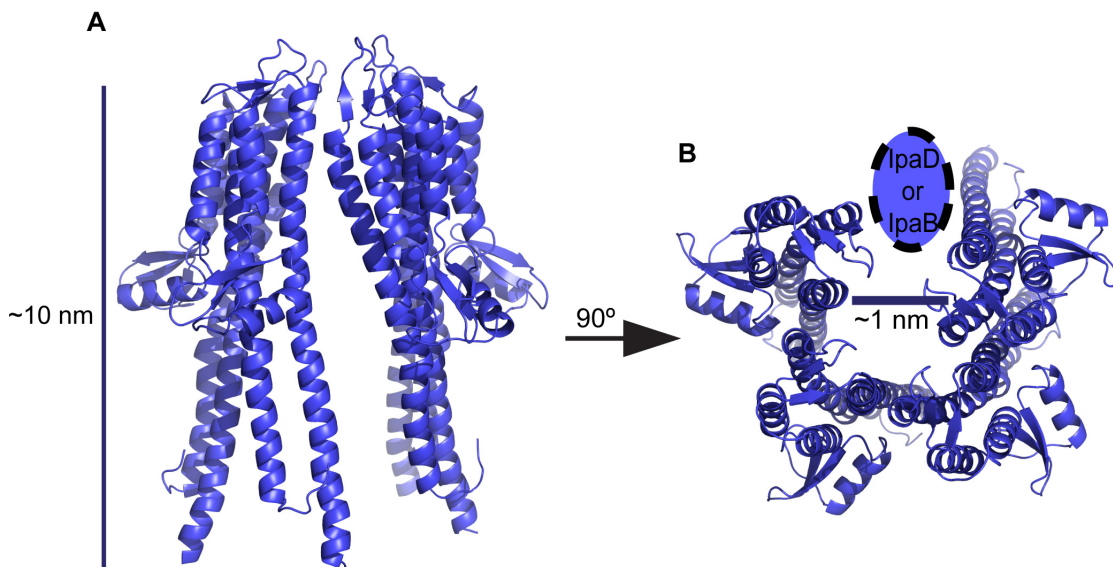


**Fig. 1-8 – Atomic Model of the *Shigella flexneri* T3SS SPI-1 Tip Complex**

A model of the *Shigella* tip complex is shown<sup>120</sup>. **(A)** Four subunits of IpaD are present with the C-terminus facing towards the channel lumen and the mixed  $\alpha/\beta$  domain surface exposed. **(B)** The authors suggest the other subunit (the ‘open space’, easily visible on complex visible from the top on the right of the image) could be either IpaD or IpaB (shown an ellipse with dotted line). PDB accession code is 4D3E.

#### 1.3.4. The Translocon

The tip complex is present on the bacterial surface at the distal end of the needle prior to contact with host cells<sup>103; 131; 132</sup>. Contact with the host cell is a trigger that promotes complete assembly of the T3SS apparatus by promoting the secretion and assembly of the translocon<sup>133</sup>. The translocon is a host cell membrane embedded pore created by bacterial T3SS proteins that serves as the final stage of passage for the delivery of effector proteins. The translocon is often said to be required for effector translocation, but dispensable for effector secretion. In this context, secretion is defined as protein transfer from the bacterial cytoplasm into the extracellular space, while translocation is defined as protein transfer from the bacterial cytoplasm into the host cell cytoplasm.

In the *S. Typhimurium* SPI-1 T3SS, the translocon is formed by two hydrophobic proteins, SipB (62.4 kDa) and SipC (44 kDa). Because of their difference in molecular weight and number of transmembrane regions, sometimes SipB is referred to as ‘major’ translocon component, whereas SipC is called the ‘minor’ translocon component. SipB contains an N-terminal coiled-coil region, two transmembrane regions and C-terminal amphipathic region<sup>134</sup>. The N-terminal region interacts with a chaperone, SicA, and has been shown to be responsible for self-oligomerization<sup>134</sup>. The SipB N-terminal domain is also implicated in being responsible for the interaction with the tip protein SipD<sup>135</sup>. The transmembrane and C-terminal regions are essential for interaction with host membrane components and SipC<sup>134; 136</sup>. The membrane topology of SipB suggests the N-terminal domain protrudes into the extracellular space<sup>137</sup>. SipC contains an N-terminal region, one transmembrane region and a C-terminal region<sup>138</sup>. The C-terminal region of SipC has

been shown to be important with binding of SipB<sup>139</sup>. Some reports in the literature consider the hydrophilic tip protein (SipD) as part of the translocon, although it has not been shown to insert into membranes<sup>133</sup>.

The atomic structures of the full-length translocon proteins have so far been difficult to solve due to poor stability or solubility issues in solution. However, partial structures of short major translocon peptides have been solved in complex with their cognate chaperones, such as IpaB<sup>16-72</sup> with IpgC and PopB<sup>51-59</sup> with PcrH.<sup>140; 141</sup> In addition, crystal structures of a protease resistant soluble N-terminal domain of *Salmonella* SipB and *Shigella* IpaB have been solved<sup>142</sup>. The structure of the N-terminal domain of SipB revealed an extended trimeric coiled-coil formed by three anti-parallel helices<sup>142</sup> (**Fig. 1-9**). Recently, a partial structure of *Aeromonas* AopB from residues 45 to 263 in complex with its cognate chaperone AcrH was solved by crystallography (**Fig 1-9**). This structure was unique in that it contained AopB transmembrane regions, which allowed for a working model of membrane insertion<sup>143</sup>.

Much less is known structurally about the minor translocon proteins. Short minor translocon peptides have been solved with their cognate chaperones, such as YopD<sup>56-65</sup> with SycD and PopD<sup>47-56</sup> with PcrH<sup>144; 145</sup>. The C-terminal amphipathic  $\alpha$ -helix of YopD<sup>278-300</sup> has also been solved by solution NMR<sup>146</sup> (**Fig. 1-9**). Even less is known about the assembled translocon complex. Atomic force microscopy of *E. coli* translocon in red blood cells suggests a complex of 6 to 8 total subunits with an outer diameter of 60 nm and a height of 20 nm<sup>147</sup>. The inner diameter of the pore has been estimated to be between 2 and 3.5 nm<sup>147; 148</sup>. These estimates correlate relatively well with the measured diameters of the needle (2.5 nm) and tip complex (1 nm) channels described in the above

sections. In *Pseudomonas*, single-molecule fluorescence photobleaching experiments suggests that the translocon proteins assemble a hexadecameric membrane complex with eight copies of PopB and eight copies of PopD.<sup>149</sup> Translocon proteins also have non-structural roles, such as serving as effector proteins. For example, SipC bundles F-actin in the host cytoplasm to promote invasion<sup>150; 151; 152</sup> and SipB induces macrophage programmed cell death through a caspase dependent mechanism<sup>153; 154</sup>.

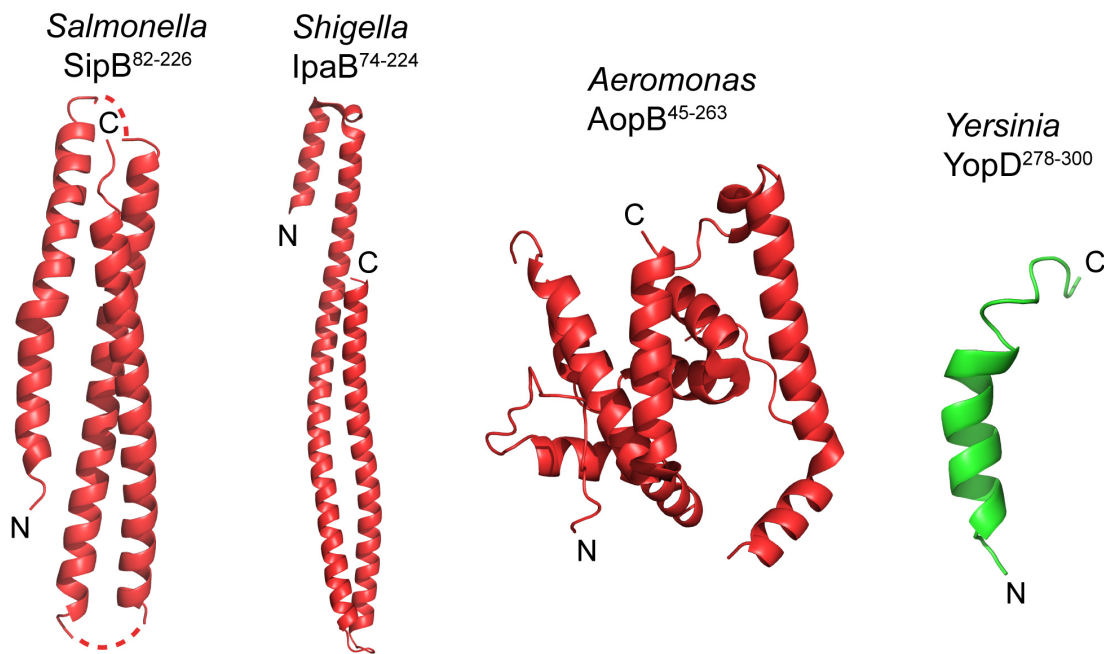


**Fig. 1-9 – Partial Structures of T3SS Translocon Proteins**

Partial structures of T3SS translocon components are shown. The N-terminal domain of the major translocon from *Salmonella*, *Shigella* and *Aeromonas* are shown in red with the N-terminus facing left. The AopB structure was solved in the presence of the chaperone AcrH (not shown here). The amphipathic helix from the minor translocon of *Yersinia* is shown on the right in green. PDB accession codes are 3TUL (SipB), 3U0C (IpaB), 3WXX (AopB) and 1KDL (YopD).

### 1.3.5. Assembly of the T3SS Apparatus

The assembly of the T3SS apparatus occurs in a hierarchal fashion<sup>155; 156</sup>. In the *Salmonella* SPI-1 T3SS, the stages of assembly are the following: *i*) assembly of the export apparatus, sorting platform and basal body, *ii*) assembly of the inner rod and needle, and *iii*) assembly of the tip and translocon<sup>156</sup>. T3SS apparatus assembly is initiated at the bacterial inner membrane by the export apparatus proteins SpaP, SpaR, SpaQ and SpaS<sup>156</sup>. The assembled export apparatus serves as a nucleation point for the formation of the inner membrane rings formed by PrgH and PrgK<sup>156</sup>. Next, the secretin InvG assembles the membrane outer rings with the help of the pilotin InvH<sup>65</sup>. This model is supported by several observations. First, the export apparatus can assemble in the absence of the rest of the needle complex<sup>156</sup>. Second, the inner membrane rings can assemble in the absence of the outer membrane secretin InvG<sup>65</sup>. Finally, *E. coli* EscC (InvG homolog) requires the inner membrane rings for efficient assembly<sup>157</sup>. The sorting platform (OrgA/OrgB/SpaO) has been suggested to exist as a pre-assembled complex prior to incorporation into the T3SS apparatus<sup>158</sup>. Incorporation of the ATPase InvC requires an assembled sorting platform<sup>56</sup>. Interestingly, the *Yersinia* Ysc apparatus is hypothesized to assemble by a reverse mechanism, where the outer membrane rings assemble first followed by the inner membrane rings, the export apparatus and sorting platform<sup>155</sup>. The final steps of assembly are not yet well established. However, it is thought that the inner rod PrgJ assembles, with the help InvJ, to serve as the inner channel of the base and serve as a platform for needle assembly<sup>159</sup>. The needle is polymerized by the addition of subunits at the growing distal end of the needle and is controlled by substrate switching. Protein refolding and conformational changes in the

needle monomer may be needed for efficient needle assembly<sup>88</sup>. The assembly of the translocon requires the tip protein<sup>109</sup>.

## 1.4. Functional Components of the T3SS

### 1.4.1. The Export Apparatus, Sorting Platform and Associated Proteins

The *Salmonella* SPI-1 T3SS export apparatus is comprised of the inner membrane proteins SpaP, SpaQ, SpaR, SpaS and InvA<sup>156</sup>. The assembled complex of these proteins is suggested to serve as the export channel for the entrance of T3SS substrates and as a docking platform for essential cytoplasmic components, such as the ATPase and inner rings<sup>156</sup>. Little is known about the structure and function of SpaP, SpaQ and SpaR. SpaS (40 kDa) is known as the T3SS autoprotease. SpaS contains an N-terminal domain that is associated with the inner membrane ring and a C-terminal domain that undergoes autoprotease cleavage to regulate substrate switching<sup>160; 161</sup>. SpaS cleavage occurs between Asp and Pro of a NPTH motif<sup>162</sup>. *Shigella* Spa40 cleavage (SpaS homolog) has been shown to be essential for interaction with other export apparatus proteins<sup>162</sup>. The C-terminal domain structure of SpaS and its *E. coli* homolog EscU have been solved<sup>163</sup>. In addition, structures of *Shigella* Spa40<sup>164</sup>, *Yersinia* YscU<sup>165</sup> and *Chlamydia* CdsU have been solved. InvA (76 kDa) is the largest member of the export apparatus and is hypothesized to form the export apparatus pore. InvA contains an N-terminal integral membrane domain linked to a C-terminal cytoplasmic domain. Structures of the monomeric C-terminal domain of InvA have been solved<sup>166; 167</sup>. In addition, crystal structure of the C-terminal cytoplasmic domain of the *Shigella* homolog MxiA revealed a nonameric ring with 15 nm width, 5 nm pore and 5.5 nm height<sup>73</sup>.

Below the export apparatus is the cytoplasmic hexameric ATPase InvC, which forms a complex with the sorting platform proteins SpaO, InvI, OrgA and OrgB<sup>168</sup>. The role of the ATPase is to promote chaperone release from their cognate T3SS effector proteins, as well to promote effector unfolding, in an ATP hydrolysis dependent manner<sup>55</sup>. The ATPase is hypothesized to be dispensable for T3SS secretion and instead is suggested to enhance secretion efficiency<sup>169</sup>. Known structures of NF-T3SS ATPases include *E. coli* hexameric EscN<sup>170</sup> and the *Salmonella* SPI-2 hexameric ATPase SsaN<sup>171</sup>. The roles of the other export apparatus proteins are not as well defined. InvI has been suggested to form the central stalk  $\gamma$  subunit of the ATPase<sup>172; 173</sup>. OrgB is suggested to form the peripheral stalk, while the function of OrgA is currently undefined<sup>172</sup>. SpaO is hypothesized to be the homolog to the flagellar C-ring. The structure of two C-terminal domains of SpaO have been recently solved by solution NMR, as well a complex between those SpaO domains and a peptide of OrgB<sup>174</sup>. Many electron microscopy studies of *in vitro* and *in situ* T3SS injectisomes failed to visualize densities of the export apparatus and sorting platform<sup>175</sup>. In contrast, *Shigella* mini-cells containing T3SS apparatuses allowed for visualization of the export apparatus/sorting platform densities<sup>56</sup>. Docking of atomic structures of sorting platform components allowed for the most complex model of the T3SS injectisome to date<sup>56</sup>.

#### 1.4.2. T3SS Chaperones

Many T3SS apparatus constituents and effectors, but not all, have cognate chaperones. In the context of the T3SS, chaperone proteins play many unique roles. First, they can deliver T3SS effectors to the ATPase/sorting platform at the cytoplasmic

interface with the base, after which they are released back into the cytoplasm<sup>55</sup>. Second, they can minimize interactions with other proteins in the bacterial cytoplasm, prevent premature oligomerization and inhibit degradation of T3SS effectors<sup>176</sup>. Unlike many eukaryotic chaperone proteins, T3SS chaperones do not usually directly contribute to protein folding or refolding.

Chaperones are categorized into different classes based on their structure and function<sup>177</sup>. The structures of many chaperones have been solved, some in complex with their cognate effector protein (**Table 1-4**). The definition of the chaperone classes varies in the literature, but three to five classes have been recognized. Class I chaperones are small (in the range of 15 kDa) acidic (pI of 4 to 5) cytoplasmic proteins that contain an  $\alpha$ - $\beta$ - $\beta$ - $\alpha$ - $\beta$ - $\beta$ - $\alpha$  fold<sup>178</sup>. The class is further divided in chaperones that interact with either one effector (class Ia) or multiple effectors (class Ib). Class II chaperones interact with the translocon proteins. Class III chaperones are sometimes considered as chaperones that bind to needle proteins<sup>62; 178</sup>, but have also been defined as specifically binding to flagellar proteins<sup>177</sup>. Other groups have referred to needle protein-binding chaperones as class V chaperones<sup>90</sup>. Class II and III/V chaperones contain many tetratricopeptide folds that are comprised of anti-parallel helices<sup>178</sup>. There are other chaperones that are so structurally distinct from other classes that they warrant their own class, such as the *E. coli* class IV chaperone CesA.

<b>Chaperone</b>	<b>Complexed with</b>	<b>Organism</b>	<b>Class</b>	<b>PDB ID</b>
InvB	SipA	<i>Salmonella</i>	IB	2FM8
SicP	SptP	<i>Salmonella</i>	IA	1JYO
SigE	n/a	<i>Salmonella</i>	IA	1K3S
IpgC	IpaB peptide	<i>Shigella</i>	II	3GZ2
Spa15	n/a	<i>Shigella</i>	IB	1RY9
CesT	n/a	<i>Escherichia</i>	IB	1K3E
CesAB	EspA	<i>Escherichia</i>	IV	1XOU
SycD [LcrH]	YopD peptide	<i>Yersinia</i>	II	4AM9
SycE	YopE	<i>Yersinia</i>	IA	1L2W
SycH	YopH	<i>Yersinia</i>	IB	4GF3
SycH	YscM2	<i>Yersinia</i>	IB	1TTW
SycN-YscB	YopN	<i>Yersinia</i>	IA	1XKP
SycT	n/a	<i>Yersinia</i>	IA	2BSJ
YscE-YscG	YscF	<i>Yersinia</i>	V	2P58
ExsC	ExsE	<i>Pseudomonas</i>	IA	3KXY
PcrH	PopB/PopD peptides	<i>Pseudomonas</i>	II	4JL0/2XC B
PscE-PscG	PscF	<i>Pseudomonas</i>	V	2UWJ
SpcS	ExoT	<i>Pseudomonas</i>	IA	4JMF
SpcU	ExoU	<i>Pseudomonas</i>	IA	3TU3
AscE-AscG	n/a	<i>Aeromonas</i>	V	3PH0
Scc3	CopN	<i>Chlamydia</i>	II	4NRH

**Table 1-4 – Atomic Structures of T3SS Chaperones**

Effector	T3SS	Biochemical Activity	Host Target(s)	Host Pathway(s) Influenced	PDB ID
GtgE	SPI-2	Cysteine protease	Rab29, Rab32, Rab38	SCV maintenance	4MI7
PipB2	SPI-1/2	?	Kinesin-1	SIF extension, SCV maintenance	2LEZ
SifA	SPI-2	GEF	Rab7, Rab9, RhoA, SKIP, Kinesin-1	SIF formation, SCV maintenance	3CXB 3HW2
SipA	SPI-1	Actin nucleator	F-actin, Caspase-3, T-plastin	Actin remodeling, Neutrophil migration	1Q5Z 2FM9
SipB	SPI-1	?	Caspase-1	Macrophage apoptosis	3TUL
SipC	SPI-1	Actin bundling	F-actin, Cytokeratins, Exo70, syntaxin-6	Actin remodeling, Neutrophil migration	n/a
SlrP	SPI-1/2	E3 ubiquitin ligase	ERdj3, Trx	Apoptosis	4PUF
SopA	SPI-1	E3 ubiquitin ligase	Caspase-3, HsRMA1, UbcH7	SCV escape, Neutrophil migration	2QZA 3SY2
SopB	SPI-1	Inositol phosphatase	Cdc24, Cdc42, Rac1, ANXA2, Rab5, VPS34	Membrane ruffling, SCV maturation	4DID
SopE	SPI-1	GEF	Cdc42, Rab5, Rac1	Actin remodeling	1GZS
SopE2	SPI-1	GEF	Cdc42, Rac1	Actin remodeling	1R9K
SptP	SPI-1	Tyrosine phosphatase	Cdc42, Rac1, VCP, Vimentin	MAPK inactivation, GTPase activation	1G4U
SpvB	SPI-2	ADP-ribosyltransferase	G-actin	SCV maintenance, Actin remodeling	2GWM
SpvC	SPI-1/2	Phosphothreonine lyase	ERK2, MAPK1, p38 JNK	MAPK inactivation	2Z8M
SrfH [SseI]	SPI-2	Acyhydrolase? Acytransferase?	Filamin A, IQGAP1, TRIP6	Macrophages migration, Dendritic cells migration	4G29
SrfJ	SPI-2	Glycoside Hydrolase	?	?	2WNW
SspH1	SPI-1/2	E3 ubiquitin ligase	PKN1	MAPK inactivation	4NKH
SspH2	SPI-2	E3 ubiquitin ligase	Filamin A, Profilin-1, UbcH5, 14-3-3, AIP, BAG2, BUB3, SGT1	Innate immune response	3G06

**Table 1-5: Atomic Structures of *Salmonella* Typhimurium T3SS Effectors**

A list of known *Salmonella* effector structures and their hypothesized functions and host cell targets. GEF - Guanine nucleotide-exchange factors. SIF – *Salmonella*-induced filaments. SCV – *Salmonella*-containing vacuole. Adapted from multiple references<sup>179; 180; 181; 182; 183</sup>

### 1.4.3. *Salmonella* Typhimurium T3SS Effectors

The main purpose of the T3SS is the translocation of effectors from the bacterial cytoplasm into the host cell. The effector proteins are the ‘work horse’ of the bacterium in the context of virulence, allowing for the initial invasion of host cells, as well as their prolonged maintenance and survival within the host. Targeting of T3SS effectors to the apparatus often depends on a structurally disordered N-terminal peptide signal sequence within the first 20 amino acids, but is also dependent on targeting via their cognate cytoplasmic chaperone<sup>184</sup>. Effectors are often specialized in each bacterium for their specific host environment infection niche. Furthermore, in bacteria that contain more than one T3SS system (such as the *Salmonella* SPI-1 and SPI-2 system), each T3SS may contain its own set of effectors with unique functions that regulate a certain stage of infection. The focus in this section is on *S. Typhimurium* effectors. Reviews of T3SS effector proteins in other bacterial systems can be obtained elsewhere<sup>180; 185; 186</sup>.

Effectors often fall into the following classes: *i*) host cytoskeleton regulators, *ii*) cell junction regulators, *iii*) *Salmonella*-containing vacuole regulators, *iv*) cell migration and cell death regulators, *v*) host transcriptional regulators, and *vi*) host immune response regulators. The currently known structures of T3SS effectors are summarized in **Table 1-5**. For an in depth review of the function of SPI-1 and SPI-2 *Salmonella* effectors refer to a reference by Ramos-Morales<sup>179</sup>. Briefly, host actin cytoskeleton is rearranged and remodeling by the activation of host cell Rho GTPases by SopE and SopB and by direct binding by SipA and SipC.<sup>183</sup> SipA, SopB and SopE contribute to the disruption of tight junctions by disrupting ZO-1 and occludin<sup>183</sup>. Biogenesis of the SCV is achieved with the help of SopB and SptP and maturation/maintenance of the SCV is dependent on SifA,

SseF and SseG, PipB2, SseJ and others<sup>183</sup>. SopA leads to transepithelial migration of neutrophils<sup>183</sup>. Epithelial cell death is promoted by AvrA, SopB, SpvB and SlrP. Macrophage cell death is promoted by SipB, SopB and PrgJ<sup>183</sup>. Transcriptional regulation of host cell genes and regulation of the host immune system occurs via an array of effectors, which includes SopB, SopE, SopE2, SipA, PipB, AvrA, SpvC, GogB and SseL<sup>179</sup>. In some cases, for example *Pseudomonas* ExoS and *Yersinia* YopE, a negative feedback mechanism for effector translocation control has been proposed where the effectors themselves are a signal for transcription and secretion<sup>187; 188</sup>.

### 1.5. Future Directions of T3SS Research

Bacterial T3SSs have been engineered as drug delivery platforms useful in biotherapeutic therapy. For example, the T3SS from *Salmonella* Typhimurium has been engineered in non-replicating nanoparticles derived from bacterial mini-cells and can deliver an antigen to eukaryotic cells both *in vitro* and *in vivo*<sup>189</sup>. Similar T3SS drug delivery platforms have been engineered in attenuated *Pseudomonas*<sup>190</sup> and *Yersinia*<sup>191</sup>. The application of this drug/antigen delivery scheme could treat diseases including viral infection<sup>192</sup>, bacterial infections<sup>193</sup>, cancer<sup>194</sup> and malaria<sup>195</sup>. Future research will further develop and evaluate bacterial T3SS based drug/antigen delivery systems.

Currently, T3SS proteins are under evaluation as potential vaccine candidates. The T3SS tip and needle are thought to be excellent candidate due to their surface presentation and contact with host cells during and prior to translocation<sup>196</sup>. Many T3SS proteins that have been shown to be immunogenic antigens, including *Salmonella* SipD, PrgI and SseB<sup>197; 198</sup>, *Shigella* IpaD, IpaB and MxiH<sup>198; 199</sup>, *Yersinia* LcrV<sup>200</sup>,

*Burkholderia* BipD, BsaL and BopE<sup>198; 201</sup>, *Pseudomonas* PcrV<sup>202</sup> and *Chlamydia* T3SS effector Tarp<sup>203</sup>. Further formulation and pre-clinical studies, including animal models, are needed to develop these T3SS proteins into potent vaccines. There are also a number of small molecules that have been discovered as T3SS inhibitors. These are reviewed in depth in Chapter 9. Together, vaccines and small molecules are potential avenues for the treatment and prevention of many diseases caused by T3SS harboring bacteria.

The amount of progress, as well as the wealth and speed of discoveries, made since the first visualization of the T3SS apparatus in 1998 (only 17 years ago) is a testament to the development of novel technologies and methods to solve new problems. However, much remains to be elucidated. There are many protein densities in current high-resolution cryo-EM maps that have not yet been accounted for (**Fig. 1-3**). Identification and localization of these unresolved T3SS components will allow for proper docking into those densities. Structures of many proteins are currently not known, including the full-length translocon proteins and components of the T3SS SPI-1 base. Structure elucidation of full-length proteins will likely require reconstitution in a membrane environment, such as liposomes or nanodiscs. Structures of many of the components of the SPI-2 apparatus remain to be solved. The ultimate goal is to develop a complete atomic model of the entire SPI-1 and SPI-2 needle apparatus.

The mechanism of secretion and activation of secretion are both poorly understood. For example, how are substrates recognized, unfolded at the T3SS base and fed into the export apparatus channel is unclear. A recently published cryo-EM of a substrate trapped T3SS has begun to resolve some questions<sup>204</sup>. Activation of secretion is hypothesized to require substrate switching, whose mechanism is not fully understood.

Furthermore, how contact with host cell membrane and extracellular molecules, such as bile salts, can relay a signal down to the T3SS base is unknown. Many T3SS effectors have been identified with unknown structures and functions that have yet to be defined. The fuel that powers the T3SS remains poorly understood. One possibility is energy derived from ATP hydrolysis by the ATPase during substrate unfolding may provide some energy for secretion<sup>46</sup>. Another mechanism has been hypothesized where proton motive force allows for rotation of the T3SS apparatus that aids in substrate travel through the channel<sup>205</sup>. These questions and more will drive T3SS research for many years to come.

## 1.6. References

1. Drakakaki, G. & Dandekar, A. (2013). Protein secretion: How many secretory routes does a plant cell have? *Plant Science* **203**, 74-78.
2. Kelly, R. B. (1985). Pathways of protein secretion in eukaryotes. *Science* **230**, 25-32.
3. Schneewind, O. & Missiakas, D. M. (2012). Protein secretion and surface display in Gram-positive bacteria. *Philos Trans R Soc Lond B Biol Sci* **367**, 1123-39.
4. Van Gijsegem, F., Genin, S. & Boucher, C. (1993). Conservation of secretion pathways for pathogenicity determinants of plant and animal bacteria. *Trends Microbiol* **1**, 175-80.
5. Gerlach, R. G. & Hensel, M. (2007). Protein secretion systems and adhesins: the molecular armory of Gram-negative pathogens. *Int J Med Microbiol* **297**, 401-15.
6. Lee, P. A., Tullman-Ercek, D. & Georgiou, G. (2006). The bacterial twin-arginine translocation pathway. *Annu Rev Microbiol* **60**, 373-95.
7. Costa, T. R., Felisberto-Rodrigues, C., Meir, A., Prevost, M. S., Redzej, A., Trokter, M. & Waksman, G. (2015). Secretion systems in Gram-negative bacteria: structural and mechanistic insights. *Nat Rev Microbiol* **13**, 343-359.
8. Baron, C. (2010). Antivirulence drugs to target bacterial secretion systems. *Current Opinion in Microbiology* **13**, 100-105.
9. Salmond, G. P. & Reeves, P. J. (1993). Membrane traffic wardens and protein secretion in gram-negative bacteria. *Trends Biochem Sci* **18**, 7-12.
10. Gemski, P., Lazere, J. R. & Casey, T. (1980). Plasmid associated with pathogenicity and calcium dependency of *Yersinia enterocolitica*. *Infect Immun* **27**, 682-5.

11. Gemski, P., Lazere, J. R., Casey, T. & Wohlhieter, J. A. (1980). Presence of a virulence-associated plasmid in *Yersinia pseudotuberculosis*. *Infect Immun* **28**, 1044-7.
12. Bolin, I. & Wolf-Watz, H. (1988). The plasmid-encoded Yop2b protein of *Yersinia pseudotuberculosis* is a virulence determinant regulated by calcium and temperature at the level of transcription. *Mol Microbiol* **2**, 237-45.
13. Michiels, T., Wattiau, P., Brasseur, R., Ruyschaert, J. M. & Cornelis, G. (1990). Secretion of Yop proteins by *Yersinia*. *Infect Immun* **58**, 2840-9.
14. Michiels, T. & Cornelis, G. R. (1991). Secretion of hybrid proteins by the *Yersinia* Yop export system. *J Bacteriol* **173**, 1677-85.
15. Isberg, R. R. & Falkow, S. (1985). A single genetic locus encoded by *Yersinia pseudotuberculosis* permits invasion of cultured animal cells by *Escherichia coli* K-12. *Nature* **317**, 262-4.
16. Galan, J. E. & Curtiss, R. (1989). Cloning and Molecular Characterization of Genes Whose Products Allow *Salmonella*-Typhimurium to Penetrate Tissue-Culture Cells. *Proceedings of the National Academy of Sciences of the United States of America* **86**, 6383-6387.
17. Galan, J. E. & Curtiss, R., 3rd. (1991). Distribution of the *invA*, -B, -C, and -D genes of *Salmonella typhimurium* among other *Salmonella* serovars: *invA* mutants of *Salmonella typhi* are deficient for entry into mammalian cells. *Infect Immun* **59**, 2901-8.
18. Kubori, T., Matsushima, Y., Nakamura, D., Uralil, J., Lara-Tejero, M., Sukhan, A., Galan, J. E. & Aizawa, S. (1998). Supramolecular structure of the *Salmonella typhimurium* type III protein secretion system. *Science* **280**, 602-605.
19. Chatterjee, S., Chaudhury, S., McShan, A. C., Kaur, K. & De Guzman, R. N. (2013). Structure and Biophysics of Type III Secretion in Bacteria. *Biochemistry* **52**, 2508-2517.
20. Cornelis, G. R. (2006). The type III secretion injectisome. *Nature Reviews Microbiology* **4**, 811-825.
21. Sekiya, K., Ohishi, M., Ogino, T., Tamano, K., Sasakawa, C. & Abe, A. (2001). Supermolecular structure of the enteropathogenic *Escherichia coli* type III secretion system and its direct interaction with the EspA-sheath-like structure. *Proc Natl Acad Sci U S A* **98**, 11638-43.
22. Soscia, C., Hachani, A., Bernadac, A., Filloux, A. & Bleves, S. (2007). Cross talk between type III secretion and flagellar assembly systems in *Pseudomonas aeruginosa*. *J Bacteriol* **189**, 3124-32.
23. Lindgren, P. B., Peet, R. C. & Panopoulos, N. J. (1986). Gene cluster of *Pseudomonas syringae* pv. "phaseolicola" controls pathogenicity of bean plants and hypersensitivity of nonhost plants. *J Bacteriol* **168**, 512-22.
24. Gopalan, S., Bauer, D. W., Alfano, J. R., Loniello, A. O., He, S. Y. & Collmer, A. (1996). Expression of the *Pseudomonas syringae* avirulence protein AvrB in plant cells alleviates its dependence on the hypersensitive response and pathogenicity (Hrp) secretion system in eliciting genotype-specific hypersensitive cell death. *Plant Cell* **8**, 1095-105.
25. Tang, X., Frederick, R. D., Zhou, J., Halterman, D. A., Jia, Y. & Martin, G. B. (1996). Initiation of Plant Disease Resistance by Physical Interaction of AvrPto and Pto Kinase. *Science* **274**, 2060-3.

26. Lackner, G., Moebius, N. & Hertweck, C. (2011). Endofungal bacterium controls its host by an hrp type III secretion system. *ISME J* **5**, 252-61.
27. Egan, F., Barret, M. & O'Gara, F. (2014). The SPI-1-like Type III secretion system: more roles than you think. *Frontiers in Plant Science* **5**.
28. Galan, J. E. & Collmer, A. (1999). Type III secretion machines: Bacterial devices for protein delivery into host cells. *Science* **284**, 1322-1328.
29. Brown, N. F. & Finlay, B. B. (2011). Potential origins and horizontal transfer of type III secretion systems and effectors. *Mob Genet Elements* **1**, 118-121.
30. Francis, M. S., Wolf-Watz, H. & Forsberg, A. (2002). Regulation of type III secretion systems. *Curr Opin Microbiol* **5**, 166-72.
31. Mavris, M., Page, A. L., Tournebize, R., Demers, B., Sansonetti, P. & Parsot, C. (2002). Regulation of transcription by the activity of the *Shigella flexneri* type III secretion apparatus. *Mol Microbiol* **43**, 1543-53.
32. Hueck, C. J. (1998). Type III protein secretion systems in bacterial pathogens of animals and plants. *Microbiol Mol Biol Rev* **62**, 379-433.
33. Gophna, U., Ron, E. Z. & Graur, D. (2003). Bacterial type III secretion systems are ancient and evolved by multiple horizontal-transfer events. *Gene* **312**, 151-163.
34. Abby, S. S. & Rocha, E. P. C. (2012). The Non-Flagellar Type III Secretion System Evolved from the Bacterial Flagellum and Diversified into Host-Cell Adapted Systems. *Plos Genetics* **8**.
35. Waterman, S. R. & Holden, D. W. (2003). Functions and effectors of the *Salmonella* pathogenicity island 2 type III secretion system. *Cellular Microbiology* **5**, 501-511.
36. Fookes, M., Schroeder, G. N., Langridge, G. C., Blondel, C. J., Mammina, C., Connor, T. R., Seth-Smith, H., Vernikos, G. S., Robinson, K. S., Sanders, M., Petty, N. K., Kingsley, R. A., Baumler, A. J., Nuccio, S. P., Contreras, I., Santiviago, C. A., Maskell, D., Barrow, P., Humphrey, T., Nastasi, A., Roberts, M., Frankel, G., Parkhill, J., Dougan, G. & Thomson, N. R. (2011). *Salmonella bongori* Provides Insights into the Evolution of the Salmonellae. *Plos Pathogens* **7**.
37. Ochman, H. & Groisman, E. A. (1996). Distribution of pathogenicity islands in *Salmonella* spp. *Infect Immun* **64**, 5410-2.
38. Abbott, S. L., Ni, F. C. & Janda, J. M. (2012). Increase in extraintestinal infections caused by *Salmonella enterica* subspecies II-IV. *Emerg Infect Dis* **18**, 637-9.
39. Garai, P., Gnanadhas, D. P. & Chakravorty, D. (2012). *Salmonella enterica* serovars Typhimurium and Typhi as model organisms Revealing paradigm of host-pathogen interactions. *Virulence* **3**, 377-388.
40. Hohmann, E. L. (2001). Nontyphoidal salmonellosis. *Clin Infect Dis* **32**, 263-9.
41. Martin, L. B. (2012). Vaccines for typhoid fever and other salmonellosis. *Curr Opin Infect Dis* **25**, 489-99.
42. Majowicz, S. E., Musto, J., Scallan, E., Angulo, F. J., Kirk, M., O'Brien, S. J., Jones, T. F., Fazil, A., Hoekstra, R. M. & International Collaboration on Enteric Disease 'Burden of Illness, S. (2010). The global burden of nontyphoidal *Salmonella* gastroenteritis. *Clin Infect Dis* **50**, 882-9.
43. Crump, J. A., Luby, S. P. & Mintz, E. D. (2004). The global burden of typhoid fever. *Bull World Health Organ* **82**, 346-53.

44. Fabrega, A. & Vila, J. (2013). Salmonella enterica serovar Typhimurium skills to succeed in the host: virulence and regulation. *Clin Microbiol Rev* **26**, 308-41.
45. Gerlach, R. G. & Hensel, M. (2007). Salmonella pathogenicity islands in host specificity, host pathogen-interactions and antibiotics resistance of Salmonella enterica. *Berl Munch Tierarztl Wochenschr* **120**, 317-27.
46. Galan, J. E., Lara-Tejero, M., Marlovits, T. C. & Wagner, S. (2014). Bacterial Type III Secretion Systems: Specialized Nanomachines for Protein Delivery into Target Cells. *Annual Review of Microbiology, Vol 68* **68**, 415-438.
47. Chakravorty, D., Rohde, M., Jager, L., Deiwick, J. & Hensel, M. (2005). Formation of a novel surface structure encoded by Salmonella Pathogenicity Island 2. *EMBO J* **24**, 2043-52.
48. Bao, X., Beatty, W. L. & Fan, H. (2012). Exploration of chlamydial type III secretion system reconstitution in Escherichia coli. *PLoS One* **7**, e50833.
49. Nans, A., Saibil, H. R. & Hayward, R. D. (2014). Pathogen-host reorganisation during Chlamydia invasion revealed by cryo-electron tomography. *Cell Microbiol*.
50. Deakin, W. J., Marie, C., Saad, M. M., Krishnan, H. B. & Broughton, W. J. (2005). NopA is associated with cell surface appendages produced by the type III secretion system of Rhizobium sp strain NGR234. *Molecular Plant-Microbe Interactions* **18**, 499-507.
51. Jin, Q. & He, S. Y. (2001). Role of the Hrp pilus in type III protein secretion in Pseudomonas syringae. *Science* **294**, 2556-8.
52. Mueller, C. A., Broz, P., Muller, S. A., Ringler, P., Erne-Brand, F., Sorg, I., Kuhn, M., Engel, A. & Cornelis, G. R. (2005). The V-antigen of Yersinia forms a distinct structure at the tip of injectosome needles. *Science* **310**, 674-6.
53. Tamano, K., Aizawa, S. & Sasakawa, C. (2002). Purification and detection of Shigella type III secretion needle complex. *Methods Enzymol* **358**, 385-92.
54. Galan, J. E. (1999). Interaction of Salmonella with host cells through the centisome 63 type III secretion system. *Curr Opin Microbiol* **2**, 46-50.
55. Akeda, Y. & Galan, J. E. (2005). Chaperone release and unfolding of substrates in type III secretion. *Nature* **437**, 911-915.
56. Hu, B., Morado, D. R., Margolin, W., Rohde, J. R., Arizmendi, O., Picking, W. L., Picking, W. D. & Liu, J. (2015). Visualization of the type III secretion sorting platform of Shigella flexneri. *Proc Natl Acad Sci U S A* **112**, 1047-52.
57. Goddard, T. D., Huang, C. C. & Ferrin, T. E. (2007). Visualizing density maps with UCSF Chimera. *J Struct Biol* **157**, 281-7.
58. Aizawa, S. I. (2001). Bacterial flagella and type III secretion systems. *FEMS Microbiol Lett* **202**, 157-64.
59. Buttner, D. (2012). Protein Export According to Schedule: Architecture, Assembly, and Regulation of Type III Secretion Systems from Plant- and Animal-Pathogenic Bacteria. *Microbiology and Molecular Biology Reviews* **76**, 262-310.
60. Gazi, A. D., Sarris, P. F., Fadouloglou, V. E., Charova, S. N., Mathioudakis, N., Panopoulos, N. J. & Kokkinidis, M. (2012). Phylogenetic analysis of a gene cluster encoding an additional, rhizobial-like type III secretion system that is narrowly distributed among Pseudomonas syringae strains. *BMC Microbiol* **12**, 188.
61. Sun, G. W. & Gan, Y. H. (2010). Unraveling type III secretion systems in the highly versatile Burkholderia pseudomallei. *Trends in Microbiology* **18**, 561-568.

62. Burkinshaw, B. J. & Strynadka, N. C. (2014). Assembly and structure of the T3SS. *Biochim Biophys Acta*.
63. Bergeron, J. R., Worrall, L. J., Sgourakis, N. G., Dimairo, F., Pfuetzner, R. A., Felise, H. B., Vuckovic, M., Yu, A. C., Miller, S. I., Baker, D. & Strynadka, N. C. (2013). A Refined Model of the Prototypical Salmonella SPI-1 T3SS Basal Body Reveals the Molecular Basis for Its Assembly. *PLoS Pathog* **9**, e1003307.
64. Hodgkinson, J. L., Horsley, A., Stabat, D., Simon, M., Johnson, S., da Fonseca, P. C. A., Morris, E. P., Wall, J. S., Lea, S. M. & Blocker, A. J. (2009). Three-dimensional reconstruction of the Shigella T3SS transmembrane regions reveals 12-fold symmetry and novel features throughout. *Nature Structural & Molecular Biology* **16**, 477-485.
65. Schraidt, O., Lefebvre, M. D., Brunner, M. J., Schmied, W. H., Schmidt, A., Radics, J., Mechtler, K., Galan, J. E. & Marlovits, T. C. (2010). Topology and Organization of the Salmonella typhimurium Type III Secretion Needle Complex Components. *Plos Pathogens* **6**.
66. Bergeron, J. R., Worrall, L. J., De, S., Sgourakis, N. G., Cheung, A. H., Lameignere, E., Okon, M., Wasney, G. A., Baker, D., McIntosh, L. P. & Strynadka, N. C. (2015). The modular structure of the inner-membrane ring component PrgK facilitates assembly of the type III secretion system basal body. *Structure* **23**, 161-72.
67. McDowell, M. A., Johnson, S., Deane, J. E., Cheung, M., Roehrich, A. D., Blocker, A. J., McDonnell, J. M. & Lea, S. M. (2011). Structural and Functional Studies on the N-terminal Domain of the Shigella Type III Secretion Protein MxiG. *Journal of Biological Chemistry* **286**, 30606-30614.
68. Barison, N., Lambers, J., Hurwitz, R. & Kolbe, M. (2012). Interaction of MxiG with the cytosolic complex of the type III secretion system controls Shigella virulence. *FASEB J* **26**, 1717-26.
69. Daefler, S. & Russel, M. (1998). The Salmonella typhimurium InvH protein is an outer membrane lipoprotein required for the proper localization of InvG. *Mol Microbiol* **28**, 1367-80.
70. Lario, P. I., Pfuetzner, R. A., Frey, E. A., Creagh, L., Haynes, C., Maurelli, A. T. & Strynadka, N. C. (2005). Structure and biochemical analysis of a secretin pilot protein. *EMBO J* **24**, 1111-21.
71. Crago, A. M. & Koronakis, V. (1998). Salmonella InvG forms a ring-like multimer that requires the InvH lipoprotein for outer membrane localization. *Molecular Microbiology* **30**, 47-56.
72. Spreter, T., Yip, C. K., Sanowar, S., Andre, I., Kimbrough, T. G., Vuckovic, M., Pfuetzner, R. A., Deng, W. Y., Yu, A. C., Finlay, B. B., Baker, D., Miller, S. I. & Strynadka, N. C. J. (2009). A conserved structural motif mediates formation of the periplasmic rings in the type III secretion system. *Nature Structural & Molecular Biology* **16**, 468-476.
73. Abrusci, P., Vergara-Irigaray, M., Johnson, S., Beeby, M. D., Hendrixson, D. R., Roversi, P., Friede, M. E., Deane, J. E., Jensen, G. J., Tang, C. M. & Lea, S. M. (2013). Architecture of the major component of the type III secretion system export apparatus. *Nat Struct Mol Biol* **20**, 99-104.
74. Yang, H., Tan, Y., Zhang, T., Tang, L., Wang, J., Ke, Y., Guo, Z., Yang, X., Yang, R. & Du, Z. (2013). Identification of Novel Protein-Protein Interactions of

Yersinia pestis Type III Secretion System by Yeast Two Hybrid System. *PLoS One* **8**, e54121.

75. Lefebvre, M. D. & Galan, J. E. (2014). The inner rod protein controls substrate switching and needle length in a Salmonella type III secretion system. *Proc Natl Acad Sci U S A* **111**, 817-22.

76. Wood, S. E., Jin, J. & Lloyd, S. A. (2008). YscP and YscU switch the substrate specificity of the Yersinia type III secretion system by regulating export of the inner rod protein YscI. *J Bacteriol* **190**, 4252-62.

77. Marlovits, T. C., Kubori, T., Lara-Tejero, M., Thomas, D., Unger, V. M. & Galan, J. E. (2006). Assembly of the inner rod determines needle length in the type III secretion injectisome. *Nature* **441**, 637-640.

78. Wee, D. H. & Hughes, K. T. (2015). Molecular ruler determines needle length for the Salmonella Spi-1 injectisome. *Proc Natl Acad Sci U S A* **112**, 4098-103.

79. Zhong, D., Lefebvre, M., Kaur, K., McDowell, M. A., Gdowski, C., Jo, S., Wang, Y., Benedict, S. H., Lea, S. M., Galan, J. E. & De Guzman, R. N. (2012). The Salmonella type III secretion system inner rod protein PrgJ is partially folded. *J Biol Chem* **287**, 25303-11.

80. Radics, J., Konigsmaier, L. & Marlovits, T. C. (2013). Structure of a pathogenic type 3 secretion system in action. *Nat Struct Mol Biol*.

81. Kubori, T., Sukhan, A., Aizawa, S. I. & Galan, J. E. (2000). Molecular characterization and assembly of the needle complex of the Salmonella typhimurium type III protein secretion system. *Proceedings of the National Academy of Sciences of the United States of America* **97**, 10225-10230.

82. Minamino, T. & Pugsley, A. P. (2005). Measure for measure in the control of type III secretion hook and needle length. *Mol Microbiol* **56**, 303-8.

83. Mota, L. J., Journet, L., Sorg, I., Agrain, C. & Cornelis, G. R. (2005). Bacterial injectisomes: Needle length does matter. *Science* **307**, 1278-1278.

84. Kenjale, R., Wilson, J., Zenk, S. F., Saurya, S., Picking, W. L., Picking, W. D. & Blocker, A. (2005). The needle component of the type III secretion apparatus of Shigella regulates the activity of the secretion apparatus. *J Biol Chem* **280**, 42929-37.

85. Deane, J. E., Roversi, P., Cordes, F. S., Johnson, S., Kenjale, R., Daniell, S., Booy, F., Picking, W. D., Picking, W. L., Blocker, A. J. & Lea, S. M. (2006). Molecular model of a type III secretion system needle: Implications for host-cell sensing. *Proc Natl Acad Sci U S A* **103**, 12529-33.

86. Wang, Y., Ouellette, A. N., Egan, C. W., Rathinavelan, T., Im, W. & De Guzman, R. N. (2007). Differences in the electrostatic surfaces of the type III secretion needle proteins PrgI, BsaL, and MxiH. *Journal of Molecular Biology* **371**, 1304-1314.

87. Zhang, L. L., Wang, Y., Picking, W. L., Picking, W. D. & De Guzman, R. N. (2006). Solution structure of monomeric BsaL, the type III secretion needle protein of Burkholderia pseudomallei. *Journal of Molecular Biology* **359**, 322-330.

88. Poyraz, O., Schmidt, H., Seidel, K., Delissen, F., Ader, C., Tenenboim, H., Goosmann, C., Laube, B., Thunemann, A. F., Zychlinsky, A., Baldus, M., Lange, A., Griesinger, C. & Kolbe, M. (2010). Protein refolding is required for assembly of the type three secretion needle. *Nature Structural & Molecular Biology* **17**, 788-U26.

89. Quinaud, M., Ple, S., Job, V., Contreras-Martel, C., Simorre, J. P., Attree, I. & Dessen, A. (2007). Structure of the heterotrimeric complex that regulates type III

- secretion needle formation. *Proceedings of the National Academy of Sciences of the United States of America* **104**, 7803-7808.
90. Sun, P., Tropea, J. E., Austin, B. P., Cherry, S. & Waugh, D. S. (2008). Structural characterization of the *Yersinia pestis* type III secretion system needle protein YscF in complex with its heterodimeric chaperone YscE/YscG. *J Mol Biol* **377**, 819-30.
91. Quinaud, M., Chabert, J., Faudry, E., Neumann, E., Lemaire, D., Pastor, A., Elsen, S., Dessen, A. & Attree, I. (2005). The PscE-PscF-PscG complex controls type III secretion needle biogenesis in *Pseudomonas aeruginosa*. *J Biol Chem* **280**, 36293-300.
92. Sal-Man, N., Setiapatra, D., Scholz, R., Deng, W., Yu, A. C., Strynadka, N. C. & Finlay, B. B. (2013). EscE and EscG are cochaperones for the type III needle protein EscF of enteropathogenic *Escherichia coli*. *J Bacteriol* **195**, 2481-9.
93. Galkin, V. E., Schmied, W. H., Schraidt, O., Marlovits, T. C. & Egelman, E. H. (2010). The Structure of the *Salmonella typhimurium* Type III Secretion System Needle Shows Divergence from the Flagellar System. *Journal of Molecular Biology* **396**, 1392-1397.
94. Loquet, A., Sgourakis, N. G., Gupta, R., Giller, K., Riedel, D., Goosmann, C., Griesinger, C., Kolbe, M., Baker, D., Becker, S. & Lange, A. (2012). Atomic model of the type III secretion system needle. *Nature* **486**, 276-+.
95. Demers, J. P., Habenstein, B., Loquet, A., Kumar Vasa, S., Giller, K., Becker, S., Baker, D., Lange, A. & Sgourakis, N. G. (2014). High-resolution structure of the *Shigella* type-III secretion needle by solid-state NMR and cryo-electron microscopy. *Nat Commun* **5**, 4976.
96. Rathinavelan, T., Zhang, L., Picking, W. L., Weis, D. D., De Guzman, R. N. & Im, W. (2010). A repulsive electrostatic mechanism for protein export through the type III secretion apparatus. *Biophys J* **98**, 452-61.
97. Jessen, D. L., Osei-Owusu, P., Toosky, M., Roughead, W., Bradley, D. S. & Nilles, M. L. (2014). Type III Secretion Needle Proteins Induce Cell Signaling and Cytokine Secretion via Toll-Like Receptors. *Infect Immun* **82**, 2300-9.
98. Yang, J., Zhao, Y., Shi, J. & Shao, F. (2013). Human NAIP and mouse NAIP1 recognize bacterial type III secretion needle protein for inflammasome activation. *Proc Natl Acad Sci U S A* **110**, 14408-13.
99. Osei-Owusu, P., Jessen Condry, D. L., Toosky, M., Roughead, W., Bradley, D. S. & Nilles, M. L. (2015). The N terminus of type III secretion needle protein YscF from *Yersinia pestis* functions to modulate innate immune responses. *Infect Immun* **83**, 1507-22.
100. Cordes, F. S., Komoriya, K., Larquet, E., Yang, S. X., Egelman, E. H., Blocker, A. & Lea, S. M. (2003). Helical structure of the needle of the type III secretion system of *Shigella flexneri*. *Journal of Biological Chemistry* **278**, 17103-17107.
101. Journet, L., Agrain, C., Broz, P. & Cornelis, G. R. (2003). The needle length of bacterial injectisomes is determined by a molecular ruler. *Science* **302**, 1757-60.
102. Bergeron, J. R., Fernandez, L., Wasney, G. A., Vuckovic, M., Reffuveille, F., Hancock, R. E. & Strynadka, N. C. (2016). The Structure of a Type 3 Secretion System (T3SS) Ruler Protein Suggests a Molecular Mechanism for Needle Length Sensing. *J Biol Chem* **291**, 1676-91.

103. Lara-Tejero, M. & Galan, J. E. (2009). Salmonella enterica Serovar Typhimurium Pathogenicity Island 1-Encoded Type III Secretion System Translocases Mediate Intimate Attachment to Nonphagocytic Cells. *Infection and Immunity* **77**, 2635-2642.
104. Knutton, S., Rosenshine, I., Pallen, M. J., Nisan, I., Neves, B. C., Bain, C., Wolff, C., Dougan, G. & Frankel, G. (1998). A novel EspA-associated surface organelle of enteropathogenic Escherichia coli involved in protein translocation into epithelial cells. *EMBO J* **17**, 2166-76.
105. Roehrich, A. D., Guillosoou, E., Blocker, A. J. & Martinez-Argudo, I. (2013). Shigella IpaD has a dual role: signal transduction from the type III secretion system needle tip and intracellular secretion regulation. *Molecular Microbiology* **87**, 690-706.
106. Veenendaal, A. K. J., Hodgkinson, J. L., Schwarzer, L., Stabat, D., Zenk, S. F. & Blocker, A. J. (2007). The type III secretion system needle tip complex mediates host cell sensing and translocon insertion. *Molecular Microbiology* **63**, 1719-1730.
107. Schiavolin, L., Meghraoui, A., Cherradi, Y., Biskri, L., Botteaux, A. & Allaoui, A. (2013). Functional insights into the Shigella type III needle tip IpaD in secretion control and cell contact. *Mol Microbiol*.
108. Costa, T. R. D., Edqvist, P. J., Broms, J. E., Ahlund, M. K., Forsberg, A. & Francis, M. S. (2010). YopD Self-assembly and Binding to LcrV Facilitate Type III Secretion Activity by Yersinia pseudotuberculosis. *Journal of Biological Chemistry* **285**, 25269-25284.
109. Goure, J., Pastor, A., Faudry, E., Chabert, J., Dessen, A. & Attree, I. (2004). The V antigen of Pseudomonas aeruginosa is required for assembly of the functional PopB/PopD translocation pore in host cell membranes. *Infect Immun* **72**, 4741-50.
110. Chatterjee, S., Zhong, D., Nordhues, B. A., Battaile, K. P., Lovell, S. & De Guzman, R. N. (2011). The crystal structures of the Salmonella type III secretion system tip protein SipD in complex with deoxycholate and chenodeoxycholate. *Protein Sci* **20**, 75-86.
111. Johnson, S., Roversi, P., Espina, M., Olive, A., Deane, J. E., Birket, S., Field, T., Picking, W. D., Blocker, A. J., Galyov, E. E., Picking, W. L. & Lea, S. M. (2007). Self-chaperoning of the type III secretion system needle tip proteins IpaD and BipD. *Journal of Biological Chemistry* **282**, 4035-4044.
112. Chaudhury, S., Battaile, K. P., Lovell, S., Plano, G. V. & De Guzman, R. N. (2013). Structure of the Yersinia pestis tip protein LcrV refined to 1.65 Å resolution. *Acta Crystallogr Sect F Struct Biol Cryst Commun* **69**, 477-81.
113. Yip, C. K., Finlay, B. B. & Strynadka, N. C. (2005). Structural characterization of a type III secretion system filament protein in complex with its chaperone. *Nat Struct Mol Biol* **12**, 75-81.
114. Barta, M. L., Hickey, J., Kemege, K. E., Lovell, S., Battaile, K. P. & Hefty, P. S. (2013). Structure of CT584 from Chlamydia trachomatis refined to 3.05 Å resolution. *Acta Crystallogr Sect F Struct Biol Cryst Commun* **69**, 1196-201.
115. Rathinavelan, T., Lara-Tejero, M., Lefebvre, M., Chatterjee, S., McShan, A. C., Guo, D. C., Tang, C., Galan, J. E. & De Guzman, R. N. (2014). NMR model of PrgI-SipD interaction and its implications in the needle-tip assembly of the Salmonella type III secretion system. *J Mol Biol* **426**, 2958-69.

116. Lunelli, M., Hurwitz, R., Lambers, J. & Kolbe, M. (2011). Crystal Structure of PrgI-SipD: Insight into a Secretion Competent State of the Type Three Secretion System Needle Tip and its Interaction with Host Ligands. *Plos Pathogens* **7**.
117. Lee, V. T., Tam, C. & Schneewind, O. (2000). LcrV, a substrate for *Yersinia enterocolitica* type III secretion, is required for toxin targeting into the cytosol of HeLa cells. *Journal of Biological Chemistry* **275**, 36869-36875.
118. Matson, J. S. & Nilles, M. L. (2001). LcrG-LcrV interaction is required for control of yops secretion in *Yersinia pestis*. *Journal of Bacteriology* **183**, 5082-5091.
119. Creasey, E. A., Friedberg, D., Shaw, R. K., Umanski, T., Knutton, S., Rosenshine, I. & Frankel, G. (2003). CesAB is an enteropathogenic *Escherichia coli* chaperone for the type-III translocator proteins EspA and EspB. *Microbiology* **149**, 3639-47.
120. Cheung, M., Shen, D. K., Makino, F., Kato, T., Roehrich, A. D., Martinez-Argudo, I., Walker, M. L., Murillo, I., Liu, X., Pain, M., Brown, J., Frazer, G., Mantell, J., Mina, P., Todd, T., Sessions, R. B., Namba, K. & Blocker, A. J. (2015). Three-dimensional electron microscopy reconstruction and cysteine-mediated crosslinking provide a model of the type III secretion system needle tip complex. *Mol Microbiol* **95**, 31-50.
121. Cheng, Q., Barboule, N., Frit, P., Gomez, D., Bombarde, O., Couderc, B., Ren, G. S., Salles, B. & Calsou, P. (2011). Ku counteracts mobilization of PARP1 and MRN in chromatin damaged with DNA double-strand breaks. *Nucleic Acids Research* **39**, 9605-9619.
122. Broz, P., Mueller, C. A., Muller, S. A., Philippsen, A., Sorg, I., Engel, A. & Cornelis, G. R. (2007). Function and molecular architecture of the *Yersinia* injectisome tip complex. *Mol Microbiol* **65**, 1311-20.
123. Stensrud, K. F., Adam, P. R., La Mar, C. D., Olive, A. J., Lushington, G. H., Sudharsan, R., Shelton, N. L., Givens, R. S., Picking, W. L. & Picking, W. D. (2008). Deoxycholate interacts with IpaD of *Shigella flexneri* in inducing the recruitment of IpaB to the type III secretion apparatus needle tip. *J Biol Chem* **283**, 18646-54.
124. Olive, A. J., Kenjale, R., Espina, M., Moore, D. S., Picking, W. L. & Picking, W. D. (2007). Bile salts stimulate recruitment of IpaB to the *Shigella flexneri* surface, where it colocalizes with IpaD at the tip of the type III secretion needle. *Infection and Immunity* **75**, 2626-2629.
125. Pope, L. M., Reed, K. E. & Payne, S. M. (1995). Increased Protein Secretion and Adherence to Hela-Cells by *Shigella* Spp Following Growth in the Presence of Bile-Salts. *Infection and Immunity* **63**, 3642-3648.
126. Prouty, A. M. & Gunn, J. S. (2000). *Salmonella enterica* serovar typhimurium invasion is repressed in the presence of bile. *Infection and Immunity* **68**, 6763-6769.
127. Barta, M. L., Guragain, M., Adam, P., Dickenson, N. E., Patil, M., Geisbrecht, B. V., Picking, W. L. & Picking, W. D. (2012). Identification of the bile salt binding site on IpaD from *Shigella flexneri* and the influence of ligand binding on IpaD structure. *Proteins-Structure Function and Bioinformatics* **80**, 935-945.
128. Wang, Y., Nordhues, B. A., Zhong, D. & De Guzman, R. N. (2010). NMR characterization of the interaction of the *Salmonella* type III secretion system protein SipD and bile salts. *Biochemistry* **49**, 4220-6.

129. Dickenson, N. E., Zhang, L., Epler, C. R., Adam, P. R., Picking, W. L. & Picking, W. D. (2011). Conformational changes in IpaD from *Shigella flexneri* upon binding bile salts provide insight into the second step of type III secretion. *Biochemistry* **50**, 172-80.
130. Pais, S. V., Milho, C., Almeida, F. & Mota, L. J. (2013). Identification of novel type III secretion chaperone-substrate complexes of *Chlamydia trachomatis*. *PLoS One* **8**, e56292.
131. Espina, M., Olive, A. J., Kenjale, R., Moore, D. S., Ausar, S. F., Kaminski, R. W., Oaks, E. V., Middaugh, C. R., Picking, W. D. & Picking, W. L. (2006). IpaD localizes to the tip of the type III secretion system needle of *Shigella flexneri*. *Infection and Immunity* **74**, 4391-4400.
132. Pettersson, J., Holmstrom, A., Hill, J., Leary, S., Frithz-Lindsten, E., von Euler-Matell, A., Carlsson, E., Titball, R., Forsberg, A. & Wolf-Watz, H. (1999). The V-antigen of *Yersinia* is surface exposed before target cell contact and involved in virulence protein translocation. *Mol Microbiol* **32**, 961-76.
133. Mattei, P. J., Faudry, E., Job, V., Izore, T., Attree, I. & Dessen, A. (2011). Membrane targeting and pore formation by the type III secretion system translocon. *Febs Journal* **278**, 414-426.
134. Hume, P. J., McGhie, E. J., Hayward, R. D. & Koronakis, V. (2003). The purified *Shigella* IpaB and *Salmonella* SipB translocators share biochemical properties and membrane topology. *Molecular Microbiology* **49**, 425-439.
135. Dickenson, N. E., Arizmendi, O., Patil, M. K., Toth, R. T. t., Middaugh, C. R., Picking, W. D. & Picking, W. L. (2013). N-Terminus of IpaB Provides a Potential Anchor to the *Shigella* Type III Secretion System Tip Complex Protein IpaD. *Biochemistry*.
136. Ryndak, M. B., Chung, H., London, E. & Bliska, J. B. (2005). Role of predicted transmembrane domains for type III translocation, pore formation, and signaling by the *Yersinia pseudotuberculosis* YopB protein. *Infect Immun* **73**, 2433-43.
137. McGhie, E. J., Hume, P. J., Hayward, R. D., Torres, J. & Koronakis, V. (2002). Topology of the *Salmonella* invasion protein SipB in a model bilayer. *Molecular Microbiology* **44**, 1309-1321.
138. Osiecki, J. C., Barker, J., Picking, W. L., Serfis, A. B., Berring, E., Shah, S., Harrington, A. & Picking, W. D. (2001). IpaC from *Shigella* and SipC from *Salmonella* possess similar biochemical properties but are functionally distinct. *Molecular Microbiology* **42**, 469-481.
139. Myeni, S. K., Wang, L. & Zhou, D. (2013). SipB-SipC complex is essential for translocon formation. *PLoS One* **8**, e60499.
140. Lokareddy, R. K., Lunelli, M., Eilers, B., Wolter, V. & Kolbe, M. (2010). Combination of Two Separate Binding Domains Defines Stoichiometry between Type III Secretion System Chaperone IpgC and Translocator Protein IpaB. *Journal of Biological Chemistry* **285**, 39965-39975.
141. Discola, K. F., Forster, A., Boulay, F., Simorre, J. P., Attree, I., Dessen, A. & Job, V. (2014). Membrane and chaperone recognition by the major translocator protein PopB of the type III secretion system of *Pseudomonas aeruginosa*. *J Biol Chem* **289**, 3591-601.
142. Barta, M. L., Dickenson, N. E., Patil, M., Keightley, A., Wyckoff, G. J., Picking, W. D., Picking, W. L. & Geisbrecht, B. V. (2012). The Structures of Coiled-Coil

- Domains from Type III Secretion System Translocators Reveal Homology to Pore-Forming Toxins. *Journal of Molecular Biology* **417**, 395-405.
143. Nguyen, V. S., Jobichen, C., Tan, K. W., Tan, Y. W., Chan, S. L., Ramesh, K., Yuan, Y., Hong, Y., Seetharaman, J., Leung, K. Y., Sivaraman, J. & Mok, Y. K. (2015). Structure of AcrH-AopB Chaperone-Translocator Complex Reveals a Role for Membrane Hairpins in Type III Secretion System Translocon Assembly. *Structure* **23**, 2022-31.
144. Schreiner, M. & Niemann, H. H. (2012). Crystal structure of the *Yersinia enterocolitica* type III secretion chaperone SycD in complex with a peptide of the minor translocator YopD. *Bmc Structural Biology* **12**.
145. Job, V., Mattei, P. J., Lemaire, D., Attree, I. & Dessen, A. (2010). Structural Basis of Chaperone Recognition of Type III Secretion System Minor Translocator Proteins. *Journal of Biological Chemistry* **285**, 23222-23230.
146. Tengel, T., Sethson, I. & Francis, M. S. (2002). Conformational analysis by CD and NMR spectroscopy of a peptide encompassing the amphipathic domain of YopD from *Yersinia*. *European Journal of Biochemistry* **269**, 3659-3668.
147. Ide, T., Laarmann, S., Greune, L., Schillers, H., Oberleithner, H. & Schmidt, M. A. (2001). Characterization of translocation pores inserted into plasma membranes by type III-secreted Esp proteins of enteropathogenic *Escherichia coli*. *Cellular Microbiology* **3**, 669-679.
148. Miki, T., Okada, N., Shimada, Y. & Danbara, H. (2004). Characterization of *Salmonella* pathogenicity island 1 type III secretion-dependent hemolytic activity in *Salmonella enterica* serovar Typhimurium. *Microbial Pathogenesis* **37**, 65-72.
149. Romano, F. B., Tang, Y., Rossi, K. C., Monopoli, K. R., Ross, J. L. & Heuck, A. P. (2016). Type 3 Secretion translocators spontaneously assemble a hexadecameric transmembrane complex. *J Biol Chem*.
150. Myeni, S. K. & Zhou, D. G. (2010). The C Terminus of SipC Binds and Bundles F-actin to Promote *Salmonella* Invasion. *Journal of Biological Chemistry* **285**, 13357-13363.
151. Chang, J. H., Myeni, S. K., Lin, T. L., Wu, C. C., Staiger, C. J. & Zhou, D. G. (2007). SipC multimerization promotes actin nucleation and contributes to *Salmonella*-induced inflammation. *Molecular Microbiology* **66**, 1548-1556.
152. Chang, J. H., Chen, J. & Zhou, D. G. (2005). Delineation and characterization of the actin nucleation and effector translocation activities of *Salmonella* SipC. *Molecular Microbiology* **55**, 1379-1389.
153. Hersh, D., Monack, D. M., Smith, M. R., Ghori, N., Falkow, S. & Zychlinsky, A. (1999). The *Salmonella* invasin SipB induces macrophage apoptosis by binding to caspase-1. *Proceedings of the National Academy of Sciences of the United States of America* **96**, 2396-2401.
154. Hernandez, L. D., Pypaert, M., Flavell, R. A. & Galan, J. E. (2003). A *Salmonella* protein causes macrophage cell death by inducing autophagy. *Journal of Cell Biology* **163**, 1123-1131.
155. Diepold, A. & Wagner, S. (2014). Assembly of the bacterial type III secretion machinery. *FEMS Microbiol Rev*.
156. Wagner, S., Konigsmaier, L., Lara-Tejero, M., Lefebvre, M., Marlovits, T. C. & Galan, J. E. (2010). Organization and coordinated assembly of the type III secretion

- export apparatus. *Proceedings of the National Academy of Sciences of the United States of America* **107**, 17745-17750.
157. Gauthier, A., Puente, J. L. & Finlay, B. B. (2003). Secretin of the enteropathogenic *Escherichia coli* type III secretion system requires components of the type III apparatus for assembly and localization. *Infect Immun* **71**, 3310-9.
158. Lara-Tejero, M., Kato, J., Wagner, S., Liu, X. Y. & Galan, J. E. (2011). A Sorting Platform Determines the Order of Protein Secretion in Bacterial Type III Systems. *Science* **331**, 1188-1191.
159. Sukhan, A., Kubori, T., Wilson, J. & Galan, J. E. (2001). Genetic analysis of assembly of the *Salmonella enterica* serovar typhimurium type III secretion-associated needle complex. *Journal of Bacteriology* **183**, 1159-1167.
160. Sorg, I., Wagner, S., Amstutz, M., Muller, S. A., Broz, P., Lussi, Y., Engel, A. & Cornelis, G. R. (2007). YscU recognizes translocators as export substrates of the *Yersinia injectisome*. *Embo Journal* **26**, 3015-3024.
161. Thomassin, J. L., He, X. & Thomas, N. A. (2011). Role of EscU auto-cleavage in promoting type III effector translocation into host cells by enteropathogenic *Escherichia coli*. *Bmc Microbiology* **11**.
162. Botteaux, A., Kayath, C. A., Page, A. L., Jouihri, N., Sani, M., Boekema, E., Biskri, L., Parsot, C. & Allaoui, A. (2010). The 33 carboxyl-terminal residues of Spa40 orchestrate the multi-step assembly process of the type III secretion needle complex in *Shigella flexneri*. *Microbiology-Sgm* **156**, 2807-2817.
163. Zarivach, R., Deng, W., Vuckovic, M., Felise, H. B., Nguyen, H. V., Miller, S. I., Finlay, B. B. & Strynadka, N. C. (2008). Structural analysis of the essential self-cleaving type III secretion proteins EscU and SpaS. *Nature* **453**, 124-7.
164. Deane, J. E., Graham, S. C., Mitchell, E. P., Flot, D., Johnson, S. & Lea, S. M. (2008). Crystal structure of Spa40, the specificity switch for the *Shigella flexneri* type III secretion system. *Mol Microbiol* **69**, 267-76.
165. Lountos, G. T., Austin, B. P., Nallamsetty, S. & Waugh, D. S. (2009). Atomic resolution structure of the cytoplasmic domain of *Yersinia pestis* YscU, a regulatory switch involved in type III secretion. *Protein Sci* **18**, 467-74.
166. Worrall, L. J., Vuckovic, M. & Strynadka, N. C. J. (2010). Crystal structure of the C-terminal domain of the *Salmonella* type III secretion system export apparatus protein InvA. *Protein Science* **19**, 1091-1096.
167. Lilic, M., Quezada, C. M. & Stebbins, C. E. (2010). A conserved domain in type III secretion links the cytoplasmic domain of InvA to elements of the basal body. *Acta Crystallographica Section D-Biological Crystallography* **66**, 709-713.
168. Lara-Tejero, M., Kato, J., Wagner, S., Liu, X. & Galan, J. E. (2011). A sorting platform determines the order of protein secretion in bacterial type III systems. *Science* **331**, 1188-91.
169. Erhardt, M., Mertens, M. E., Fabiani, F. D. & Hughes, K. T. (2014). ATPase-independent type-III protein secretion in *Salmonella enterica*. *PLoS Genet* **10**, e1004800.
170. Zarivach, R., Vuckovic, M., Deng, W. Y., Finlay, B. B. & Strynadka, N. C. J. (2007). Structural analysis of a prototypical ATPase from the type III secretion system. *Nature Structural & Molecular Biology* **14**, 131-137.
171. Allison, S. E., Tuinema, B. R., Everson, E. S., Sugiman-Marangos, S., Zhang, K., Junop, M. S. & Coombes, B. K. (2014). Identification of the Docking Site between a

- Type III Secretion System ATPase and a Chaperone for Effector Cargo. *Journal of Biological Chemistry* **289**, 23734-23744.
172. Romo-Castillo, M., Andrade, A., Espinosa, N., Feria, J. M., Soto, E., Diaz-Guerrero, M. & Gonzalez-Pedrajo, B. (2014). EscO, a Functional and Structural Analog of the Flagellar FliJ Protein, Is a Positive Regulator of EscN ATPase Activity of the Enteropathogenic *Escherichia coli* Injectisome. *Journal of Bacteriology* **196**, 2227-2241.
173. Evans, L. D. & Hughes, C. (2009). Selective binding of virulence type III export chaperones by FliJ escort orthologues InvI and YscO. *FEMS Microbiol Lett* **293**, 292-7.
174. Notti, R. Q., Bhattacharya, S., Lilic, M. & Stebbins, C. E. (2015). A common assembly module in injectisome and flagellar type III secretion sorting platforms. *Nat Commun* **6**, 7125.
175. Kawamoto, A., Morimoto, Y. V., Miyata, T., Minamino, T., Hughes, K. T., Kato, T. & Namba, K. (2013). Common and distinct structural features of *Salmonella* injectisome and flagellar basal body. *Sci Rep* **3**, 3369.
176. Letzelter, M., Sorg, I., Mota, L. J., Meyer, S., Stalder, J., Feldman, M., Kuhn, M., Callebaut, I. & Cornelis, G. R. (2006). The discovery of SycO highlights a new function for type III secretion effector chaperones. *EMBO J* **25**, 3223-33.
177. Parsot, C., Hamiaux, C. & Page, A. L. (2003). The various and varying roles of specific chaperones in type III secretion systems. *Curr Opin Microbiol* **6**, 7-14.
178. Thomas, N. A., Ma, I., Prasad, M. E. & Rafuse, C. (2012). Expanded roles for multicargo and class 1B effector chaperones in type III secretion. *J Bacteriol* **194**, 3767-73.
179. Ramos-Morales, F. (2012). Impact of *Salmonella enterica* Type III Secretion System Effectors on the Eukaryotic Host Cell. *ISRN Cell Biology*, 1-36.
180. Galan, J. E. (2007). SnapShot: Effector proteins of type III secretion systems. *Cell* **130**, 192-U5.
181. Tosi, T., Pflug, A., Discola, K. F., Neves, D. & Dessen, A. (2013). Structural basis of eukaryotic cell targeting by type III secretion system (T3SS) effectors. *Res Microbiol*.
182. LaRock, D. L., Chaudhary, A. & Miller, S. I. (2015). Salmonellae interactions with host processes. *Nat Rev Microbiol* **13**, 191-205.
183. Haraga, A., Ohlson, M. B. & Miller, S. I. (2008). Salmonellae interplay with host cells. *Nature Reviews Microbiology* **6**, 53-66.
184. Buchko, G. W., Niemann, G., Baker, E. S., Belov, M. E., Smith, R. D., Heffron, F., Adkins, J. N. & McDermott, J. E. (2010). A multi-pronged search for a common structural motif in the secretion signal of *Salmonella enterica* serovar Typhimurium type III effector proteins. *Molecular Biosystems* **6**, 2448-2458.
185. Trosky, J. E., Liverman, A. D. & Orth, K. (2008). *Yersinia* outer proteins: Yops. *Cell Microbiol* **10**, 557-65.
186. Mueller, K. E., Plano, G. V. & Fields, K. A. (2014). New frontiers in type III secretion biology: the *Chlamydia* perspective. *Infect Immun* **82**, 2-9.
187. Cisz, M., Lee, P. C. & Rietsch, A. (2008). ExoS controls the cell contact-mediated switch to effector secretion in *Pseudomonas aeruginosa*. *J Bacteriol* **190**, 2726-38.
188. Aili, M., Isaksson, E. L., Carlsson, S. E., Wolf-Watz, H., Rosqvist, R. & Francis, M. S. (2008). Regulation of *Yersinia* Yop-effector delivery by translocated YopE. *Int J Med Microbiol* **298**, 183-92.

189. Carleton, H. A., Lara-Tejero, M., Liu, X. & Galan, J. E. (2013). Engineering the type III secretion system in non-replicating bacterial minicells for antigen delivery. *Nat Commun* **4**, 1590.
190. Epaulard, O., Toussaint, B., Quenee, L., Derouazi, M., Bosco, N., Villiers, C., Le Berre, R., Guery, B., Filopon, D., Crombez, L., Marche, P. N. & Polack, B. (2006). Antitumor immunotherapy via antigen delivery from a live attenuated genetically engineered *Pseudomonas aeruginosa* type III secretion system-based vector. *Mol Ther* **14**, 656-61.
191. Russmann, H., Gerdemann, U., Igwe, E. I., Panthel, K., Heesemann, J., Garbom, S., Wolf-Watz, H. & Geginat, G. (2003). Attenuated *Yersinia pseudotuberculosis* carrier vaccine for simultaneous antigen-specific CD4 and CD8 T-cell induction. *Infect Immun* **71**, 3463-72.
192. Kotton, C. N., Lankowski, A. J., Scott, N., Sisul, D., Chen, L. M., Raschke, K., Borders, G., Boaz, M., Spentzou, A., Galan, J. E. & Hohmann, E. L. (2006). Safety and immunogenicity of attenuated *Salmonella enterica* serovar Typhimurium delivering an HIV-1 Gag antigen via the *Salmonella* Type III secretion system. *Vaccine* **24**, 6216-24.
193. Juarez-Rodriguez, M. D., Arteaga-Cortes, L. T., Kader, R., Curtiss, R., 3rd & Clark-Curtiss, J. E. (2012). Live attenuated *Salmonella* vaccines against *Mycobacterium tuberculosis* with antigen delivery via the type III secretion system. *Infect Immun* **80**, 798-814.
194. Nishikawa, H., Sato, E., Briones, G., Chen, L. M., Matsuo, M., Nagata, Y., Ritter, G., Jager, E., Nomura, H., Kondo, S., Tawara, I., Kato, T., Shiku, H., Old, L. J., Galan, J. E. & Gnjatic, S. (2006). In vivo antigen delivery by a *Salmonella typhimurium* type III secretion system for therapeutic cancer vaccines. *J Clin Invest* **116**, 1946-54.
195. Tartz, S., Russmann, H., Kamanova, J., Sebo, P., Sturm, A., Heussler, V., Fleischer, B. & Jacobs, T. (2008). Complete protection against *P. berghei* malaria upon heterologous prime/boost immunization against circumsporozoite protein employing *Salmonella* type III secretion system and *Bordetella adenylate cyclase* toxoid. *Vaccine* **26**, 5935-5943.
196. Markham, A. P., Barrett, B. S., Esfandiary, R., Picking, W. L., Picking, W. D., Joshi, S. B. & Middaugh, C. R. (2010). Formulation and Immunogenicity of a Potential Multivalent Type III Secretion System-Based Protein Vaccine. *Journal of Pharmaceutical Sciences* **99**, 4497-4509.
197. Reynolds, C. J., Jones, C., Blohmke, C. J., Darton, T. C., Goudet, A., Sergeant, R., Maillere, B., Pollard, A. J., Altmann, D. M. & Boyton, R. J. (2014). The serodominant secreted effector protein of *Salmonella*, SseB, is a strong CD4 antigen containing an immunodominant epitope presented by diverse HLA class II alleles. *Immunology* **143**, 438-46.
198. Barrett, B. S., Markham, A. P., Esfandiary, R., Picking, W. L., Picking, W. D., Joshi, S. B. & Middaugh, C. R. (2010). Formulation and Immunogenicity Studies of Type III Secretion System Needle Antigens as Vaccine Candidates. *Journal of Pharmaceutical Sciences* **99**, 4488-4496.
199. Martinez-Becerra, F. J., Chen, X. T., Dickenson, N. E., Choudhari, S. P., Harrison, K., Clements, J. D., Picking, W. D., Van De Verg, L. L., Walker, R. I. & Picking, W. L. (2013). Characterization of a Novel Fusion Protein from IpaB and IpaD of *Shigella* spp. and Its Potential as a Pan-*Shigella* Vaccine. *Infection and Immunity* **81**, 4470-4477.

200. Sun, W., Sanapala, S., Henderson, J. C., Sam, S., Olinzock, J., Trent, M. S. & Curtiss, R., 3rd. (2014). LcrV delivered via type III secretion system of live attenuated *Yersinia pseudotuberculosis* enhances immunogenicity against pneumonic plague. *Infect Immun* **82**, 4390-404.
201. Haque, A., Chu, K., Easton, A., Stevens, M. P., Galyov, E. E., Atkins, T., Titball, R. & Bancroft, G. J. (2006). A live experimental vaccine against *Burkholderia pseudomallei* elicits CD4+ T cell-mediated immunity, priming T cells specific for 2 type III secretion system proteins. *J Infect Dis* **194**, 1241-8.
202. Holder, I. A., Neely, A. N. & Frank, D. W. (2001). PcrV immunization enhances survival of burned *Pseudomonas aeruginosa*-infected mice. *Infect Immun* **69**, 5908-10.
203. Wang, J., Chen, L. L., Chen, F., Zhang, X. Y., Zhang, Y. Q., Baseman, J., Perdue, S., Yeh, I. T., Shain, R., Holland, M., Bailey, R., Mabey, D., Yu, P. & Zhong, G. M. (2009). A chlamydial type III-secreted effector protein (Tarp) is predominantly recognized by antibodies from humans infected with *Chlamydia trachomatis* and induces protective immunity against upper genital tract pathologies in mice. *Vaccine* **27**, 2967-2980.
204. Dohlich, K., Zumsteg, A. B., Goosmann, C. & Kolbe, M. (2014). A substrate-fusion protein is trapped inside the Type III Secretion System channel in *Shigella flexneri*. *PLoS Pathog* **10**, e1003881.
205. Ohgita, T., Hayashi, N., Hama, S., Tsuchiya, H., Gotoh, N. & Kogure, K. (2013). A novel effector secretion mechanism based on proton-motive force-dependent type III secretion apparatus rotation. *FASEB J* **27**, 2862-72.

## Chapter 2. Assignment of ILV Methyl Resonances of SipD<sup>Δ38</sup>

[Some of the data in this chapter has been published with the following citation: McShan AC, Kaur K, Chatterjee S, Knight KM, De Guzman RN. NMR Identification of the Binding Surfaces Involved in the Salmonella and Shigella Type III Secretion Tip-Translocon Protein-Protein Interactions. *Proteins*. 2016]

### 2.1. Introduction

SipD is the hydrophilic tip protein from the *Salmonella* Typhimurium SPI-1 T3SS (see section 1.3.3. for review). SipD is known to interact with T3SS apparatus components, including the needle protein PrgI<sup>1;2</sup> and the major translocon protein SipB<sup>3</sup>. SipD is also known to interact with biological molecules, such as bile salts<sup>4</sup>, to help regulate secretion of T3SS effectors. Furthermore, because SipD is present at the distal end of the needle and exposed to the extracellular environment prior to and during infection, it is an essential interaction hub and represents an excellent candidate for drug discovery<sup>5</sup>. SipD contains 343 amino acids and has a molecular weight of 37.1 kDa. The atomic structure of SipD has been solved by X-ray crystallography<sup>6;7</sup>. Unfortunately, it does not crystallize in complex with other T3SS proteins, such as PrgI and SipB, likely due to weak protein-protein interactions or presence of disordered regions. These observations prompted the characterization of the interaction between SipD with PrgI or SipB by NMR spectroscopy, due to the sensitivity of NMR to characterize protein interactions from nM to mM affinity<sup>8</sup> and availability for amino acid residue specific information. Backbone and side-chain amide resonances of SipD<sup>39-343</sup> C244S (herein called SipD<sup>Δ38</sup>) were assigned to 93% previously<sup>4</sup>. The N-terminal residues 1-38 were not included in the NMR construct of SipD<sup>Δ38</sup> because those residues were structurally disordered and interfered with obtaining good quality 2D <sup>1</sup>H-<sup>15</sup>N TROSY NMR data. Nevertheless, in the 2D <sup>1</sup>H-<sup>15</sup>N TROSY spectrum many SipD<sup>Δ38</sup> resonances were

overlapped due to the complexity of the spectra of a large protein (>300 NMR peaks), which made analysis of any interactions tedious and unreliable for overlapping residues. For this reason, we proposed to isotopically label SipD<sup>Δ38</sup> in such a manner that resulted in a less complex NMR spectrum, but still allowed for significant coverage of potential interaction surfaces. To this end, I chose isoleucine, leucine and valine (ILV) side-chain methyls. ILV <sup>13</sup>C-methyl labeling is a method that was developed and popularized by Lewis Kay and co-workers<sup>9</sup>. In this method, α-ketoacids, such as α-ketobutyrate and α-ketoisovalerate, serve as biosynthetic precursors for isotopically labeled Ile and Leu/Val side-chain methyl carbons, respectively<sup>10</sup> (**Fig. 2-1**). ILV methyl probes are useful because of the following: *i*) they allow for good correlations and favorable relaxation properties for high molecular weight proteins<sup>11</sup>, *ii*) are generally more sensitive than amide resonances because the signal averaging from three protons<sup>12</sup>, *iii*) are good probes to study protein dynamics<sup>13</sup>, and *iv*) reduce complexity of the system compared to amide labeling by reducing the number of peaks observed. Here, ILV <sup>13</sup>C-methyl labeled SipD<sup>Δ38</sup> was expressed and purified. Subsequently, the 2D <sup>1</sup>H-<sup>13</sup>C HSQC NMR spectrum of ILV methyl labeled SipD<sup>Δ38</sup> was acquired and the corresponding resonances were assigned by a combination of site-directed mutagenesis and 3D NMR.

## 2.2. Materials and Methods

### 2.2.1. Expression and Purification of Perdeuterated SipD<sup>Δ38</sup>

*Salmonella* Typhimurium strain SL1344 T3SS SPI-1 tip protein SipD<sup>Δ38</sup> was previously subcloned<sup>6</sup> into a modified pET-21a expression vector containing an N-terminal His<sub>6</sub> tag followed by a tobacco etch virus (TEV) protease cleavage site and β1

streptococcal protein G (GB1) as a solubility tag<sup>14</sup>. Isotopically labeled <sup>15</sup>N/ILV <sup>13</sup>C-methyl SipD<sup>Δ38</sup> (perdeuterated) was expressed in *E. coli* BL21(DE3) DNAY cells in 1 liter of 1× M9 minimal media with antibiotics in D<sub>2</sub>O at 37°C containing 1 g/L <sup>15</sup>NH<sub>4</sub>Cl (Sigma-Aldrich, St. Louis, MO) and 2 g/L deuterated d<sup>7</sup>-D-glucose (Cambridge Isotope Laboratories, Inc.). At an OD<sub>600</sub> of 0.4 the growth medium was supplemented with 60 mg of 2-ketobutyric acid-4-<sup>13</sup>C (#571342 Sigma; which labels the isoleucine <sup>13</sup>Cδ1 methyl group) and 100 mg of 2-keto-3-(methyl-<sup>13</sup>C)-butyric-4-<sup>13</sup>C acid (#571334 Sigma; which labels the leucine <sup>13</sup>Cδ and the valine <sup>13</sup>Cγ methyl groups) dissolved in 1 mL sterile water. This protocol was adapted from a previous ILV <sup>13</sup>C-methyl labeling protocol<sup>10</sup>. Recombinant protein expression was induced with 1 mM isopropyl-β-D-thiogalactopyrandoside (IPTG) at an OD<sub>600</sub> of 0.8 and cell growth was continued overnight at 15°C. Bacterial cells were harvested by centrifugation at 4000 rpm for 10 minutes, resuspended with 30 mL binding buffer (500 mM NaCl, 20 mM Tris-HCl, 5 mM imidazole, pH 8.0, 1 mM phenylmethanesulfonyl fluoride) and sonicated on ice. Sonication was performed using a Branson Digital Sonifier for 5 minutes and 20 seconds at amplitude 32% with 2 second on pulses and 6 second off pulses. The cell lysate was centrifuged for 10 minutes at 13000 rpm. Next, 700 μL of 5% (v/v) polyethyleneimine was added to the supernatant, which was centrifuged again to remove further cellular debris. The supernatant was loaded onto a 10 mL Ni<sup>2+</sup>-affinity chromatography column (Gold Biotechnology), the column was washed with 150 mL binding buffer (500 mM NaCl, 20 mM Tris-HCl, 5 mM imidazole, pH 8.0) and bound protein was eluted with 40 mL elution buffer (500 mM NaCl, 20 mM Tris-HCl, 250 mM imidazole, pH 8.0). Eluted proteins was then incubated in 250 μL of 0.04 mM recombinant TEV protease in TEV

protease buffer (50 mM Tris-HCl, pH 8.0, 0.5 mM EDTA, 1 mM DTT, 20 mM NaCl) at 20°C overnight and then purified by Ni<sup>2+</sup>-affinity chromatography to separate protein from the affinity tag. All purified proteins were dialyzed into NMR buffer (see below) and concentrated using Amicon Ultra 3K (Millipore) filtration columns. Protein concentrations were measured by the absorbance at A<sub>280</sub>.

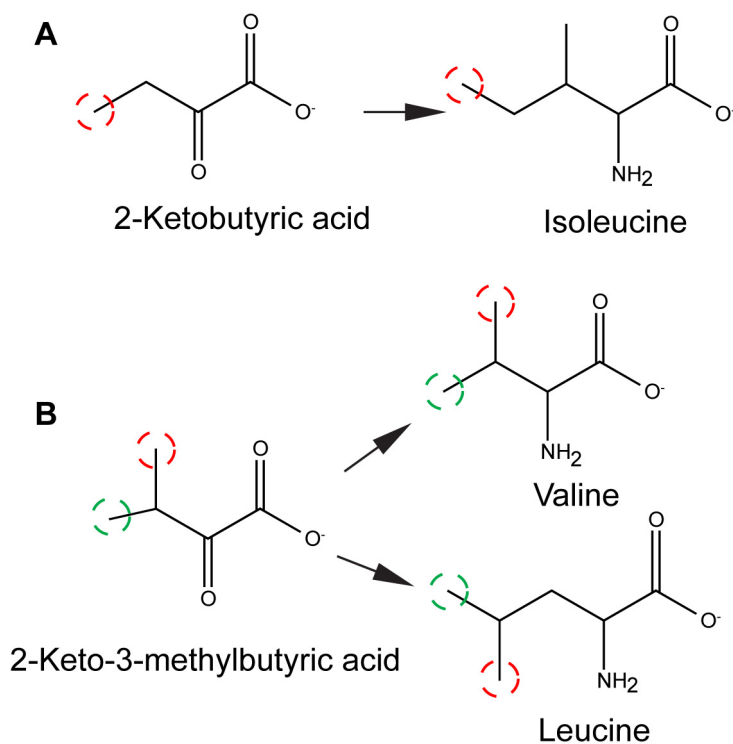


**Fig. 2-1 – ILV Side-Chain Methyl Isotope Labeling Strategy**

(A) 2-ketobutyric acid is a precursor for the labeling of isoleucine methyl carbon  $\delta 1$  (red dotted circle). One methyl carbon atom is labeled. Therefore one NMR peak is observed for each Ile in a 2D <sup>1</sup>H-<sup>13</sup>C HSQC experiment. (B) 2-keto-3-methylbutyric acid ( $\alpha$ -ketoisovalerate) is a precursor for the labeling of valine methyl carbons  $\gamma 1$  and  $\gamma 2$  and leucine methyl carbons  $\delta 1$  and  $\delta 2$  (green and red dotted circles). Two methyl carbon atoms are labeled on each amino acid. Therefore two NMR peaks are observed for each Val and Leu in a 2D <sup>1</sup>H-<sup>13</sup>C HSQC experiment. Structures created in ChemBioDraw 14.

### 2.2.2. $^1\text{H}$ - $^{13}\text{C}$ HSQC of Perdeuterated SipD $^{\Delta 38}$

Data was collected using a Bruker Avance 800 MHz spectrometer equipped with a cryogenic triple resonance probe and were processed using NMRPipe<sup>15</sup> and analyzed using NMRView<sup>16</sup>. As a reference for the 3D HMQC-NOESY, a high quality 2D  $^1\text{H}$ - $^{13}\text{C}$  HSQC spectra (pulse sequence hsqcetgp) was acquired using 0.9 mM perdeuterated  $^{15}\text{N}$ /ILV  $^{13}\text{C}$ -methyl labeled SipD $^{\Delta 38}$  dissolved in NMR buffer (20 mM NaCl, 10 mM sodium phosphate, pH 7.4) then lyophilized and resuspended in 100% (v/v) D<sub>2</sub>O at 30°C. Acquisition parameters were 8 scans with 1024 complex points ( $^1\text{H}$ ) and 256 complex points ( $^{13}\text{C}$ ) with sweep width 10.01 ppm for  $^1\text{H}$  centered at 4.69 ppm and 20 ppm for  $^{13}\text{C}$  centered at 19 ppm.

### 2.2.3. 3D $^{13}\text{C}$ - $^1\text{H}$ - $^{13}\text{C}$ HMQC-NOESY-HMQC of Perdeuterated SipD $^{\Delta 38}$

For 3D NMR data acquisition, 0.9 mM perdeuterated  $^{15}\text{N}$ /ILV  $^{13}\text{C}$ -methyl labeled SipD $^{\Delta 38}$  was dissolved in NMR buffer then lyophilized and resuspended in 100% (v/v) D<sub>2</sub>O. The 3D  $^1\text{H}$ - $^{13}\text{C}$  HMQC-NOESY experiment was acquired using 8 scans with 2048 complex points ( $^1\text{H}$ ), 80 complex points ( $^{13}\text{C}$ ) and 100 complex points (NOE  $^{13}\text{C}$ ) with a mixing time (D8) of 300 milliseconds and relaxation delay (D1) of 2 seconds. Sweep widths were 10.01 ppm for  $^1\text{H}$  centered at 4.69 ppm and 20.0 ppm for  $^{13}\text{C}$  centered at 19.0 ppm.

### 2.2.4. Assignment Strategy and Data Analysis

ILV methyls were assigned using a methodology reported by Xiao and co-workers<sup>17</sup>. First, isoleucine-to-leucine point mutants of SipD $^{\Delta 38}$  were created using

Quikchange kit (Stratagene) and confirmed by DNA sequencing. Ile-to-Leu mutants provided Ile methyl assignments as an anchor of stereospecific Leu/Val methyl resonance assignments from through-space  $^1\text{H}$ - $^1\text{H}$  nuclear Overhauser effects (NOEs) observed in the 3D HMQC-NOESY experiment in combination with distance information from the previously determined X-ray crystal structure of SipD $^{\Delta 38}$  (PDB ID 3NZZ). NMR data acquisition for SipD $^{\Delta 38}$  Ile-to-Leu point mutants was similar to that described in section 2.2.2.

## 2.3. Results

### 2.3.1. SipD $^{\Delta 38}$ Purification and Ile Methyl Assignments

Analysis of the position of ILV residues on the crystal structure of SipD $^{\Delta 38}$  showed that ILVs covered most surfaces of the protein, suggesting that ILV methyls were a suitable probe for interaction studies involving SipD (**Fig. 2-2**). Notably, one surface remained relatively free of ILVs: the side of helix  $\alpha_8$  facing the surface of the SipD (**Fig. 2-2**). SipD $^{\Delta 38}$  contains 12 isoleucines, 33 leucines and 18 valines. Therefore, the 2D  $^1\text{H}$ - $^{13}\text{C}$  HSQC spectrum of ILV  $^{13}\text{C}$ -methyl labeled SipD $^{\Delta 38}$  was expected to show 114 NMR peaks (12 Ile + 2x33 Leu + 2x18 Val).

To serve as an anchor point for assignment of Leu/Val methyl resonances in the 2D  $^1\text{H}$ - $^{13}\text{C}$  HSQC SipD $^{\Delta 38}$  spectrum, 12 Ile-to-Leu point mutations of SipD $^{\Delta 38}$  were created. Point mutants were constructed using site-directed mutagenesis and confirmed with DNA sequencing. Each SipD $^{\Delta 38}$  Ile-to-Leu point mutant was expressed and purified. A representative example of the purification of perdeuterated SipD $^{\Delta 38}$  is shown in **Fig. 2-3**. Two-dimensional  $^1\text{H}$ - $^{13}\text{C}$  HSQC NMR datasets were acquired for each SipD $^{\Delta 38}$  point

mutant. In those experiments, one Ile methyl peak was expected to disappear from the Ile methyl region of the HSQC spectrum (the average chemical shift of ile  $\delta 1$  carbon is 13.5 ppm and  $\delta 1$  proton is 0.67 ppm)<sup>18</sup>, hence its corresponding assignment. Four examples of the Ile-to-Leu mutagenesis assignment strategy can be seen in **Fig. 2-4**. In this manner the 12 isoleucine of SipD <sup>$\Delta 38$</sup>  were unambiguously assigned.

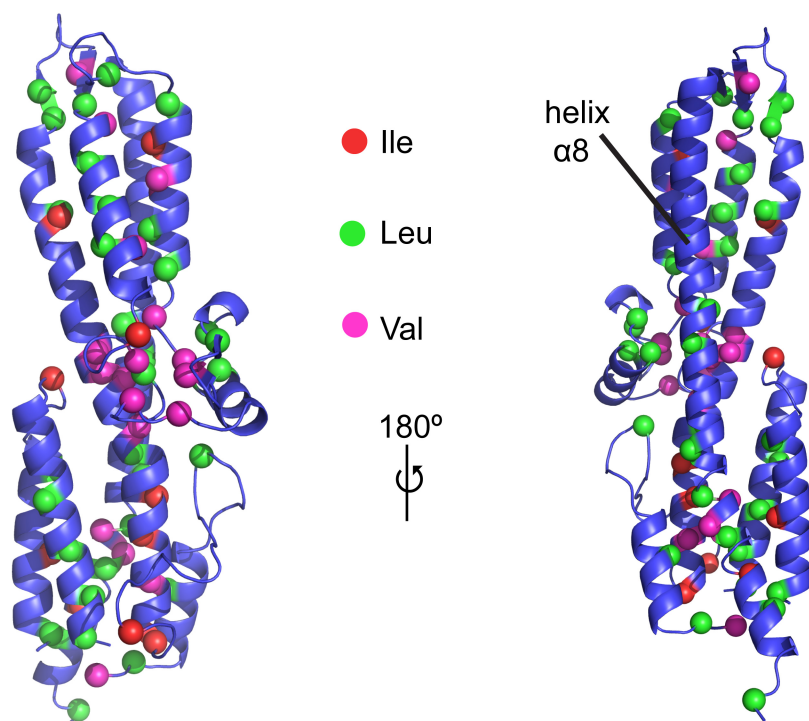


**Fig. 2-2 – Position of ILV Residues on SipD <sup>$\Delta 38$</sup>**

The position of Ile (red), Leu (green) and Val (magenta) residues on SipD <sup>$\Delta 38$</sup>  is shown. ILVs cover most of the protein, except for an extended region of helix  $\alpha 8$ . PDB ID for this crystal structure of SipD <sup>$\Delta 38$</sup>  is 3NZZ.

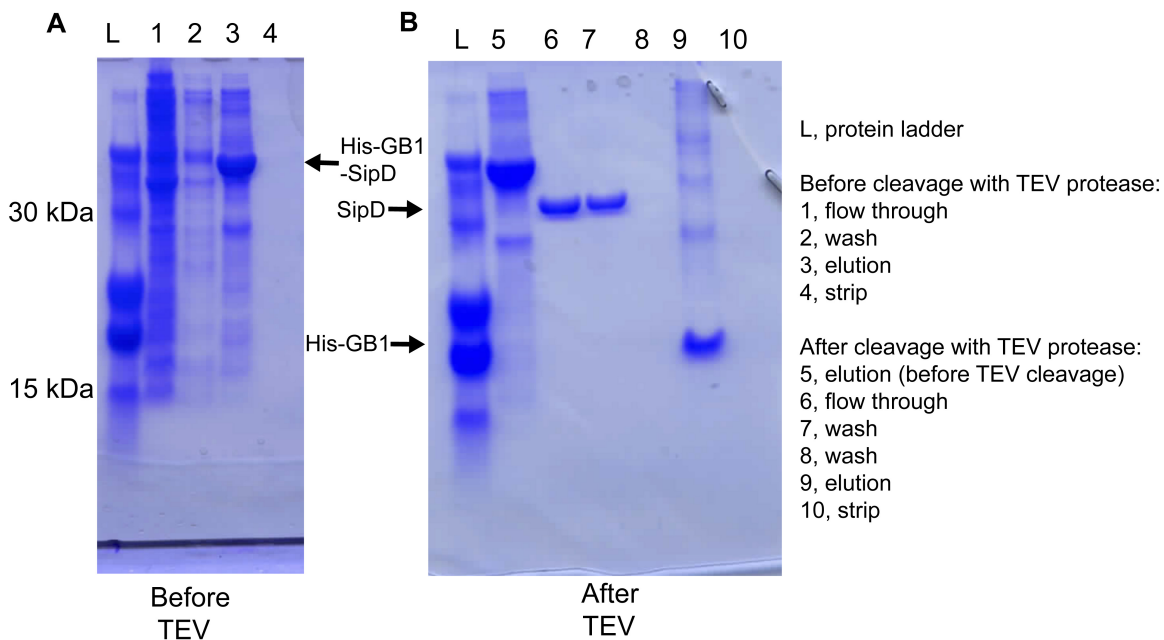


**Fig. 2-3 – SDS-PAGE Gel of SipD<sup>Δ38</sup> Purification**

Nickel column affinity purification of perdeuterated <sup>15</sup>N/ILV <sup>13</sup>C-methyl labeled SipD<sup>Δ38</sup> is shown. **(A)** An SDS-PAGE gel of the Ni<sup>2+</sup> column purification before cleavage with TEV protease. Lane 3 contains His-GB1- SipD<sup>Δ38</sup> (42.3 kDa). **(B)** An SDS-PAGE gel of the Ni<sup>2+</sup> column purification after cleavage with TEV protease. Lane 6 and 7 contain purified isotopically labeled SipD<sup>Δ38</sup> (33.3 kDa) and lane 9 contains cleaved His-GB1 (9 kDa).

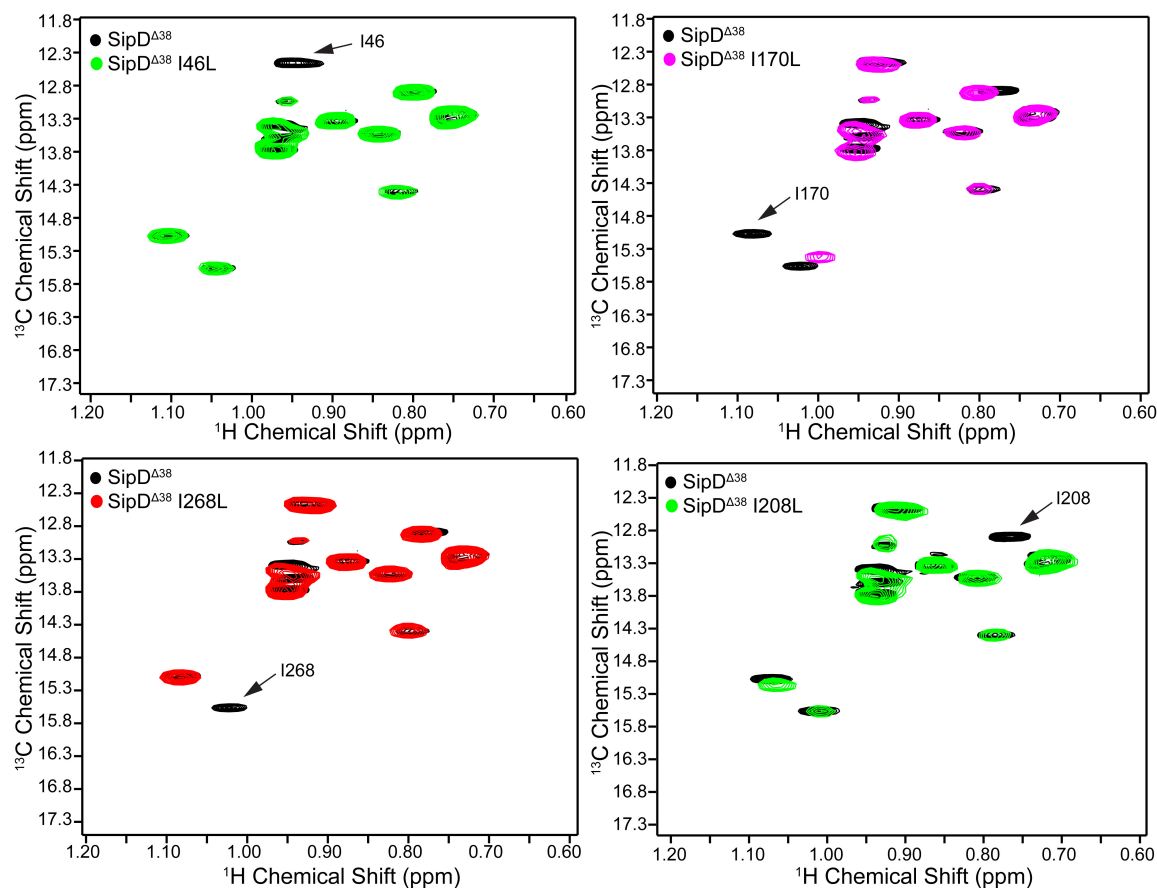


**Fig. 2-4 – Examples of SipD $^{\Delta 38}$  Assignment Strategy Using Ile-to-Leu Point Mutants**  
 The 2D  $^1\text{H}$ - $^{13}\text{C}$  HSQC spectra of four different SipD $^{\Delta 38}$  Ile-to-Leu point mutants allowed for unambiguous assignment of I46  $\delta 1$ , I170  $\delta 1$ , I208  $\delta 1$  and I268  $\delta 1$ . In all cases, there was a clear example of peak disappearance, allowing for Ile methyl assignment (indicated with an arrow).

### 2.3.2. SipD<sup>Δ38</sup> Leu and Val Methyl Assignments by 3D NMR

The 2D <sup>1</sup>H-<sup>13</sup>C HSQC spectra of <sup>15</sup>N/ILV <sup>13</sup>C-methyl labeled SipD<sup>Δ38</sup> showed 114 of 114 predicted methyl resonances. Eventually, 100% assignment of ILV methyl resonances of SipD<sup>Δ38</sup> was achieved through the combination of site-directed mutagenesis (**Fig. 2-4**), through-space <sup>1</sup>H-<sup>1</sup>H nuclear Overhauser effects (NOEs) observed using a 3D HMQC-NOESY dataset of perdeuterated <sup>15</sup>N/ILV <sup>13</sup>C-methyl labeled SipD<sup>Δ38</sup> and distance information provided from the crystal structure of SipD<sup>Δ38</sup>. In a typical assignment strategy, the strip for an assigned Ile methyl (by site-directed mutagenesis) would be analyzed in NMRView (an example with Ile 208 Cδ is shown in **Fig. 2-5**). Next, the strip for each corresponding Leu/Val NOE that the Ile observed would be identified. If that Leu/Val residue had an NOE with the Ile, it should also have a back NOE with the Ile (blue line at the top of **Fig. 2-5A** goes through all residues, showing each residue has an NOE with Ile 208). Next, the crystal structure of SipD<sup>Δ38</sup> would be utilized to measure the distance of the closest residues (< 10Å) to the specific Ile (shown in **Fig. 2-5B**). The distance to the Ile residue should correlate with the strength of the NOE observed. This method allowed for an assignment of a large number of Leu/Val residues. After that, the remaining Leu/Val residues were assigned using a similar method using confident Leu/Val assignments as the reference. The final stereospecific assignment of each SipD<sup>Δ38</sup> ILV methyl resonance is found in **Fig. 2-6**. These assignments were later largely confirmed in Chapter 3 when comparing overlapping ILV methyl resonances with SipD<sup>Δ132</sup>, which lacked residues 39-131 (**Fig. 3-4**). The ILV methyl resonances assigned to the 39-131 region did not show up in the spectrum of SipD<sup>Δ132</sup>, increasing the confidence of their assignment.

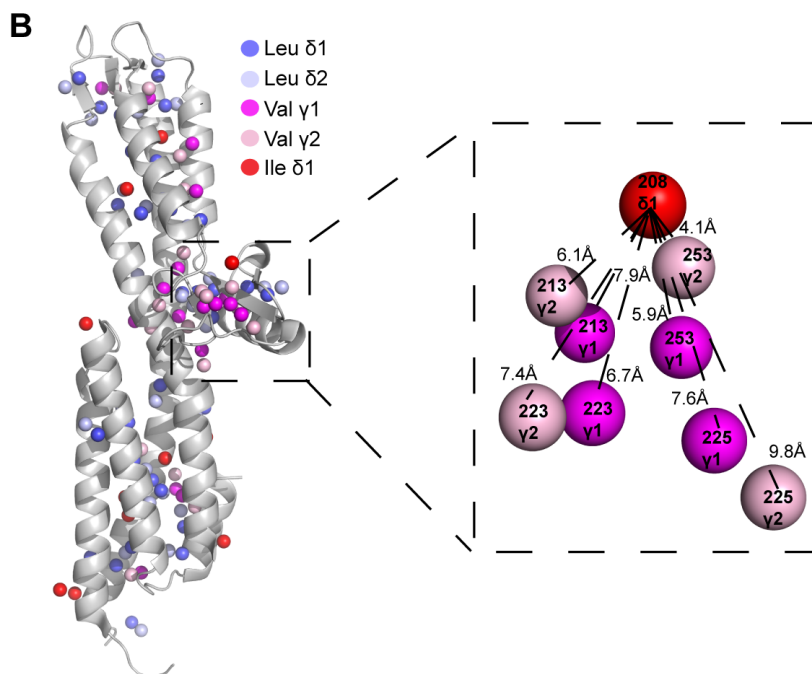
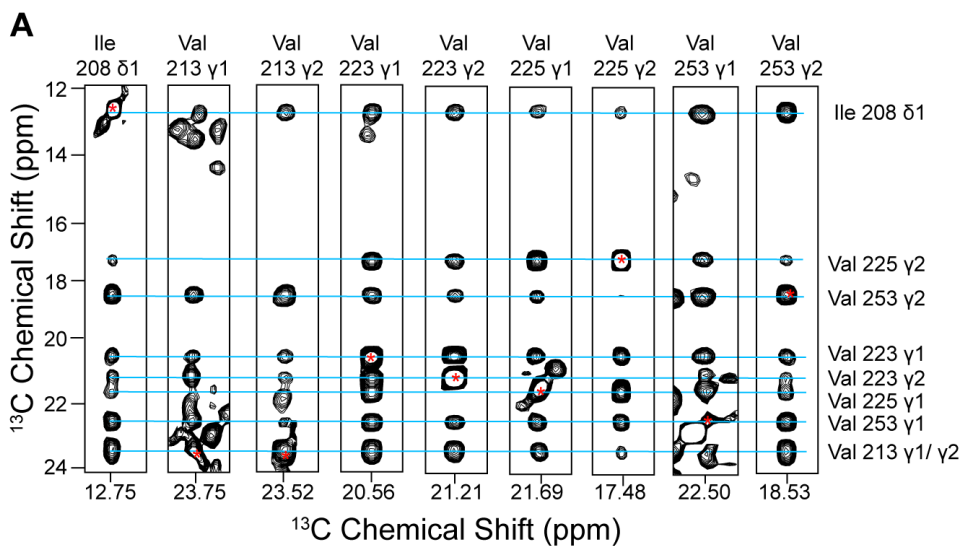


**Fig. 2-5 – Representative Example of SipD<sup>A38</sup> Leu/Val Assignment From 3D Data**

(A) Strips taken from 3D <sup>13</sup>C-<sup>1</sup>H-<sup>13</sup>C HMQC-NOESY-HMQC NMR experiment of SipD<sup>A38</sup>. Red asterisks indicate the diagonal peak of each residue. Peaks not marked with an asterisk are NOE cross peaks. Blue line is shown to indicate residues that have an NOE with other residues of the same spin system. (B) Distance information from the crystal structure of SipD<sup>A38</sup> was utilized (Ile in red, Leu in blue and Val in pink). An expanded view of the region shown as strips in A is shown with distance measurements that correlated to the strength of NOEs with Ile 208 (Ile δ1 in red, Val γ2 in light pink, Val γ1 in dark pink).

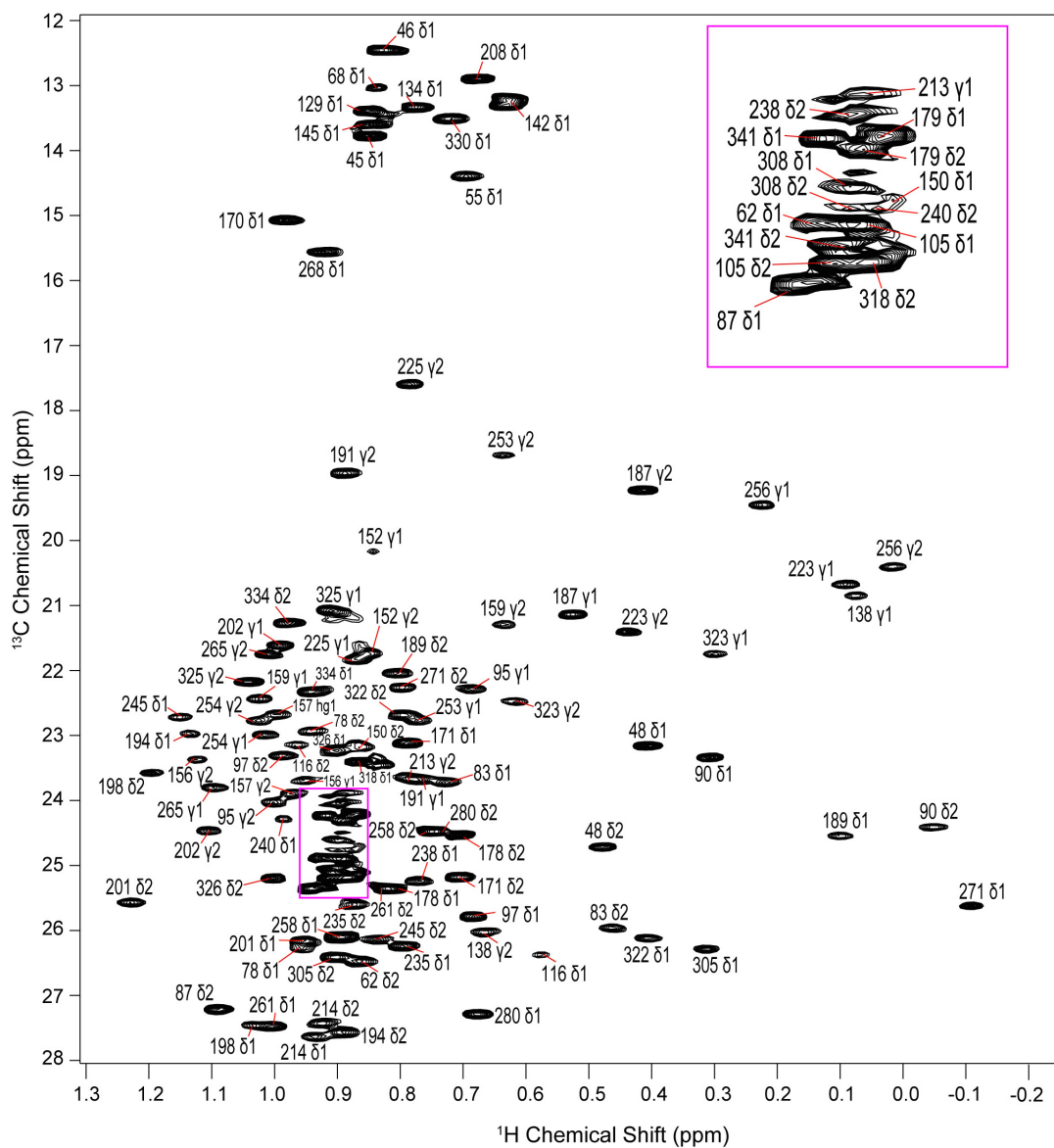


**Fig. 2-6 – Complete Assignment of ILV Methyl Resonances of SipD $^{\Delta 38}$**   
 The 2D  $^1\text{H}$ - $^{13}\text{C}$  HSQC spectrum of SipD $^{\Delta 38}$  with stereospecific resonance assignments of ILV side-chain methyl residues ( $\delta 1$  for Ile,  $\delta 1$  or  $\delta 2$  or Leu and  $\gamma 1$  and  $\gamma 2$  for Val). An expanded view of the clustered region is shown in the magenta box.

## 2.4. Discussion

Here, the ILV  $^{13}\text{C}$ -methyl NMR peaks of SipD $^{\Delta 38}$  were assigned. Assignment of ILV  $^{13}\text{C}$ -methyl resonances allow for completely new sets of NMR experiments to be performed that could complement typical  $^{15}\text{N}$  labeling. The favorable relaxation properties of ILV methyls should allow for interaction studies where amide peaks would be broadened out. Indeed, later chapters of this dissertation will show that SipD $^{\Delta 38}$  ILV methyl assignments aided in elucidating interactions between SipD $^{\Delta 38}$  with the needle (Chapter 4), the translocon (Chapter 7) and small molecules (Chapter 10).

Importantly, 100% of ILV methyls of SipD $^{\Delta 38}$  could be assigned (**Fig. 2-6**). However, there were two resonances in the Leu/Val ppm range of the 2D  $^1\text{H}$ - $^{13}\text{C}$  HSQC SipD $^{\Delta 38}$  spectrum that could not be assigned because they did not have an NOE with any other resonance (data not shown). It is likely that that each Leu/Val resonance should at least see an NOE with its stereo partner. Furthermore, because all ILV residues were accounted for in the assignment, these peaks are likely experimental noise or experimental artifacts.

In conclusion, a strategy utilizing isoleucine to leucine point mutation, 3D HMQC-NOESY-HMQC experiments and distance measurements with the SipD $^{\Delta 38}$  crystal structure was a successful method for the assignment of ILV methyl resonances.

## 2.5. Accession Codes

NMR assignment of SipD $^{\Delta 38}$  ILV  $^{13}\text{C}$ -methyl resonances have been deposited into the BioMagResBank with the accession number 26739.

## 2.6. References

1. Rathinavelan, T., Lara-Tejero, M., Lefebvre, M., Chatterjee, S., McShan, A. C., Guo, D. C., Tang, C., Galan, J. E. & De Guzman, R. N. (2014). NMR model of PrgI-SipD interaction and its implications in the needle-tip assembly of the Salmonella type III secretion system. *J Mol Biol* **426**, 2958-69.
2. Rathinavelan, T., Tang, C. & De Guzman, R. N. (2011). Characterization of the Interaction between the Salmonella Type III Secretion System Tip Protein SipD and the Needle Protein PrgI by Paramagnetic Relaxation Enhancement. *Journal of Biological Chemistry* **286**, 4922-4930.
3. Kaur, K., Chatterjee, S. & De Guzman, R. N. (2016). Characterization of the Shigella and Salmonella Type III Secretion System Tip-Translocon Protein-Protein Interaction by Paramagnetic Relaxation Enhancement. *ChemBiochem*.
4. Wang, Y., Nordhues, B. A., Zhong, D. & De Guzman, R. N. (2010). NMR characterization of the interaction of the Salmonella type III secretion system protein SipD and bile salts. *Biochemistry* **49**, 4220-6.
5. McShan, A. C. & De Guzman, R. N. (2015). The Bacterial Type III Secretion System as a Target for Developing New Antibiotics. *Chemical Biology & Drug Design* **85**, 30-42.
6. Chatterjee, S., Zhong, D., Nordhues, B. A., Battaile, K. P., Lovell, S. & De Guzman, R. N. (2011). The crystal structures of the Salmonella type III secretion system tip protein SipD in complex with deoxycholate and chenodeoxycholate. *Protein Sci* **20**, 75-86.
7. Lunelli, M., Hurwitz, R., Lambers, J. & Kolbe, M. (2011). Crystal Structure of PrgI-SipD: Insight into a Secretion Competent State of the Type Three Secretion System Needle Tip and its Interaction with Host Ligands. *Plos Pathogens* **7**.
8. Vinogradova, O. & Qin, J. (2012). NMR as a Unique Tool in Assessment and Complex Determination of Weak Protein-Protein Interactions. *Nmr of Proteins and Small Biomolecules* **326**, 35-45.
9. Goto, N. K., Gardner, K. H., Mueller, G. A., Willis, R. C. & Kay, L. E. (1999). A robust and cost-effective method for the production of Val, Leu, Ile ( $\delta$  1) methyl-protonated  $^{15}\text{N}$ -,  $^{13}\text{C}$ -,  $^2\text{H}$ -labeled proteins. *J Biomol NMR* **13**, 369-74.
10. Tugarinov, V., Kanelis, V. & Kay, L. E. (2006). Isotope labeling strategies for the study of high-molecular-weight proteins by solution NMR spectroscopy. *Nat Protoc* **1**, 749-54.
11. Gardner, K. H., Rosen, M. K. & Kay, L. E. (1997). Global folds of highly deuterated, methyl-protonated proteins by multidimensional NMR. *Biochemistry* **36**, 1389-401.
12. Hajduk, P. J., Augeri, D. J., Mack, J., Mendoza, R., Yang, J. G., Betz, S. F. & Fesik, S. W. (2000). NMR-based screening of proteins containing C-13-labeled methyl groups. *Journal of the American Chemical Society* **122**, 7898-7904.

13. Tugarinov, V. & Kay, L. E. (2005). Methyl groups as probes of structure and dynamics in NMR studies of high-molecular-weight proteins. *Chembiochem* **6**, 1567-+.
14. Huth, J. R., Bewley, C. A., Jackson, B. M., Hinnebusch, A. G., Clore, G. M. & Gronenborn, A. M. (1997). Design of an expression system for detecting folded protein domains and mapping macromolecular interactions by NMR. *Protein Sci* **6**, 2359-64.
15. Delaglio, F., Grzesiek, S., Vuister, G. W., Zhu, G., Pfeifer, J. & Bax, A. (1995). NMRPipe: a multidimensional spectral processing system based on UNIX pipes. *J Biomol NMR* **6**, 277-93.
16. Johnson, B. A. (2004). Using NMRView to visualize and analyze the NMR spectra of macromolecules. *Methods Mol Biol* **278**, 313-52.
17. Xiao, Y., Lee, T., Latham, M. P., Warner, L. R., Tanimoto, A., Pardi, A. & Ahn, N. G. (2014). Phosphorylation releases constraints to domain motion in ERK2. *Proc Natl Acad Sci U S A* **111**, 2506-11.
18. Rule, G. S. & Hitchens, T. K. (2006). *Fundamentals of protein NMR spectroscopy*. Focus on structural biology, Springer, Dordrecht.

## Chapter 3. NMR Characterization of SipD<sup>Δ132</sup>

### 3.1. Introduction

The N-terminal  $\alpha$ -helical domain of the *Salmonella* tip protein SipD resembles the  $\alpha$ -helical hairpin structure of the needle protein PrgI<sup>1</sup>. Furthermore, the N-terminal  $\alpha$ -helical domain of SipD has been shown to function as a self-chaperone and is hypothesized to become displaced by PrgI during interaction at the distal end of the needle<sup>2</sup>. For these reasons, a construct of SipD that lacked the N-terminal domain, residues 39-131, was subcloned (herein called SipD<sup>Δ132</sup>). SipD<sup>Δ132</sup> crystallized, but failed to form co-crystals with PrgI (data not shown). Because backbone and side-chain amide<sup>3</sup> and ILV methyl resonances (**Fig. 2-6**) of SipD<sup>Δ38</sup> were previously assigned, SipD<sup>Δ132</sup> was characterized by NMR spectroscopy for use in protein titration experiments to test whether SipD<sup>Δ132</sup> would bind tighter to PrgI than SipD<sup>Δ38</sup>. It was hypothesized that because SipD contains distinct protein domains, the overall chemical environment of most residues would not change significantly following deletion of its N-terminal domain. If this were the case, comparison the 2D <sup>1</sup>H-<sup>15</sup>N TROSY and 2D <sup>1</sup>H-<sup>13</sup>C HSQC spectra of SipD<sup>Δ38</sup> should allow for the assignment of SipD<sup>Δ132</sup>. Here, SipD<sup>Δ132</sup> is compared to SipD<sup>Δ38</sup> by circular dichroism (CD) and solution NMR spectroscopy. Amide and ILV methyl assignments are successfully transferred from SipD<sup>Δ38</sup> to SipD<sup>Δ132</sup>.

### 3.2. Materials and Methods

#### 3.2.1. Expression and Purification of SipD<sup>Δ132</sup>

SipD<sup>Δ38</sup> was purified as mentioned in Chapter 2. *Salmonella* Typhimurium strain SL1344 T3SS SPI-1 tip protein SipD 133-343 C244S (SipD<sup>Δ132</sup>) was subcloned into a

modified pET-21a expression vector containing an N-terminal His<sub>6</sub> tag followed by a TEV protease cleavage site and GB1 as a solubility tag. Isotopically labeled <sup>15</sup>N/ILV <sup>13</sup>C-methyl SipD<sup>Δ132</sup> was expressed and purified in *E. coli* BL21(DE3) DNAY cells as described for SipD<sup>Δ38</sup> in Chapter 2. Purified proteins were dialyzed into NMR buffer and concentrated using Amicon Ultra 3K (Millipore) filtration columns. Protein concentrations were measured by the absorbance at A<sub>280</sub>.

### 3.2.2. Circular Dichroism of SipD<sup>Δ38</sup> and SipD<sup>Δ132</sup>

Far-UV CD experiments were acquired using a JASCO J-815 Spectropolarimeter. CD spectra of SipD<sup>Δ38</sup> and SipD<sup>Δ132</sup> were acquired using 0.05 mg/mL protein in 2 mL sterile water in a quartz cuvette. A water blank was acquired and subtracted from each CD spectra of SipD. To assess the protein secondary structure, CD spectra were acquired from 190 to 260 nm in triplicate at 20°C with a scan rate of 50 nm/minute. To assess protein stability and folding, thermal denaturation experiments were performed by measuring ellipticity at 222 nm over a temperature range of 20°C to 90°C with a ramp rate of 2°C/minute. The experimental CD values of ellipticity (mdeg) were converted to molar ellipticity ( $\theta = \text{deg cm}^2/\text{dmol}$ ). The melting temperature ( $T_m$ ) was calculated using JASCO J-815 software.

### 3.2.3. <sup>1</sup>H-<sup>15</sup>N TROSY of SipD<sup>Δ38</sup> and SipD<sup>Δ132</sup> and Transfer of Assignments

NMR data was collected using a Bruker Avance 800 MHz spectrometer equipped with a cryogenic triple resonance probe and were processed using NMRPipe<sup>4</sup> and analyzed using NMRView<sup>5</sup>. For 2D <sup>1</sup>H-<sup>15</sup>N TROSY experiments, data was acquired on 0.3 mM <sup>15</sup>N/ILV <sup>13</sup>C-methyl labeled SipD<sup>Δ38</sup> or SipD<sup>Δ132</sup> in NMR buffer (20 mM NaCl,

10 mM sodium phosphate, pH 7.4 and 10% D<sub>2</sub>O) at 30°C. The Bruker pulse sequence *trosetf3gpsi* was compared to the pulse sequence *troxy3gppsi19.2*. After comparison, *troxy3gppsi19.2* was chosen as the primary 2D <sup>1</sup>H-<sup>15</sup>N TROSY experiment because it was much more sensitive. Typical acquisition parameters were 16 scans with 2048 complex points (<sup>1</sup>H) and 128 complex points (<sup>15</sup>N) with sweep width 10.01 ppm for <sup>1</sup>H centered at 4.69 ppm and 17.9 ppm for <sup>15</sup>N centered at 119 ppm. Backbone and side-chain amide assignments were transferred from SipD<sup>Δ38</sup> using assignment by Wang and co-workers<sup>3</sup>.

#### 3.2.4. <sup>1</sup>H-<sup>13</sup>C HSQC of SipD<sup>Δ38</sup> and SipD<sup>Δ132</sup> and Transfer of Assignments

For 2D <sup>1</sup>H-<sup>13</sup>C HSQC experiments, data was acquired on 0.3 mM <sup>15</sup>N/ILV <sup>13</sup>C-methyl labeled SipD<sup>Δ38</sup> or SipD<sup>Δ132</sup> dissolved in NMR buffer at 30°C. Acquisition parameters were 8 scans with 1024 complex points (<sup>1</sup>H) and 256 complex points (<sup>13</sup>C) with sweep width 10.01 ppm for <sup>1</sup>H centered at 4.69 ppm and 20 ppm for <sup>13</sup>C centered at 19 ppm. Ile-to-leu point mutants of SipD<sup>Δ132</sup> were created by site-directed mutagenesis using a QuikChange kit (Stratagene) and confirmed by DNA sequencing. SipD<sup>Δ132</sup> mutants were expressed and purified as described in section 3.2.2 and NMR data was acquired as described in section 3.2.3. Leu/Val <sup>13</sup>C-methyl carbon assignments were transferred from the ILV methyl assignments of SipD<sup>Δ38</sup> as described in Chapter 2.

### 3.3. Results

#### 3.3.1. Circular Dichroism of SipD<sup>Δ38</sup> and SipD<sup>Δ132</sup>

CD was used to determine whether SipD<sup>Δ38</sup> and SipD<sup>Δ132</sup> contained similar secondary structure characteristics. Typical of  $\alpha$ -helical proteins, both SipD constructs

showed minima at 208 nm and 222 nm (**Fig. 3-1A**). The  $\theta_{222/208}$  ratio was 0.96 for SipD $^{\Delta 38}$  and 0.97 for SipD $^{\Delta 132}$ . Both SipD constructs contained  $\theta_{222/208}$  ratios close to 1, which indicates the presence of a coiled-coil<sup>6</sup>, as expected from the crystal structure of SipD<sup>7; 8</sup>. In addition, the two SipD constructs showed slightly different thermal denaturation profiles. SipD $^{\Delta 38}$  contained two melting temperatures ( $T_m$ ) at 61°C and 75°C, while SipD $^{\Delta 132}$  contained a single  $T_m$  at 75°C (**Fig. 3-1B**). The absence of the 61°C  $T_m$  in the SipD $^{\Delta 132}$  melting curve likely corresponds to the removal of the N-terminal  $\alpha$ -helical domain. Together, the CD experiments suggested that SipD $^{\Delta 38}$  and SipD $^{\Delta 132}$  contain similar secondary structure characteristics and that the removal of the N-terminal domain did not drastically alter the overall folding of SipD.

### 3.3.2. $^1H$ - $^{15}N$ TROSY of SipD $^{\Delta 38}$ and SipD $^{\Delta 132}$ and Transfer of Assignments

Previous 2D  $^1H$ - $^{15}N$  TROSY experiments required long acquisition times for low protein concentration (>8 hrs for 0.3 mM protein). Therefore, the previously used TROSY pulse sequence (trosetf3gpsi) was compared to a potentially more sensitive TROSY pulse sequence (troty3gppsi19.2). Both experiments were acquired on 0.3 mM SipD $^{\Delta 38}$  and took 3 hours. Better signal resolution was achieved with the pulse sequence troty3gppsi19.2 when the same experimental parameters were used (**Fig. 3-2A**). A likely explanation is that the troty3gppsi19.2 pulse sequence contains WATERGATE and improved sensitivity by altering the  $G_z$  gradient (**Fig. 3-3A**).

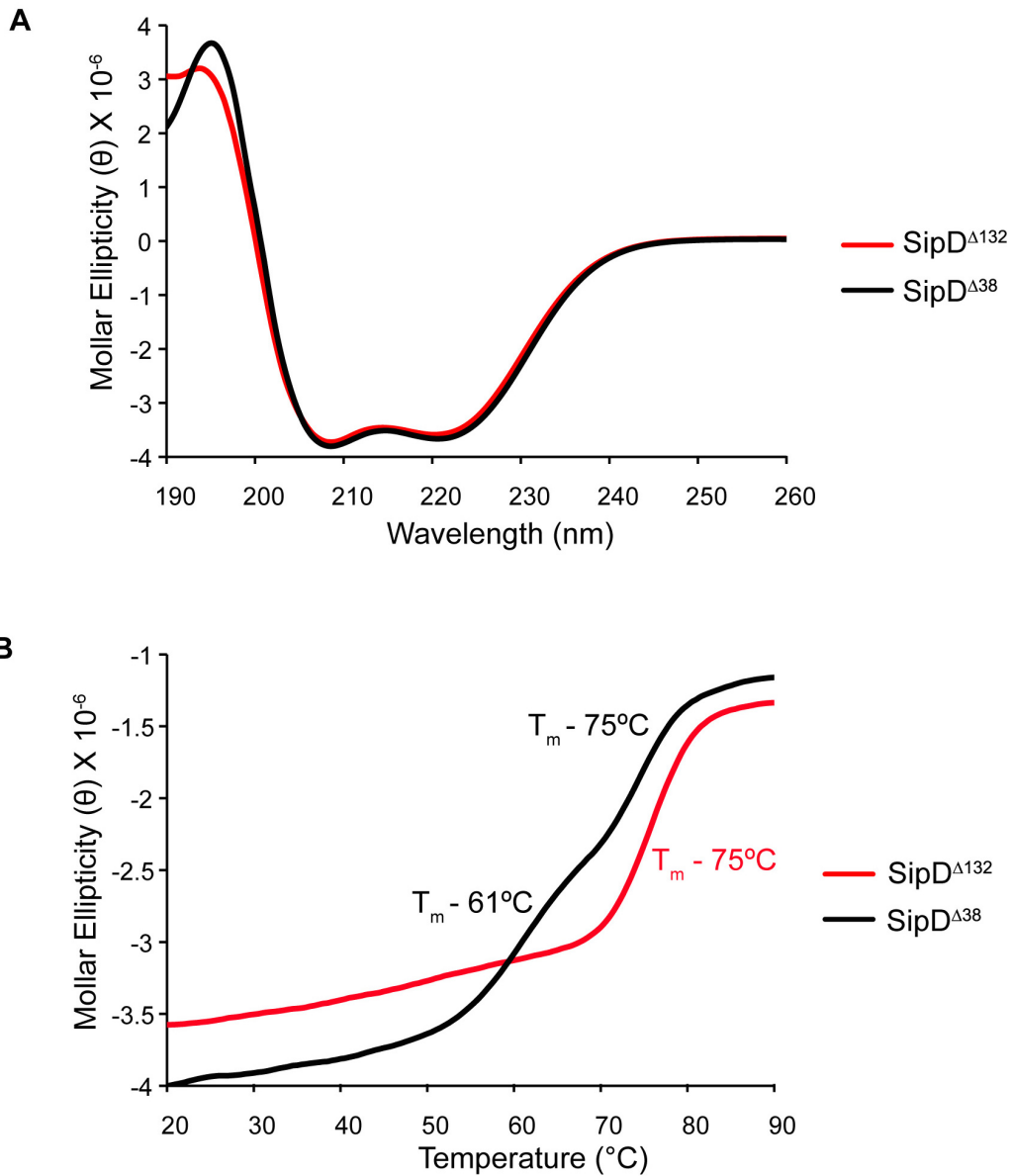


**Fig. 3-1 – Circular Dichroism of SipD $^{\Delta 38}$  and SipD $^{\Delta 132}$**

(A) Far-UV CD spectra from 190 nm to 260 nm of SipD $^{\Delta 38}$  (black) and SipD $^{\Delta 132}$  (red). Peak minima at 208 nm and 222 nm are typical of  $\alpha$ -helical proteins. (B) Terminal denaturation profile monitoring the ellipticity at 222 nm of SipD $^{\Delta 38}$  (black) and SipD $^{\Delta 132}$  (red) from 20 $^{\circ}\text{C}$  to 90 $^{\circ}\text{C}$ . SipD $^{\Delta 38}$  shows two  $T_m$ s at 61 $^{\circ}\text{C}$  and 75 $^{\circ}\text{C}$ , while SipD $^{\Delta 132}$  shows a single  $T_m$  at 75 $^{\circ}\text{C}$ .

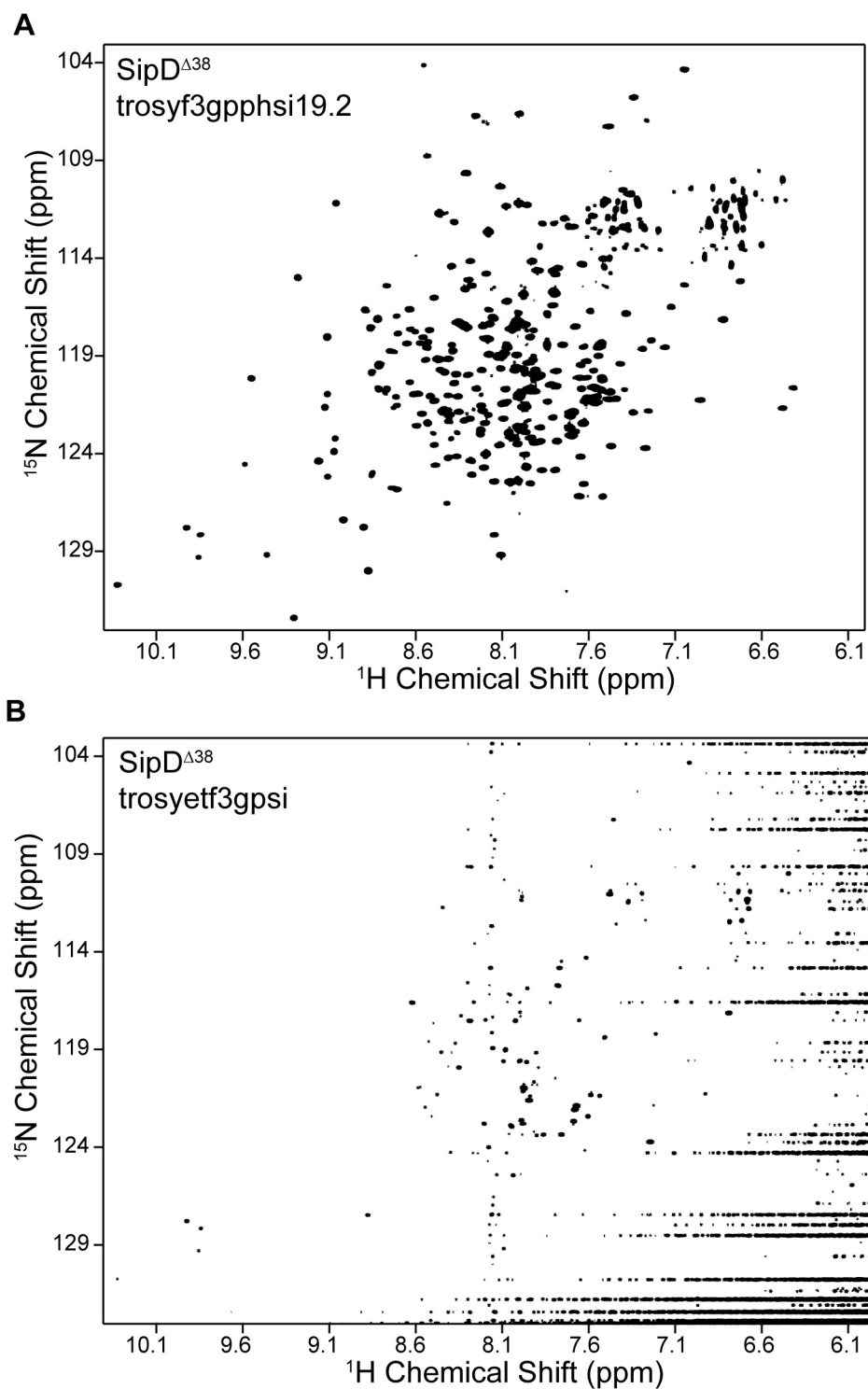


**Fig. 3-2 – Testing Trosytf3gpsi vs. Trosy3gppsi19.2 with SipD $\Delta$ 38**

Comparison of 2D  $^1\text{H}$ - $^{15}\text{N}$  TROSY spectra of 0.3 mM SipD $\Delta$ 38 using two different Bruker pulse sequences under the same experimental conditions. (A) trosyf3gppsi19.2 is more sensitive and NMR peaks are more well-resolved than the data acquired using (B) the pulse sequence trosytf3gpsi.

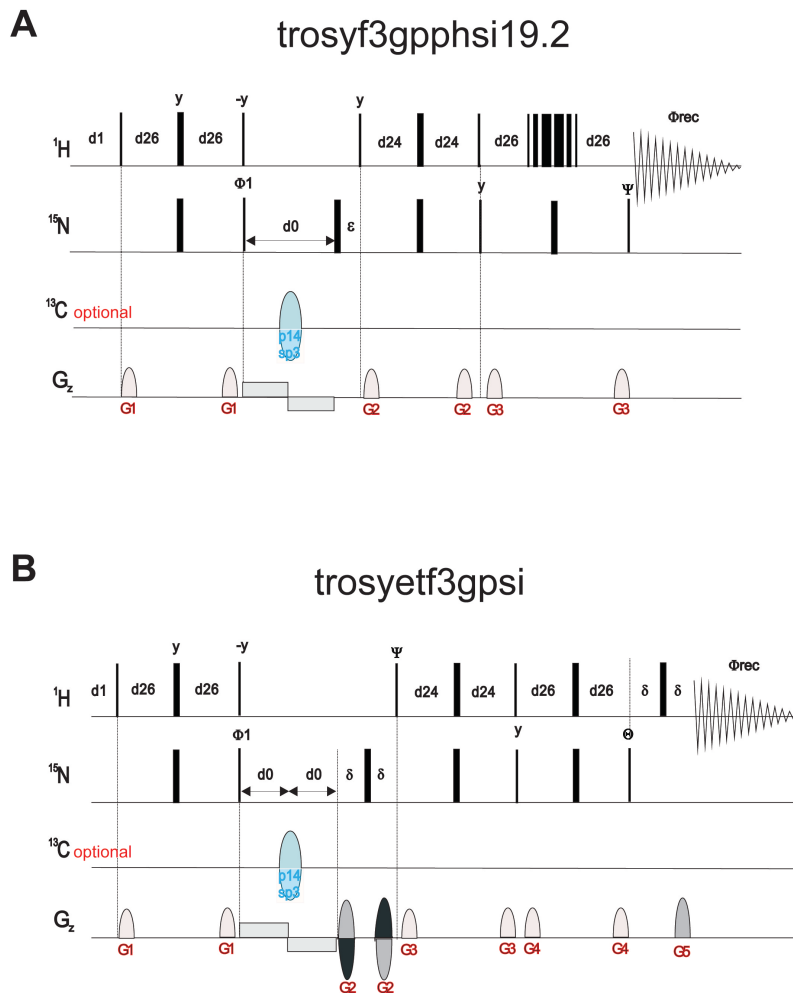


**Fig. 3-3 – Comparison of Trosyf3gppsi19.2 and Trosyettf3gpsi Bruker Pulse Programs**

Cartoon representation of the pulse sequences of (A) trosyf3gppsi19.2 and (B) trosyettf3gpsi. Figure adapted from the Pulse Program Catalogue for TOPSPIN v1.3. NMRGuide v4.0.

Two-dimensional  $^1\text{H}$ - $^{15}\text{N}$  TROSY datasets were acquired on  $^{15}\text{N}$  labeled SipD $^{\Delta 38}$  and SipD $^{\Delta 132}$ . In support of my initial hypothesis that deletion of the N-terminal residues of SipD (residues 38-131) would not greatly alter its overall structure, many NMR peaks overlapped between the two spectra (**Fig. 3-4**). Because the chemical shift values of most residues were similar between the constructs, the backbone and side-chain amide assignments from SipD $^{\Delta 38}$  could be unambiguously transferred to SipD $^{\Delta 132}$  (**Fig. 3-5**). In fact, transfer of assignments allowed for coverage of 82% of backbone and side-chain amide resonances of SipD $^{\Delta 132}$ . In comparison, 93% of amide resonances of SipD $^{\Delta 38}$  were previously assigned by Wang and co-workers<sup>3</sup>.

### 3.3.3. $^1\text{H}$ - $^{13}\text{C}$ HSQC of SipD $^{\Delta 38}$ and SipD $^{\Delta 132}$ and Transfer of Assignments

In a similar method used for the assignment of ILV methyls of SipD $^{\Delta 38}$  in Chapter 2, Ile-to-Leu point mutants of SipD $^{\Delta 132}$  were created. Four examples of isoleucine assignment using Ile-to-Leu mutants are shown in **Fig. 3-6**. These experiments allowed for unambiguous methyl assignment for the 7 isoleucine methyls present in SipD $^{\Delta 132}$ . Two-dimensional  $^1\text{H}$ - $^{15}\text{N}$  HSQC datasets were acquired on ILV  $^{13}\text{C}$ -methyl labeled SipD $^{\Delta 38}$  and SipD $^{\Delta 132}$ . As with the amide resonances (**Fig. 3-4**), many ILV  $^{13}\text{C}$ -methyl NMR peaks had similar chemical shift values, confirming the hypothesis that removal of the N-terminal domain of SipD did not greatly alter the structure of SipD (**Fig. 3-7**). Because of peak overlap, the ILV methyl assignments from SipD $^{\Delta 38}$  could be transferred to SipD $^{\Delta 132}$  (**Fig. 3-8**). Transfer of assignments allowed for coverage of 76% of ILV methyl resonances of SipD $^{\Delta 132}$ . In comparison, 100% of ILV methyl resonances of SipD $^{\Delta 38}$  were previously assigned in Chapter 2.

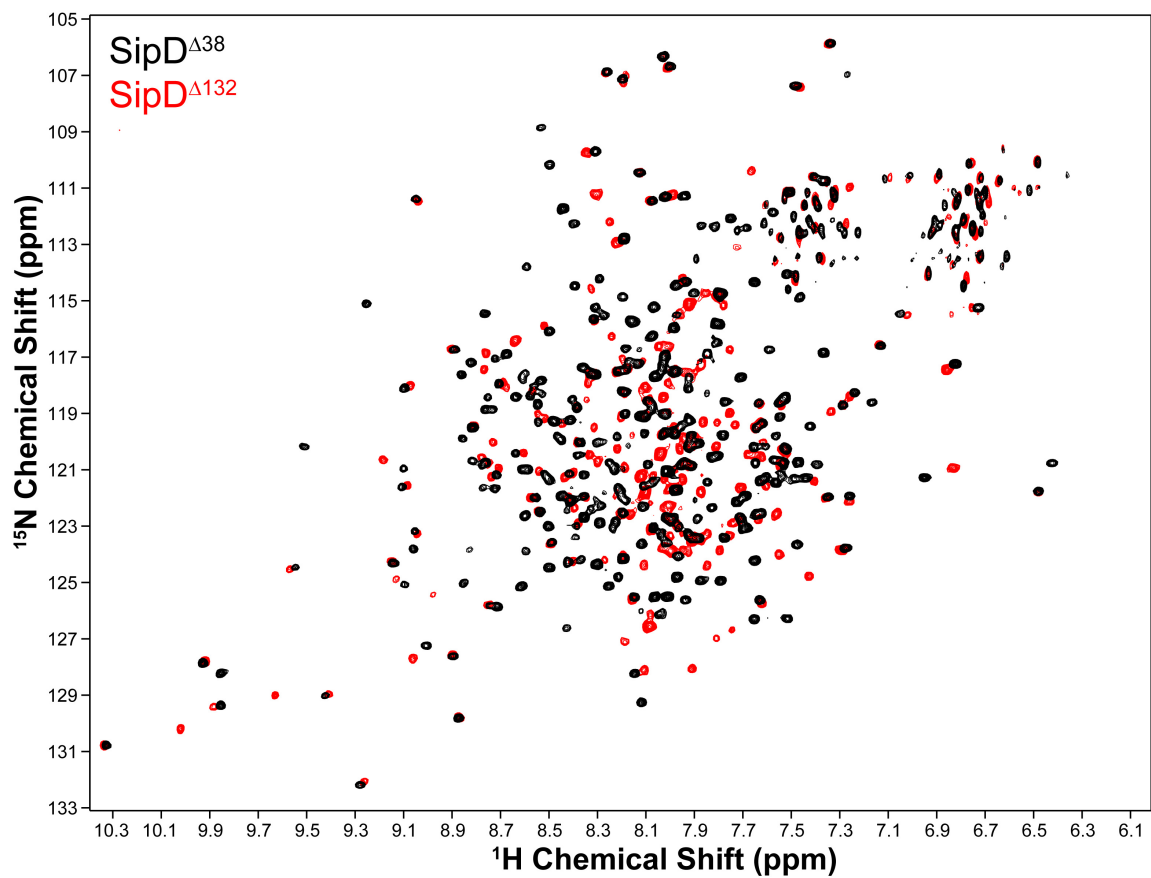


**Fig. 3-4– Comparison of the Amide Resonances of SipD<sup>Δ38</sup> and SipD<sup>Δ132</sup>**  
 Overlay of the 2D <sup>1</sup>H-<sup>15</sup>N TROSY spectra of SipD<sup>Δ38</sup> (black) and SipD<sup>Δ132</sup> (red). Many NMR peaks show the similar chemical shift values. In other cases, peaks disappeared. These disappearing peaks primarily belong to assignments of SipD residues from 39 to 131. In some cases, new peaks appeared. These new peaks are likely due to a major change in chemical shift values for residues along the SipD coiled-coil surface that was previously in contact with the N-terminal  $\alpha$ -helical domain.



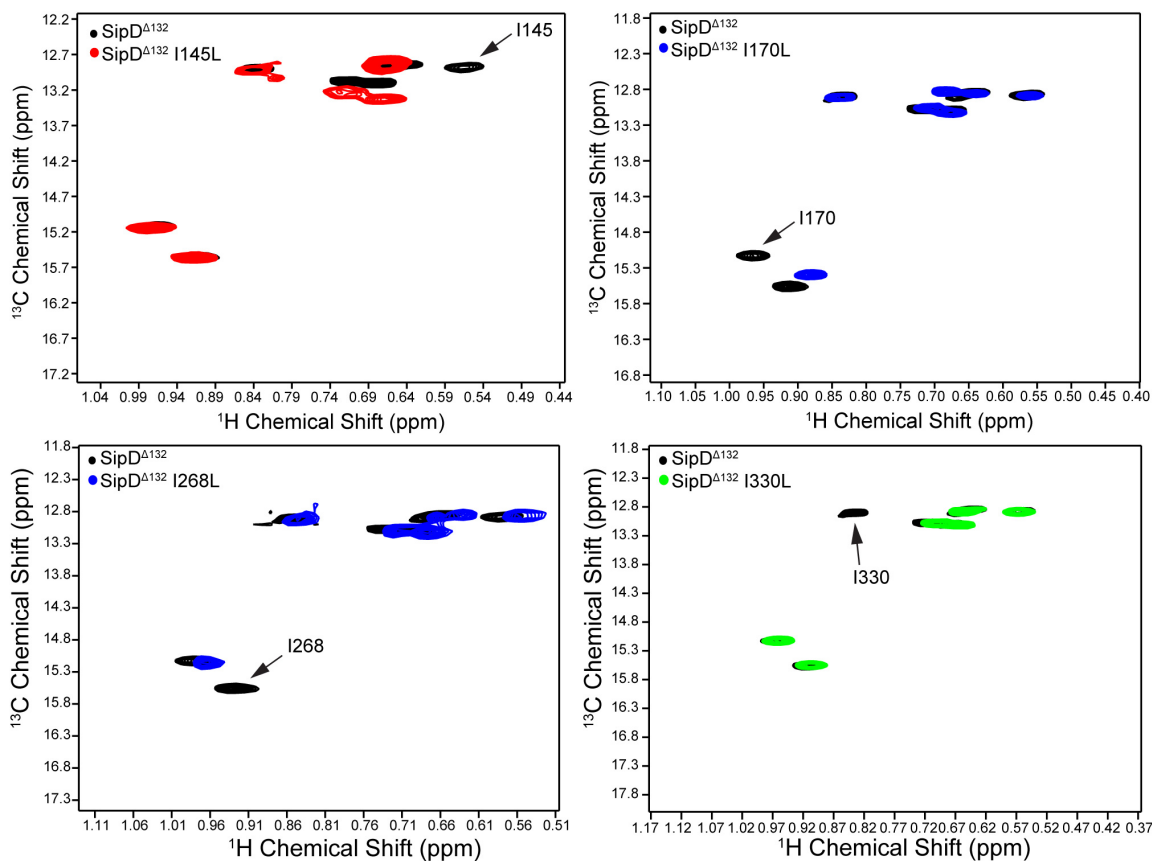


**Fig. 3-6 – Ile-to-Leu Point Mutation Allows for Assignment of SipD<sup>Δ132</sup> Ile Methyls**  
 The 2D <sup>1</sup>H-<sup>13</sup>C HSQC spectra of four isoleucine-to-leucine point mutants of SipD<sup>Δ132</sup>. In each case, one Ile methyl peak clearly disappears, allowing for unambiguous assignment. Using this method, the 7 isoleucine methyl Cδ resonances of SipD<sup>Δ132</sup> were assigned.

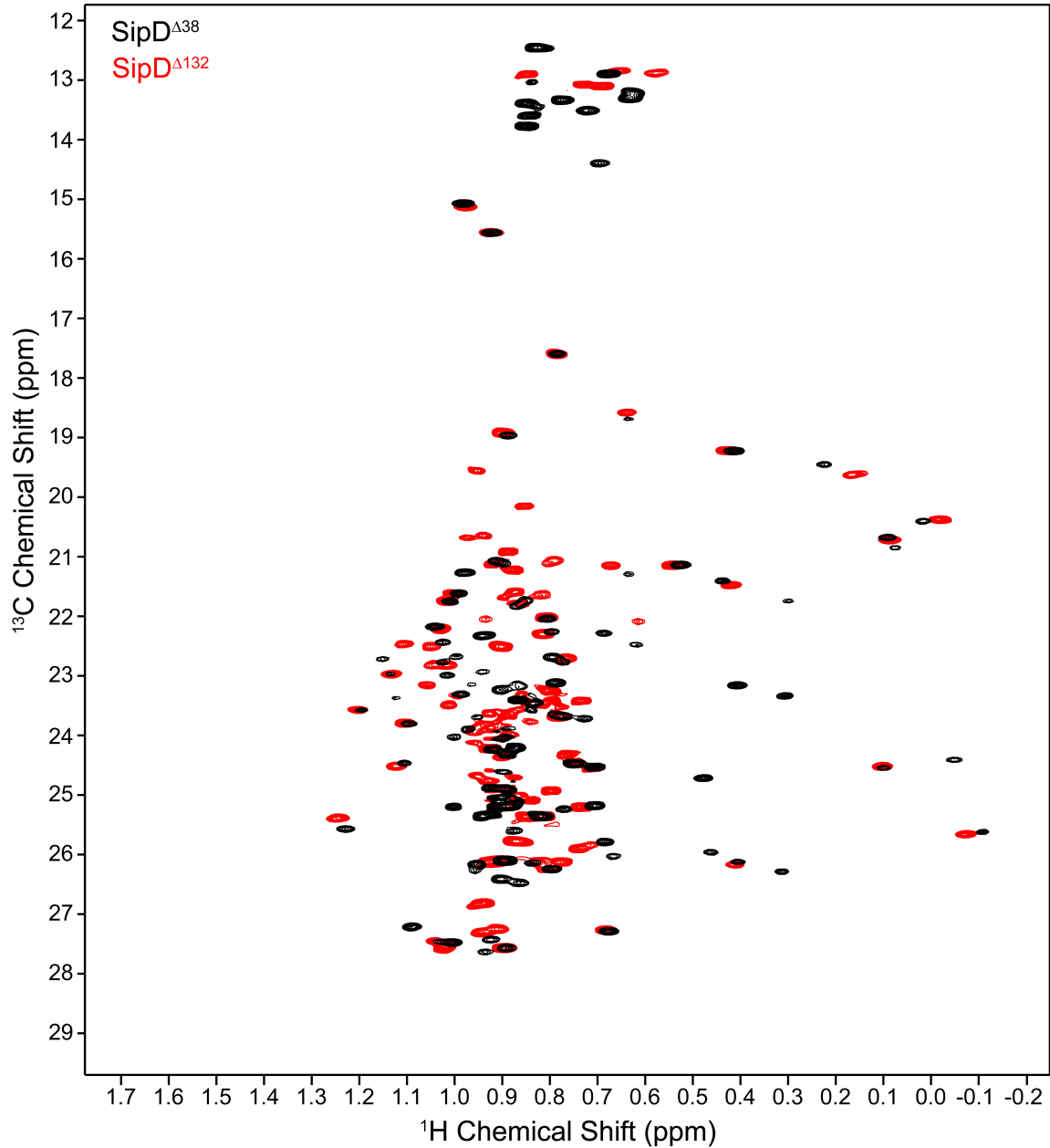


**Fig. 3-7 – Comparison of ILV Methyl Resonances of SipD<sup>Δ38</sup> and SipD<sup>Δ132</sup>**  
 Overlay of two 2D <sup>1</sup>H-<sup>13</sup>C HSQC spectra of SipD<sup>Δ38</sup> (black) and SipD<sup>Δ132</sup> (red). Many ILV methyl peaks have chemical shift values that are similar. In other cases, peaks disappeared. These disappearing peaks primarily belong to assignments of SipD residues from 39 to 131. In some cases, new peaks appeared. These new peaks are likely due to a major change in chemical shift values for residues along the SipD coiled-coil surface that was previously in contact with the N-terminal α-helical domain.

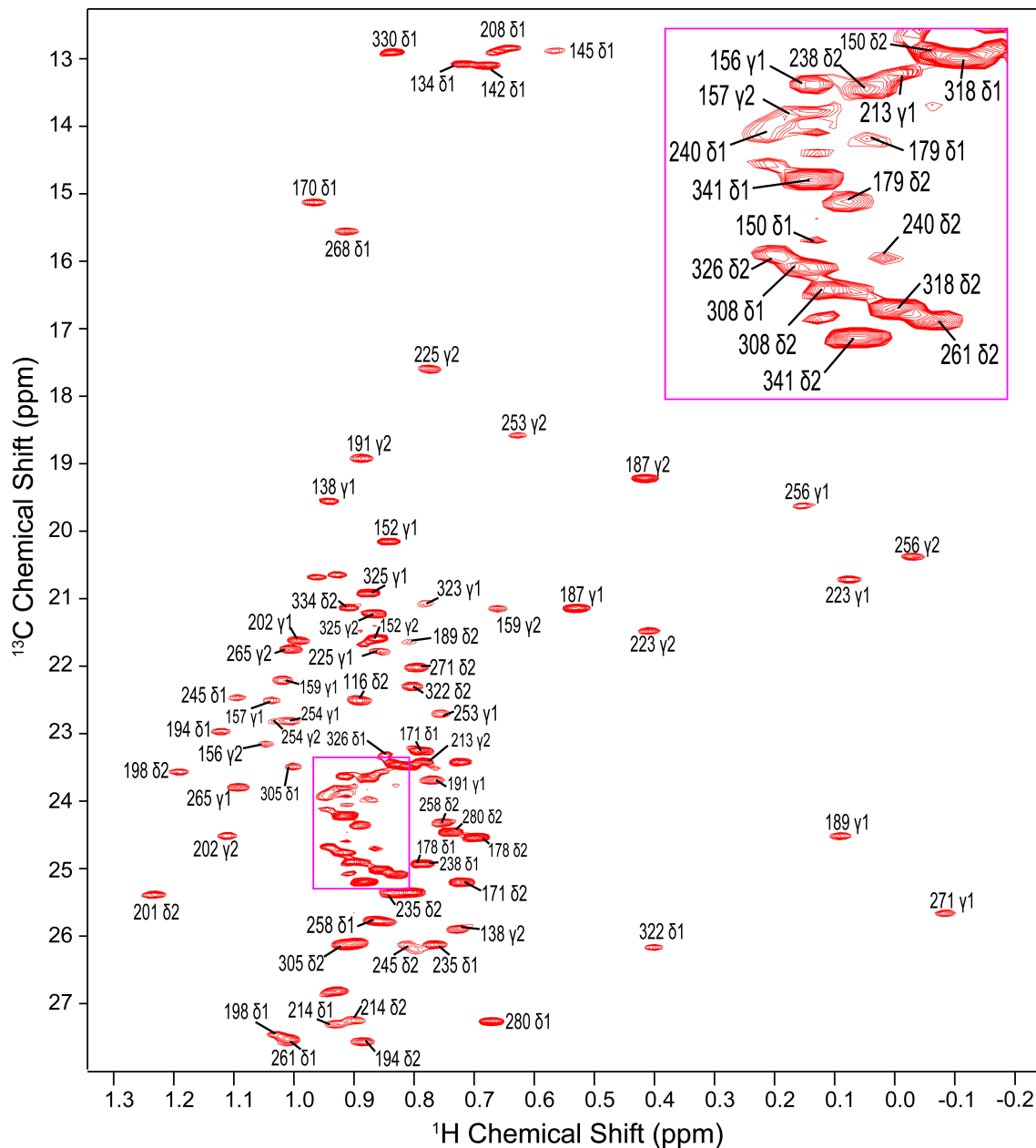


**Fig. 3-8 – ILV Methyl Assignments of SipD<sup>Δ132</sup>**

The 2D <sup>1</sup>H-<sup>13</sup>C HSQC spectrum of SipD<sup>Δ132</sup> with corresponding ILV <sup>13</sup>C-methyl assignments. Because of the majority of peaks contained similar chemical values with ILV methyl resonances of SipD<sup>Δ38</sup>, 76% of ILV methyl resonances in SipD<sup>Δ132</sup> could be assigned. Each peak is labeled with its corresponding SipD stereospecific residue number (δ1 for Ile, δ1 and δ2 for Leu, γ1 and γ2 for Val).

### 3.4. Discussion

Here, a SipD construct lacking its N-terminal  $\alpha$ -helical hairpin domain (SipD $^{\Delta 132}$ ) was compared to a construct containing its N-terminal domain (SipD $^{\Delta 38}$ ). I hypothesized that the removal of the N-terminal of SipD $^{\Delta 38}$  would not greatly alter the overall structure of SipD. If this were indeed the case, assignment transfer of NMR peaks from SipD $^{\Delta 38}$  to SipD $^{\Delta 132}$  should be possible because the overall chemical environment and chemical shift values of the SipD NMR peaks would be similar. CD experiments showed that SipD $^{\Delta 38}$  and SipD $^{\Delta 132}$  contained similar secondary structure with similar  $\theta_{222/208}$  ratios (**Fig. 3-1A**). Thermal denaturation experiments showed that SipD $^{\Delta 38}$  contained two melting temperatures at 61°C and 75°C, while SipD $^{\Delta 132}$  contained a single melting temperature at 75°C (**Fig. 3-1B**). The absence of the 61°C  $T_m$  in the SipD $^{\Delta 132}$  thermal denaturation profile is likely due to the removal of the N-terminal  $\alpha$ -helical domain. Comparison of two 2D  $^1\text{H}$ - $^{15}\text{N}$  TROSY pulse sequences, *trotyf3gppsi19.2* and *trotyetf3gpsi*, showed that *trotyf3gppsi19.2* is a much more sensitive pulse sequence for TROSY data acquisition with SipD (**Fig. 3-2**). This *trotyf3gppsi19.2* pulse sequence reduced data acquisition times three-fold and resulted in NMR peaks with much less line broadening than *trotyetf3gpsi*. Pulse sequence *trotyetf3gpsi* is a phase-sensitive *ge*-2D  $^1\text{H}$ - $^{15}\text{N}$  TROSY using *echo-antiecho*, while *trotyf3gppsi19.2* is a phase-sensitive *ge*-2D  $^1\text{H}$ - $^{15}\text{N}$  TROSY using *WATERGATE* and improved sensitivity by altering the  $G_z$  gradient (**Fig. 3-3**). An overlay of the 2D  $^1\text{H}$ - $^{15}\text{N}$  TROSY (**Fig. 3-4**) and 2D  $^1\text{H}$ - $^{13}\text{C}$  HSQC (**Fig. 3-7**) spectra showed that the chemical environment of many SipD residues was not changed by the removal of the N-terminal domain. Some new peaks appeared that are likely the residues along the coiled-coil of SipD that were previously in contact with the N-terminal

$\alpha$ -helical domain. In the case of those residues, the removal of the N-terminal domain altered their chemical environment, corresponding in a large change in chemical shift. However, this was only a small proportion of SipD residues (<10%). In summary, the transfer of 82% of amide (**Fig. 3-5**) and 76% of ILV methyl (**Fig. 3-8**) resonances to SipD <sup>$\Delta$ 132</sup> from SipD <sup>$\Delta$ 38</sup> was achieved. Amide and ILV methyl assignments of SipD <sup>$\Delta$ 132</sup> presented here can be used to elucidate its interaction with the needle PrgI and the translocon SipB.

### 3.5. References

1. Rathinavelan, T., Lara-Tejero, M., Lefebvre, M., Chatterjee, S., McShan, A. C., Guo, D. C., Tang, C., Galan, J. E. & De Guzman, R. N. (2014). NMR model of PrgI-SipD interaction and its implications in the needle-tip assembly of the Salmonella type III secretion system. *J Mol Biol* **426**, 2958-69.
2. Johnson, S., Roversi, P., Espina, M., Olive, A., Deane, J. E., Birket, S., Field, T., Picking, W. D., Blocker, A. J., Galyov, E. E., Picking, W. L. & Lea, S. M. (2007). Self-chaperoning of the type III secretion system needle tip proteins IpaD and BipD. *Journal of Biological Chemistry* **282**, 4035-4044.
3. Wang, Y., Nordhues, B. A., Zhong, D. & De Guzman, R. N. (2010). NMR characterization of the interaction of the Salmonella type III secretion system protein SipD and bile salts. *Biochemistry* **49**, 4220-6.
4. Delaglio, F., Grzesiek, S., Vuister, G. W., Zhu, G., Pfeifer, J. & Bax, A. (1995). NMRPipe: a multidimensional spectral processing system based on UNIX pipes. *J Biomol NMR* **6**, 277-93.
5. Johnson, B. A. (2004). Using NMRView to visualize and analyze the NMR spectra of macromolecules. *Methods Mol Biol* **278**, 313-52.
6. Wallimann, P., Kennedy, R. J., Miller, J. S., Shalongo, W. & Kemp, D. S. (2003). Dual wavelength parametric test of two-state models for circular dichroism spectra of helical polypeptides: anomalous dichroic properties of alanine-rich peptides. *J Am Chem Soc* **125**, 1203-20.
7. Chatterjee, S., Zhong, D., Nordhues, B. A., Battaile, K. P., Lovell, S. & De Guzman, R. N. (2011). The crystal structures of the Salmonella type III secretion system tip protein SipD in complex with deoxycholate and chenodeoxycholate. *Protein Sci* **20**, 75-86.
8. Lunelli, M., Hurwitz, R., Lambers, J. & Kolbe, M. (2011). Crystal Structure of PrgI-SipD: Insight into a Secretion Competent State of the Type Three Secretion System Needle Tip and its Interaction with Host Ligands. *Plos Pathogens* **7**.

## Chapter 4. NMR Characterization of the Protein-Protein Interaction of the Tip SipD and Needle PrgI of *Salmonella*

### 4.1. Introduction

Based on the structure similarity between the  $\alpha$ -helical hairpin structure of the *Salmonella* T3SS needle protein PrgI and the N-terminal  $\alpha$ -helical domain of the tip protein SipD, it has been hypothesized that PrgI could displace the N-terminal domain of SipD upon assembly of the tip/needle complex<sup>1</sup>. To test whether removal of the N-terminal domain (residues 39 to 131) of SipD affected its binding affinity with PrgI, solution NMR spectroscopy was used to examine the interaction between a soluble and functional PrgI V65A, V67A mutant<sup>2</sup> (herein called PrgI\*) and a SipD construct containing the N-terminal domain (SipD <sup>$\Delta$ 38</sup>) or lacking the N-terminal domain (SipD <sup>$\Delta$ 132</sup>). Previous NMR data was collected using PrgI<sup>CA5</sup>, a C-terminal deletion mutant that prevented self-oligomerization and allowed for concentration to mM amounts for NMR<sup>3</sup>. Unfortunately the PrgI<sup>CA5</sup> mutant is not functional in invasion assays. Therefore, PrgI\* was used because it was a functional mutant in invasion assays and gave good quality NMR data<sup>2</sup>. Here, NMR spectroscopy is used to show that PrgI\* interacts with SipD <sup>$\Delta$ 132</sup> with greater affinity when compared to SipD <sup>$\Delta$ 38</sup>.

### 4.2. Materials and Methods

#### 4.2.1. Protein Expression and Purification

Isotopically <sup>15</sup>N/ILV <sup>13</sup>C-methyl labeled SipD <sup>$\Delta$ 38</sup> and SipD <sup>$\Delta$ 132</sup> were expressed and purified as described in Chapter 2. *Salmonella* Typhimurium strain SL1344 T3SS SPI-1 needle protein PrgI\*<sup>2</sup> was subcloned into a modified pET-21a expression vector

containing an N-terminal His<sub>6</sub> tag followed by a TEV protease cleavage site and GB1 as a solubility tag. Isotopically <sup>15</sup>N/ILV <sup>13</sup>C-methyl labeled PrgI\* was expressed in *E. coli* BL21(DE3) DNAY cells in 1 liter of 1× M9 minimal media with 30 µg/mL kanamycin and 100 µg/mL carbenicillin at 37°C containing 1 g/L <sup>15</sup>NH<sub>4</sub>Cl (Sigma-Aldrich, St. Louis, MO) and 2 g/L D-glucose. At an OD<sub>600</sub> of 0.4, the growth medium was supplemented with 60 mg/L of 2-ketobutyric acid-4-<sup>13</sup>C-sodium salt hydrate (#571342 Sigma) and 100 mg/L of 2-keto-3-(methyl-<sup>13</sup>C)-butyric-4-<sup>13</sup>C acid sodium salt (#571334 Sigma). Recombinant protein expression was induced with 1 mM IPTG at an OD<sub>600</sub> of 0.6 and cell growth was continued overnight at 15°C.

Bacterial cells were harvested by centrifugation at 4000 rpm for 10 mins, resuspended with binding buffer (500 mM NaCl, 20 mM Tris-HCl, 5 mM imidazole, pH 8.0, 1 mM phenylmethanesulfonyl fluoride) at 4°C and sonicated while keeping lysate ice-cold. Cells were sonicated using a Branson Digital Sonifier for 5 minutes and 20 seconds at amplitude 32% with 2 second on pulses and 6 second off pulses. The cell lysate was centrifuged for 10 minutes at 13,000 rpm. Next, 700 µL of 5% polyethyleneimine was added to the supernatant, which was centrifuged again to remove further cellular debris. The supernatant was loaded onto a 10 mL Ni<sup>2+</sup>-affinity chromatography column (Gold Biotechnology), the column was washed with 150 mL binding buffer (500 mM NaCl, 20 mM Tris-HCl, 5 mM imidazole, pH 8.0) and bound protein was eluted with 40 mL elution buffer (500 mM NaCl, 20 mM Tris-HCl, 250 mM imidazole, pH 8.0). The column elutions were incubated overnight at room temperature with 250 µL of 0.04 mM recombinant TEV protease in TEV protease buffer (50 mM Tris-HCl, pH 8.0, 0.5 mM EDTA, 1 mM DTT, 20 mM NaCl). The digest was then

purified by Ni<sup>2+</sup>-affinity chromatography using binding and elution buffer as mentioned above to separate protein from the affinity tag. All purified proteins were dialyzed into NMR buffer and concentrated using Amicon Ultra 3K (Millipore) filtration columns. Protein concentrations were determined by the absorbance at A<sub>280</sub>.

#### 4.2.2. <sup>1</sup>H-<sup>15</sup>N TROSY of SipD and <sup>1</sup>H-<sup>15</sup>N HSQC of PrgI\*

NMR data was collected using a Bruker Avance 800 MHz spectrometer equipped with a cryogenic triple resonance probe and were processed using NMRPipe<sup>4</sup> and analyzed using NMRView<sup>5</sup>. Two-dimensional <sup>1</sup>H-<sup>15</sup>N TROSY spectra were acquired at 30°C using 0.2 mM of <sup>15</sup>N/ILV <sup>13</sup>C-methyl labeled SipD<sup>Δ38</sup> or SipD<sup>Δ132</sup> in NMR buffer (50 mM NaCl, 10 mM sodium phosphate, pH 7.4 and 10% D<sub>2</sub>O). For PrgI\*, 2D <sup>1</sup>H-<sup>15</sup>N HSQC spectra were acquired at 30°C using 0.2 mM of <sup>15</sup>N/ILV <sup>13</sup>C-methyl labeled PrgI\* in NMR buffer. Typical acquisition parameters were 16 scans with 2048 complex points (<sup>1</sup>H) and 128 complex points (<sup>15</sup>N) with sweep width 10.01 ppm for <sup>1</sup>H centered at 4.69 ppm and 17.9 ppm for <sup>15</sup>N centered at 119 ppm.

#### 4.2.3. <sup>1</sup>H-<sup>13</sup>C HSQC of SipD and PrgI\*

Two-dimensional <sup>1</sup>H-<sup>13</sup>C HSQC spectra were acquired at 30°C using 0.2 mM <sup>15</sup>N/ILV <sup>13</sup>C-methyl labeled SipD<sup>Δ38</sup>, SipD<sup>Δ132</sup> or PrgI\* in NMR buffer. Acquisition parameters were 8 scans with 1024 complex points (<sup>1</sup>H) and 256 complex points (<sup>13</sup>C) with sweep width 10.01 ppm for <sup>1</sup>H centered at 4.69 ppm and 20 ppm for <sup>13</sup>C centered at 19 ppm.

#### 4.2.4. NMR Titrations Between PrgI\* and SipD<sup>Δ38</sup> or SipD<sup>Δ132</sup>

For NMR titration experiments, 0.2 mM of <sup>15</sup>N/ILV <sup>13</sup>C-methyl labeled SipD<sup>Δ38</sup> was titrated with unlabeled PrgI\* at a 1:4 mole ratio. In addition, 0.2 mM <sup>15</sup>N/ILV <sup>13</sup>C-methyl labeled SipD<sup>Δ132</sup> was titrated with unlabeled PrgI\* at increasing SipD:PrgI mole ratios, up to 1:4. SipD:PrgI\* ratios above 1:4 were not used because PrgI\* began to polymerize above 1 mM. Similarly, 0.2 mM of <sup>15</sup>N/ILV <sup>13</sup>C-methyl labeled PrgI\* was titrated with unlabeled SipD<sup>Δ132</sup> at increasing PrgI:SipD molar ratios, up to 1:4.

Amide and ILV methyl assignments of SipD<sup>Δ38</sup> and SipD<sup>Δ132</sup> used were described in Chapter 2 and Chapter 3. Assignment of the amide peaks of PrgI\* were transferred from the previous assignment of the PrgI\* 2D <sup>1</sup>H-<sup>15</sup>N HSQC spectrum by Poyraz and co-workers<sup>2</sup>. Peak intensity analysis of the SipD:PrgI\* 1:2 mole ratio over the mole 1:0 ratio was performed. Affected residues were mapped onto the crystal structure of SipD (PDB ID 3NZZ) or PrgI (PDB ID 2KV7).

### 4.3. Results

#### 4.3.1. Titration of SipD<sup>Δ38</sup> and SipD<sup>Δ132</sup> with PrgI\*

NMR titration experiments were performed to test the hypothesis that PrgI\* would interact with greater affinity to a SipD construct lacking an N-terminal domain (SipD<sup>Δ132</sup>) than a SipD construct containing an N-terminal domain (SipD<sup>Δ38</sup>). Isotopically <sup>15</sup>N/ILV <sup>13</sup>C-methyl labeled SipD<sup>Δ38</sup> was titrated with unlabeled PrgI\* and the titration was monitored by acquiring 2D <sup>1</sup>H-<sup>15</sup>N TROSY and 2D <sup>1</sup>H-<sup>13</sup>C HSQC datasets. Titration of SipD<sup>Δ38</sup> with PrgI\* at a SipD<sup>Δ38</sup>:PrgI\* mole ratio of 1:4 showed little or no change in SipD NMR peak position or peak intensity, suggesting a lack of interaction between

PrgI\* with amides of SipD<sup>Δ38</sup> (**Fig. 4-1**). Similarly, a lack of interaction was observed between SipD<sup>Δ38</sup> and PrgI\* in 2D <sup>1</sup>H-<sup>13</sup>C HSQC experiments (**Fig. 4-2**), suggesting PrgI\* also did not affect ILV methyl peaks of SipD<sup>Δ38</sup>. Together, these experiments showed a lack of interaction between SipD<sup>Δ38</sup> and PrgI\* as monitored by solution NMR.

In contrast, when <sup>15</sup>N/ILV <sup>13</sup>C-methyl labeled SipD<sup>Δ132</sup> truncated construct was titrated with increasing concentrations of PrgI\*, chemical shift perturbations of specific SipD<sup>Δ132</sup> amide peaks were observed in a concentration dependent manner (**Fig. 4-3A**). Peak changes were primarily due to decreased peak intensity due to broadening, such as D190, E228 and S331 (**Fig. 4-3B**), indicating the interaction was in the intermediate exchange NMR time-scale<sup>6</sup>. Similarly, the interaction between SipD<sup>Δ132</sup> and PrgI\* in ILV titrations was observed (**Fig. 4-4A**), showing PrgI\* also affected the ILV methyl peaks of SipD<sup>Δ132</sup> (**Fig. 4-4B**). Interestingly, new peaks appeared in the 2D <sup>1</sup>H-<sup>13</sup>C HSQC spectra of SipD<sup>Δ132</sup> upon titration with PrgI\* (**Fig. 4-4A & Fig. 4-5, arrows**). An attempt was made to assign the new SipD peaks using ZZ-exchange experiments, but was unsuccessful. Peak intensity analysis of the <sup>15</sup>N titration of SipD<sup>Δ132</sup> and PrgI\* at a 1:2 mole ratio showed a cluster of affected residues, including W135, D147 and V323, at the bottom of the SipD<sup>Δ132</sup> coiled-coil (**Fig. 4-6A**). However, some residues were also affected at the distal end of SipD<sup>Δ132</sup>, such as D269 (**Fig. 4-6A**). Similarly, peak intensity analysis of the ILV titration of SipD<sup>Δ132</sup>:PrgI\* showed a cluster of affected residues, including I145, L326 and L334, at the bottom of the SipD<sup>Δ132</sup> coiled-coil, but some residues were also affected at the distal end of SipD<sup>Δ132</sup> (**Fig. 4-6B**). Together, NMR titrations showed that, unlike SipD<sup>Δ38</sup>, SipD<sup>Δ132</sup> interacted with PrgI\* and a cluster of affected residues are at the bottom of the SipD coiled-coil.

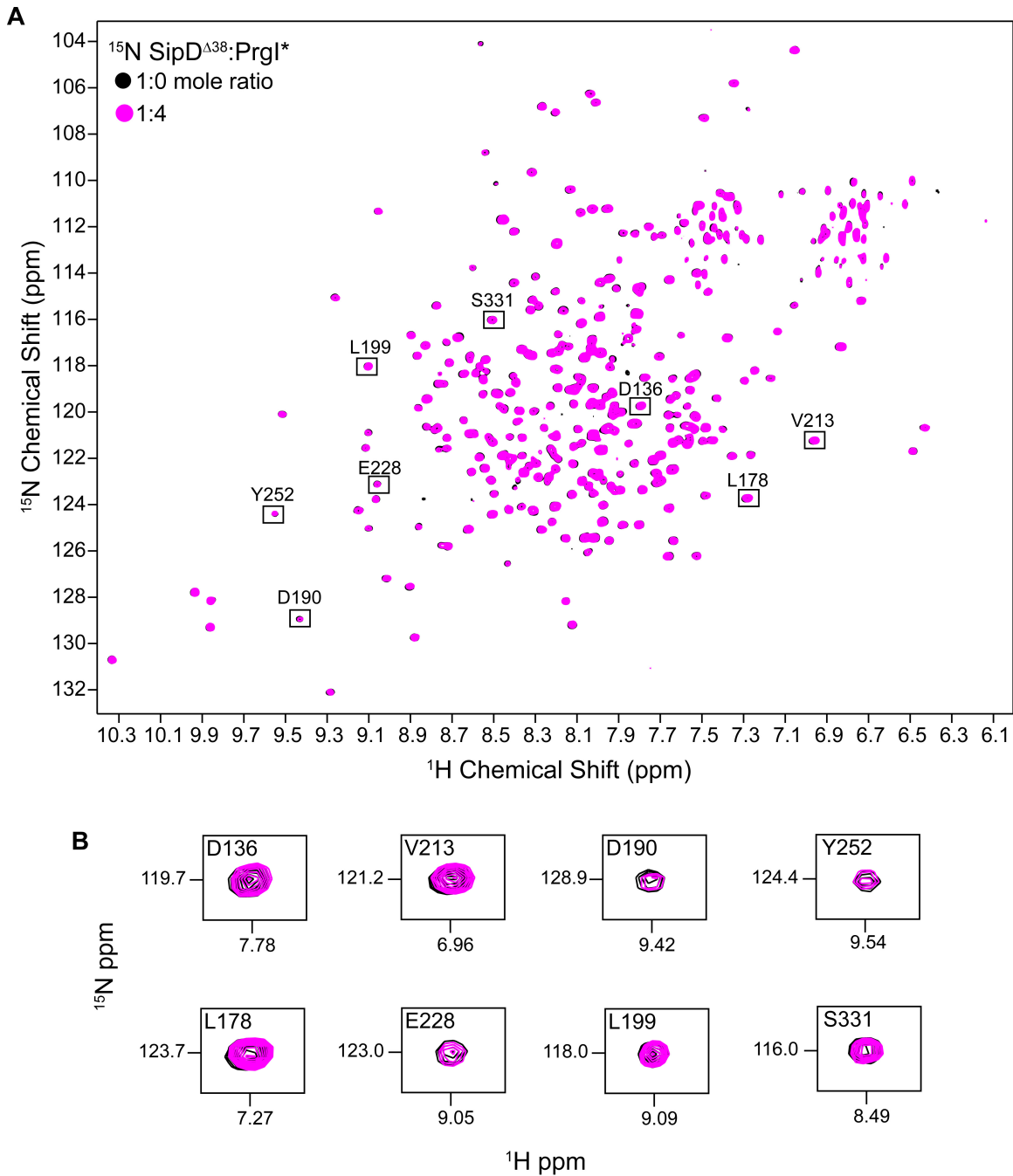


**Fig. 4-1 –  $^{15}\text{N}$  Titration of SipD $^{\Delta 38}$  with PrgI\***  
**(A)** Overlay of two 2D  $^1\text{H}$ - $^{15}\text{N}$  TROSY spectra of  $^{15}\text{N}$ /ILV  $^{13}\text{C}$ -methyl labeled SipD $^{\Delta 38}$  without PrgI\* (1:0, black) or in the presence of PrgI\* (1:4, magenta). No significant changes in peak chemical shift position or peak intensity were observed. **(B)** An expanded view of eight selected SipD amide peaks from the  $^{15}\text{N}$  titration is shown.

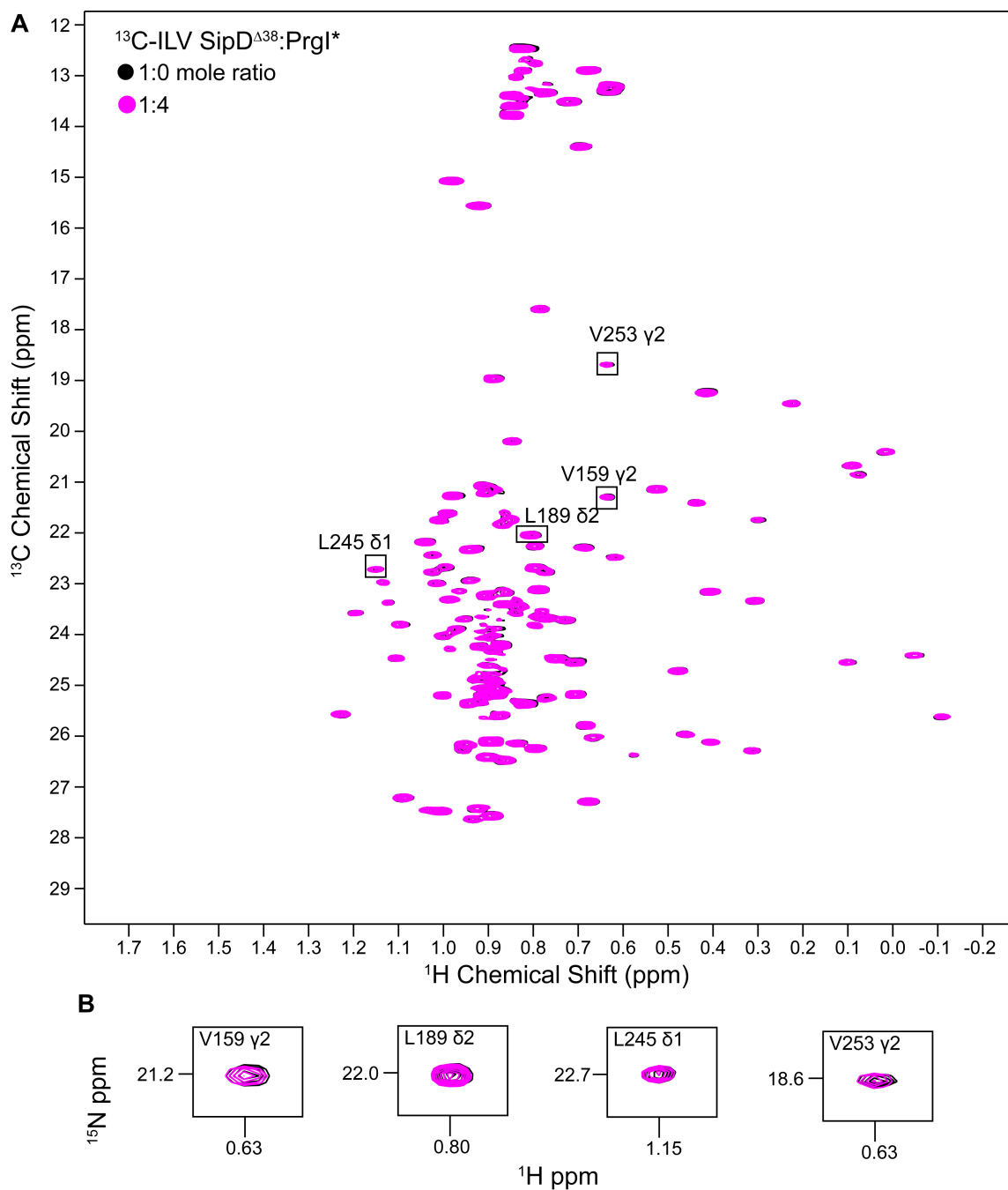


**Fig. 4-2 – ILV Titration of SipD $^{\Delta 38}$  with PrgI\***

(A) Overlay of two 2D  $^1\text{H}$ - $^{13}\text{C}$  HSQC spectra of  $^{15}\text{N}$ /ILV  $^{13}\text{C}$ -methyl labeled SipD $^{\Delta 38}$  without PrgI\* (1:0, black) or in the presence of PrgI\* (1:4, magenta). No changes in peak chemical shift position or peak intensity were observed. (B) An expanded view of four selected SipD peaks from the ILV titration is shown.

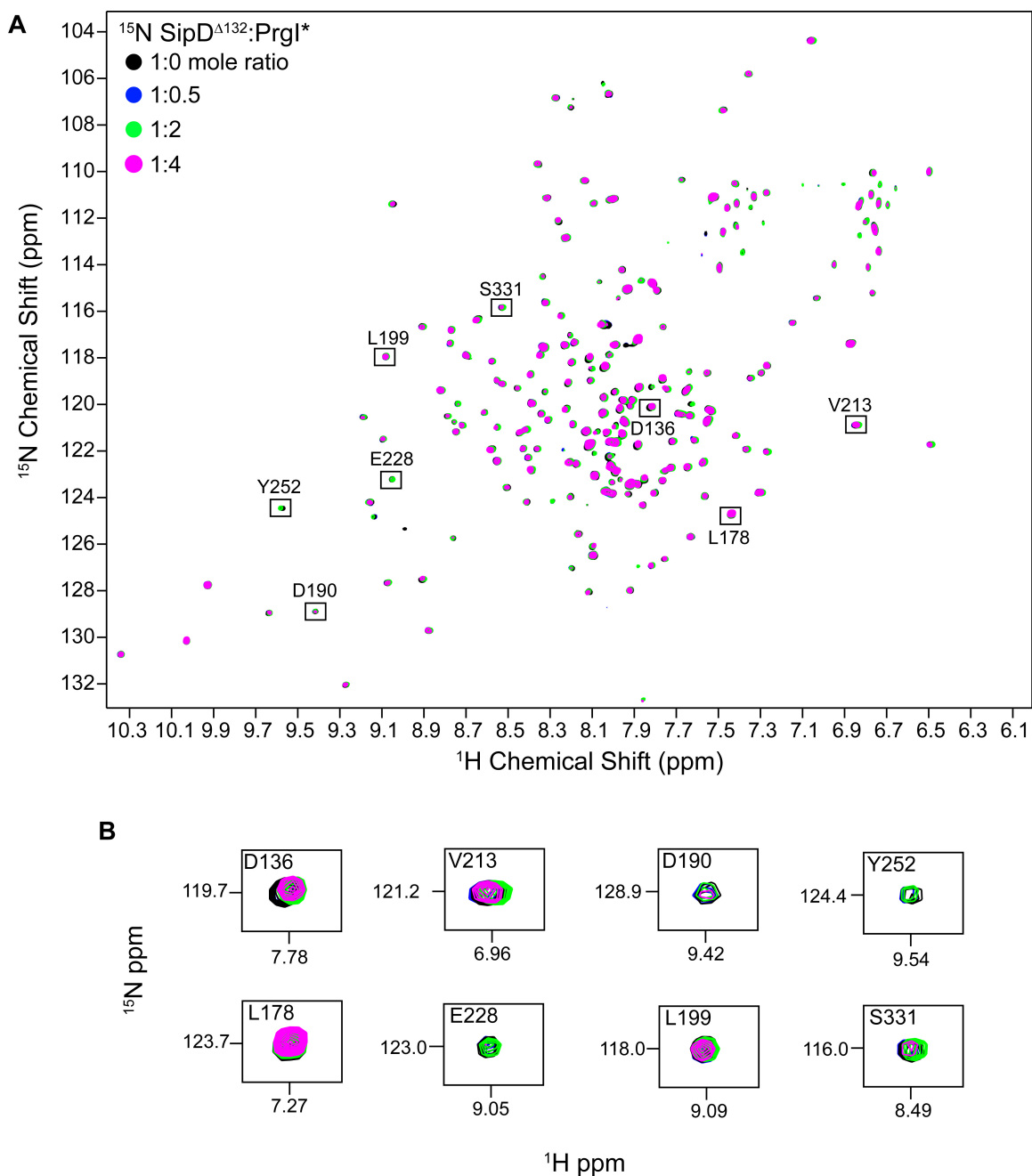


**Fig. 4-3 –  $^{15}\text{N}$  Titration of SipD $^{\Delta 132}$  with PrgI\***

**(A)** Overlay of four 2D  $^1\text{H}$ - $^{15}\text{N}$  TROSY spectra of  $^{15}\text{N}/\text{ILV}$   $^{13}\text{C}$ -methyl labeled SipD $^{\Delta 132}$  titrated with PrgI\* at increasing SipD $^{\Delta 132}$ :PrgI\* mole ratios (black 1:0; blue 1:0.5; green 1:2; magenta 1:4). Changes in peak intensity were observed, indicating interaction between the two proteins. **(B)** An expanded view of eight selected SipD amide peaks from the  $^{15}\text{N}$  titration is shown.

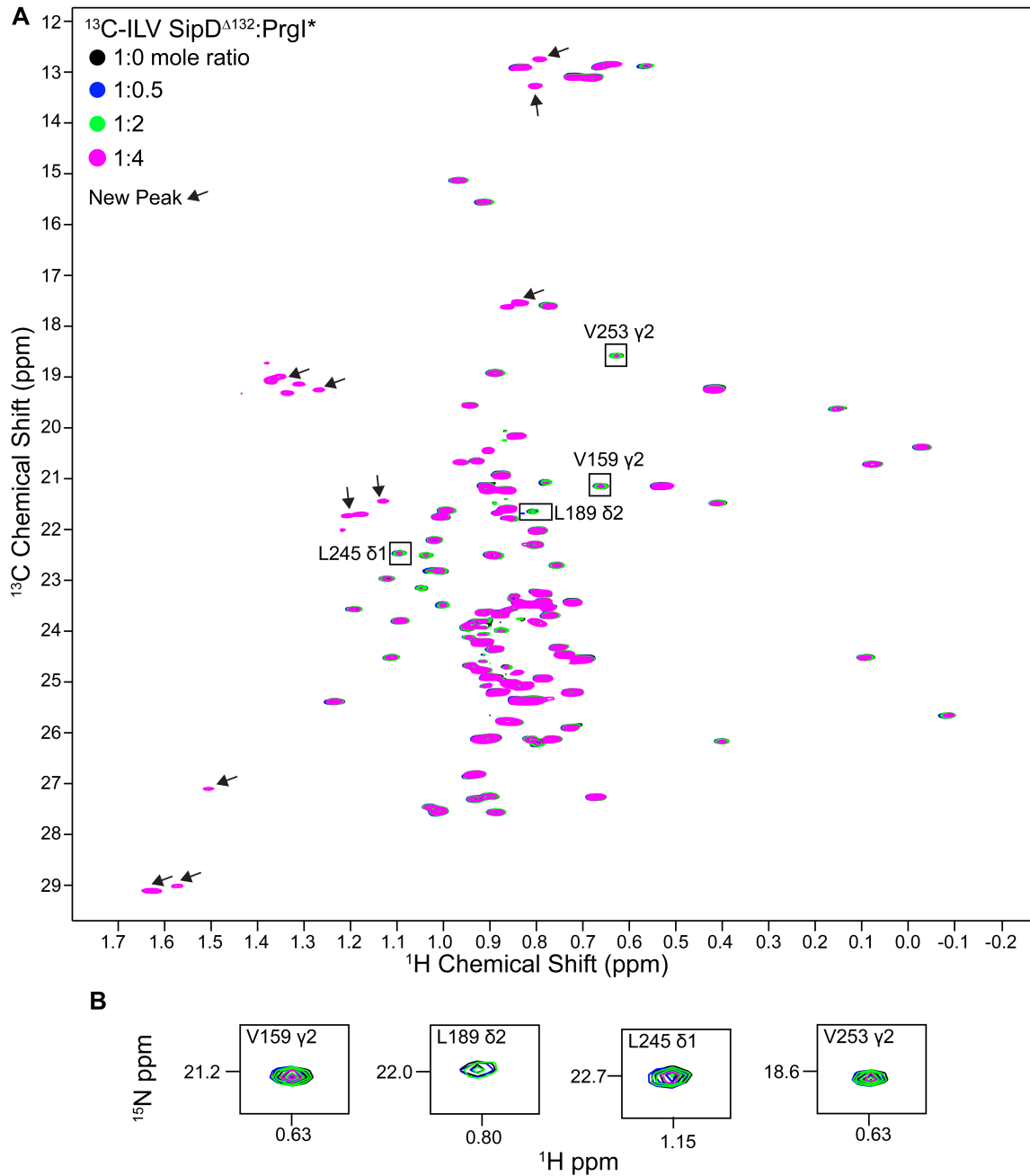


**Fig. 4-4 –ILV Titration of SipD $^{\Delta 132}$  with PrgI\***

(A) Overlay of four 2D  $^1\text{H}$ - $^{13}\text{C}$  HSQC spectra of  $^{15}\text{N}$ /ILV  $^{13}\text{C}$ -methyl SipD $^{\Delta 132}$  titrated with PrgI\* at increasing SipD $^{\Delta 132}$ :PrgI\* mole ratios (black 1:0; blue 1:0.5; green 1:2; magenta 1:4). Changes in peak intensity were observed, indicating interaction between the two proteins. New peaks observed upon titration with PrgI\* are indicated with arrows. (B) An expanded view of four selected SipD peaks from the ILV titration is shown.

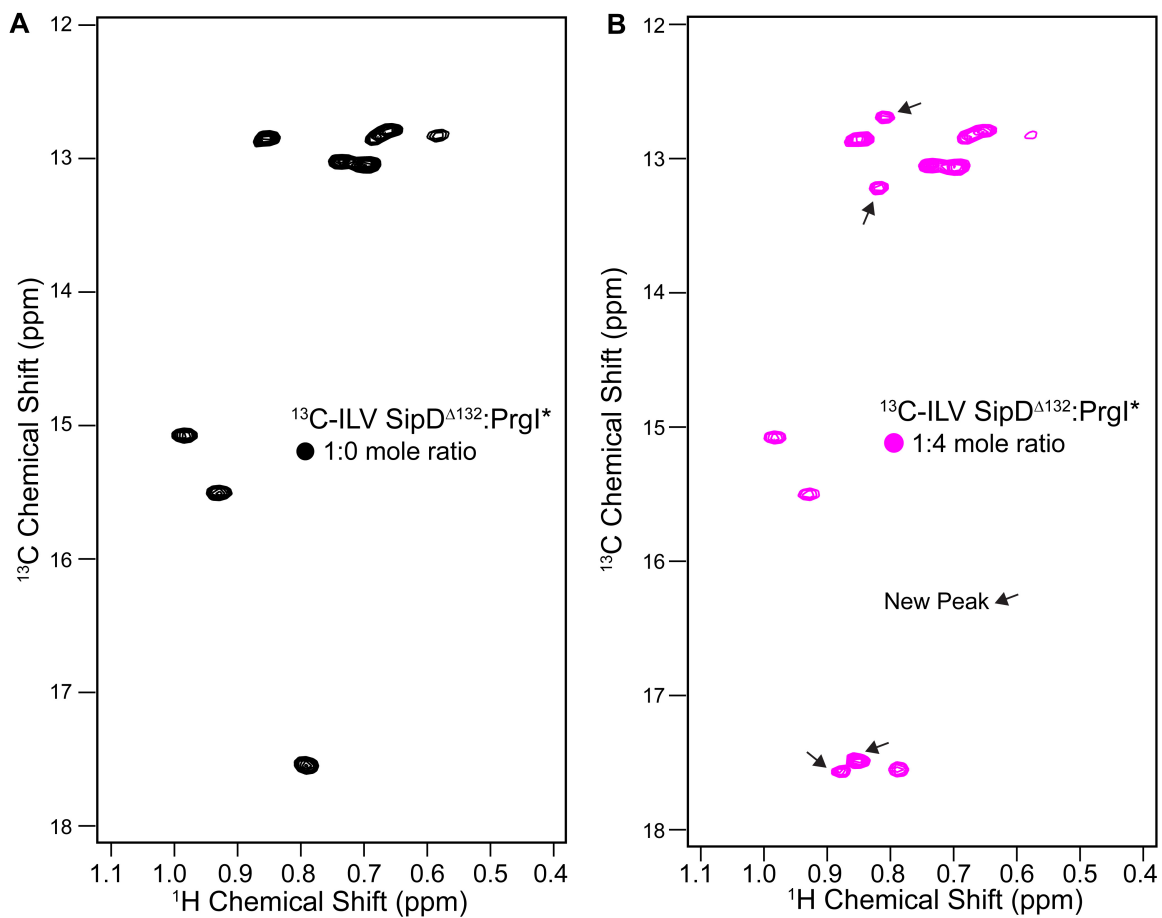


**Fig. 4-5 – New Peaks from ILV Titration of SipD $^{\Delta 132}$  with PrgI\***

An expanded region taken from the 2D  $^1\text{H}$ - $^{13}\text{C}$  HSQC spectrum in Fig. 4-4 showing the appearance of new SipD $^{\Delta 132}$  ILV methyl peaks upon titration with PrgI\*. SipD $^{\Delta 132}$ :PrgI\* mole ratio of 1:0 is shown in (A) and 1:4 in (B). New peaks are denoted with an arrow.

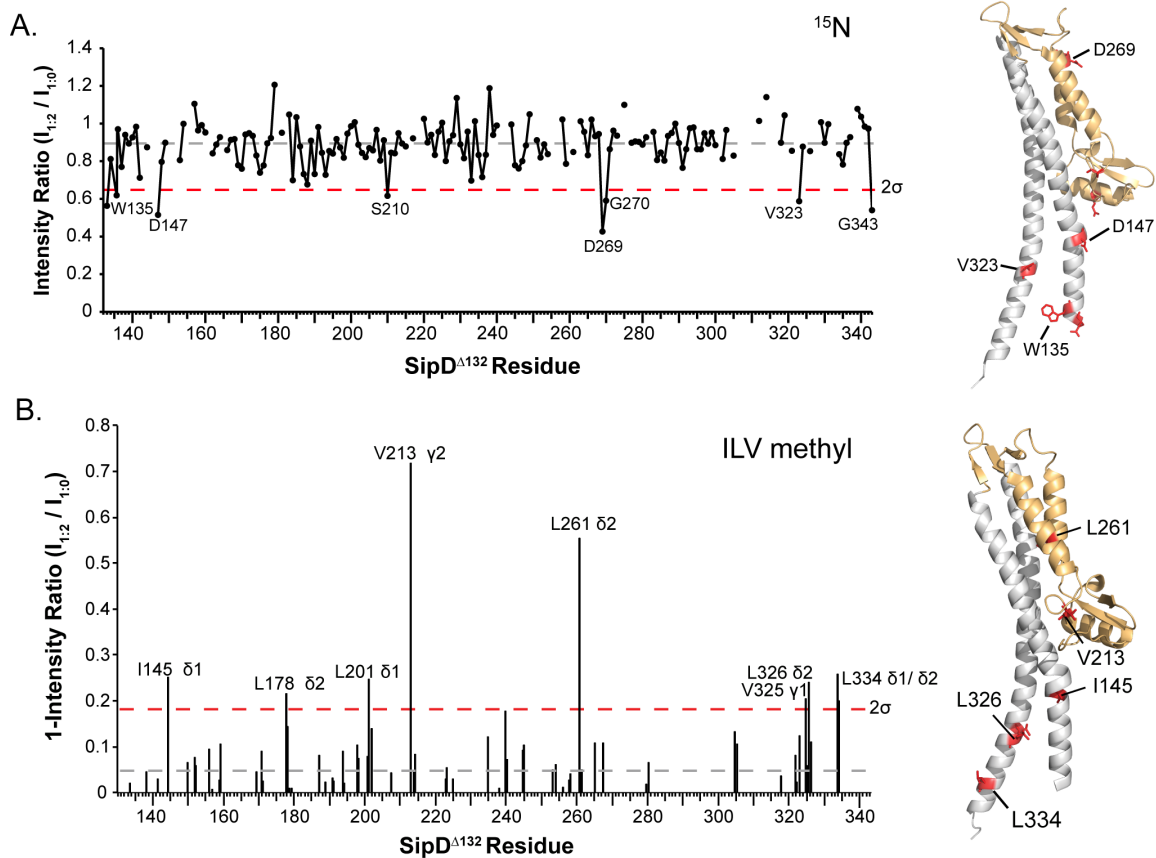


**Fig. 4-6 – Peak Intensity Analysis of  $^{15}\text{N}$  and ILV Titrations of SipD $^{\Delta 132}$  with PrgI\***  
**(A)** Peak intensity analysis of the  $^{15}\text{N}$  titration of SipD $^{\Delta 132}$  with PrgI\* at a mole ratio of 1:2 compared to 1:0. **(B)** Peak intensity analysis of the ILV titration of SipD $^{\Delta 132}$  with PrgI\* at a mole ratio of 1:2 compared to 1:0. In **(A)** and **(B)** affected residues are mapped onto the crystal structure of SipD.

#### 4.3.2. Titration of PrgI\* with SipD<sup>Δ132</sup>

To identify which PrgI\* residues were affected upon titration with SipD<sup>Δ132</sup>, <sup>15</sup>N/ILV <sup>13</sup>C-methyl labeled PrgI\* was titrated with unlabeled SipD<sup>Δ132</sup> and monitored by acquiring 2D <sup>1</sup>H-<sup>15</sup>N HSQC and 2D <sup>1</sup>H-<sup>13</sup>C HSQC datasets. Titration of <sup>15</sup>N/ILV PrgI\* with increasing concentrations of SipD<sup>Δ132</sup> up to a PrgI\*: SipD<sup>Δ132</sup> mole ratio of 1:4 resulted in chemical shift perturbations of specific PrgI\* amide peaks in a concentration dependent manner (**Fig. 4-7A**). Peak changes were a combination of decreased peak intensities due to broadening, as well as changes in chemical shift position (**Fig. 4-7B**), indicating that some residues were in intermediate exchange NMR time-scale, whereas other residues were in the fast exchange NMR time-scale<sup>6</sup>. Peak intensity analysis of the PrgI\*: SipD<sup>Δ132</sup> interaction at a 1:2 mole ratio showed a cluster of affected residues, including W5, L9, L76, Q24 and Y57, at the middle of the  $\alpha$ -helical hairpin and near the N- and C-termini of the PrgI\* (**Fig. 4-7C**). Chemical shift deviation analysis was not performed because only a few PrgI\* peaks were in the fast exchange NMR time-scale and most of the residues that underwent fast exchange were also in intermediate exchange, such as S6 and the W5 side-chain (**Fig. 4-7B**). In addition, interaction between SipD<sup>Δ132</sup> and PrgI\* in 2D <sup>1</sup>H-<sup>13</sup>C HSQC experiments was observed (**Fig. 4-8**), showing SipD<sup>Δ132</sup> also affected ILV methyl resonances of PrgI\*. Unfortunately, PrgI\* ILV methyl titration analysis was not performed because its ILV methyl have not been assigned. Together, amide and ILV experiments confirmed an interaction between SipD<sup>Δ132</sup> and PrgI\* with cluster of affected residues at the middle of the  $\alpha$ -helical hairpin and at the N- and C-termini of PrgI\*.

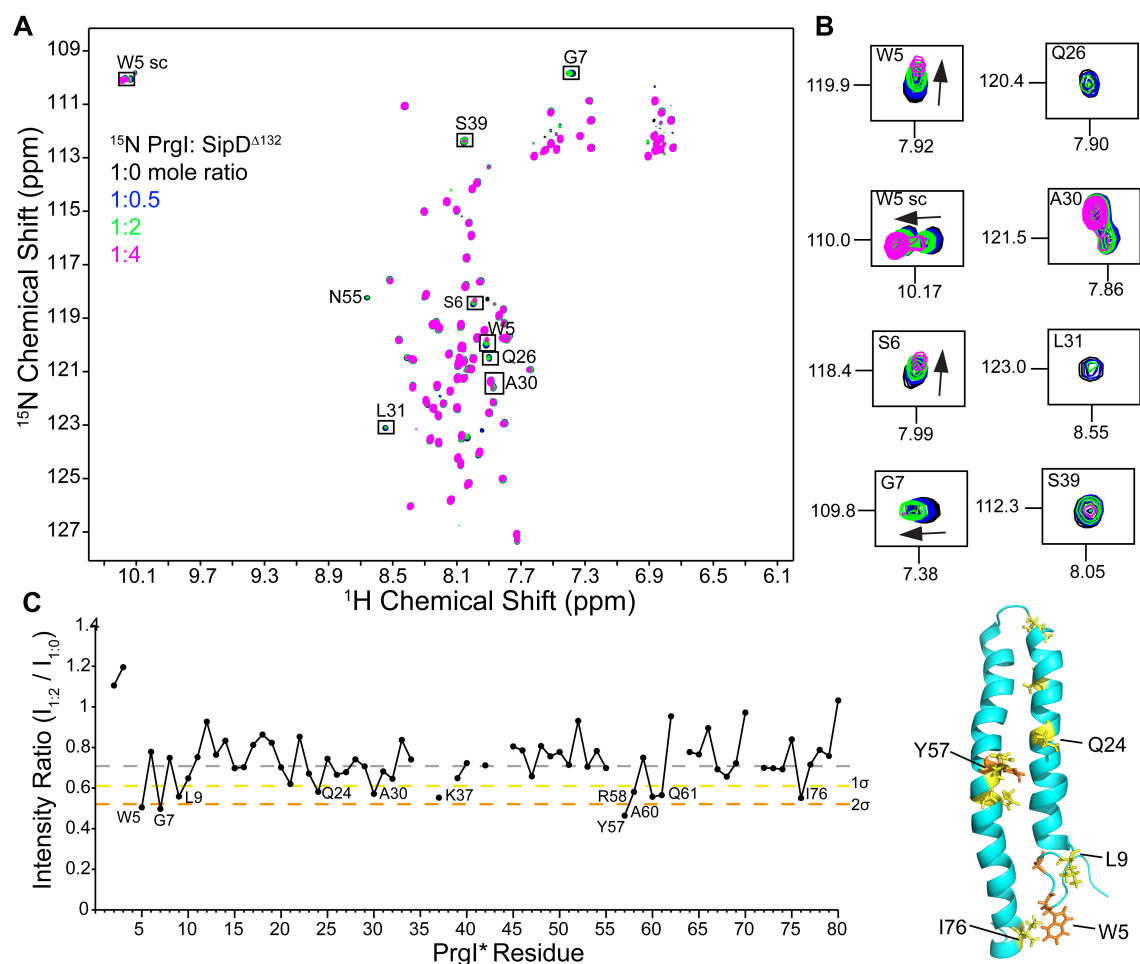


**Fig. 4-7 –  $^{15}\text{N}$  Titration of PrgI\* with SipD $\Delta 132$**

(A) Overlay of four 2D  $^1\text{H}$ - $^{15}\text{N}$  HSQC spectra of  $^{15}\text{N}$ /ILV  $^{13}\text{C}$ -methyl labeled PrgI\* titrated with SipD $\Delta 132$  at increasing PrgI\*:SipD $\Delta 132$  mole ratios (black 1:0; blue 1:0.5; green 1:2; magenta 1:4). Changes in peak intensity and chemical shift position were observed, indicating an interaction between the two proteins. (B) An expanded view of eight selected PrgI\* amide peaks from the  $^{15}\text{N}$  titration is shown. (C) Peak intensity analysis of the PrgI\*:SipD $\Delta 132$  interaction at a mole ratio of 1:2 compared to 1:0. Affected residues are mapped onto the crystal structure of PrgI\*.

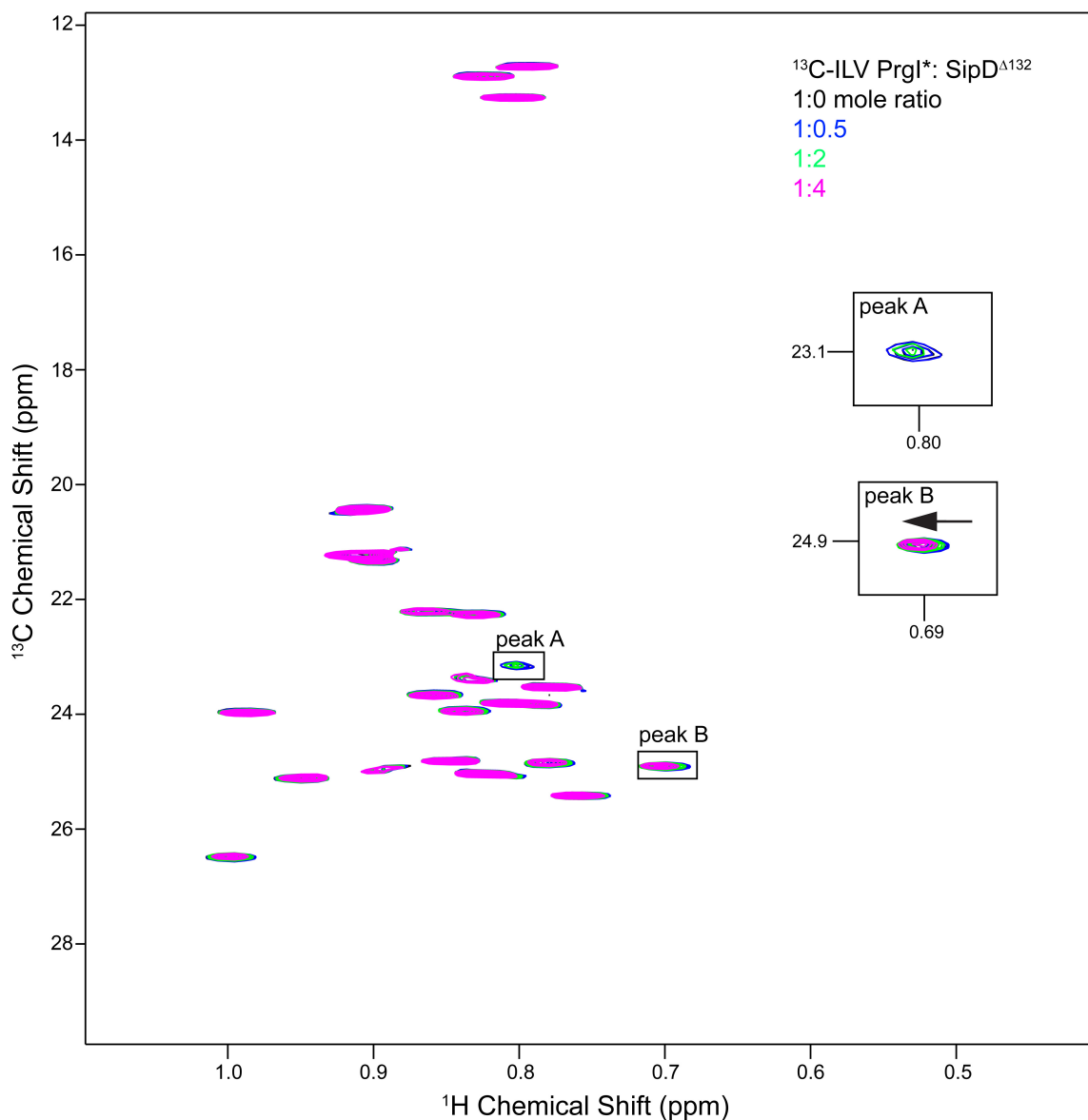


**Fig. 4-8 – ILV Titration of PrgI\* with SipD $\Delta^{132}$**

(A) Overlay of four 2D  $^1\text{H}$ - $^{13}\text{C}$  HSQC spectra of  $^{15}\text{N}$ /ILV  $^{13}\text{C}$ -methyl labeled PrgI\* titrated with SipD $\Delta^{132}$  at increasing PrgI\*:SipD $\Delta^{132}$  molar ratios (black 1:0; blue 1:0.5; green 1:2; magenta 1:4). Changes in peak intensity and chemical shift position were observed, indicating an interaction between the two proteins. An expanded view of two selected PrgI\* residues, called peak A and peak B due to lack of assignments, is shown. ILV methyl resonances of PrgI\* have not been assigned. Therefore, analysis of the interaction was not performed.

#### 4.4. Discussion

NMR titrations were performed to test the hypothesis that a SipD construct lacking its N-terminal domain (SipD<sup>Δ132</sup>) would interact with PrgI\* with greater affinity than a SipD construct containing its N-terminal domain (SipD<sup>Δ38</sup>). Both amide and ILV titrations of <sup>15</sup>N/ILV labeled SipD<sup>Δ38</sup> with PrgI\* showed a lack of interaction as observed by solution NMR (**Fig. 4-1 & Fig. 4-2**). In contrast, at the same molar ratio, an interaction was observed between <sup>15</sup>N/ILV SipD<sup>Δ132</sup> and PrgI\* (**Fig. 4-3 & Fig. 4-4**). Analysis of the <sup>15</sup>N and ILV methyl titrations of <sup>15</sup>N/ILV SipD<sup>Δ132</sup> with PrgI\* at 1:2 molar ratio showed a cluster of affected residues at the bottom of the SipD coiled-coil, suggesting a likely interaction site with PrgI\* (**Fig. 4-6A & Fig. 4-6B**). Interestingly, a few SipD<sup>Δ132</sup> residues at its distal region were also affected upon titration of PrgI\* (**Fig. 4-6A and Fig. 4-6B**). However, these could be due to a conformational change of SipD<sup>Δ132</sup> upon binding by PrgI\*. This explanation is plausible because residues at the distal end of SipD<sup>Δ38</sup> were not affected upon titration with PrgI\* in the presence of the SipD N-terminal domain (**Fig. 4-1 & Fig. 4-2**). Importantly, experiments monitoring amide and ILV peaks of SipD are in agreement. Together, these data support the hypothesis that the removal of the N-terminal  $\alpha$ -helical hairpin of SipD allows for a stronger interaction with PrgI\*.

Likewise, NMR titrations were also performed between <sup>15</sup>N/ILV PrgI\* and SipD<sup>Δ132</sup>. Results of <sup>15</sup>N titrations indicated that the affected PrgI\* residues clustered at middle of the  $\alpha$ -helical hairpin and at the N- and C-termini of PrgI\*, suggesting a likely interaction site with SipD<sup>Δ132</sup> (**Fig. 4-7C**). ILV titrations also show interaction between PrgI\* and SipD<sup>Δ132</sup> (**Fig. 4-8**). However, the ILV methyl peaks of PrgI\* have not been

assigned so titration analysis was not performed. The 2D  $^1\text{H}$ - $^{13}\text{C}$  HSQC of PrgI\* showed the expected 29 ILV methyl peaks (3 isoleucines, 8 leucines and 5 valines, with each isoleucine showing only one peak and each valine and leucine showing two peaks each). Therefore, in the future assignment of PrgI\* ILV methyl resonances is possible because of the good quality NMR data.

The interaction between PrgI\* and SipD $^{\Delta 132}$  as detected by solution NMR is weak (in the  $\mu\text{M}$  range) because NMR titration experiments showed residues in intermediate and/or fast exchange NMR time-scale. However, new peaks did appear in the ILV titrations of  $^{15}\text{N}$ /ILV SipD $^{\Delta 132}$  with PrgI\* (**Fig. 4-5B, arrows**), but not in the ILV titrations of  $^{15}\text{N}$ /ILV PrgI\* with SipD $^{\Delta 132}$  (**Fig. 4-8**). Interestingly, none of the original SipD $^{\Delta 132}$  ILV methyl peaks disappeared (**Fig. 4-4**), as one might expect if the new peaks were due to a true slow exchange phenomenon. There was an attempt made to identify and assign the new SipD $^{\Delta 132}$  peaks using NMR experiments (by EXSY/ZZ-exchange) to no avail. Although the assignment of the new peaks is unknown, it is possible that the new peaks are due to a conformational change in the ILV methyls of SipD $^{\Delta 132}$  in the presence of PrgI\*. Although the amide resonance of SipD $^{\Delta 132}$  did not show any signs of huge conformational change upon titration with PrgI\* (**Fig. 4-3A**), the ILV methyl resonances may be more sensitive to slight conformational changes than amide resonances.

#### 4.5. References

1. Rathinavelan, T., Lara-Tejero, M., Lefebvre, M., Chatterjee, S., McShan, A. C., Guo, D. C., Tang, C., Galan, J. E. & De Guzman, R. N. (2014). NMR model of PrgI-SipD interaction and its implications in the needle-tip assembly of the Salmonella type III secretion system. *J Mol Biol* **426**, 2958-69.

2. Poyraz, O., Schmidt, H., Seidel, K., Delissen, F., Ader, C., Tenenboim, H., Goosmann, C., Laube, B., Thunemann, A. F., Zychlinsky, A., Baldus, M., Lange, A., Griesinger, C. & Kolbe, M. (2010). Protein refolding is required for assembly of the type three secretion needle. *Nature Structural & Molecular Biology* **17**, 788-U26.
3. Wang, Y., Ouellette, A. N., Egan, C. W., Rathinavelan, T., Im, W. & De Guzman, R. N. (2007). Differences in the electrostatic surfaces of the type III secretion needle proteins PrgI, BsaL, and MxiH. *Journal of Molecular Biology* **371**, 1304-1314.
4. Delaglio, F., Grzesiek, S., Vuister, G. W., Zhu, G., Pfeifer, J. & Bax, A. (1995). NMRPipe: a multidimensional spectral processing system based on UNIX pipes. *J Biomol NMR* **6**, 277-93.
5. Johnson, B. A. (2004). Using NMRView to visualize and analyze the NMR spectra of macromolecules. *Methods Mol Biol* **278**, 313-52.
6. Kleckner, I. R. & Foster, M. P. (2011). An introduction to NMR-based approaches for measuring protein dynamics. *Biochim Biophys Acta* **1814**, 942-68.

## Chapter 5. Characterization of the SipD and PrgI Interaction by Fluorescence Spectroscopy

[Some of the data in this chapter has been published with the following citation:  
Rathinavelan T, Lara-Tejero M, Lefebvre M, Chatterjee S, McShan AC, Guo DC, Tang C, Galan JE, De Guzman RN. NMR Model of PrgI-SipD Interaction and Its Implications in the Needle-Tip Assembly of the Salmonella Type III Secretion System. *J. Mol. Biol.* 426, 2958-2969, 2014]

### 5.1. Introduction

The NMR titration experiments outlined in Chapter 4 support the hypothesis that PrgI interacts more strongly with SipD in the absence of the N-terminal domain of SipD. In those studies, isotopically labeled SipD<sup>Δ38</sup> (which contained N-terminal domain) or SipD<sup>Δ132</sup> (which lacked the N-terminal domain) was titrated with PrgI\*, a soluble and functional full-length PrgI V65A, V67A mutant<sup>1</sup>. Protein-protein interaction was clearly observed between PrgI\* with SipD<sup>Δ132</sup> (**Fig. 4-3 & Fig. 4-4**), but not between PrgI\* and SipD<sup>Δ38</sup> (**Fig. 4-1 & Fig. 4-2**). The SipD-PrgI interaction was also observed by NMR paramagnetic relaxation enhancement experiments between PrgI<sup>CA5</sup> and SipD<sup>Δ100</sup>, another construct of SipD lacking its N-terminal domain<sup>2</sup>. PrgI<sup>CA5</sup> is a PrgI truncation mutant of the last 5 residues of PrgI, which rendered the protein monomeric at sub-millimolar concentrations<sup>3</sup>. However, unlike PrgI\*, the PrgI<sup>CA5</sup> mutant is not functional in biological invasion assays. The SipD<sup>Δ100</sup> construct is an N-terminal domain mutant that contained a short helix and random coil (residues 101-131) at the bottom of the coiled-coil. To complement our NMR interaction studies, two protein binding assays were developed between PrgI\* and SipD<sup>Δ100</sup> utilizing fluorescence polarization (FP) or Förster resonance energy transfer (FRET). Fluorescence based protein binding assays were utilized because of the following: *i*) affinity measurements of SipD mutants to PrgI could be readily

tested, and *ii*) they could potentially be adapted for high throughput screens for inhibitors of the SipD/PrgI interaction<sup>4</sup>. In addition, an *in vitro* *Salmonella* invasion assay was used to evaluate the ability of SipD with mutations at the coiled-coil region to invade human intestinal epithelial Henle-407 cells. In support of our NMR data, which suggested the bottom of the SipD coiled-coil was the major interaction site for PrgI (**Fig. 4-6**), the fluorescence binding assays presented here were ultimately used to correlate a decrease in bacterial invasion due to SipD coiled-coil mutants with a decrease in SipD/PrgI binding affinity.

## 5.2. Materials and Methods

### 5.2.1. Site-Directed Mutagenesis, Protein Expression and Purification

Fluorescent labeling was achieved by the attachment of maleimide-conjugated fluorophore to a cysteine residue in the proteins<sup>5</sup>. SipD contains a wild-type cysteine, C244S, but this cysteine was mutated for NMR studies to generate higher quality NMR data. Therefore, C244S was kept as a background SipD mutation in all studies so the same construct used for NMR and fluorescent binding assays. PrgI\* does not contain a wild-type cysteine. Therefore, cysteine mutants were made using a QuikChange kit (Stratagene) and confirmed by DNA sequencing. Sites chosen for mutagenesis were non-conserved residues that were surface exposed based on the known atomic structures of SipD<sup>6</sup> and PrgI<sup>1</sup>. Constructs included SipD<sup>Δ38</sup>/SipD<sup>Δ100</sup> K173C and PrgI\* L31C. In addition, a total of 10 cysteine point mutants, as well as double or triple SipD<sup>Δ100</sup> coiled-coil mutants (along helix  $\alpha_4$  or  $\alpha_8$ ) were made for use in the fluorescence polarization studies using a QuikChange kit and confirmed by DNA sequencing. All mutant

constructs were expressed and purified in LB broth as previously described (Chapter 2 and Chapter 3 for SipD and Chapter 4 for PrgI\*).

### 5.2.2. Fluorophore Conjugation of Proteins

Maleimide conjugated fluorophore was used to label SipD<sup>Δ38</sup> K173C, SipD<sup>Δ100</sup> K173C and PrgI\* L31C at their respective cysteine residue. Before labeling, all proteins were dialyzed into 1× PBS, pH 7.4. A 10 fold excess of tris(2-carboxyethyl)phosphine (TCEP) to protein was used to reduce disulfide bonds for 30 minutes at 25°C. A 20 fold excess of dye to protein was resuspended in 1 mL of 1× PBS, pH 7.4 for Alexa Fluor 488-C<sub>5</sub>-Maleimide or Alexa Fluor 647-C<sub>2</sub>-Maleimide (Invitrogen), which labeled PrgI\* and SipD, respectively. Abbreviations for dyes used are AF488 (Alexa Fluor 488-C<sub>5</sub>-Maleimide) and AF647 (Alexa Fluor 647-C<sub>2</sub>-Maleimide). Fluorophore was added drop wise to the reduced protein solution while mixing and allowed to react for 3 hours in the dark at 25°C. The unreacted dye was removed by dialysis in 1× PBS, pH 7.4 followed by passage through an Amicon Ultra 3K (Millipore) filtration column. The percent labeling efficiency was estimated by acquiring the UV-visible absorption spectra of fluorophore labeled protein between 400 and 800 nm. Beer's Law was then used to determine the labeled protein concentration:  $A = \epsilon cl$ , where A is the absorption maxima, l is the path length and  $\epsilon$  is the fluorophore extinction coefficient ( $\epsilon = 265,000 \text{ cm}^{-1} \text{ M}^{-1}$  for AF657;  $\epsilon = 72,000 \text{ cm}^{-1} \text{ M}^{-1}$  for AF488). The percent labeling efficiency was determined by calculating the ratio of the fluorophore labeled protein over the initial unlabeled protein concentration and multiplying by 100%.

### 5.2.3. Fluorescence Polarization (FP)

FP provides a readout of the average angular displacement of a fluorophore during its excited lifetime. This displacement is dependent on the rate of rotational diffusion of the fluorophore labeled molecule<sup>4</sup>. Therefore, FP provides a measure of molecule volume change (or change in rotational diffusion rate) that occurs upon binding. FP experiments were performed by titrating 25 nM of AF488 labeled PrgI\* L31C with increasing concentrations of unlabeled SipD<sup>Δ38</sup> or SipD<sup>Δ100</sup>. The baseline signal of the fluorometer was removed by first using the buffer 1× PBS, pH 7.4 alone. The average of measured data points (n=5) was subtracted from a base polarization value of 25 nM PrgI\*-AF488 without any unlabeled SipD added. The difference in millipolarization ( $\Delta mP$ ) was plotted against increasing concentrations of unlabeled SipD to obtain a binding curve. The FP binding curve was fitted with Origin (OriginLab, Northampton, MA). All FP data was collected using a Varian Cary Eclipse Fluorescence Spectrophotometer at 25°C.

### 5.2.4. Förster Resonance Energy Transfer (FRET)

FRET was used to determine distance specific information on the protein-protein interactions. Fluorescence emission spectra were examined for different combinations of fluorophore labeled proteins. Emission spectra (n = 3) were collected between 500 nm and 800 nm using an excitation wavelength of 480 nm, excitation and emission slit widths of 5 nm, and an integration time of 0.1 seconds. All data was collected on a Varian Cary Eclipse Fluorescence Spectrophotometer at 25°C.

FRET efficiency was calculated from emission spectra as follows:

$$E = 1 - \frac{F_{DA}}{F_D}$$

where  $E$  is the energy transfer efficiency,  $F_{DA}$  is the donor fluorescence FRET in the presence of the acceptor, and  $F_D$  is the donor fluorescence in the absence of the acceptor. Once the FRET efficiency is known, the distance between the FRET dye pairs,  $r$ , was calculated from the following formula:

$$r = R_0 \left( \frac{1}{E} - 1 \right)^{1/6}$$

where  $R_0$  is the Förster distance between two FRET pairs at which  $E = 50\%$ . An  $R_0$  value of  $56\text{\AA}$  was used for the FRET pairs (AF488 donor with AF647 acceptor) in this study (Invitrogen).

#### 5.2.5. *Salmonella* Invasion Assay

A *Salmonella* invasion assay was used to test whether SipD coiled-coil mutants influenced the ability of *Salmonella* to invade a cultured human epithelial cell line (Henle 407 cells, ATCC #CCL6) following a method previously described<sup>6</sup> and using wild-type or *sipD* knock-out *Salmonella* Typhimurium SL1344<sup>6</sup>. Single, double, or triple point mutations were introduced by PCR in the plasmid pRK2-SipD<sup>6</sup>, which harbors full-length SipD. Mutations were confirmed by DNA sequencing. For the invasion assay, 100 ng of each pRK2-SipD mutant plasmid was introduced into 45  $\mu\text{L}$  of electrocompetent *sipD* knock out *Salmonella* cells by electroporation at 1.7 kV for 6 seconds then plated onto LB-agar plates. A single bacterial colony was grown for 10 hours without aeration at 37°C in 10 mL LB broth containing 25  $\mu\text{g}/\text{mL}$  trimethoprim, 100  $\mu\text{g}/\text{mL}$  carbenicillin and 25  $\mu\text{g}/\text{mL}$  chloramphenicol. The overnight culture was dilution 1:10 in LB media containing 1 mM IPTG and grown without aeration at 37°C until the  $\text{OD}_{600}$  was 0.4.

Henle-407 cells were grown in the 24-well plates in Dulbecco's modified Eagle's medium (DMEM) with 10% (v/v) fetal bovine serum at 37°C and 5% CO<sub>2</sub>. A 1:4 dilution of a confluent 75 cm<sup>2</sup> flask was used to seed the 24-well plates. Prior to addition of bacteria, each well was washed with 500 μL DMEM. When the OD<sub>600</sub> reached 0.4, bacterial cultures were added (~10 μL but the amount added was adjusted to correct for differences in the OD<sub>600</sub> when multiple cultures were used) to the Henle-407 cells in 300 μL DMEM and incubated at 37°C for 1 hour in 5% CO<sub>2</sub>. Wells were then washed three times with 500 μL DMEM containing 5% fetal bovine serum and 50 μg/mL Gentamicin then incubated for 1.5 hours at 37°C in 5% CO<sub>2</sub> to kill any extracellular bacteria. Wells were then rinsed with 500 μL DMEM and cells were lysed with 200 μL 1% Triton X-100 dissolved in 1× PBS, pH 7.4 for 10 minutes. Finally, 50 μL of a 1:1000 dilution of the cell lysate was spread onto LB agar plates without antibiotics and incubated overnight at 37°C. Percent invasiveness was calculated by counting the number of colonies on each plate. The *sipD*<sup>-</sup> strain complemented with the wild-type SipD pRK2 plasmid taken as representing 100% invasiveness. Therefore, the percent invasion of all other mutations were relative the *sipD*<sup>+</sup> strain. Error bars representative of three replicate experiments are shown.

### 5.3. Results

#### 5.3.1. Fluorophore Conjugation to PrgI\* and SipD<sup>Δ38</sup>/SipD<sup>Δ100</sup>

Cysteine point mutations were generated by PCR for the attachment of maleimide-conjugated fluorophore. These included SipD<sup>Δ38</sup> K173C, SipD<sup>Δ100</sup> K173C and PrgI\* L31C. Circular dichroism experiments confirmed that the cysteine point mutant

proteins contained similar secondary structure characteristics to their non-cysteine containing parent protein (data not shown). PrgI\* L31C was labeled with AF488 and SipD<sup>Δ38</sup>/SipD<sup>Δ100</sup> K173C were labeled with AF647. AF488 and AF647 were chosen as the FRET dye pair because their R<sub>0</sub> value of 56 Å is in the range that we hypothesized the distance between K173C of SipD and L31C of PrgI to be based on our NMR data showing that PrgI interacts at the bottom of the SipD coiled-coil. UV-visible absorption spectra show that proteins were labeled with their respective fluorophore (**Fig. 5-1**). Protein fluorophore labeling efficiency was estimated to be 70% for PrgI\* L31C-AF488 and 80% for SipD<sup>Δ38</sup>/SipD<sup>Δ100</sup> K173C-AF647. Circular dichroism experiments showed that the conjugation of fluorophore to PrgI\* and SipD did not greatly change their secondary structure characteristics (**Fig. 5-2**).

### 5.3.2. Fluorescence Polarization of PrgI\* and SipD<sup>Δ38</sup>/SipD<sup>Δ100</sup>

Fluorescence polarization was used as a protein binding assay between PrgI and SipD mutant constructs. Titration of 25 nM PrgI\* L31C-AF488 with increasing concentrations of unlabeled SipD<sup>Δ38</sup> resulted in slight changes in polarization, but the binding curve was not close to saturation so it could not be fitted to determine a dissociation constant (**Fig. 5-3**). In contrast, titration of PrgI\* L31C-AF488 with unlabeled SipD<sup>Δ100</sup> resulted in larger changes in polarization and the dissociation constant between PrgI\* and SipD<sup>Δ100</sup> was determined to be  $108 \pm 11 \mu\text{M}$  (**Fig. 5-3**). Together, these data agree with the conclusion of the NMR experiments in Chapter 4 that the removal of the N-terminal domain of SipD allows for a tighter interaction with PrgI\* and that the interaction is in the  $\mu\text{M}$  range.

The effect of point mutations along the SipD<sup>Δ100</sup> coiled-coil were tested for interaction against PrgI\*. The dissociation constant for a few of the mutants was within five-fold of the original value (S148E was 189 ± 21 μM, V157K was 334 ± 162 μM and S313 was 420 ± 294 μM) indicating small changes protein binding affinity (**Fig. 5-3**). The dissociation constant could not be measured for some mutants, such as D320R and V323K, because binding curves did not reach saturation, indicating weak interaction (**Fig. 5-3**). Because protein-protein interactions often occur across large surface areas, the effect of double or triple mutations in the SipD<sup>Δ100</sup> coiled-coil on the interaction with PrgI\* were additionally tested. All double and triple mutants of SipD<sup>Δ100</sup> had small changes in fluorescence polarization, indicating weak interaction with PrgI\* (**Fig. 5-3**). Importantly, circular dichroism showed that all SipD<sup>Δ100</sup> mutants contained similar secondary structure characteristics to SipD<sup>Δ100</sup>, for example  $\theta_{222/208}$  ratios near 1, indicating that the changes in protein binding were not the result of major changes in SipD<sup>Δ100</sup> structure (**Fig. 5-5**).

### 5.3.3. FRET of PrgI\* and SipD<sup>Δ38</sup>/SipD<sup>Δ100</sup>

FRET was used to assay the interaction between PrgI\* L31C-AF488 (donor) and SipD<sup>Δ38</sup> or SipD<sup>Δ100</sup> K173C-AF647 (acceptor). In agreement with the results of NMR and FP experiments, FRET was observed between PrgI\* and SipD<sup>Δ100</sup>, but not between PrgI\* and SipD<sup>Δ38</sup> (**Fig. 5-4**). FRET efficiency was used to estimate that the distance between PrgI\* L31C-AF488 and SipD<sup>Δ100</sup> K173C-AF647 was 44Å. In comparison, the distance between K173, which is at the top of the SipD coiled-coil, and D320, which is at the bottom of the SipD coiled-coil, in the SipD structure<sup>6</sup> was 40Å. Therefore, FRET

distance measurements are in agreement with the hypothesis that PrgI\* interacts with the bottom of the coiled-coil surface of SipD.

#### 5.3.4. *Salmonella* Invasion Assay

The ability of a *Salmonella* Typhimurium strain containing single, double or triple mutations in the SipD coiled-coiled region to invade human intestinal epithelial cells (Henle-407) was tested. Deletion of SipD (*sipD*<sup>-</sup>) eliminated the ability of *Salmonella* to invade Henle-407 cells (**Fig. 5-6**). However, invasion could be rescued by complementing *Salmonella* with a plasmid containing wild-type SipD (*sipD*<sup>+</sup>) (**Fig. 5-6**). *Salmonella* containing SipD S148E resulted in 100% invasion (**Fig. 5-6**). In contrast, *Salmonella* containing other SipD single mutations, such as V157K, S313E, D320R and V323K, had partially decreased invasiveness (**Fig. 5-6**). *Salmonella* containing double or triple SipD mutants were completely non-invasive (**Fig. 5-6**). Importantly, these SipD mutants were properly folded in circular dichroism studies (**Fig. 5-5**), indicating that the observed decrease in invasion was not due to gross structural changes in SipD brought upon by the mutations. Together, these data suggests that SipD coiled-coil mutants decreased invasiveness of *Salmonella* to human intestinal epithelial cells *in vitro*.

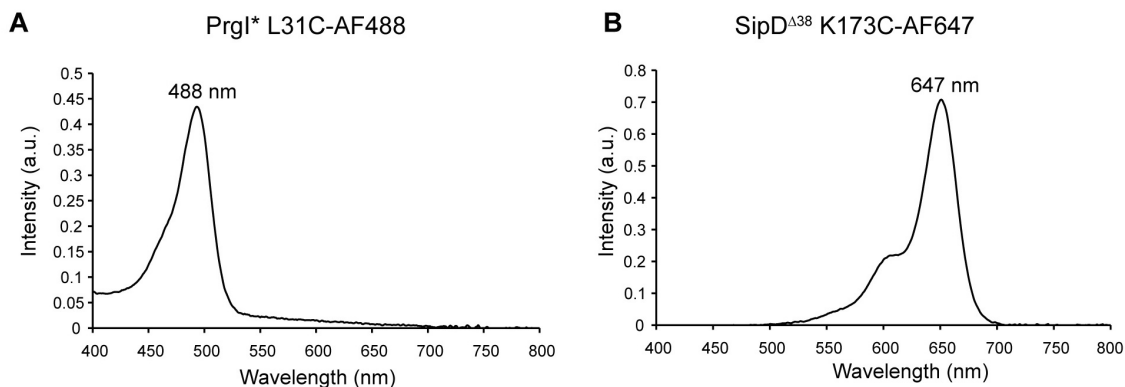


**Fig. 5-1 – UV-Vis Absorption Spectra of Fluorophore Labeled PrgI\* and SipD<sup>Δ38</sup>**  
 UV-visible absorption spectra of (A) AF488 labeled PrgI\* L31C and (B) AF647 labeled SipD<sup>Δ38</sup> K173C. The maxima of the spectra are labeled and correlate with the expected adsorption maxima of their respective fluorophore.

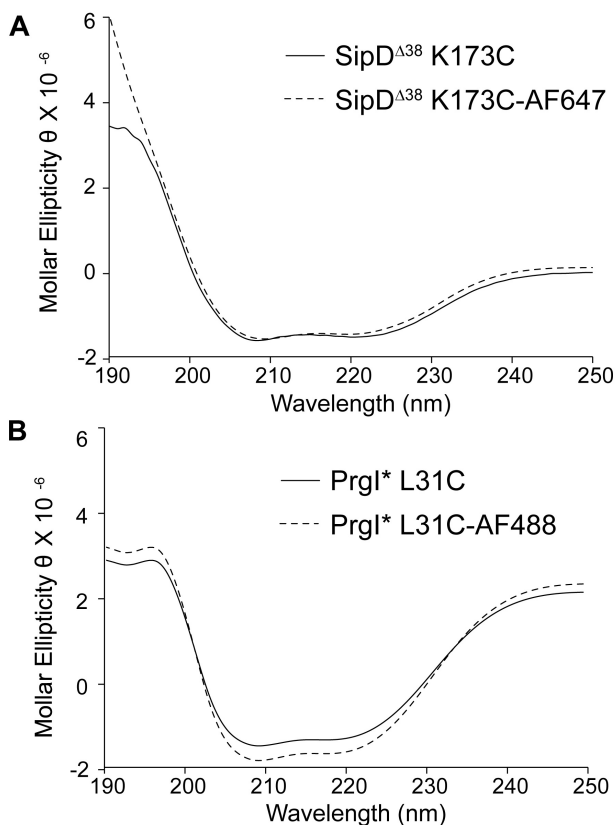


**Fig. 5-2 – Circular Dichroism of Fluorophore Labeled PrgI\* and SipD<sup>Δ38</sup>**  
 Far-UV CD spectra of fluorophore labeled (A) SipD<sup>Δ38</sup> K173C and (B) PrgI\* L31C are shown. Both proteins show CD minima at 208 and 222, which is typical of highly  $\alpha$ -helical proteins. CD shows the secondary structure characteristics of fluorophore labeled protein (dotted line) are similar to non-fluorophore labeled protein (solid line). Similar results were observed for SipD<sup>Δ100</sup> K173-AF647, which is not shown here.

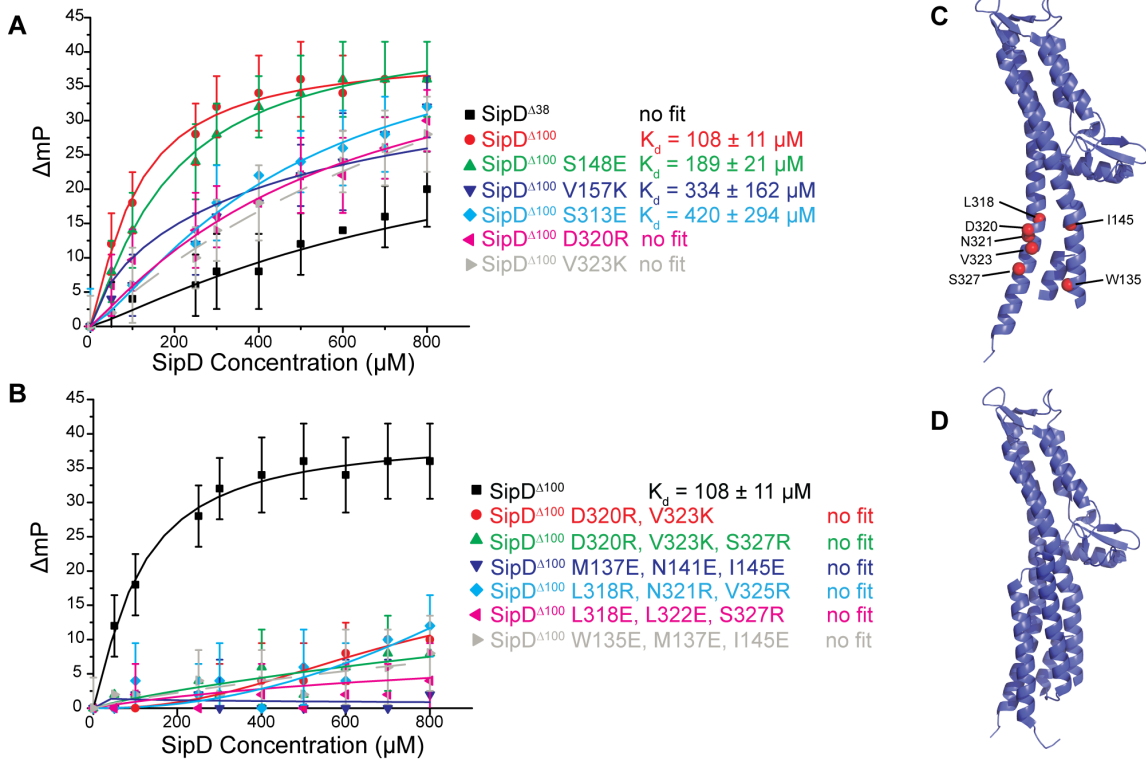


**Fig. 5-3 – Fluorescence Polarization of PrgI\*-AF488 and SipD $\Delta^{38}$ /SipD $\Delta^{100}$**

FP of 25 nM PrgI\* L31C-AF488 with increasing concentrations of unlabeled SipD $\Delta^{38}$  or SipD $\Delta^{100}$  (including single, double or triple coiled-coiled SipD mutants) is shown. The change in millipolarization is plotted vs. the concentration of SipD added. Each data point contains error bars for its replicates ( $n=5$ ). **(A)** SipD $\Delta^{38}$  weakly interacted with PrgI\* (could not determine a  $K_d$ ), while the PrgI\*/SipD $\Delta^{100}$   $K_d$  was determined to be 108  $\mu\text{M}$ . Single mutations either had a small effect on the  $K_d$  of the PrgI-SipD interaction (S148E or V157K or S313E) or moderately affected the interaction (D320R or V323K). **(B)** All of the double or triple SipD $\Delta^{100}$  coiled-coiled mutants drastically reduced its ability to bind PrgI\*. **(C)** The location of the residues used in FP experiments mapped onto the structure of SipD $\Delta^{100}$  as a reference. **(D)** The crystal structure of SipD $\Delta^{38}$  for comparison with SipD $\Delta^{100}$ .

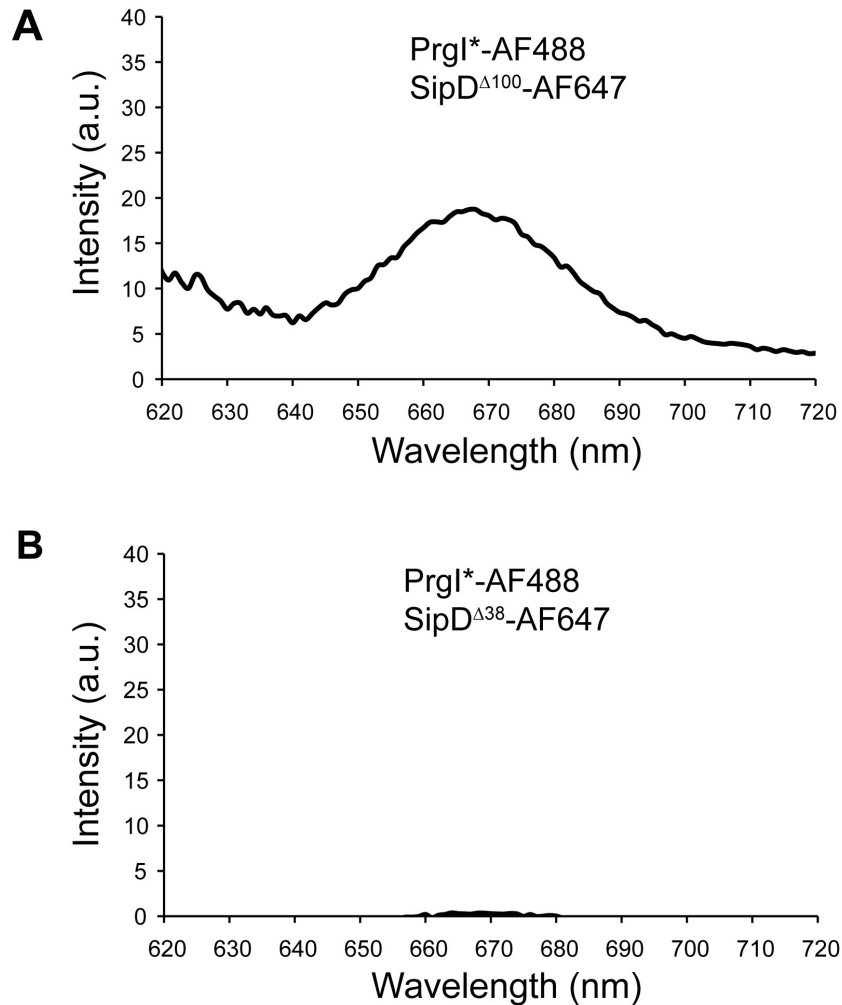


**Fig. 5-4 – FRET of PrgI\*-AF488 and SipD<sup>Δ38</sup>/SipD<sup>Δ100</sup>-AF647**  
**(A)** FRET performed with PrgI\* L31C-AF488 (donor) and SipD<sup>Δ100</sup> K173C-AF647 (acceptor). A clear FRET signal is observed. **(B)** FRET performed with PrgI\* L31C-AF488 (donor) and SipD<sup>Δ38</sup> K173C-AF647 (acceptor). No significant FRET signal was observed.

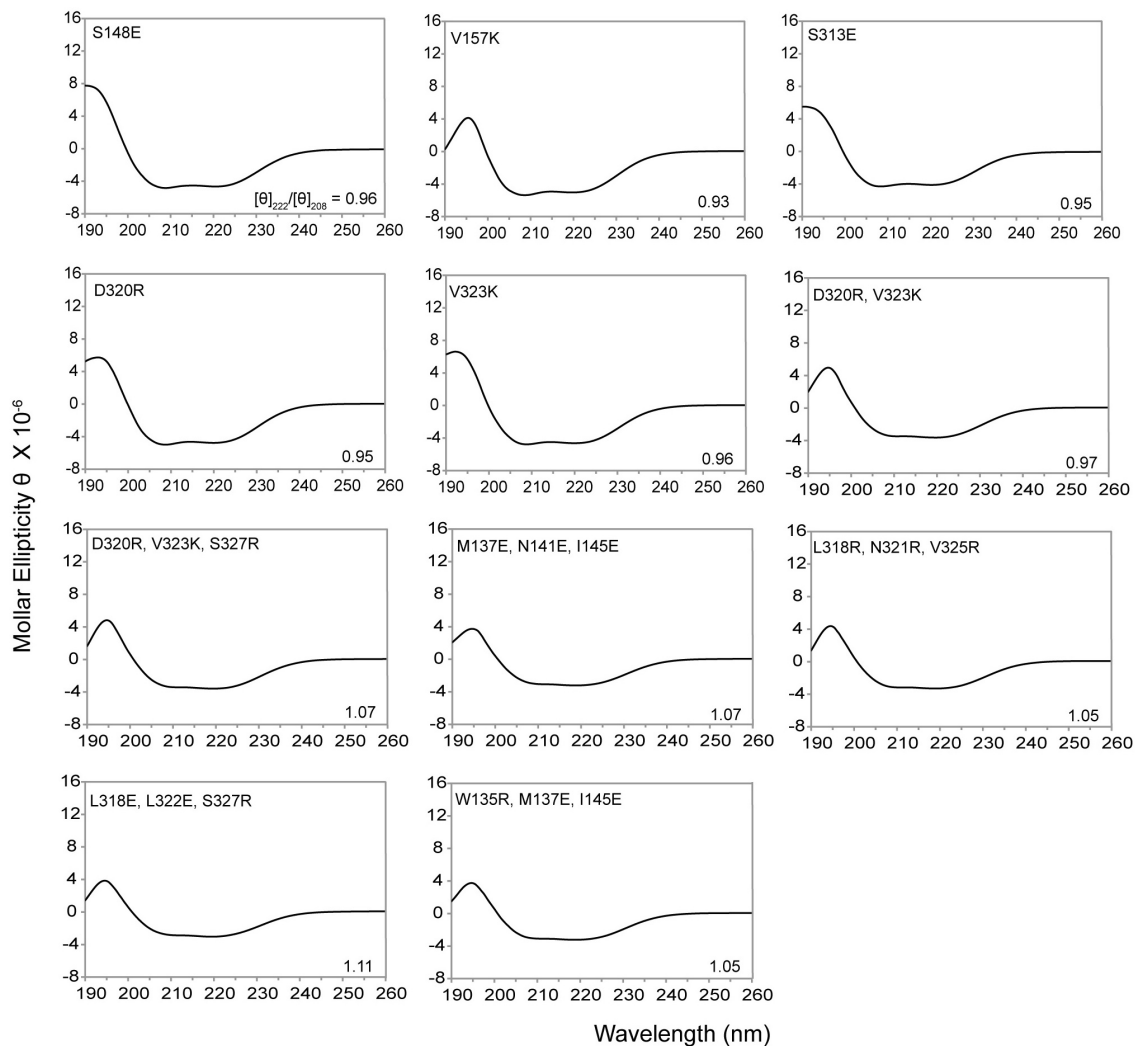


**Fig. 5-5– Circular Dichroism of SipD<sup>Δ100</sup> Mutants**

Far-UV CD spectra of SipD<sup>Δ100</sup> coiled-coil mutants used for FP and invasion assay experiments are shown. All proteins show CD minima at 208 and 222, which is typical of highly  $\alpha$ -helical proteins. The  $\theta_{222/208}$  ratio for each protein is shown in the bottom right handle corner of each spectrum. For comparison, the  $\theta_{222/208}$  ratio for SipD<sup>Δ100</sup> was 0.96, so all the SipD<sup>Δ100</sup> coiled-coil mutants contained similar secondary structure characteristics, indicating the mutations did not drastically alter the structure of SipD<sup>Δ100</sup>. Thermal denaturation experiments all showed a single  $T_m$  at 75°C as expected for wild-type SipD<sup>Δ100</sup>.

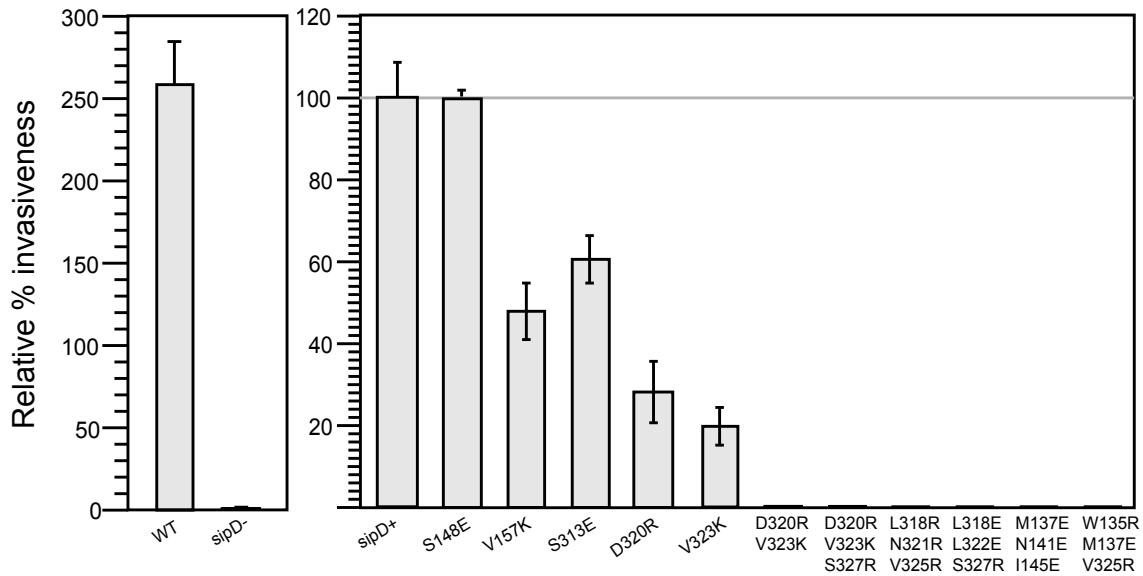


**Fig. 5-6 – *Salmonella* Invasion Assay of SipD Coiled-Coil Mutants**  
 Invasion assay between *Salmonella* Typhimurium strain SL1344 and intestinal epithelial Henle-407 cells is shown. Invasion is relative to the knock out *Salmonella* strain complemented with a SipD plasmid (*sipD*<sup>+</sup>). The *Salmonella sipD*<sup>-</sup> mutant was completely non-invasive. Adding back wild-type SipD (*sipD*<sup>+</sup>) to the *sipD*<sup>-</sup> *Salmonella* strain complemented invasion, but below wild-type (WT) levels. All SipD<sup>1-343</sup> coiled-coil mutations (except S148E) reduced invasion. Triple SipD *Salmonella* mutants were completely non-invasive. Data in collaboration with Dr. Srirupa Chatterjee.

#### 5.4. Discussion

In Chapter 4, results of solution NMR experiments showed that removal of the N-terminal domain of SipD (residues 39-131) allowed for tighter binding to PrgI\*. Here, results of both FP (Fig. 5-3) and FRET (Fig. 5-4) experiments are in agreement with solution NMR experiments. Results of FP experiments indicated a dissociation constant of  $108 \pm 11 \mu\text{M}$  between PrgI\* and SipD<sup>Δ100</sup>, but the interaction between PrgI\* and SipD<sup>Δ38</sup> was much weaker and did not produce a saturated binding curve (Fig. 5-3). Similarly, significant FRET signal was observed between PrgI\* and SipD<sup>Δ100</sup>, but not

SipD<sup>Δ38</sup> (**Fig. 5-4**). The distance between PrgI\* L31 and SipD<sup>Δ100</sup> K173 was estimated by FRET to be 44Å (**Fig. 5-4**). Importantly, this is the approximate distance from the top to the bottom of the SipD coiled-coil (K173 to D320 is 40Å). Together, NMR, FP and FRET data are in agreement that PrgI\* interacts more strongly with a SipD lacking its N-terminal domain and PrgI\* interacts at the bottom of the coiled-coil of SipD.

To correlate the FP and FRET results with a biological assay, invasion assays were performed between intestinal epithelial Henle-407 cells and a *Salmonella* Typhimurium *sidD* knockout strain complemented with a plasmid containing single, double or triple mutations in the SipD. Point mutants, except for S148E, decreased invasion, but double and triple mutants completely knocked out the ability of *Salmonella* to invade Henle-407 cells (**Fig. 5-6**). Importantly, the decrease in invasion results correlated well with decreased protein binding affinity between PrgI\* and SipD measured by FP (**Fig. 5-3**). For example, the SipD S148 mutant that had a wild-type level of invasion (**Fig. 5-6**) also had a dissociation constant most similar to the PrgI\* and SipD<sup>Δ100</sup> interaction (**Fig. 5-3**). In addition, the triple mutations that decreased invasion to below 1% (**Fig 5-6**) did not significantly change the polarization of PrgI\* (**Fig. 5-3**). Together, invasion assay is in agreement with NMR, FP and FRET experiments, and further support the hypothesis that PrgI interacts with the bottom of the coiled-coil of SipD.

## 5.5. References

1. Poyraz, O., Schmidt, H., Seidel, K., Delissen, F., Ader, C., Tenenboim, H., Goosmann, C., Laube, B., Thunemann, A. F., Zychlinsky, A., Baldus, M., Lange, A., Griesinger, C. & Kolbe, M. (2010). Protein refolding is required for

- assembly of the type three secretion needle. *Nature Structural & Molecular Biology* **17**, 788-U26.
2. Rathinavelan, T., Tang, C. & De Guzman, R. N. (2011). Characterization of the Interaction between the Salmonella Type III Secretion System Tip Protein SipD and the Needle Protein PrgI by Paramagnetic Relaxation Enhancement. *Journal of Biological Chemistry* **286**, 4922-4930.
  3. Darboe, N., Kenjale, R., Picking, W. L., Picking, W. D. & Middaugh, C. R. (2006). Physical characterization of MxiH and PrgI, the needle component of the type III secretion apparatus from Shigella and Salmonella. *Protein Science* **15**, 543-552.
  4. Lea, W. A. & Simeonov, A. (2011). Fluorescence polarization assays in small molecule screening. *Expert Opin Drug Discov* **6**, 17-32.
  5. Kim, Y., Ho, S. O., Gassman, N. R., Korlann, Y., Landorf, E. V., Collart, F. R. & Weiss, S. (2008). Efficient site-specific labeling of proteins via cysteines. *Bioconjug Chem* **19**, 786-91.
  6. Chatterjee, S., Zhong, D., Nordhues, B. A., Battaile, K. P., Lovell, S. & De Guzman, R. N. (2011). The crystal structures of the Salmonella type III secretion system tip protein SipD in complex with deoxycholate and chenodeoxycholate. *Protein Sci* **20**, 75-86.

## Chapter 6. CD and NMR Characterization of SipB N-Terminal

### Ectodomain Constructs

#### 6.1. Introduction

The atomic structure of full-length SipB, the major translocon protein from *Salmonella* Typhimurium, is currently unknown. Expression and purification of full-length SipB results in low yields, requires co-expression and subsequent separation from its cognate chaperone SicA<sup>1</sup>, and incorporation into membrane or membrane-like environments for stability and proper folding. The N-terminal domain of SipB, which has been modeled as an ectodomain upon host membrane insertion<sup>2</sup>, is known to interact with the tip protein SipD<sup>3;4</sup>. To determine the interaction surface of the tip-translocon protein-protein interaction, soluble constructs of the SipB N-terminal ectodomain were designed. One N-terminal SipB construct containing residues 82 to 240 (herein called SipB<sup>82-240</sup>) has previously been characterized<sup>5</sup>. Notably, SipB<sup>82-240</sup> contained a similar region to the crystal structure of SipB from 82 to 226<sup>6</sup>. However, a recent report by Dickenson and co-workers<sup>3</sup> suggested that the extreme N-terminal residues IpaB, the SipB homolog in *Shigella*, from 11 to 27 were essential for the interaction with the *Shigella* tip protein IpaD. To test the role of the extreme N-terminal residues of SipB, two additional SipB constructs were designed that included the residues 11 to 81. These two constructs were SipB<sup>11-232</sup> and SipB<sup>11-312</sup>. The residues from 232 to 312 were included in the latter construct because they are predicted to form an  $\alpha$ -helix that could potentially increase the surface area of SipB for SipD to interact with. Here, the expression, purification and characterization of SipB<sup>82-240</sup>, SipB<sup>11-232</sup> and SipB<sup>11-312</sup> are described.

## 6.2. Materials and Methods

### 6.2.1. Protein Expression and Purification

*Salmonella* Typhimurium strain SL1344 SPI-1 major translocon protein SipB<sup>11-232</sup> or SipB<sup>11-312</sup> were subcloned using NdeI/XhoI restriction sites into a pET-22b plasmid that contained a C-terminal His tag. The forward primer had the sequence 5' AGTTCGCATATGAGCGGATATACCCAA 3'. The reverse primers had the sequence 5' GTCGCTCTCGAGTCCCTGGAATTTGGT 3' (for SipB<sup>11-232</sup>) and 5' GTCGCTCTCGAGGCGGTTTCGTTTCCTC 3' (for SipB<sup>11-312</sup>). Subcloning was confirmed by DNA sequencing. SipB<sup>82-240</sup> was previously subcloned into a pET-22b plasmid using a similar protocol. Isotopically <sup>15</sup>N/<sup>13</sup>C-methyl labeled SipB<sup>11-232</sup>, SipB<sup>11-312</sup> or SipB<sup>82-240</sup> were expressed in *E. coli* BL21(DE3) DNAY cells in 1 liter of 1× M9 minimal media with 30 µg/mL kanamycin and 100 µg/mL carbenicillin at 37°C. Cultures additionally contained 1 g/L <sup>15</sup>N<sub>4</sub>CL (Sigma-Aldrich, St. Louis, MO) and 2 g/L D-glucose. At an OD<sub>600</sub> of 0.4 the growth medium was supplemented with 60 mg/L of 2-ketobutyric acid-4-<sup>13</sup>C-sodium salt hydrate (Sigma #571342) and 100 mg/L of 2-keto-3-(methyl-<sup>13</sup>C)-butyric-4-<sup>13</sup>C acid sodium salt (Sigma #571334). Recombinant protein expression was induced with 1 mM IPTG at an OD<sub>600</sub> of 0.8 and cell growth was continued overnight at 15°C.

Bacterial cells were harvested by centrifugation at 4000 rpm for 10 minutes, resuspended with binding buffer (500 mM NaCl, 20 mM Tris-HCl, 5 mM imidazole, pH 8.0, 1 mM phenylmethanesulfonyl fluoride) at 4°C and sonicated while keeping the lysate ice-cold. Cells were sonicated using a Branson Digital Sonifier for 5 minutes and 20 seconds at amplitude 32% with 2 second on pulses and 6 second off pulses. The cell

lysate was centrifuged for 10 minutes at 13000 rpm. Next, 700  $\mu$ L of 5% polyethyleneimine was added to the supernatant, which was centrifuged again to remove further cellular debris. The supernatant was loaded on a 5 mL Ni<sup>2+</sup>-affinity chromatography column (Gold Biotechnology) and the column was washed with 150 mL binding buffer (500 mM NaCl, 20 mM Tris-HCl, 5 mM imidazole, pH 8.0) and bound protein was eluted using 40 mL elution buffer (500 mM NaCl, 20 mM Tris-HCl, 250 mM imidazole, pH 8.0). Fractions containing the target protein were dialyzed into NMR buffer (50 mM NaCl, 20 mM sodium phosphate, pH 7.4) and concentrated using Amicon Ultra 3K (Millipore) filtration columns. Protein concentrations were determined by absorbance at A<sub>280</sub>.

#### 6.2.2. Size Exclusion Chromatography (SEC)

To determine the oligomeric state of SipB constructs, size exclusion chromatography was performing utilizing a Superdex 75 SEC column with a column height of 51 cm and a bed volume of 300 mL (GE Healthcare). The SEC column was equilibrated with 300 mL of filtered and de-gassed SEC buffer (150 mM NaCl, 0.5 mM DTT, 10 mM Tris-HCl, pH 8.0). Next, 2 mL of 0.4 mM SipB<sup>11-232</sup> or SipB<sup>11-312</sup> was loaded onto the SEC column. Typical parameters used for SEC runs were 1 mL/min flow rate and 0.3 MPa pressure while acquiring 6 mL elution fractions. The SEC column was calibrated using protein standards of known molecular weights, including Blue Dextran (200 kDa), Albumin (66 kDa), Carbonic Anhydrase (29 kDa), Cytochrome C (12.4 kDa) and Aprotinin (6.5 kDa). To calculate the partition coefficient ( $K_{av}$ ) values for the protein standards, the equation  $K_{av} = (V_e - V_0) / (V_c - V_0)$  was used, where  $V_e$  = elution volume,  $V_0$

= void volume,  $V_c$  = column volume, and  $K_{av}$  = partition coefficient. The logarithm of the molecular weight (y-axis) vs  $K_{av}$  (x-axis) for each protein standard was then plotted to obtain the standard curve,  $y = -0.4207x + 2.118$ , where  $y = K_{av}$  and  $x = \log$  molecular weight in Daltons. The  $K_{av}$  obtained from the SEC run for each SipB construct was then used to estimate its molecular weight (or oligomeric state) using the standard curve equation.

### 6.2.3. Circular Dichroism (CD)

Far-UV CD experiments were acquired using a JASCO J-815 Spectropolarimeter. The CD samples for SipB<sup>11-232</sup> or SipB<sup>11-312</sup> were prepared with 0.05 mg/mL protein in 2 mL sterile water in a quartz cuvette. A water blank was acquired and subtracted from each protein spectra. CD spectra were acquired from 190 to 260 nm in triplicate at 20°C with a scan rate of 50 nm/minute. Thermal denaturation experiments were performed by measuring ellipticity at 222 nm over a temperature range of 20°C to 80°C with a ramp rate of 2°C/minute. The experimental CD values of ellipticity (mdeg) were converted to molar ellipticity ( $\theta = \text{deg cm}^2/\text{dmol}$ ). The melting temperature ( $T_m$ ) was calculated using JASCO J-815 software.

### 6.2.4. NMR Spectroscopy

All NMR data was collected using a Bruker Avance 800 MHz spectrometer equipped with a cryogenic triple resonance probe and were processed using NMRPipe<sup>7</sup> and analyzed using NMRView<sup>8</sup>. Two-dimensional <sup>1</sup>H-<sup>15</sup>N TROSY spectra were acquired at 30°C using 0.3 mM of <sup>15</sup>N/ILV <sup>13</sup>C-methyl labeled SipB<sup>11-232</sup> or SipB<sup>11-312</sup> in NMR

buffer (50 mM NaCl, 20 mM sodium phosphate, pH 7.4) containing 10% D<sub>2</sub>O. Typical acquisition parameters were 128 scans with 2048 complex points (<sup>1</sup>H) and 128 complex points (<sup>15</sup>N) with sweep width 10.01 ppm for <sup>1</sup>H centered at 4.69 ppm and 17.9 ppm for <sup>15</sup>N centered at 119 ppm. Two-dimensional <sup>1</sup>H-<sup>13</sup>C HSQC spectra were acquired at 30°C using 0.3 mM of <sup>15</sup>N/ILV <sup>13</sup>C-methyl labeled SipB<sup>11-232</sup> or SipB<sup>11-312</sup> in NMR buffer containing 10% (v/v) D<sub>2</sub>O. Typical acquisition parameters were 16 scans with 1024 complex points (<sup>1</sup>H) and 256 complex points (<sup>13</sup>C) with sweep width 10.01 ppm for <sup>1</sup>H centered at 4.69 ppm and 20 ppm for <sup>13</sup>C centered at 19 ppm.

### 6.3. Results

#### 6.3.1. Purification of SipB<sup>11-232</sup>, SipB<sup>11-312</sup> and SipB<sup>82-240</sup>

The crystal structure<sup>6</sup> of the SipB N-terminal domain contained residues 82 to 226 (**Fig. 6-1**) and is similar to a previously SipB construct, SipB<sup>82-240</sup>, that was characterized by solution NMR<sup>5</sup>. Based on the observation that the extreme N-terminal residues (11 to 27) of IpaB, the SipB homolog from *Shigella*, were reported to be important for the interaction with the tip IpaD<sup>3</sup>, two constructs of SipB containing the extreme N-terminal residues were subcloned and tested for expression. The IpaB residues 11 to 27 are homologous to SipB residues 13 to 34 based on primary protein sequence alignment. Therefore, both SipB<sup>11-232</sup> and SipB<sup>11-312</sup> contained the N-terminal residues reported to be essential for the interaction with the tip protein<sup>3</sup>. SipB<sup>11-232</sup> and SipB<sup>11-312</sup>, as well as SipB<sup>82-240</sup>, expressed in high amounts and were easily purified by affinity chromatography (**Fig. 6-1B**). The molecular weights were 25.2 kDa for SipB<sup>11-232</sup>, 34.2 kDa for SipB<sup>11-312</sup> and 18 kDa for SipB<sup>82-240</sup>. Therefore, the SipB constructs that were

purified showed the correct molecular weights by SDS-PAGE (**Fig. 6-1B**). Interestingly, some SipB<sup>11-312</sup> protein came out in the flow through, which was possibly due to the saturation of the binding capacity of the nickel column (**Fig. 6-1B, lane 5**). The protein gel results for the purification for SipB<sup>11-232</sup> and SipB<sup>11-312</sup> showed single band purity compared to the purification for SipB<sup>82-240</sup> (**Fig. 6-1B**). However, dialysis of SipB<sup>82-240</sup> led to removal of most residual host cell impurities<sup>5</sup>.

### 6.3.2. SEC of SipB<sup>11-232</sup> and SipB<sup>11-312</sup>

Following purification, proteins were concentrated to sub-millimolar concentrations and loaded onto a size exclusion chromatography (SEC) column to determine the oligomeric state of SipB<sup>11-232</sup> and SipB<sup>11-312</sup>. Passage of proteins through an SEC column showed two major elution peaks for SipB<sup>11-232</sup> (**Fig. 6-2A**) and one peak for SipB<sup>11-312</sup> (**Fig. 6-2B**). The SipB<sup>11-232</sup> peaks were estimated to be populations of trimers and dimers (**Fig. 6-2A**) based on a standard curve constructed using proteins of known molecular weights, whereas the SipB<sup>11-312</sup> peak was estimated to be a trimer (**Fig. 6-2B**). An SDS-PAGE gel of the SEC column elutions showed oligomeric populations could revert to monomeric species in the presence of SDS detergent (**Fig. 6-2**). In comparison, SEC of SipB<sup>82-240</sup> also showed two major elution peaks, one that was estimated to be a trimer and one that was estimated to be a larger oligomeric population<sup>5</sup>. Together, this data suggests SipB N-terminal domain constructs have a tendency to oligomerize in solution at sub-millimolar concentrations.

### 6.3.3. CD of SipB<sup>11-232</sup> and SipB<sup>11-312</sup>

Circular dichroism was used to determine the secondary structure characteristics of SipB<sup>11-232</sup> and SipB<sup>11-312</sup>. The far-UV CD spectra of SipB<sup>11-232</sup> and SipB<sup>11-312</sup> overlapped and showed minima at 208 and 222 nm, which are characteristics of highly  $\alpha$ -helical proteins (**Fig. 6-3A**). SipB<sup>11-232</sup> and SipB<sup>11-312</sup> showed  $\theta_{222/208}$  ratios of 1.03 and 1.04, respectively, indicative of coiled-coil containing proteins<sup>9</sup>. Terminal denaturation curves of SipB<sup>11-232</sup> and SipB<sup>11-312</sup> were also similar and both proteins contained a single thermal melt (**Fig. 6-3B**). The thermal melt was calculated as 59.3°C for SipB<sup>11-232</sup> and 57.5°C for SipB<sup>11-312</sup>. In comparison, SipB<sup>82-240</sup> had a  $\theta_{222/208}$  ratio of 1.14 and a thermal melt of 59.8°C<sup>5</sup>. Together, these data suggest that the inclusion of the extreme N-terminal residues (11 to 81) did not result in gross structural changes of the N-terminal ectodomain of SipB.

### 6.3.4. NMR Spectroscopy of SipB<sup>11-232</sup>, SipB<sup>11-312</sup> and SipB<sup>82-240</sup>

My aim was to develop an optimal construct of SipB for NMR titration studies with SipB. To this end, NMR data were acquired on <sup>15</sup>N/ILV <sup>13</sup>C-methyl labeled SipB<sup>11-232</sup>, SipB<sup>11-312</sup> and SipB<sup>82-240</sup> to determine which construct provided the best quality NMR spectra. The optimal temperature for the experiments were determined to be 30°C based on 1D <sup>1</sup>H experiments. In two-dimensional <sup>1</sup>H-<sup>15</sup>N TROSY experiments, amide peaks were observed for all three SipB constructs (**Fig. 6-4**). However, the highest resolution and largest <sup>1</sup>H dispersion was achieved with SipB<sup>82-240</sup> (**Fig. 6-4C**), whereas the lowest resolution and smallest <sup>1</sup>H dispersion was observed with SipB<sup>11-312</sup> (**Fig. 6-4B**). The number of amide peaks that were expected were ~230 for SipB<sup>11-232</sup> and ~300 for SipB<sup>11-</sup>

<sup>312</sup>. However, less than half of the expected peaks were observed with both constructs and furthermore many of the amide peaks observed were broad (**Fig. 6-4A & Fig. 6-4B**). In contrast, the 2D <sup>1</sup>H-<sup>15</sup>N TROSY spectrum of SipB<sup>82-240</sup> showed more than 50% of expected amide peaks and peaks were well resolved (**Fig. 6-4C**). Two-dimensional <sup>1</sup>H-<sup>13</sup>C HSQC experiments are in agreement with TROSY experiments, showing that the most well resolved ILV methyl peaks were observed with SipB<sup>82-240</sup> (**Fig. 6-5C**). Together, the results suggest SipB<sup>82-240</sup> showed better quality NMR spectra compared to SipB<sup>11-232</sup> or SipB<sup>11-312</sup>.

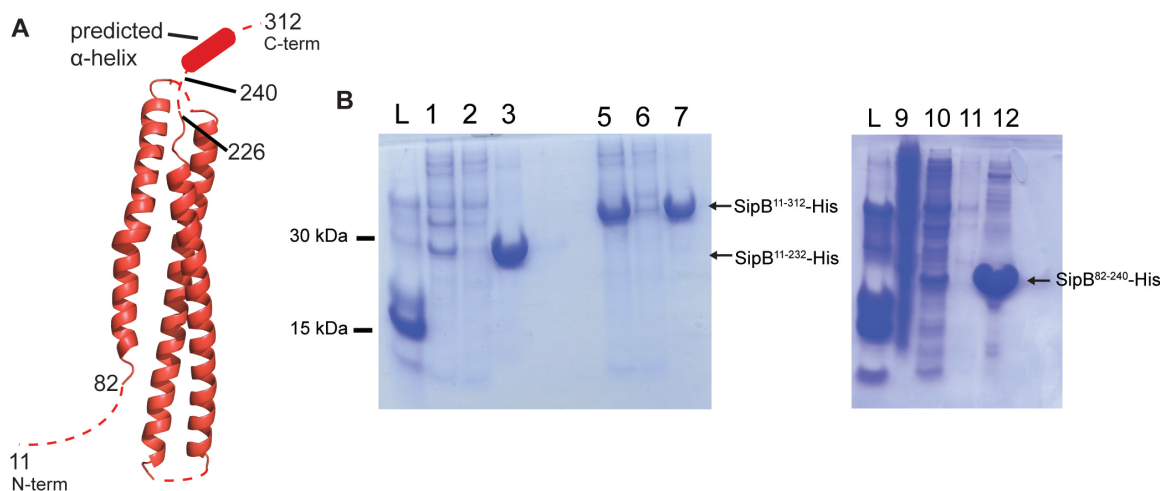


**Fig. 6-1 – Purification of SipB N-Terminal Domain Constructs**

(A) The crystal structure of SipB<sup>82-226</sup> (PDB ID 3TUL). Regions of unknown structure (11 to 81 and 226-312) are indicated with dotted red line. Residues 226-312 are predicted to form an  $\alpha$ -helix. (B) SDS-PAGE gels showing purification of His-tagged SipB<sup>11-232</sup> (25.2 kDa), SipB<sup>11-312</sup> (34.2 kDa) and SipB<sup>82-240</sup> (18 kDa). L is the protein ladder. Lanes 1, 5 and 9 are the flow through from loading the cell lysate after sonicated onto the Ni<sup>2+</sup> column. Lanes 2, 6, 10 and 11 are from Ni<sup>2+</sup> column after washes with binding buffer. Lanes 3, 7 and 12 are the column elutions and contain the purified protein.

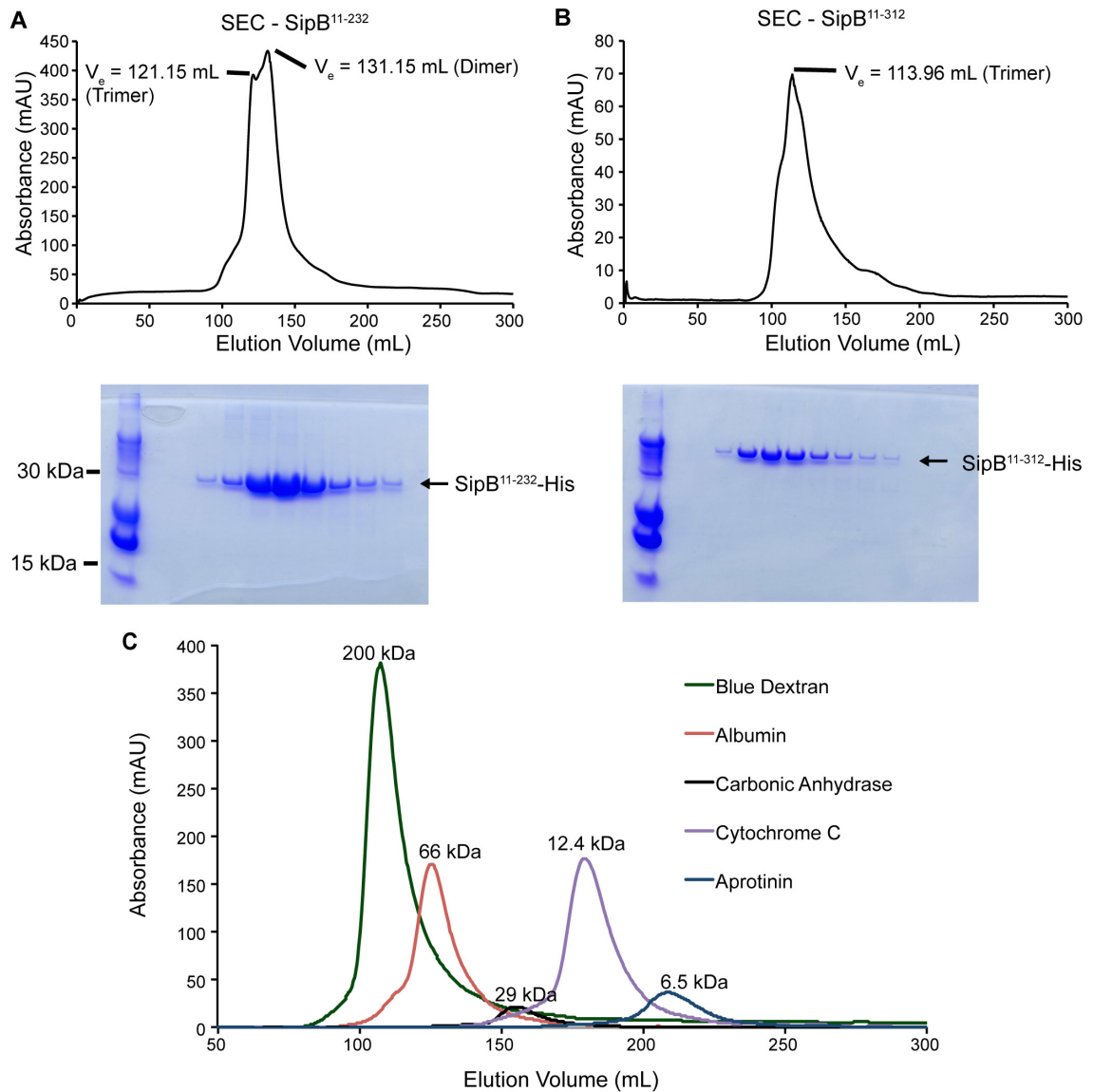


**Fig. 6-2 – SEC of SipB N-Terminal Domain Constructs**

(A) SEC elution profile of SipB<sup>11-232</sup> shows two major peaks estimated to form trimers (75.6 kDa) and dimers (50.4 kDa). The SDS-PAGE gel of SEC column elutions shows SipB<sup>11-232</sup> as a monomer (25.2 kDa). (B) SEC elution profile of SipB<sup>11-312</sup> shows one major peak that was estimated to form trimers (102.6 kDa). The SDS-PAGE gel of SEC column elutions shows SipB<sup>11-312</sup> as a monomer (34.2 kDa). (C) SEC elution protein of protein standards.

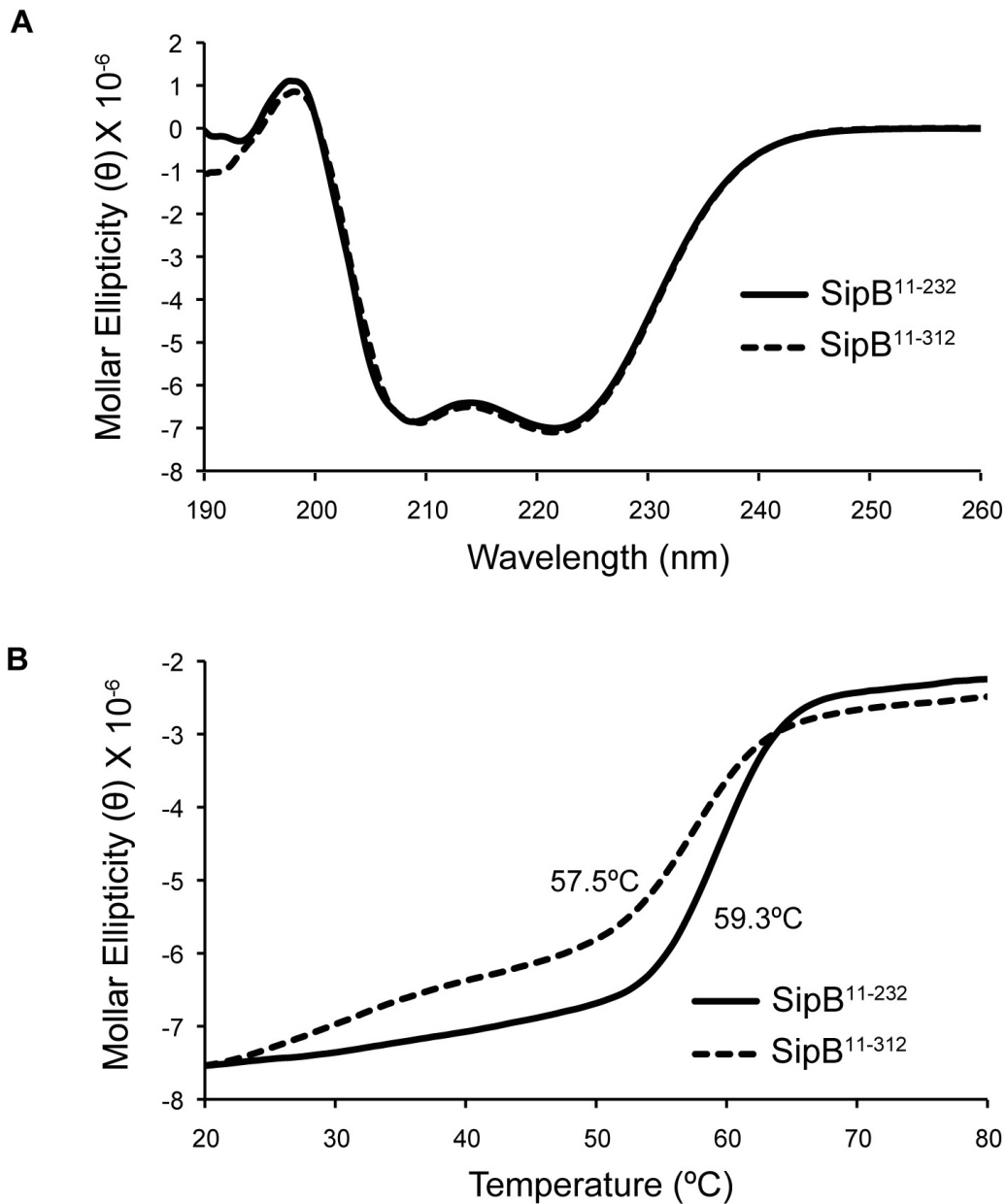


**Fig. 6-3 – CD of SipB N-Terminal Domain Constructs**

(A) Far-UV CD spectrum of SipB<sup>11-232</sup> (solid line) compared with SipB<sup>11-312</sup> (dotted line). Both proteins show minima at 208 and 222 nm and  $\theta_{222/208}$  ratios near 1, characteristic of  $\alpha$ -helical and coiled-coil containing proteins. (B) Thermal denaturation experiments show a thermal melt of 59.3°C for SipB<sup>11-232</sup> (solid line) and 57.5°C for SipB<sup>11-312</sup> (dotted line).

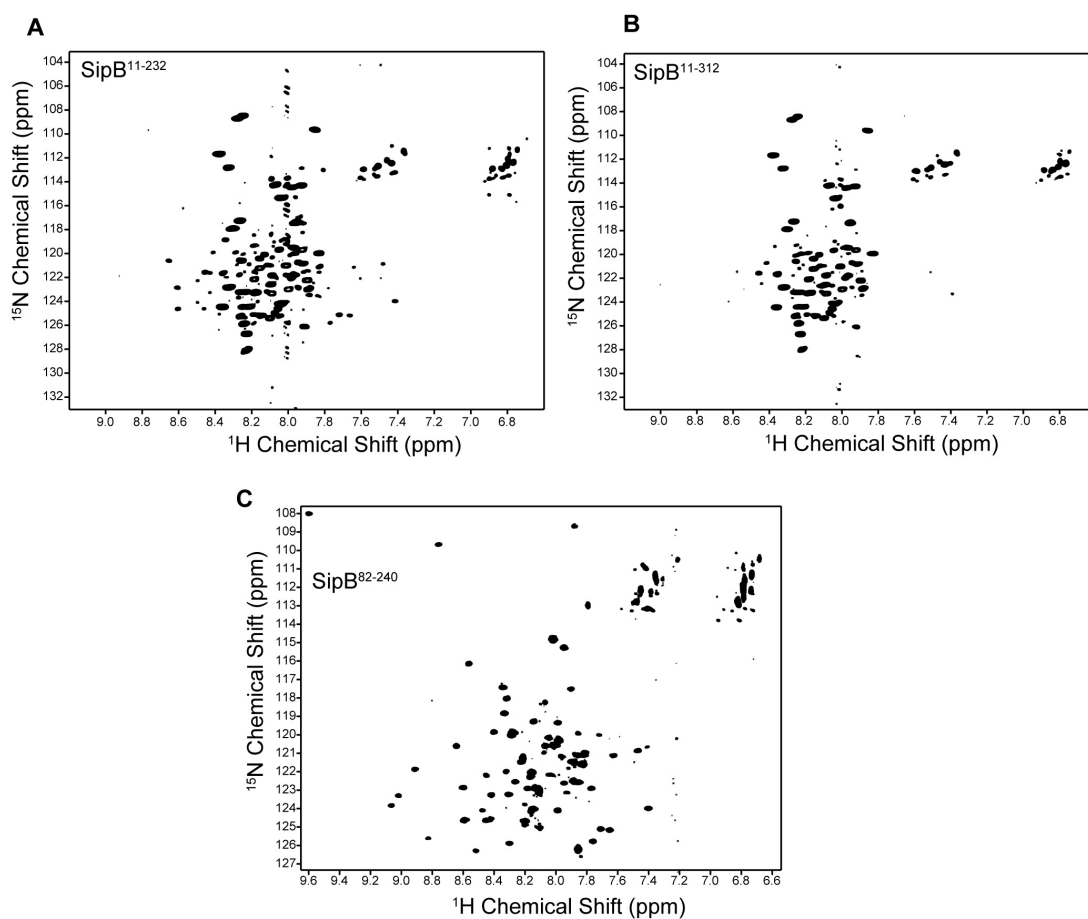


**Fig. 6-4 –  $^1\text{H}$ - $^{15}\text{N}$  TROSY of SipB N-Terminal Domain Constructs**

Two-dimensional  $^1\text{H}$ - $^{15}\text{N}$  TROSY spectra of (A) SipB<sup>11-232</sup>, (B) SipB<sup>11-312</sup> (C) SipB<sup>82-240</sup>. The amide peaks of SipB<sup>82-240</sup> are well dispersed ( $> 1$  ppm for  $^1\text{H}$ ), well-resolved and the spectrum contains more than 50% of expected amide peaks. In contrast, amide peaks of SipB<sup>11-232</sup> and SipB<sup>11-312</sup> are not as well dispersed ( $< 1$  ppm for  $^1\text{H}$ ), many are broad and the spectrum contains less than 50% of expected peaks.

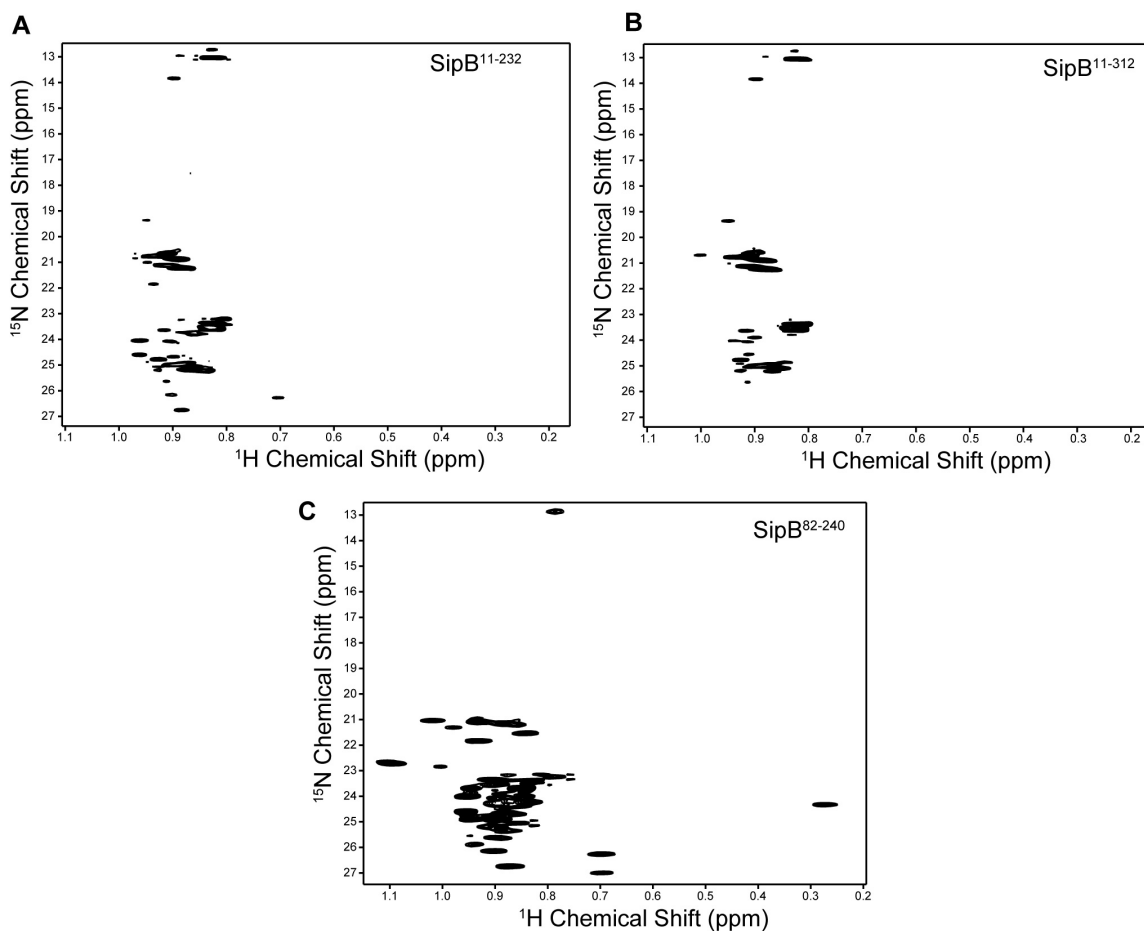
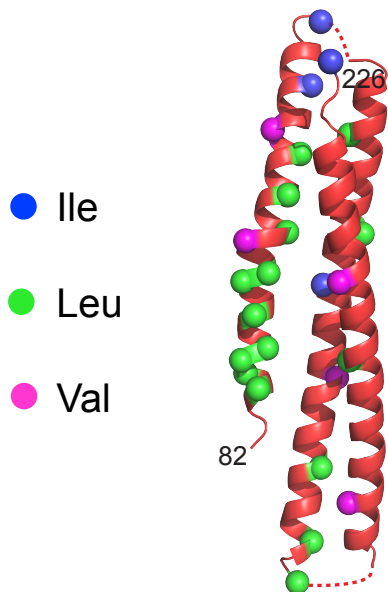


**Fig. 6-5 –  $^1\text{H}$ - $^{13}\text{C}$  HSQC of SipB N-Terminal Domain Constructs**  
 Two-dimensional  $^1\text{H}$ - $^{13}\text{C}$  HSQC spectra of (A) SipB<sup>11-232</sup>, (B) SipB<sup>11-312</sup>, (C) SipB<sup>82-240</sup>. SipB<sup>82-240</sup> ILV methyl peaks are well dispersed ( $\sim 1$  ppm for  $^1\text{H}$ ), well resolved and contains more than 70% of expected ILV methyl peaks. SipB<sup>11-232</sup> and SipB<sup>11-312</sup> are not as well dispersed ( $< 0.4$  ppm for  $^1\text{H}$ ), have broad peaks and contain less than 50% of expected ILV methyl peaks. Expected number of peaks is 52 for SipB<sup>82-240</sup> (4 Ile, 18 Leu, 6 Val), 71 for SipB<sup>11-232</sup> (5 Ile, 23 Leu, 10 Val) and 93 for SipB<sup>11-312</sup> (7 Ile, 30 Leu, 13 Val). The positions of ILV residues on SipB<sup>82-226</sup> are shown in Fig. 6-6.

**Fig. 6-6 – Positions of ILV residues on SipB<sup>82-226</sup>**



Position of Ile (blue), Leu (green) and Val (magenta) residues on the crystal structure of the N-terminal domain of SipB<sup>82-226</sup> (PDB ID 3TUL). The structure of the regions 11-81 and 226-312 have not yet been solved, but contain additional ILV residues.

#### 6.4. Discussion

SipB<sup>11-232</sup> and SipB<sup>11-312</sup> express in high yields, can be purified by Ni<sup>2+</sup> affinity chromatography (**Fig. 6-1**) and are soluble up to sub-millimolar concentrations. Results from SEC experiments suggest that SipB<sup>11-232</sup> exists in populations of dimers and trimers (**Fig. 6-2A**), whereas SipB<sup>11-312</sup> exists in primarily populations of trimers (**Fig. 6-2B**). An SDS-PAGE gel of the SEC column elutions could reduce the oligomeric state of both constructs back to their monomeric form in the presence of detergent (**Fig. 6-2**). These data are in agreement with the observation of trimeric species of *Shigella* IpaB (SipB homolog) constructs<sup>10, 11</sup>. Circular dichroism experiments suggest both SipB<sup>11-232</sup> and SipB<sup>11-312</sup> contain  $\alpha$ -helical characteristics with the presence of a coiled-coil because they have  $\theta_{222/208}$  ratios near 1.0 (**Fig. 6-3A**). In addition, both SipB constructs have similar

thermal melts: 59.3°C for SipB<sup>11-232</sup> and 57.5°C for SipB<sup>11-312</sup> (**Fig. 6-3B**). Unfortunately, SipB<sup>11-232</sup> and SipB<sup>11-312</sup> are not optimal NMR constructs. Two-dimensional <sup>1</sup>H-<sup>15</sup>N TROSY (**Fig. 6-4**) and <sup>1</sup>H-<sup>13</sup>C HSQC (**Fig. 6-5**) experiments showed less peaks than would be expected for both amide and ILV methyl experiments. First, this could be due to populations of high-molecular weight oligomeric SipB in solution as observed by SEC experiments. Dimers or trimers of SipB would likely not be optimal for NMR experiments due to slower molecular tumbling resulting in relaxation. Second, broad NMR peaks might be observed because the residues 11-81 are disordered (as suggested by secondary structure prediction) and mask the NMR signal of the remaining structured regions. This is likely a contributing factor, because SipB<sup>82-240</sup>, which also forms oligomers in solution, has much better <sup>1</sup>H signal dispersion and peak resolution in NMR experiments (**Fig. 6-4C & Fig. 6-5C**). Unfortunately, SipB<sup>82-240</sup> spectra are still lacking many of the expected peaks (~30%), so assignment of amide or ILV methyl resonances of SipB<sup>82-240</sup> would be challenging.

## 6.5. References

1. Hayward, R. D., McGhie, E. J. & Koronakis, V. (2000). Membrane fusion activity of purified SipB, a Salmonella surface protein essential for mammalian cell invasion. *Molecular Microbiology* **37**, 727-739.
2. McGhie, E. J., Hume, P. J., Hayward, R. D., Torres, J. & Koronakis, V. (2002). Topology of the Salmonella invasion protein SipB in a model bilayer. *Molecular Microbiology* **44**, 1309-1321.
3. Dickenson, N. E., Arizmendi, O., Patil, M. K., Toth, R. T. t., Middaugh, C. R., Picking, W. D. & Picking, W. L. (2013). N-Terminus of IpaB Provides a Potential Anchor to the Shigella Type III Secretion System Tip Complex Protein IpaD. *Biochemistry*.
4. Kaur, K., Chatterjee, S. & De Guzman, R. N. (2016). Characterization of the Shigella and Salmonella Type III Secretion System Tip-Translocon Protein-Protein Interaction by Paramagnetic Relaxation Enhancement. *ChemBiochem*.

5. Chatterjee, S. (2013). Characterization of the Structure, Function, and Protein-Protein Interactions Involved in the Assembly of the Type III Secretion System Tip Complex and the Translocon of Salmonella and Shigella, University of Kansas.
6. Barta, M. L., Dickenson, N. E., Patil, M., Keightley, A., Wyckoff, G. J., Picking, W. D., Picking, W. L. & Geisbrecht, B. V. (2012). The Structures of Coiled-Coil Domains from Type III Secretion System Translocators Reveal Homology to Pore-Forming Toxins. *Journal of Molecular Biology* **417**, 395-405.
7. Delaglio, F., Grzesiek, S., Vuister, G. W., Zhu, G., Pfeifer, J. & Bax, A. (1995). NMRPipe: a multidimensional spectral processing system based on UNIX pipes. *J Biomol NMR* **6**, 277-93.
8. Johnson, B. A. (2004). Using NMRView to visualize and analyze the NMR spectra of macromolecules. *Methods Mol Biol* **278**, 313-52.
9. Wallimann, P., Kennedy, R. J., Miller, J. S., Shalongo, W. & Kemp, D. S. (2003). Dual wavelength parametric test of two-state models for circular dichroism spectra of helical polypeptides: anomalous dichroic properties of alanine-rich peptides. *J Am Chem Soc* **125**, 1203-20.
10. Hume, P. J., McGhie, E. J., Hayward, R. D. & Koronakis, V. (2003). The purified Shigella IpaB and Salmonella SipB translocators share biochemical properties and membrane topology. *Molecular Microbiology* **49**, 425-439.
11. Dickenson, N. E., Choudhari, S. P., Adam, P. R., Kramer, R. M., Joshi, S. B., Middaugh, C. R., Picking, W. L. & Picking, W. D. (2013). Oligomeric states of the Shigella translocator protein IpaB provide structural insights into formation of the type III secretion translocon. *Protein Sci* **22**, 614-27.

## Chapter 7. Identification of the Binding Surfaces Involved in the *Salmonella* Tip-Translocon Protein-Protein Interaction

[Some of the data in this chapter has been published with the following citation: McShan AC, Kaur K, Chatterjee S, Knight KM, De Guzman RN. NMR Identification of the Binding Surfaces Involved in the *Salmonella* and *Shigella* Type III Secretion Tip-Translocon Protein-Protein Interactions. *Proteins*. In press, 2016]

### 7.1. Introduction

How the *Salmonella* SPI-1 T3SS tip protein SipD and the translocon protein SipB interact is poorly understood. The N-terminal ectodomain of SipB has been suggested to interact with SipD due to homology with the *Shigella* IpaB/IpaD system, where N-terminal domain of IpaB was shown to interact with IpaD by fluorescence spectroscopy<sup>1</sup>. Although the atomic structure of full-length SipB is unavailable, the crystal structure of a protease resistant core of the SipB N-terminal domain (residues 82-226) has been solved<sup>2</sup>. Dickenson and co-workers<sup>1</sup> reported that residues 11-27 of the IpaB were essential for the interaction with the *Shigella* tip protein IpaD. IpaB residues 11-27 are homologous to SipB residues 13-34 based on primary protein sequence alignment. In Chapter 6 two constructs of the N-terminal ectodomain of SipB containing the extreme N-terminal residues were subcloned and characterized: SipB<sup>11-232</sup> and SipB<sup>11-312</sup>. The residues 232-312 were included in the latter construct because they are predicted to form an  $\alpha$ -helix, which could potentially increase the surface area of SipB for SipD to interact with. Chapter 2 and Chapter 3 described the assignment of amide and ILV methyl resonances of SipD <sup>$\Delta$ 38</sup> and SipD <sup>$\Delta$ 132</sup>. Here, NMR titration experiments were performed between isotopically <sup>15</sup>N/ILV <sup>13</sup>C-methyl labeled SipD <sup>$\Delta$ 38</sup> or SipD <sup>$\Delta$ 132</sup> with unlabeled SipB<sup>11-232</sup> or SipB<sup>11-312</sup>. NMR results show the distal region of tip protein SipD is the surface that interacts with the N-terminal ectodomain of SipB.

## 7.2. Materials and Methods

### 7.2.1. Protein Expression and Purification

Isotopically  $^{15}\text{N}/\text{ILV}$   $^{13}\text{C}$ -methyl labeled SipD $^{\Delta 38}$  or SipD $^{\Delta 132}$  were prepared as described in Chapter 2 and Chapter 3 in 1L of 1× M9 medium. Unlabeled SipB $^{11-232}$  or SipB $^{11-312}$  were prepared in *E. coli* BL21(DE3) DNAY cells in 1L of LB media containing 30 µg/mL kanamycin and 100 µg/mL carbenicillin at 37°C. Protein expression was induced with 1 mM IPTG at an OD $_{600}$  of 0.8 and cell growth was continued overnight at 15°C. SipB $^{11-232}$  and SipB $^{11-312}$  constructs were purified as described in Chapter 6.

### 7.2.2. $^1\text{H}$ - $^{15}\text{N}$ TROSY of SipD $^{\Delta 38}$ and SipD $^{\Delta 132}$

All NMR data was collected using a Bruker Avance 800 MHz spectrometer equipped with a cryogenic triple resonance probe and were processed using NMRPipe<sup>3</sup> and analyzed using NMRView<sup>4</sup>. Two-dimensional  $^1\text{H}$ - $^{15}\text{N}$  TROSY spectra were acquired at 30°C using 0.2 mM of  $^{15}\text{N}/\text{ILV}$   $^{13}\text{C}$ -methyl labeled SipD $^{\Delta 38}$  or SipD $^{\Delta 132}$  in NMR buffer (50 mM NaCl, 10 mM sodium phosphate, pH 7.4 and 10% D $_2$ O). Typical acquisition parameters were 128 scans with 2048 complex points ( $^1\text{H}$ ) and 128 complex points ( $^{15}\text{N}$ ) with sweep width 10.01 ppm for  $^1\text{H}$  centered at 4.69 ppm and 17.9 ppm for  $^{15}\text{N}$  centered at 119 ppm.

### 7.2.3. $^1\text{H}$ - $^{13}\text{C}$ HSQC of SipD $^{\Delta 38}$ and SipD $^{\Delta 132}$

Two-dimensional  $^1\text{H}$ - $^{13}\text{C}$  HSQC spectra were acquired at 30°C using 0.2 mM of  $^{15}\text{N}/\text{ILV}$   $^{13}\text{C}$ -methyl labeled SipD $^{\Delta 38}$  or SipD $^{\Delta 132}$  in NMR buffer. Typical acquisition

parameters were 16 scans with 1024 complex points ( $^1\text{H}$ ) and 256 complex points ( $^{13}\text{C}$ ) with sweep width 10.01 ppm for  $^1\text{H}$  centered at 4.69 ppm and 20 ppm for  $^{13}\text{C}$  centered at 19 ppm.

#### 7.2.4. NMR Titrations and Data Analysis

For NMR titration experiments, 0.2 mM of isotopically  $^{15}\text{N}/\text{ILV}$   $^{13}\text{C}$ -methyl labeled SipD $^{\Delta 38}$  or SipD $^{\Delta 132}$  were titrated with unlabeled SipB $^{11-232}$  or SipB $^{11-312}$  at SipD:SipB mole ratios of 1:0, 1:0.5, 1:1 and 1:2. To determine whether temperature affected the new SipD peaks that appeared upon titration with SipB, 2D  $^1\text{H}$ - $^{13}\text{C}$  HSQC spectra of the SipD $^{\Delta 38}$ :SipB $^{11-232}$  complex at a 1:2 mole ratio were acquired using the parameters outlined in section 7.2.2. with the temperatures 10°C, 20°C, 30°C and 40°C. Affected residues were mapped onto the crystal structure of SipD $^5$  (PDB ID 3NZZ).

### 7.3. Results

#### 7.3.1. Titration of $^{15}\text{N}/\text{ILV}$ SipD $^{\Delta 38}$ with SipB $^{11-232}$

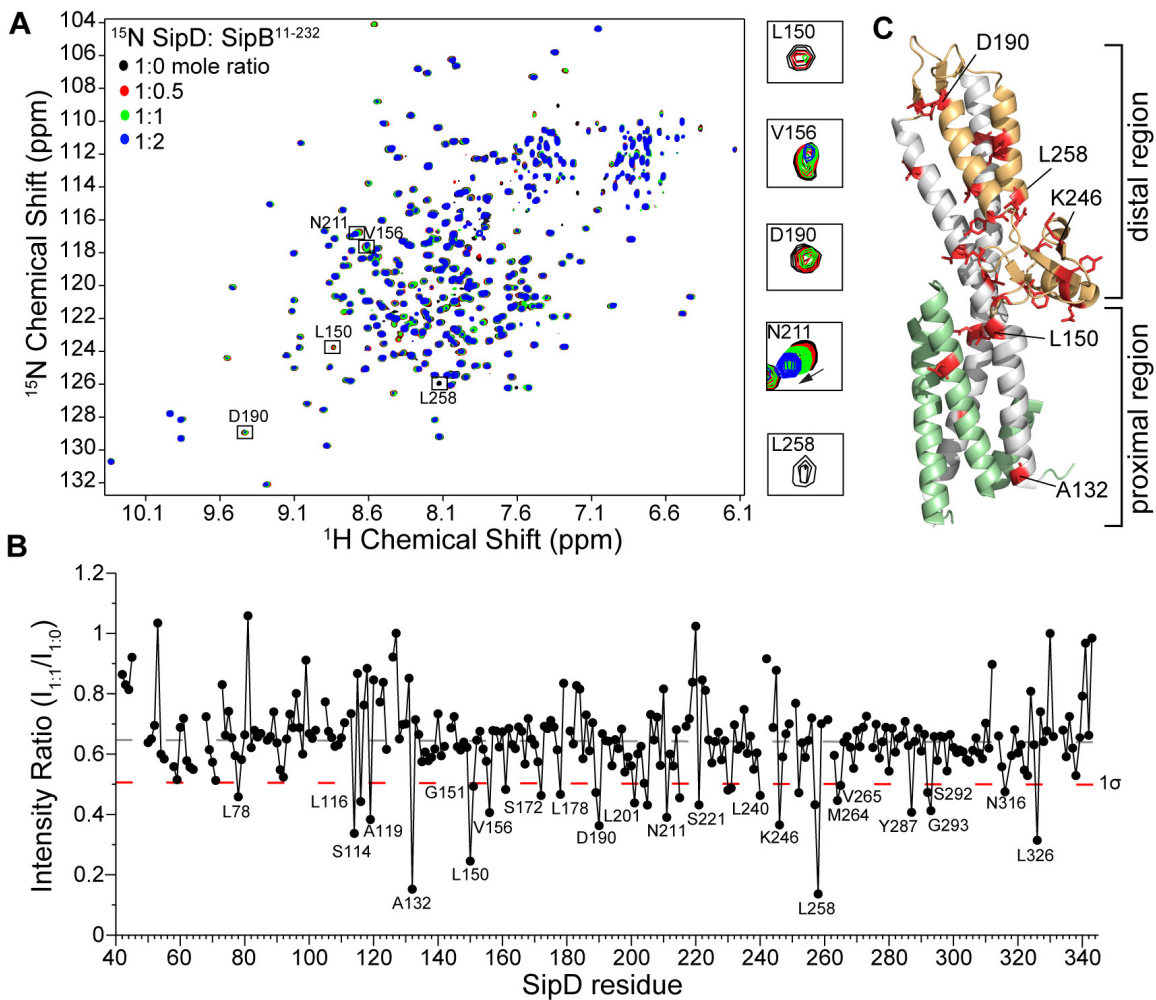
NMR methods were used to identify the surfaces involved in the tip-translocon interaction by titrating the *Salmonella* SipB $^{11-232}$  major translocon protein into  $^{15}\text{N}/\text{ILV}$  labeled SipD $^{\Delta 38}$  tip protein and monitoring the titrations by acquiring 2D  $^1\text{H}$ - $^{15}\text{N}$  TROSY data sets. Results of NMR titrations showed a concentration dependent decrease in intensities of many SipD $^{\Delta 38}$  amide peaks (**Fig. 7-1A**) indicating complex formation to be primarily in the intermediate exchange NMR time scale. In addition, some SipD $^{\Delta 38}$  residues, such as N211, K302 and G220 (**Fig. 7-1A**), showed chemical shift deviations with increasing concentrations of SipB $^{11-232}$  indicating these residues were in the fast

exchange NMR time scale. Importantly, there were also many SipD<sup>Δ38</sup> peaks, such as A99, G176, S270, that did not undergo signal broadening, even at a SipD<sup>Δ38</sup>:SipB<sup>11-232</sup> mole ratio of 1:2, indicating that complex formation did not result in protein aggregation, which would have broadened out all of the amide peaks of SipD<sup>Δ38</sup>. To identify the SipD<sup>Δ38</sup> residues that were most perturbed by SipB<sup>11-232</sup>, the peak intensity ratio ( $I_{1:1}/I_{1:0}$ ) was calculated for each non-overlapped SipD<sup>Δ38</sup> peak at a SipD<sup>Δ38</sup>:SipB<sup>11-232</sup> molar ratio of 1:1 (**Fig. 7-1B**). Residues with peak intensity ratios lower than the average minus one standard deviation were mapped onto the structure of SipD (**Fig. 7-1C**). SipD<sup>Δ38</sup> residues that were most affected by SipB<sup>11-232</sup> were primarily hydrophobic (L78, L116, A132, L150, G151, V156, L178, L240, L258 and L326) and some polar (S114, N211, K246, N316) residues. The affected residues clustered in the distal region of SipD (**Fig. 7-1C**), suggesting that this region of SipD is involved in the interaction with SipB.

The simultaneous labeling of SipD<sup>Δ38</sup> with <sup>15</sup>N and ILV methyls allowed the titration with SipB<sup>11-232</sup> to be monitored firstly by 2D <sup>1</sup>H-<sup>15</sup>N TROSY data sets to query the effect of the interaction on the <sup>15</sup>N amides of SipD<sup>Δ38</sup>, the results of which are shown above (**Fig. 7-1**), and secondly by 2D <sup>1</sup>H-<sup>13</sup>C HSQC to query the effect of SipB<sup>11-232</sup> on the ILV methyls of SipD<sup>Δ38</sup>. Like the results of the amide titrations (**Fig. 7-1**), most of the affected SipD<sup>Δ38</sup> ILV methyl peaks showed decreased peak intensities with a few residues showing chemical shift deviations, such as I46 (**Fig. 7-2A**) and I129. To identify which SipD<sup>Δ38</sup> ILV methyl peaks were perturbed upon complex formation with SipB<sup>11-232</sup>, the peak intensity ratio ( $I_{1:1}/I_{1:0}$ ) was plotted as the difference from 1, which signified no change in peak intensity upon complex formation (**Fig. 7-2B**). In agreement with the results of amide titration (**Fig. 7-1C**), the affected ILV methyl residues clustered at the

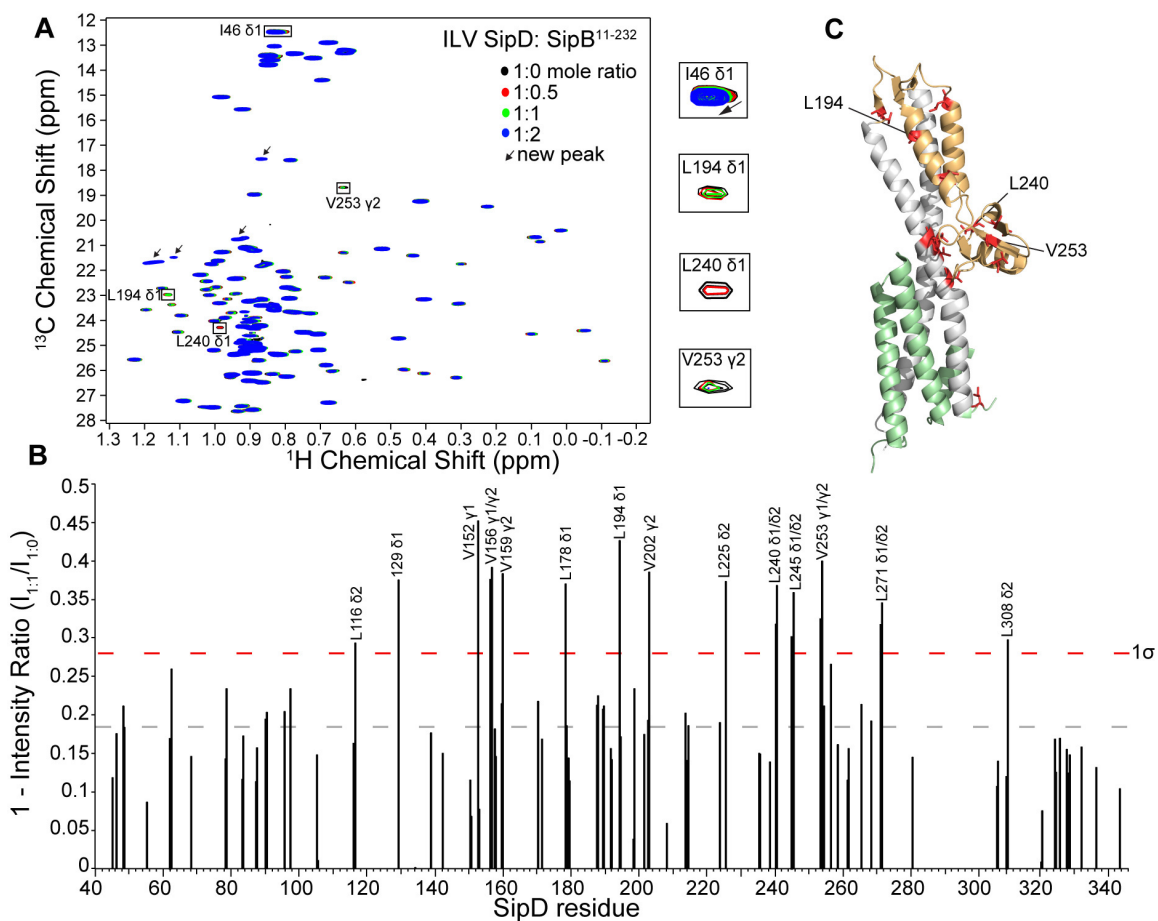
distal region of SipD<sup>Δ38</sup> (**Fig. 7-2C**). Importantly, there were residues that were affected in ILV methyl titrations that were also affected in <sup>15</sup>N titrations, such as V156, L178 and L240 (**Fig. 7-1B & Fig. 7-2B**).

Unlike the <sup>15</sup>N titrations, the appearance of new slow-exchange ILV methyl peaks was observed in the 2D <sup>1</sup>H-<sup>13</sup>C HSQC SipD<sup>Δ38</sup> spectra upon titration with SipB<sup>11-232</sup> (**Fig. 7-3B, arrows**). These slow exchange peaks are most likely due to conformational change of methyl groups upon binding<sup>6</sup>. Slow exchange peaks are also indicative of tighter binding interaction in the nanomolar range. However, the measured affinity of the SipD-SipB interaction is in the range of 30 to 60 μM (**Fig. 8-3A, B**). EXSY (or ZZ-exchange) NMR experiments<sup>7</sup> were performed with a range of mixing times in an attempt to identify the new SipD<sup>Δ38</sup> ILV methyl peaks, but were unsuccessful. Because exchange is a temperature dependent phenomenon, 2D <sup>1</sup>H-<sup>13</sup>C HSQC data sets of the titration of ILV SipD<sup>Δ38</sup> with SipB<sup>11-232</sup> at a mole ratio of 1:2 were acquired at different temperatures to see if an increase in temperature would lead to signal broadening into the intermediate exchange range, leading to coalescence of signals<sup>6</sup>. Two-dimensional <sup>1</sup>H-<sup>13</sup>C HSQC experiments were acquired at 10°C, 20°C, 30°C and 40°C (**Fig. 7-4A**). An increase temperature resulted in chemical shift deviations for most resonances, including both original SipD<sup>Δ38</sup> ILV peaks (**Fig. 7-4A**) and the new ILV peaks (**Fig. 7-4B**). Based on these data, it is difficult to say whether the new SipD<sup>Δ38</sup> ILV methyl peaks are truly due to slow exchange induced upon binding to SipB<sup>11-232</sup>.



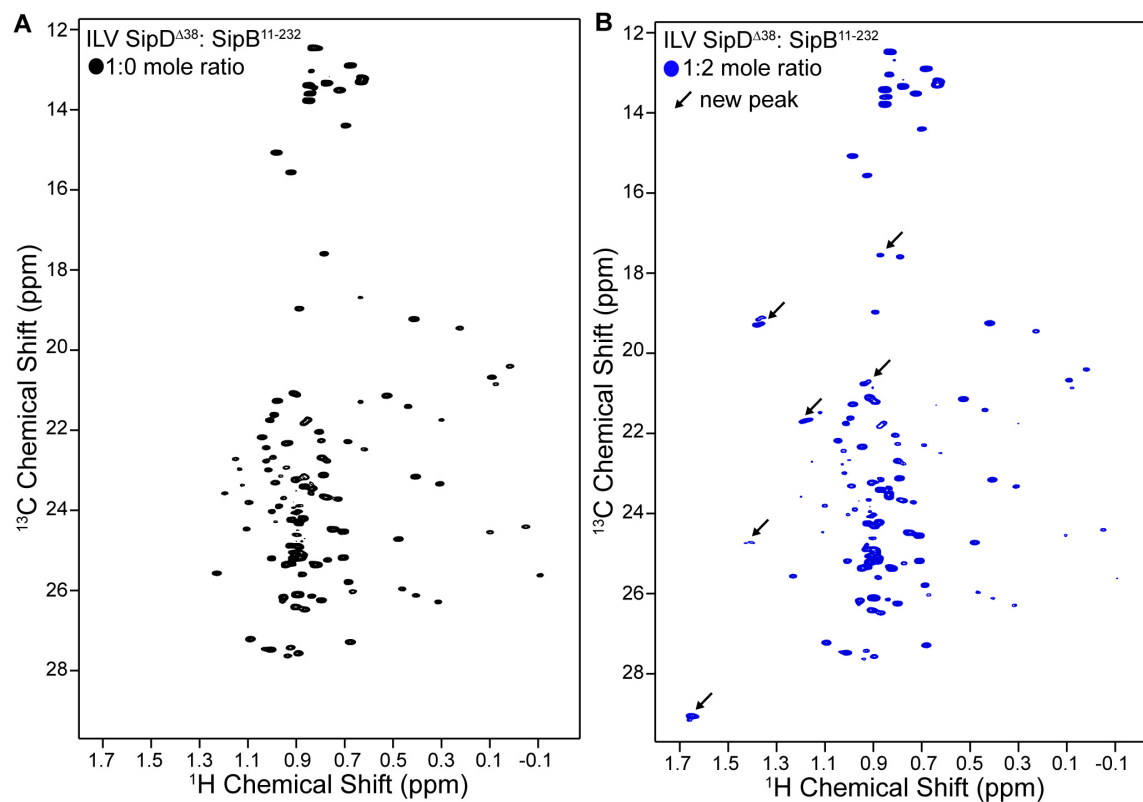
### 7-1 – $^{15}\text{N}$ Titration of SipD $^{\Delta 38}$ with SipB<sup>11-232</sup>

(A) Overlay of four 2D  $^1\text{H}$ - $^{15}\text{N}$  TROSY spectra of  $^{15}\text{N}/\text{ILV}$  SipD $^{\Delta 38}$  with increasing concentrations of unlabeled SipB<sup>11-232</sup>. (B) Plot of the peak intensity ratio of complex ( $I_{1:1}$ ) vs free ( $I_{1:0}$ ) for the SipD $^{\Delta 38}$ :SipB<sup>11-232</sup> complex at is shown with the average peak intensity ratio (dash gray line) and one standard deviation from the average ( $1\sigma$ , dashed red line). (C) Residues (colored red) with peak intensity ratio ( $I_{1:1}/I_{1:0}$ ) lower than  $1\sigma$  were mapped onto the crystal structure of SipD [N-terminal hairpin is green, the coiled-coil is gray and the mixed  $\alpha/\beta$  region is orange].

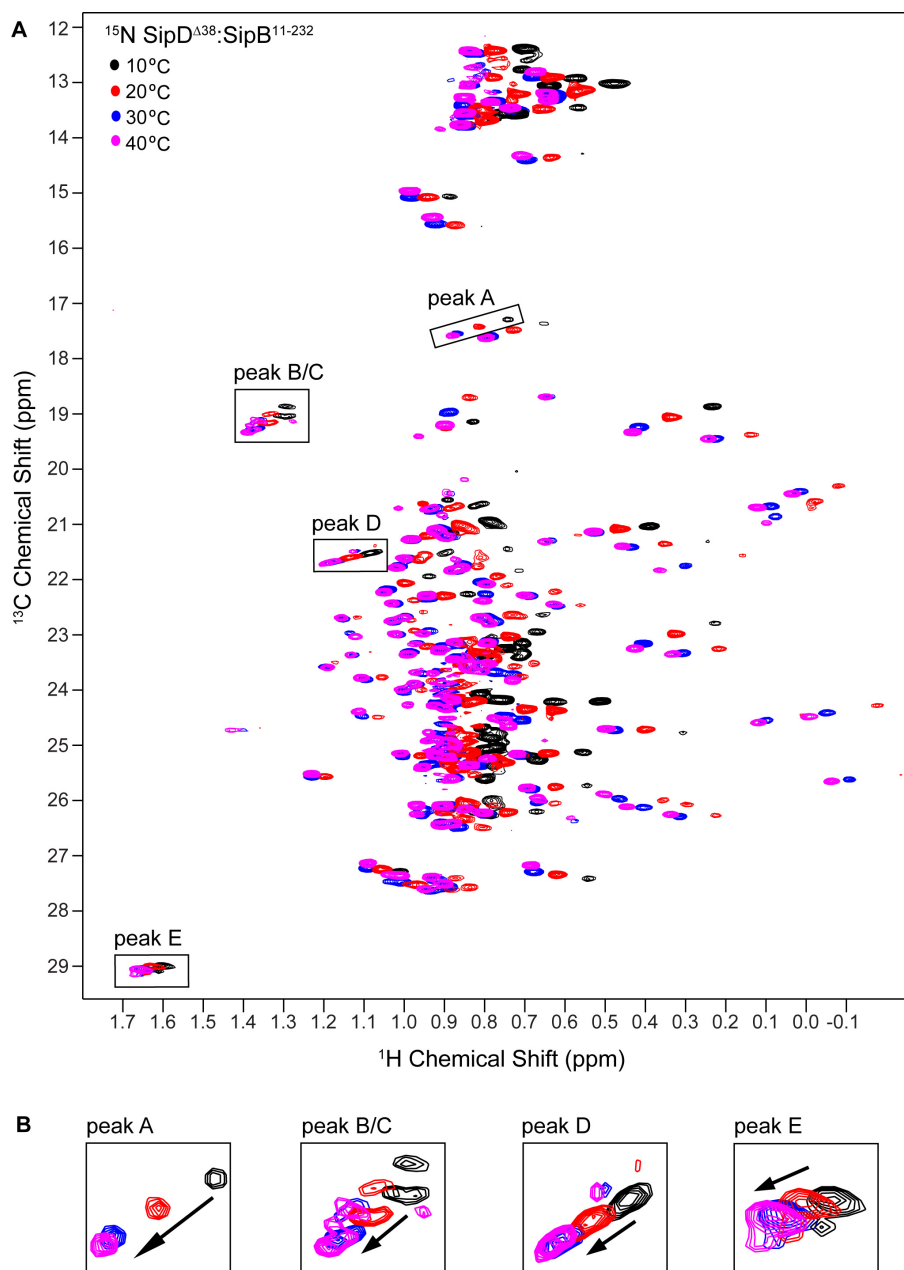


### 7-2 – ILV Titration of SipD <sup>$\Delta$ 38</sup> with SipB<sup>11-232</sup>

(A) Overlay of four 2D  $^1\text{H}$ - $^{13}\text{C}$  HSQC spectra of  $^{15}\text{N}$ /ILV SipD <sup>$\Delta$ 38</sup> titrated with increasing concentrations of unlabeled SipB<sup>11-232</sup>. (B) Plot of peak intensities ratios subtracted from one ( $1 - I_{1:1}/I_{1:0}$ ) of the SipD <sup>$\Delta$ 38</sup>:SipB<sup>11-232</sup> complex with the average value (dashed gray line) and one standard deviation from the average ( $1\sigma$ , dashed red line). (C) Residues (colored red) with  $(1 - I_{1:1}/I_{1:0})$  value greater than  $1\sigma$  were mapped onto the crystal structure of SipD [N-terminal hairpin is green, the coiled-coil is gray and the mixed  $\alpha/\beta$  region is orange].



**7-3 – New SipD<sup>Δ38</sup> ILV Methyl Peaks Appear Upon Titration with SipB<sup>11-232</sup>**  
 Two-dimensional <sup>1</sup>H-<sup>13</sup>C HSQC spectra of <sup>15</sup>N/ILV labeled SipD<sup>Δ38</sup> alone (**A**) or in the presence of SipB<sup>11-232</sup> at a SipD<sup>Δ38</sup>:SipB<sup>11-232</sup> molar ratio of 1:2 (**B**). New ILV methyl peaks that appear upon titration with SipB<sup>11-232</sup> are indicated with an arrow.



**7-4 – Effect of Temperature on the  $^1\text{H}$ - $^{13}\text{C}$  HSQC of the  $\text{SipD}^{\Delta 38}:\text{SipB}^{11-232}$  Complex**  
**(A)** Four 2D  $^1\text{H}$ - $^{13}\text{C}$  HSQC spectra of  $^{15}\text{N}$ /ILV labeled  $\text{SipD}^{\Delta 38}$  titrated with  $\text{SipB}^{11-232}$  at a  $\text{SipD}^{\Delta 38}:\text{SipB}^{11-232}$  mole ratio of 1:2 at various temperatures. New ILV peaks that appeared upon titration with  $\text{SipB}^{11-232}$  are indicated in boxes. **(B)** An expansion of four selected new ILV peaks taken from **(A)**. Peak assignment is unknown so they are designated peak A through E.

### 7.3.2. Titration of $^{15}\text{N}/\text{ILV SipD}^{\Delta 38}$ with $\text{SipB}^{11-312}$

$\text{SipB}^{11-312}$  was titrated into  $^{15}\text{N}/\text{ILV SipD}^{\Delta 38}$  to query the effect of SipB residues 232-312, which are predicted to form an  $\alpha$ -helix, on the tip-translocon interaction. Unfortunately, titration of  $^{15}\text{N}/\text{ILV SipD}^{\Delta 38}$  with  $\text{SipB}^{11-312}$  resulted in spectral collapse and signal broadening of most  $\text{SipD}^{\Delta 38}$  peaks in both 2D  $^1\text{H}$ - $^{15}\text{N}$  TROSY (**Fig. 7-5A**) and 2D  $^1\text{H}$ - $^{13}\text{C}$  HSQC experiments (**Fig. 7-5B**). In the 2D  $^1\text{H}$ - $^{15}\text{N}$  TROSY experiments, many new amide peaks were observed between 124 to 132 ppm ( $^{15}\text{N}$  axis) and 7.5 to 8.3 ppm ( $^1\text{H}$  axis) (**Fig. 7-5A**). Spectral collapse first appeared during the first titration point at a  $\text{SipD}^{\Delta 38}:\text{SipB}^{11-312}$  mole ratio of 1:0.5, but many more peaks were broadened out at the 1:2 ratio (**Fig. 7-5**). Therefore, titration analysis was not plausible at any molar ratio. From these experiments alone it is unclear why the  $\text{SipD}^{\Delta 38}$  spectra collapsed upon titration with  $\text{SipB}^{11-312}$ , though it is likely due to protein aggregation induced upon binding of oligomeric SipB.

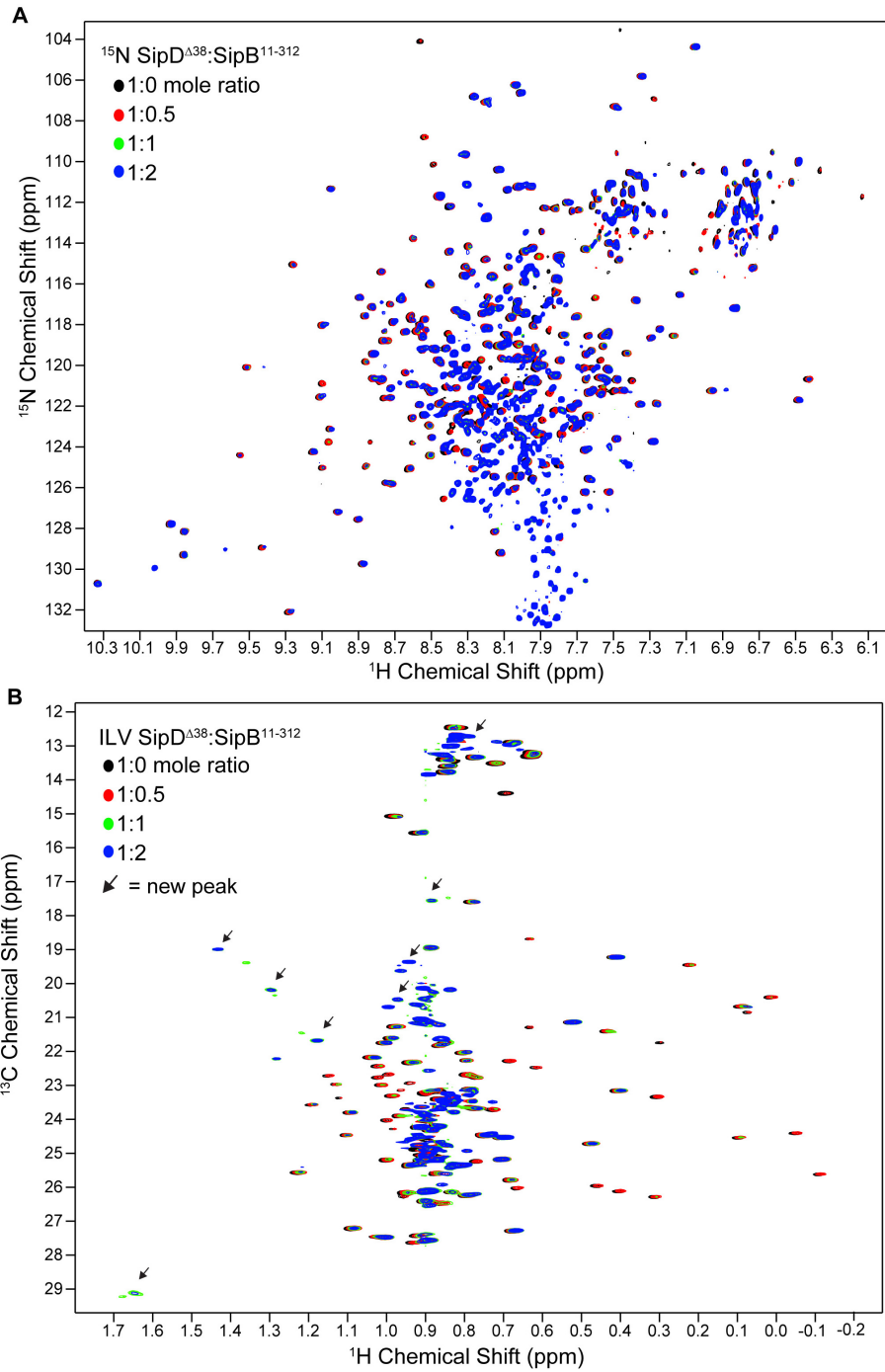
### 7.3.3. Titration of $^{15}\text{N}/\text{ILV SipD}^{\Delta 132}$ with $\text{SipB}^{11-232}$ and $\text{SipB}^{11-312}$

Residues in the distal region of SipD are affected upon titration with  $\text{SipB}^{11-232}$  (**Fig. 7-1C & Fig. 7-2C**), while residues in the proximal region of SipD, the bottom of the coiled-coil, are important for the interaction with the needle protein PrgI<sup>8</sup>. Therefore, it was hypothesized that removal of the N-terminal  $\alpha$ -helical domain of SipD (residues 39-131) would not have a large effect on the tip-translocon interaction. To test the role of the N-terminal  $\alpha$ -helical domain of SipD in the interaction of the tip and translocon, NMR titrations were performed between  $^{15}\text{N}/\text{ILV SipD}^{\Delta 132}$ , which lacks the N-terminal domain, and unlabeled  $\text{SipB}^{11-232}$  or  $\text{SipB}^{11-312}$ . NMR titrations between  $^{15}\text{N}/\text{ILV SipD}^{\Delta 132}$

with unlabeled SipB<sup>11-232</sup> monitored by 2D <sup>1</sup>H-<sup>15</sup>N TROSY showed a concentration dependent decrease in the peak intensity of specific SipD<sup>Δ132</sup> amide peaks, such as L189, D190 and Y252 (**Fig. 7-6A**), indicating complex formation to be primarily in the intermediate exchange NMR time scale. In addition, some SipD<sup>Δ132</sup> residues showed chemical shift deviations, such as G251 (**Fig. 7-6A**). Furthermore, unlike in the <sup>15</sup>N titration of SipD<sup>Δ38</sup> and SipB<sup>11-232</sup> (**Fig. 7-1A**), new SipD<sup>Δ132</sup> amide peaks were observed upon titration with SipB<sup>11-232</sup> (**Fig. 7-6A, arrows**). Together, this data suggest the SipD<sup>Δ132</sup> and SipB<sup>11-232</sup> complex to contain a mix of slow, intermediate and fast exchange on an NMR time scale, with most residues in intermediate exchange. Importantly, there were also many peaks that did not undergo significant signal broadening up to a SipD<sup>Δ132</sup>:SipB<sup>11-232</sup> molar ratio of 1:2, indicating that complex formation did not result in protein aggregation. Because there were only a few residues with significant chemical shift deviations, only intensity reduction was quantified. The peak intensity ratio ( $I_{1:1}/I_{1:0}$ ) was calculated for each non-overlapping SipD<sup>Δ132</sup> amide peak (**Fig. 7-6B**). Residues with peak intensity lower than the average intensity minus one standard deviation were mapped onto the structure of SipD<sup>Δ132</sup> (**Fig. 7-6C**). SipD<sup>Δ132</sup> residues that were affected were primarily hydrophobic (L190, L240, V254) or polar (D169, N196, Q233, Q266) residues (**Fig. 7-6C**). As with the results of <sup>15</sup>N titration between SipD<sup>Δ38</sup> and SipB<sup>11-232</sup> (**Fig. 7-1C**), the affected residues of SipD<sup>Δ132</sup> upon titration with SipB<sup>11-232</sup> clustered in the distal end (**Fig. 7-6C**). NMR titrations were additionally performed between <sup>15</sup>N/ILV SipD<sup>Δ132</sup> and unlabeled SipB<sup>11-312</sup>, which contained additional residues 232-312 that are predicted to form an  $\alpha$ -helix, and monitored by 2D <sup>1</sup>H-<sup>15</sup>N TROSY experiments. Interestingly, unlike the <sup>15</sup>N titration of SipD<sup>Δ38</sup> with SipB<sup>11-312</sup>, which resulted in spectral

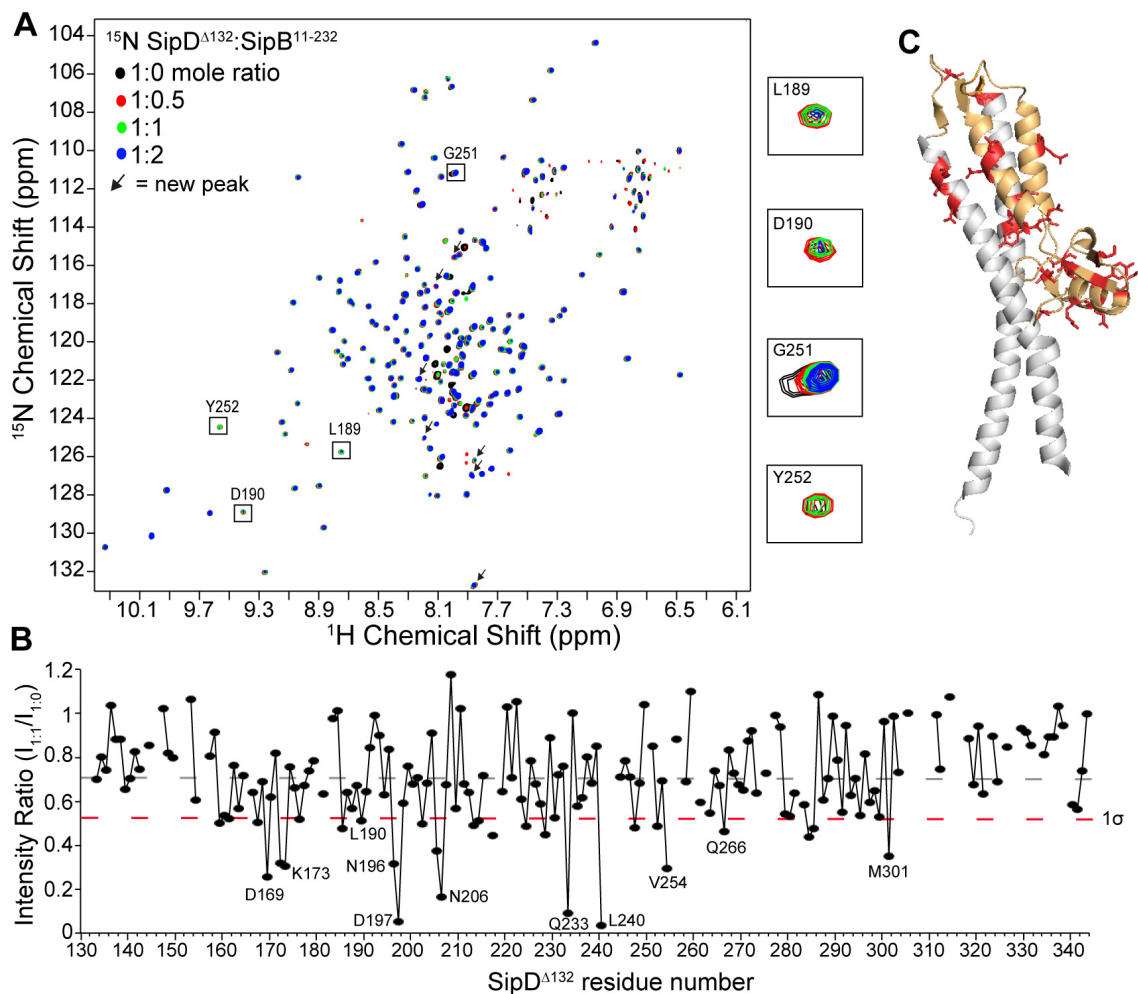
collapse (**Fig. 7-5A**), titration of  $^{15}\text{N}/\text{ILV SipD}^{\Delta 132}$  with  $\text{SipB}^{11-312}$  resulted in a concentration dependent decrease in the peak intensity of specific  $\text{SipD}^{\Delta 132}$  amide resonances without spectral collapse (**Fig. 7-7A**). In agreement with  $^{15}\text{N}$  titrations between  $\text{SipD}^{\Delta 132}$  and  $\text{SipB}^{11-232}$  (**Fig. 7-6A**), most of the affected  $\text{SipD}^{\Delta 132}$  amides showed a decrease in peak intensity due to signal broadening (**Fig. 7-7A**). The peak intensity ratio ( $I_{1:1}/I_{1:0}$ ) for each non-overlapping  $\text{SipD}^{\Delta 132}$  residue was calculated (**Fig. 7-7B**) and affected residues were mapped onto the structure of  $\text{SipD}^{\Delta 132}$  (**Fig. 7-7C**). Residues that were affected were primarily hydrophobic (L178, A217, L240) or polar (N196, Q233, K286) residues (**Fig. 7-7B**). As with the other amide titrations (**Fig. 7-1C & 7-6C**), the affected residues clearly clustered in the distal end of  $\text{SipD}^{\Delta 132}$  (**Fig. 7-7C**).

NMR titrations were additionally monitored by 2D  $^1\text{H}-^{13}\text{C}$  HSQC experiments to query the effect of  $\text{SipB}^{11-232}$  or  $\text{SipB}^{11-312}$  on the ILV methyl resonances of  $\text{SipD}^{\Delta 132}$ . Like the results of the amide titrations (**Fig. 7-6 & Fig. 7-7**), ILV titration of  $^{15}\text{N}/\text{ILV SipD}^{\Delta 132}$  with unlabeled  $\text{SipB}^{11-232}$  (**Fig. 7-8A**) or unlabeled  $\text{SipB}^{11-312}$  (**Fig. 7-9A**) resulted in a concentration dependent decrease in the peak intensity of specific  $\text{SipD}^{\Delta 132}$  ILV methyl peaks. As in the ILV titration of  $\text{SipD}^{\Delta 38}$  and  $\text{SipB}^{11-232}$  (**Fig. 7-3B**), the titration of  $\text{SipD}^{\Delta 132}$  with  $\text{SipB}^{11-232}$  (**Fig. 7-8A, arrows**) or  $\text{SipB}^{11-312}$  (**Fig. 7-9A, arrows**) resulted in the appearance of new ILV methyl peaks. In agreement with amide titrations, intensity ratio analysis showed that affected ILVs clustered at the distal end of  $\text{SipD}^{\Delta 132}$  (**Fig. 7-8C & Fig. 7-9C**). Together, ILV methyl and amide titrations are in agreement that the distal end of  $\text{SipD}^{\Delta 132}$  is the surface utilized for the tip-translocon interaction and that removal of the SipD N-terminal domain did not largely affect the interaction with SipB.



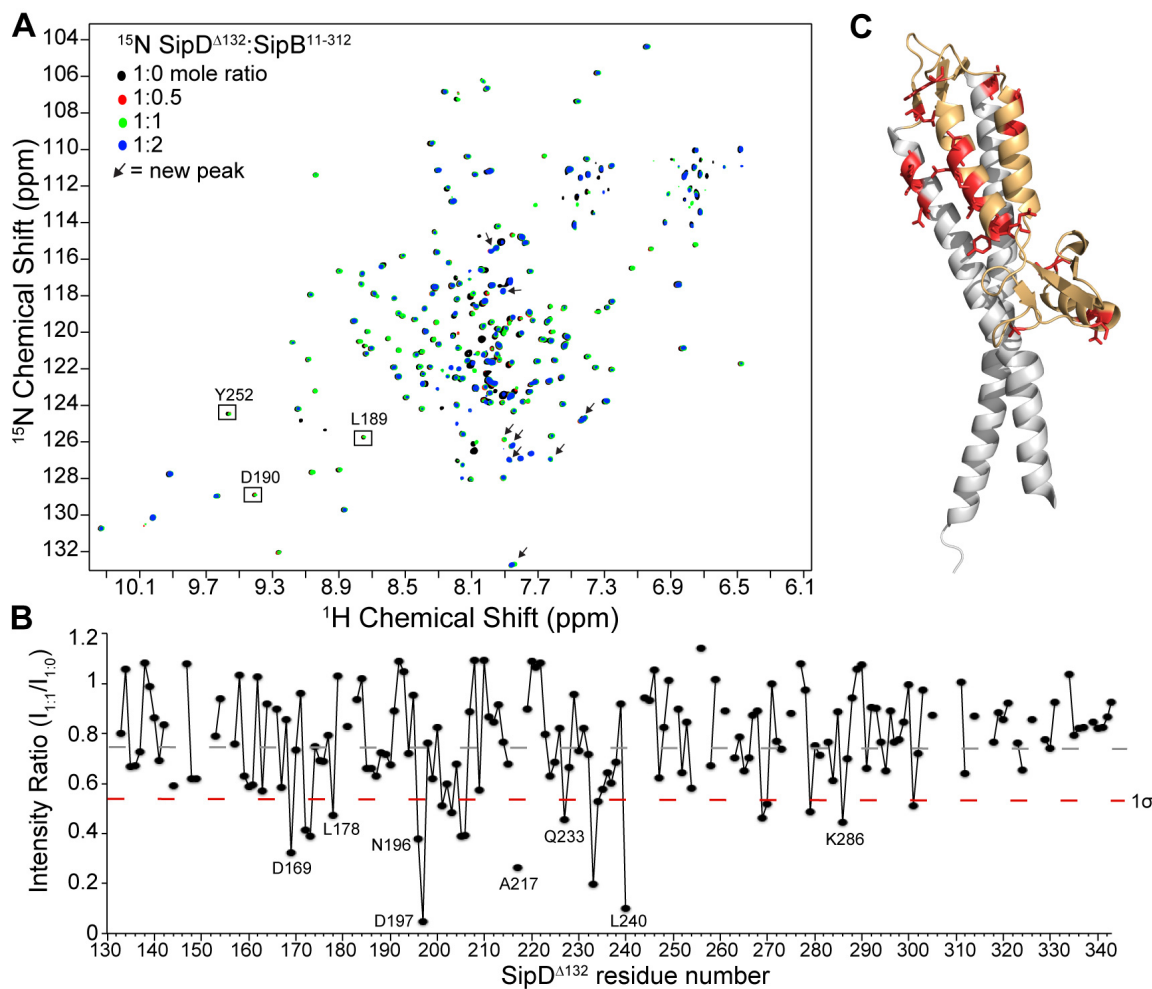
**7-5 –  $^{15}\text{N}$ /ILV Titration of SipD<sup>A38</sup> with SipB<sup>11-312</sup>**

(A) 2D  $^1\text{H}$ - $^{15}\text{N}$  TROSY and (B) 2D  $^1\text{H}$ - $^{13}\text{C}$  HSQC of  $^{15}\text{N}$ /ILV labeled SipD<sup>A38</sup> titrated with unlabeled SipB<sup>11-312</sup> at 1:0, 1:0.5, 1:1 and 1:2 mole ratios. Spectral collapse and signal broadening of many resonances occurred.



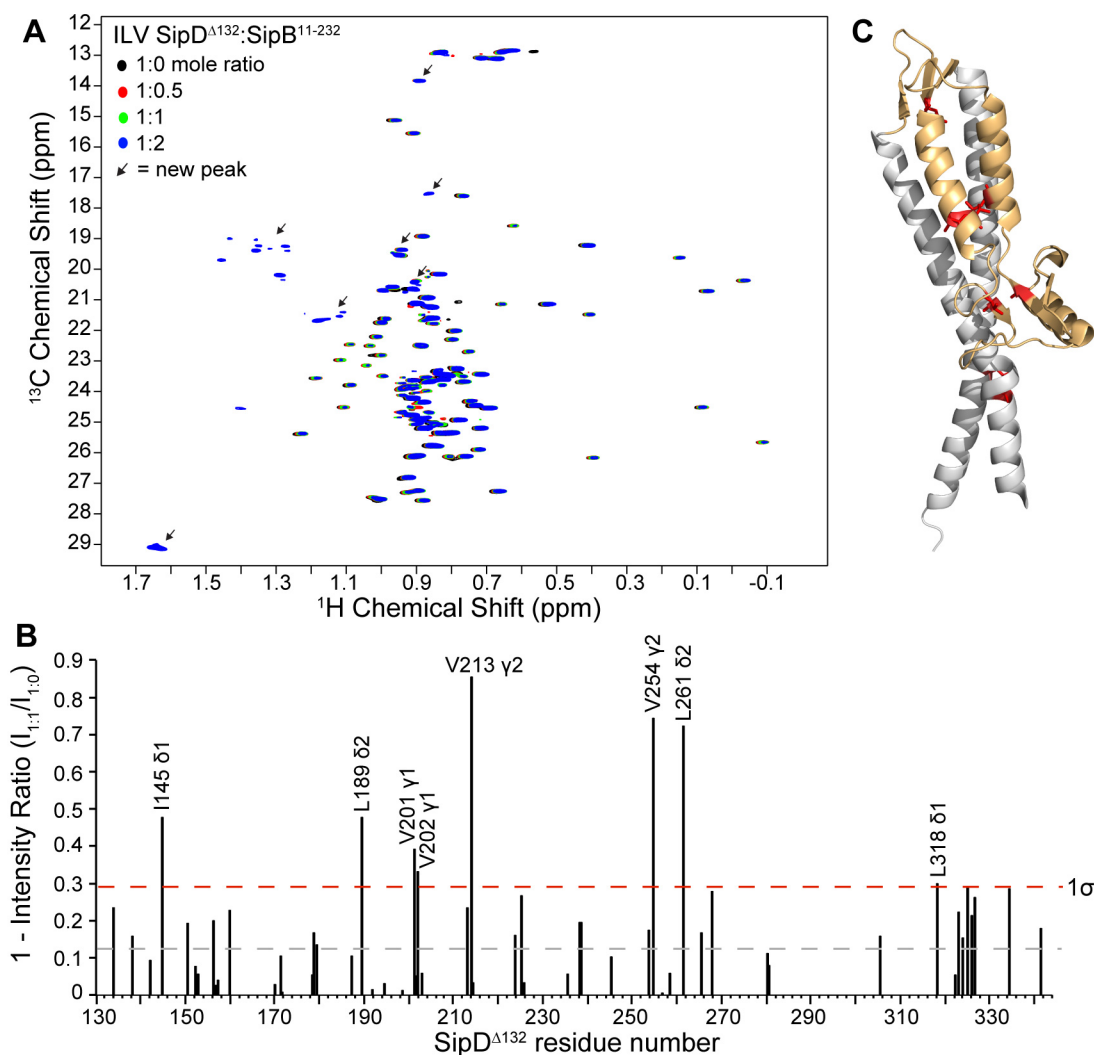
### 7-6 – $^{15}\text{N}$ Titration of SipD $^{\Delta 132}$ with SipB $^{11-232}$

(A) Overlay of four  $^1\text{H}$ - $^{15}\text{N}$  TROSY spectra of  $^{15}\text{N}$ /ILV labeled SipD $^{\Delta 132}$  titrated with unlabeled SipB $^{11-232}$  at molar ratios of 1:0, 1:0.5, 1:1 and 1:2. Four affected residues are expanded as representative interacting residues. (B) Plot showing the peak intensities ratios of the SipD $^{\Delta 132}$ : SipB $^{11-232}$  titration at 1:1 over 1:0 mole ratio. (C) Affected residues (color red) are mapped onto the structure of SipD $^{\Delta 132}$  [gray (coiled-coil) and orange (mixed  $\alpha/\beta$  domain)].



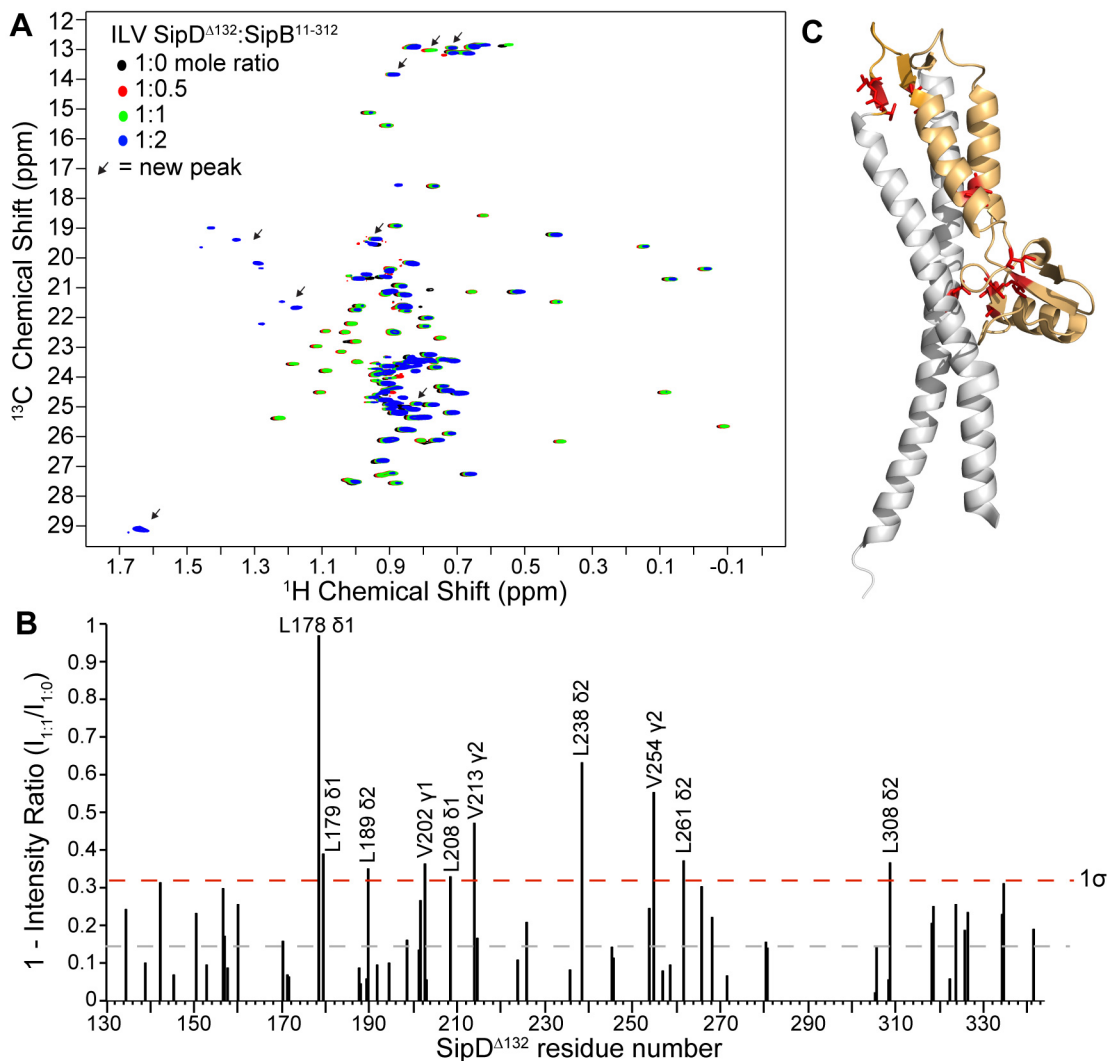
### 7-7 – $^{15}\text{N}$ Titration of SipD $\Delta 132$ with SipB $^{11-312}$

(A) Overlay of four  $^1\text{H}$ - $^{15}\text{N}$  TROSY spectra of  $^{15}\text{N}$ /ILV labeled SipD $\Delta 132$  titrated with unlabeled SipB $^{11-312}$  at molar ratios of 1:0, 1:0.5, 1:1 and 1:2. New peaks are indicated with arrows. (B) Plot showing the peak intensities ratios of the SipD $\Delta 132$ :SipB $^{11-312}$  titration at 1:1 over 1:0 mole ratio. (C) Residues that were affected (colored red) are mapped onto the structure of SipD $\Delta 132$  [gray (coiled-coil) and orange (mixed  $\alpha/\beta$  domain)].



### 7-8 – ILV Titration of SipD<sup>Δ132</sup> with SipB<sup>11-232</sup>

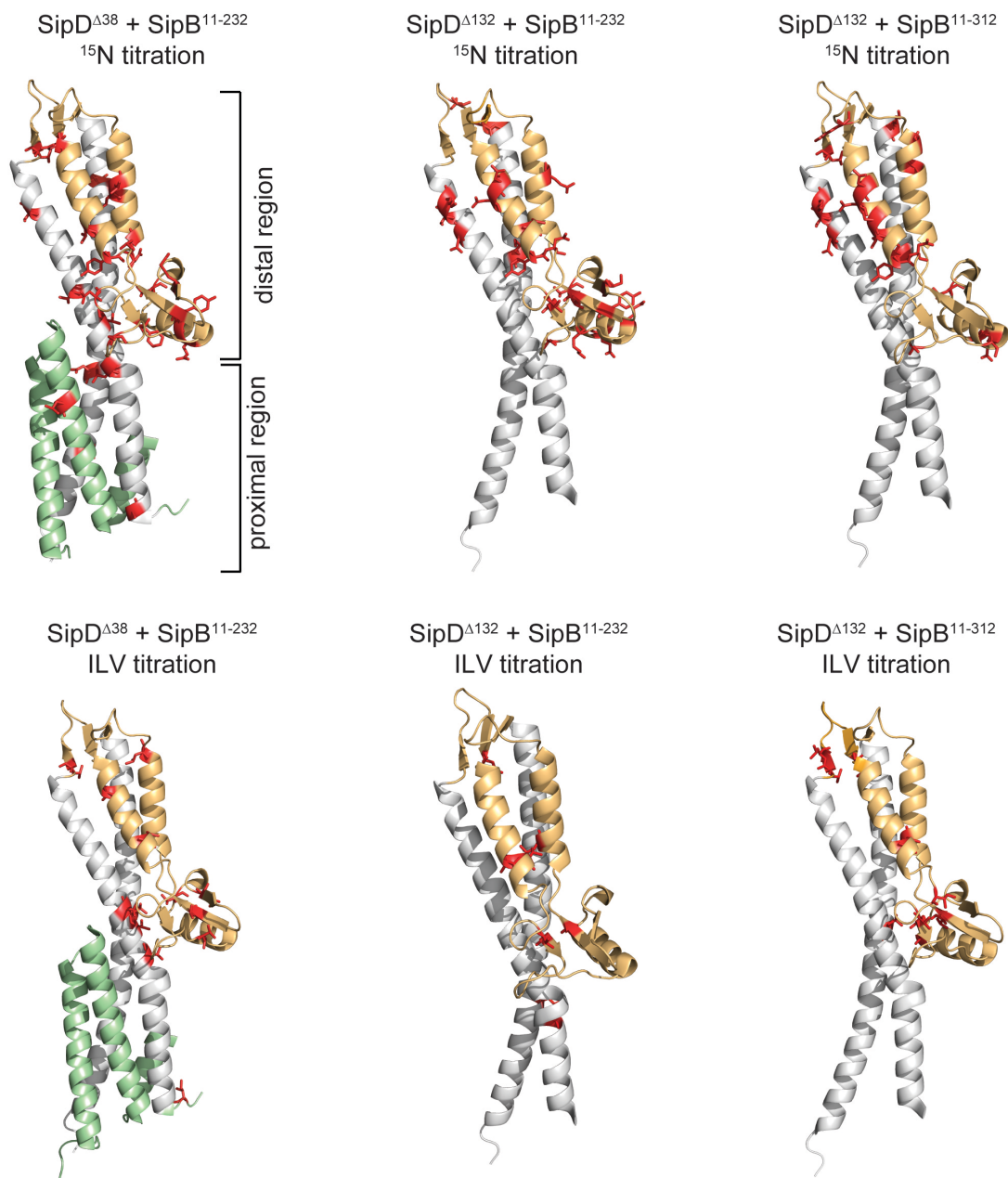
(A) Overlay of four <sup>1</sup>H-<sup>13</sup>C HSQC experiments of <sup>15</sup>N/<sup>1</sup>ILV SipD<sup>Δ132</sup> titrated with unlabeled SipB<sup>11-232</sup> at mole ratios of 1:0, 1:0.5, 1:1 and 1:2. New peaks are indicated with arrows. (B) Plot showing the peak intensities ratios of the SipD<sup>Δ132</sup>:SipB<sup>11-232</sup> titration at 1:1 over 1:0 mole ratio. (C) Residues that were affected (colored red) are mapped onto the structure of SipD<sup>Δ132</sup> [gray (coiled-coil) and orange (mixed α/β domain)].



**7-9 – ILV Methyl Titration of  $^{15}\text{N}$ - $^{13}\text{CH}_3$ -ILV SipD $^{\Delta 132}$  and Unlabeled SipB $^{11-312}$**   
**(A)** Overlay of four  $^1\text{H}$ - $^{13}\text{C}$  HSQC experiments of  $^{15}\text{N}$ /ILV SipD $^{\Delta 132}$  titrated with unlabeled SipB $^{11-312}$  at mole ratios of 1:0, 1:0.5, 1:1 and 1:2. New peaks are indicated with arrows. **(B)** Plot showing the peak intensities ratios of the SipD $^{\Delta 132}$ :SipB $^{11-312}$  titration at 1:1 over 1:0 mole ratio. **(C)** Residues that were affected (colored red) are mapped onto the structure of SipD $^{\Delta 132}$  [gray (coiled-coil) and orange (mixed  $\alpha/\beta$  domain)].

#### 7.4. Discussion

A comparison of the results from both amide and ILV methyl titrations of  $^{15}\text{N}/\text{ILV}$  SipD $^{\Delta 38}$  or SipD $^{\Delta 132}$  with unlabeled SipB $^{11-232}$  or SipB $^{11-312}$  suggest that the distal region of SipD, which includes the mixed  $\alpha/\beta$  domain, is the primary interaction surface with the N-terminal ectodomain of SipB (**Fig. 7-9**). Although NMR experiments showed a wide range of chemical exchange, most SipD residues were in intermediate exchange upon titration with the N-terminal domain of SipB, suggesting a weak interaction in the  $\mu\text{M}$  range. New SipD peaks were observed in both amide (**Fig. 7-6A & Fig 7-7A**) and ILV methyl (**Fig. 7-3B, Fig 7-8A & Fig 7-9A**) titrations upon addition of SipB $^{11-232}$  or SipB $^{11-312}$ , though unfortunately whether these resonances were due to true slow exchange could not be determined because they could not be assigned. Removal of the N-terminal  $\alpha$ -helical domain (residues 39-132) of SipD had little affect on the ability of SipD amides (**Fig. 7-1 & Fig. 7-6**) or ILV methyls (**Fig. 7-2 & Fig. 7-8**) to interact with SipB $^{11-232}$ . Furthermore, both amide and ILV methyl titrations of SipD $^{\Delta 38}$  and SipD $^{\Delta 132}$  with SipB $^{11-232}$  resulted in a similar affected surface, the distal region of SipD (**Fig. 7-9**). The titration of SipD $^{\Delta 132}$  with SipB $^{11-312}$  is in agreement with those results as well (**Fig. 7-9**). However, the titration of SipD $^{\Delta 38}$  and SipB $^{11-312}$  could not be analyzed due to spectral collapse and extensive signal broadening (**Fig. 7-5**). Interestingly, removal of the N-terminal domain of SipD allowed for interaction between SipD $^{\Delta 132}$  and SipB $^{11-312}$  without special collapse (**Fig. 7-7 & Fig. 7-9**). Why the presence of the SipD N-terminal domain affected the spectral quality with SipB $^{11-312}$ , but not SipB $^{11-232}$ , is currently unknown.



**7-10 – Comparison of results from  $^{15}\text{N}$  and ILV Titrations of SipD with SipB**  
 Comparison of the results from amide and ILV methyl titrations of SipD $\Delta 38$  or SipD $\Delta 132$  with SipB $^{11-232}$  or SipB $^{11-312}$ . Residues that were affected in each titration are mapped onto the atomic structure of SipD. In all cases, affected residues cluster at the distal region of SipD, which includes the top of the coiled-coil and the mixed  $\alpha/\beta$  domain.

## 7.5. References

1. Dickenson, N. E., Arizmendi, O., Patil, M. K., Toth, R. T. t., Middaugh, C. R., Picking, W. D. & Picking, W. L. (2013). N-Terminus of IpaB Provides a Potential Anchor to the Shigella Type III Secretion System Tip Complex Protein IpaD. *Biochemistry*.
2. Barta, M. L., Dickenson, N. E., Patil, M., Keightley, A., Wyckoff, G. J., Picking, W. D., Picking, W. L. & Geisbrecht, B. V. (2012). The Structures of Coiled-Coil Domains from Type III Secretion System Translocators Reveal Homology to Pore-Forming Toxins. *Journal of Molecular Biology* **417**, 395-405.
3. Delaglio, F., Grzesiek, S., Vuister, G. W., Zhu, G., Pfeifer, J. & Bax, A. (1995). NMRPipe: a multidimensional spectral processing system based on UNIX pipes. *J Biomol NMR* **6**, 277-93.
4. Johnson, B. A. (2004). Using NMRView to visualize and analyze the NMR spectra of macromolecules. *Methods Mol Biol* **278**, 313-52.
5. Chatterjee, S., Zhong, D., Nordhues, B. A., Battaile, K. P., Lovell, S. & De Guzman, R. N. (2011). The crystal structures of the Salmonella type III secretion system tip protein SipD in complex with deoxycholate and chenodeoxycholate. *Protein Sci* **20**, 75-86.
6. Rule, G. S. & Hitchens, T. K. (2006). *Fundamentals of protein NMR spectroscopy*. Focus on structural biology, Springer, Dordrecht.
7. Kleckner, I. R. & Foster, M. P. (2011). An introduction to NMR-based approaches for measuring protein dynamics. *Biochim Biophys Acta* **1814**, 942-68.
8. Rathinavelan, T., Lara-Tejero, M., Lefebvre, M., Chatterjee, S., McShan, A. C., Guo, D. C., Tang, C., Galan, J. E. & De Guzman, R. N. (2014). NMR model of PrgI-SipD interaction and its implications in the needle-tip assembly of the Salmonella type III secretion system. *J Mol Biol* **426**, 2958-69.

## Chapter 8. Characterization of the Interaction Between SipD and the SipB N-Terminal Domain by Fluorescence Spectroscopy

[Some of the data in this chapter has been published with the following citation: McShan AC, Kaur K, Chatterjee S, Knight KM, De Guzman RN. NMR Identification of the Binding Surfaces Involved in the Salmonella and Shigella Type III Secretion Tip-Translocon Protein-Protein Interactions. *Proteins*. 2016]

### 8.1. Introduction

The NMR titrations performed in Chapter 7 showed that the N-terminal ectodomain of SipB interacted with the tip protein SipD by solution NMR. To complement our NMR interaction studies between SipD and SipB, two protein binding assays were developed to examine the interaction between SipB<sup>82-312</sup> with SipD<sup>Δ38</sup> (which contains the N-terminal  $\alpha$ -helical domain) or SipD<sup>Δ100</sup> (which lacks the N-terminal  $\alpha$ -helical domain). The assays I developed were based on fluorescence polarization (FP) and Förster resonance energy transfer (FRET). Fluorescence based protein binding assays were utilized because of the following advantages: *i*) affinity measurements of SipD mutants and SipB could be readily tested, and *ii*) they could potentially be adapted for high throughput screens for inhibitors of the SipD/SipB interaction<sup>1</sup>. In addition, an *in vitro* *Salmonella* invasion assay was used to evaluate the ability of mutations in the SipD mixed  $\alpha/\beta$  domain to invade human intestinal epithelial Henle-407 cells. In support of our NMR studies, results of fluorescence-based assays show that SipD interacts with the N-terminal domain of SipB and removal of the N-terminal  $\alpha$ -helical domain of SipD does not largely affect the tip-translocon interaction.

### 8.2. Materials and Methods

#### 8.2.1. Site-Directed Mutagenesis, Protein Expression and Purification

Proteins were labeled for fluorescence spectroscopy by the attachment of maleimide-conjugated fluorophore to a cysteine residue in the protein<sup>2</sup>. SipD contains a wild-type cysteine, C244S, but it was mutated for to obtain higher quality NMR data of SipD<sup>Δ38</sup> so it was kept as a background mutation in all studies. SipB<sup>82-312</sup> and PrgI\* do not contain a wild-type cysteine. Therefore, a single cysteine mutation was introduced using a QuikChange kit (Stratagene) into SipB<sup>82-312</sup> and PrgI\* and confirmed by DNA sequencing. Sites chosen for mutagenesis were non-conserved residues that were surface exposed based on the atomic structures of SipD<sup>3</sup>, PrgI<sup>4</sup> and SipB<sup>5</sup>. The point mutations used in this study included SipB<sup>82-312</sup> A109C, SipB<sup>82-312</sup> D207C, SipB<sup>82-312</sup> N283C, SipB<sup>82-312</sup> E303C, SipD<sup>Δ38</sup> E230C, SipD<sup>Δ100</sup> K173C and PrgI\* L31C. All wild-type and mutant constructs were expressed and purified in LB media as previously described in Chapter 2 and Chapter 3 for SipD, Chapter 4 for PrgI\* and Chapter 6 for SipB<sup>82-312</sup>.

### 8.2.2. Fluorophore Conjugation of Proteins

Maleimide conjugated fluorophore was used to label SipD<sup>Δ38</sup> E230C, SipD<sup>Δ100</sup> K173C, PrgI\* L31C and the SipB<sup>82-312</sup> point mutants (A109C, D207C, N283C or E303C) at their respective cysteine residue. All proteins were dialyzed into 1× PBS, pH 7.4. A 10 fold excess of tris(2-carboxyethyl)phosphine (TCEP) to protein was used to reduce disulfides for 30 minutes at 25°C. A 20 fold excess of dye to protein was resuspended in 1 mL of 1× PBS, pH 7.4 for Alexa Fluor 488-C<sub>5</sub>-Maleimide, Fluorescein-C<sub>5</sub>-Maleimide or Alexa Fluor 647-C<sub>2</sub>-Maleimide (Invitrogen), which labeled PrgI\*/SipD and SipB, respectively. Abbreviations for dyes used are AF488 (Alexa Fluor 488-C<sub>5</sub>-Maleimide), FM (Fluorescein-C<sub>5</sub>-Maleimide) and AF647 (Alexa Fluor 647-C<sub>2</sub>-Maleimide).

Fluorophore was added drop wise to the reduced protein solution while mixing and allowed to react for 3 hours in the dark at 25°C. The unreacted dye was removed by dialysis in 1× PBS, pH 7.4 followed by passage through an Amicon Ultra 3K (Millipore) filtration column. The labeling efficiency was estimated by acquiring UV-visible absorption spectra with a scan between 400 and 800 nm (**Fig. 8-1**). Beer's Law was then used to determine labeled protein concentration:  $A = \epsilon cl$ , where A is the absorption maxima, l is the path length and  $\epsilon$  is the fluorophore extinction coefficients ( $\epsilon = 265,000 \text{ cm}^{-1} \text{ M}^{-1}$  for AF647;  $\epsilon = 72,000 \text{ cm}^{-1} \text{ M}^{-1}$  for AF488;  $\epsilon = 83,000 \text{ cm}^{-1} \text{ M}^{-1}$  for FM). The percent labeling efficiency was then determined by calculating the ratio of dye labeled protein over the initial unlabeled protein concentration and multiplying by 100%.

### 8.2.3. Circular Dichroism (CD)

CD was performed on proteins at 0.05 mg/mL in 2 mL of sterile H<sub>2</sub>O.

Experimental parameters were the same as those described in Chapter 3.

### 8.2.4. Fluorescence Polarization (FP)

FP provides a readout of the average angular displacement of a fluorophore during its excited lifetime. This displacement is dependent on the rate of rotational diffusion of the fluorophore labeled molecule<sup>1</sup>. Therefore, FP provides a measure of change in the molecular volume/the rotational diffusion rate that occurs upon binding. FP experiments were performed by titrating 25 nM of AF647 labeled SipB<sup>82-312</sup> (A109C, D207C, N283C or E303C) with increasing concentrations of unlabeled SipD<sup>Δ38</sup> or SipD<sup>Δ100</sup>. FP experiments were also performed with 25 nM of AF488 labeled PrgI\* L31C

titrated with increasing concentrations of unlabeled SipB<sup>82-312</sup>. In all FP experiments, the baseline signal of the fluorometer was obtained by using the buffer 1× PBS, pH 7.4 alone. The average of measured data points (n=5) was subtracted from a base polarization value of 25 nM SipB<sup>82-312</sup> (A109C, D207C, N283C or E303C)-AF647 or 25 nM PrgI\* L31C-AF488. The difference in millipolarization ( $\Delta mP$ ) was plotted against increasing concentrations of binding protein partners to obtain a binding curve. The FP binding curve was fitted with Origin (OriginLab, Northampton, MA). All FP data was collected using a Varian Cary Eclipse Fluorescence Spectrophotometer at 25°C.

#### 8.2.5. Förster Resonance Energy Transfer (FRET)

FRET was used to determine distance specific information on the protein-protein interactions. Fluorescence emission spectra were examined using different combinations of fluorophore labeled proteins. Emission spectra (n = 3) were collected between 500 nm and 800 nm using an excitation wavelength of 480 nm, excitation and emission slit widths of 5 nm, and an integration time of 0.1 seconds. All data was collected on a Varian Cary Eclipse Fluorescence Spectrophotometer at 25°C.

FRET efficiency was calculated from emission spectra as follows:

$$E = 1 - \frac{F_{DA}}{F_D}$$

where E is the energy transfer efficiency,  $F_{DA}$  is the donor fluorescence FRET in the presence of the acceptor, and  $F_D$  is the donor fluorescence in the absence of the acceptor. The distance between the FRET dye pairs,  $r$ , was calculated from the following formula:

$$r = R_0 \left( \frac{1}{E} - 1 \right)^{1/6}$$

where  $R_0$  is the Förster distance between two FRET pairs at which  $E = 50\%$ . An  $R_0$  value of  $\sim 56\text{\AA}$  was used for the FRET pairs (FM or AF488 donor with AF647 acceptor) in this study (Invitrogen).

#### 8.2.6. *Salmonella* Invasion Assay

A *Salmonella* invasion assay was used to test whether mutations in the SipD mixed  $\alpha/\beta$  domain affected the ability of *Salmonella* to invade a cultured human epithelial cell line (Henle 407 cells, ATCC #CCL6) following a method described in Chapter 5. Single, double, or triple point mutations in SipD were introduced by PCR in the plasmid pRK2-SipD, which harbors full-length SipD, and confirmed via DNA sequencing. The *sipD*<sup>-</sup> knock-out strain complemented with the wild-type SipD pRK2 plasmid was taken as 100% relative invasiveness. Therefore, the percent invasion of all other strains were relative the *sipD*<sup>+</sup> strain. Error bars were obtained from with three replicate experiments.

#### 8.2.7. Western Immunoblot Analysis

$\Delta$ SipD, +SipD and SipD mutant strains of *Salmonella typhimurium* were grown in 15 mL of LB broth containing 0.3 M NaCl and 1 mM IPTG. Cell growth was continued at 37°C at 80 rpm until the OD<sub>600</sub> reached 0.9. Bacterial cells were harvested by centrifugation at 4000 rpm for 20 minutes then passed through a 0.45  $\mu\text{m}$  pore-size filter. Proteins from the cultured supernatants were precipitated by incubating with 10% (v/v) trichloroacetic acid at 4°C for 1 hour and recovered by centrifugation at 4000 pm for 40 minutes. Pellets were resuspended in 2 mL 10% (v/v) SDS and 8 mL ice-cold acetone then incubated overnight at -20°C. After centrifugation at 4000 pm for 40 minutes, the

pellets were dried and resuspended in 100  $\mu$ L 8M Urea and 100  $\mu$ L 2 $\times$  SDS-loading dye. Proteins from whole-cell lysates (cell pellets) were resuspended in 1 mL 1 $\times$  PBS and recovered by centrifugation at 13000 rpm for 15 minutes. The pellets were resuspended in 50  $\mu$ L 1 $\times$  PBS and 50  $\mu$ L 2 $\times$  SDS-loading dye.

For Western immunoblotting analysis, proteins were separated by SDS-PAGE and transferred to a PVDF membrane for 1.5 hours at 70 mA using an ECL Semi-Dry Blotter (Amersham Biosciences). After transfer, the membrane was incubated in 5% (v/v) non-fat dry milk with shaking for 1 hr at room temperature and then incubated with primary antibody solution (1% non-fat dry milk, 0.1% Tween-20, 1 $\times$  TBS, rat anti-SipD IgG antibody) with shaking at 4 $^{\circ}$ C overnight. Following this incubation step, the membrane was rinsed three times with wash buffer (0.1% Tween-20, 1 $\times$  TBS pH 7.4). Membrane was then incubated in the secondary antibody solution (anti-rat IgG antibody conjugated to Alexa Fluor-680 in wash buffer) for 1 hr at room temperature with shaking. The membrane was then rinsed three times with wash buffer. The blot was analyzed using an ODYSSEY Infrared Imaging System (LI-COR Biosciences).

## **8.3. Results**

### *8.3.1. Fluorophore Conjugation to Proteins*

Cysteine point mutants of T3SS proteins were generated by PCR for the covalent attachment of maleimide-conjugated fluorophore. CD spectropolarimetry was used to confirm that the cysteine point mutation of recombinant proteins retained similar secondary structure characteristics to their non-cysteine containing counterparts (data not shown). All SipB<sup>82-312</sup> cysteine mutant proteins were labeled with AF647 and

SipD<sup>Δ38</sup>/SipD<sup>Δ100</sup> cysteine mutants were labeled with AF488 or FM. FM/AF488 and AF647 were chosen as the dye pair for FRET because their R<sub>0</sub> value of ~56Å is within the expected protein-protein interaction distance based on our hypothesis that the coiled-coil of SipB<sup>82-312</sup> interacts with the distal region of SipD as discussed in Chapter 7. UV-visible absorption spectra show that SipB<sup>82-312</sup> cysteine mutants were labeled with their respective fluorophore (**Fig. 8-1**). The labeling efficiency was estimated to be 87% for SipB<sup>82-312</sup> A109C-AF647, 91% for SipB<sup>82-312</sup> D207C-AF647, 85% for SipB<sup>82-312</sup> N283C-AF647 and ~81% for SipB<sup>82-312</sup> E303C-AF647. Furthermore, CD experiments showed that the conjugation of fluorophore to SipB<sup>82-312</sup> did not significantly alter its secondary structure characteristics (**Fig. 8-2**). Conjugation of fluorophore to SipD and PrgI\* showed similar results (data not shown).

### 8.3.2. FP of SipB<sup>82-312</sup> and SipD<sup>Δ38</sup>/SipD<sup>Δ100</sup>

FP was used to determine the *in vitro* binding affinity between SipD<sup>Δ38</sup> (which contains the N-terminal α-helical domain) or SipD<sup>Δ100</sup> (which lacks the N-terminal α-helical domain) with SipB<sup>82-312</sup>. FP of 25 nM AF647 labeled SipB<sup>82-312</sup> A109, D207C, N283C or E303 titrated with increasing concentrations of unlabeled SipD<sup>Δ38</sup> resulted in saturated binding curves (**Fig. 8-3**). The estimated dissociation constants for SipB<sup>82-312</sup> titrated with unlabeled SipD<sup>Δ38</sup> were 36 ± 5 μM (with SipB<sup>82-312</sup> A109C), 67 ± 12 μM (with SipB<sup>82-312</sup> D207C), 38 ± 7 μM (with SipB<sup>82-312</sup> N283C) and 44 ± 6 μM (with SipB<sup>82-312</sup> E303C) (**Fig. 8-3**). In Chapter 7, NMR titrations showed that the distal region of SipD is the primary surface for the interaction with SipB. Therefore, I hypothesized that the removal of the N-terminal α-helical domain of SipD (residues 39-100) would not

drastically affect the affinity between SipD and the N-terminal ectodomain of SipB. Indeed, removal of the N-terminal domain of SipD had little effect on the binding affinity between SipD<sup>Δ100</sup> with SipB<sup>82-312</sup> (**Fig. 8-3**). The estimated dissociation constants for SipB<sup>82-312</sup> titrated with unlabeled SipD<sup>Δ100</sup> were 42 ± 7 μM (with SipB<sup>82-312</sup> A109C), 61 ± 7 μM (with SipB<sup>82-312</sup> D207C), 37 ± 3 μM (with SipB<sup>82-312</sup> N283C) and 48 ± 7 μM (with SipB<sup>82-312</sup> E303C) (**Fig. 8-3**). Together these data suggest that the dissociation constant between SipD<sup>Δ38</sup>/SipD<sup>Δ100</sup> with SipB<sup>82-312</sup> is in the range of 30 to 60 μM, though placement of AF647 at D207 on SipB<sup>82-312</sup> results in a slight increase in the dissociation constant (**Fig. 8-3**).

### 8.3.3. FRET of SipB<sup>82-312</sup> and SipD<sup>Δ38</sup>/SipD<sup>Δ100</sup>

FRET was used to estimate the distance between the donor labeled SipD cysteine and the acceptor labeled SipB<sup>82-312</sup> cysteine. Either AF488 or FM fluorophore was attached to the distal region of SipD; at E230C for SipD<sup>Δ38</sup> and at K173C for SipD<sup>Δ100</sup> (**Fig. 8-4**). The AF647 fluorophore was attached towards the middle of the trimeric coiled-coil (D207) or C-terminus (N283) of SipB<sup>82-312</sup> (**Fig. 8-4**). FRET signal was observed for both SipD<sup>Δ38</sup> E230C-AF488 (**Fig. 8-4A**) and SipD<sup>Δ100</sup> K173C-FM (**Fig. 8-4B**) with SipB<sup>82-312</sup> D207C-AF647. FRET signal was also observed for SipD<sup>Δ38</sup> E230C-AF488 (**Fig. 8-4D**) with SipB<sup>82-312</sup> N283C-AF647. However, less FRET signal was observed between SipD<sup>Δ100</sup> K173C-FM and SipB<sup>82-312</sup> D207C-AF647 (**Fig. 8-4C**). The FRET efficiencies, E, and the estimated molecular distance, r, between each FRET pair are shown in **Table 8-1**. Together, these results agree with results of FP that showed SipD<sup>Δ38</sup> and SipD<sup>Δ100</sup> interact with SipB<sup>82-312</sup> *in vitro*. Results of FRET experiments also

suggest that the C-terminus of SipB<sup>82-312</sup> is further away from the interaction interface with the distal region of SipD than the trimeric coiled-coil of SipB<sup>82-312</sup>.

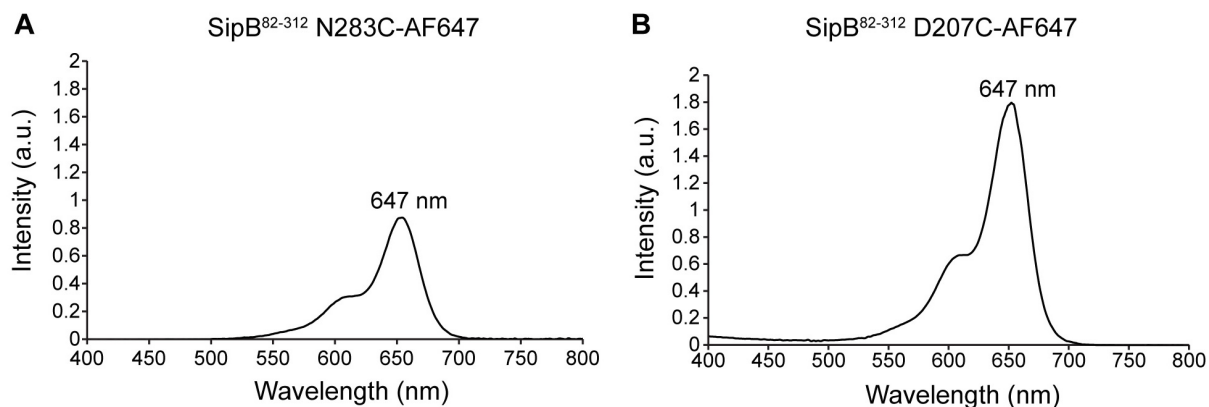


**Fig. 8-1 – UV-Vis Absorption Spectra of Fluorophore Labeled SipB<sup>82-312</sup>**  
 UV-Vis absorption spectra of AF647 labeled (A) SipB<sup>82-312</sup> N283C and (B) SipB<sup>82-312</sup> D207C. The maxima of the spectra are shown and correlate with the expected adsorption maxima of their respective fluorophore.

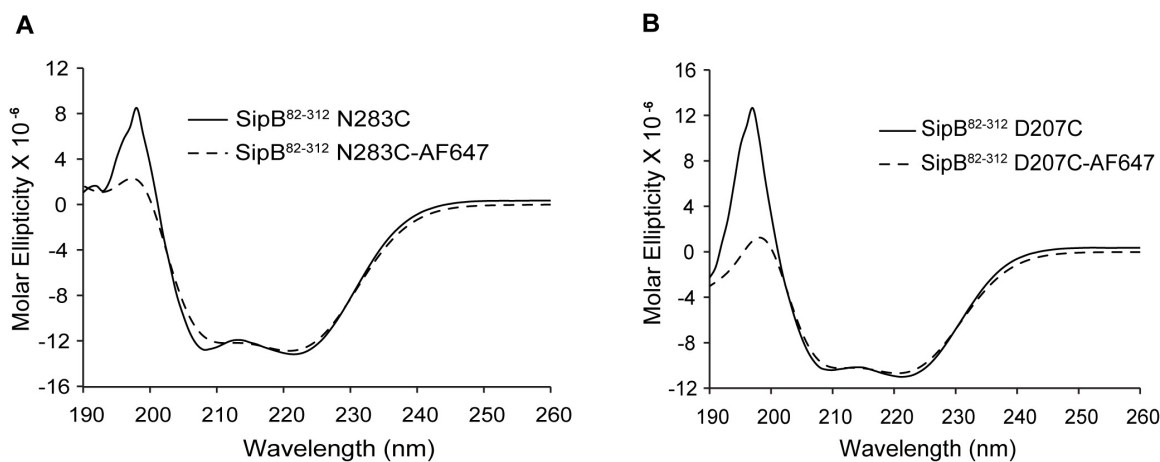


**Fig. 8-2 – Circular Dichroism of Fluorophore Labeled SipB<sup>82-312</sup>**  
 Far-UV CD spectra of non-fluorophore labeled and fluorophore labeled (A) SipB<sup>82-312</sup> N283C and (B) SipB<sup>82-312</sup> D207C and. Both proteins show CD minima at 208 and 222, which is typical of highly  $\alpha$ -helical proteins. CD shows the secondary structure characteristics of fluorophore labeled SipB<sup>82-312</sup> (dotted line) is similar to non-fluorophore labeled SipB<sup>82-312</sup> (solid line). Similar results were observed for SipB<sup>82-312</sup> A109C or E303C, which are not shown here.

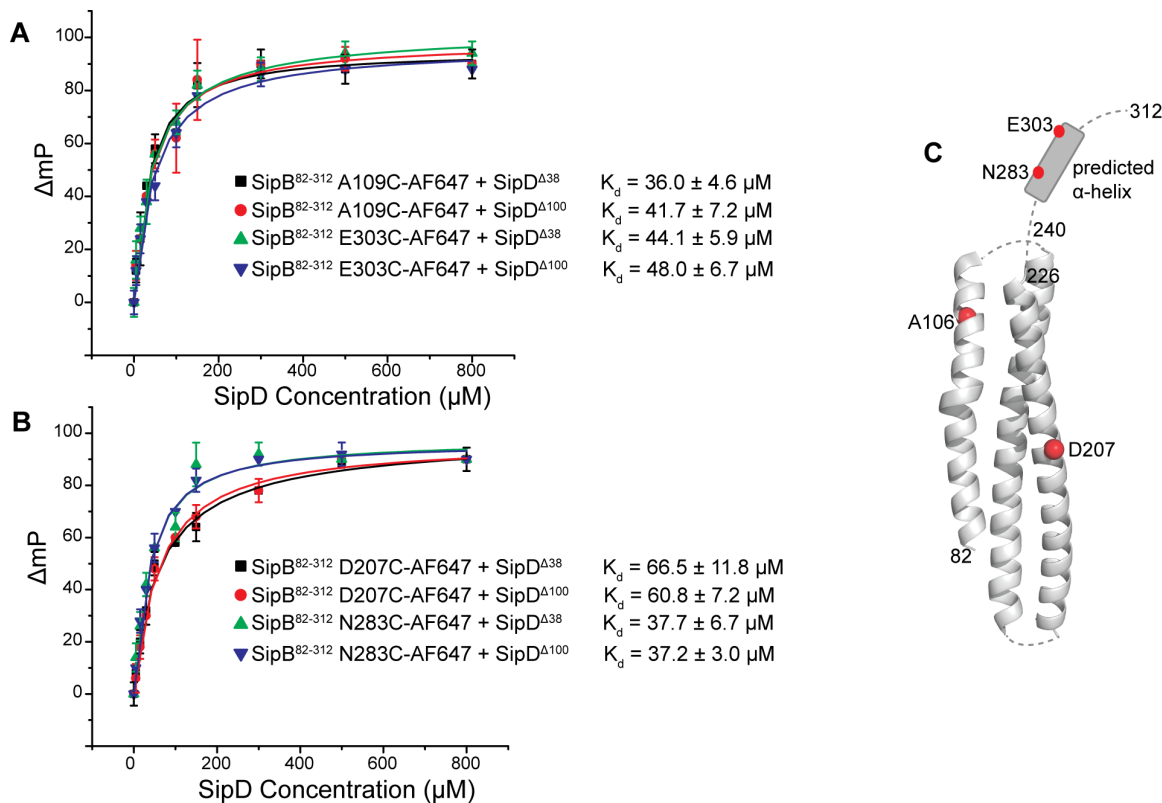


**Fig. 8-3 – Fluorescence Polarization of SipB<sup>82-312</sup>-AF647 and SipD <sup>$\Delta$ 38/ $\Delta$ 100</sup>**  
 FP of 25 nM (A) SipB<sup>82-312</sup> A109C-AF647 or E303C-AF647 and (B) SipB<sup>82-312</sup> D207C-AF647 or N283C-AF647 with increasing concentrations of unlabeled SipD <sup>$\Delta$ 38</sup> or SipD <sup>$\Delta$ 100</sup> is shown. The change in millipolarization ( $\Delta\text{mP}$ ) is shown and each data point contains error bars for its replicates ( $n=5$ ). The apparent dissociation constant for all SipB<sup>82-312</sup> and SipD <sup>$\Delta$ 38</sup>/SipD <sup>$\Delta$ 100</sup> are shown, with values ranging from 37 to 67  $\mu\text{M}$ . (C) The location of the residues that were mutated is mapped onto the structure of SipB<sup>82-226</sup> (PDB ID 3TUL) as a reference. The structure of SipB from 226-312 is unknown, but is predicted to contain an  $\alpha$ -helix.

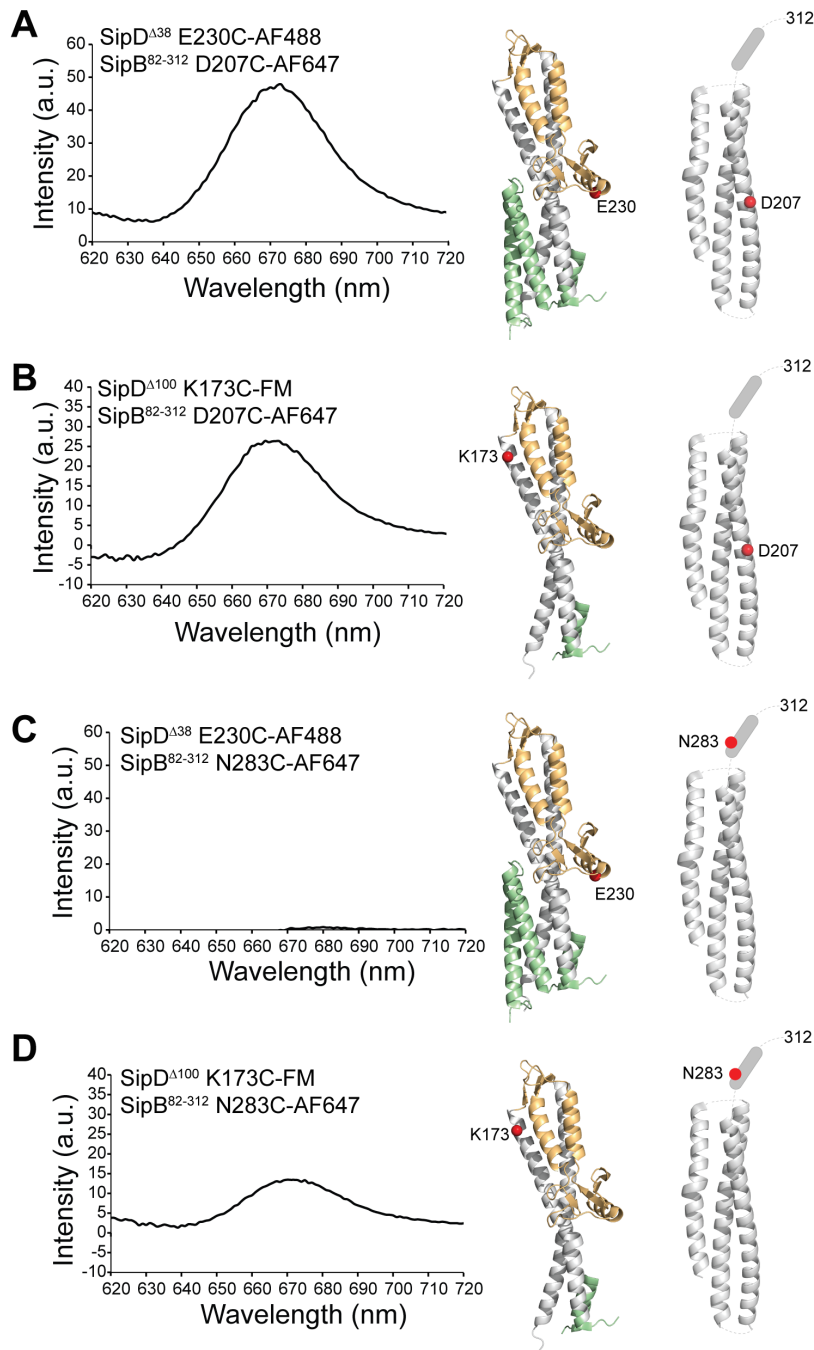


**Fig. 8-4 – FRET of SipB<sup>82-312</sup>-AF647 and SipD<sup>Δ38/Δ100</sup>-AF488/FM**  
 FRET performed with SipB<sup>82-312</sup> (D207C or N283C)-AF647 (acceptor) and SipD<sup>Δ38</sup> E230C-AF647 or SipD<sup>Δ100</sup> K173C-FM (donor). The difference between the emission spectra of the acceptor alone and the acceptor in the presence of the donor is shown. The position of the fluorophore label on the structure of SipD<sup>Δ38</sup> and SipB<sup>82-312</sup> is shown. SipD<sup>Δ38</sup> has the N-terminal domain colored in green, coiled-coil in gray and mixed  $\alpha/\beta$  domain in orange on the left. SipB<sup>82-312</sup> is colored in gray on the right.

**Table 8-1 – Calculations of SipB/SipD FRET Efficiency**

Proteins	FRET Efficiency, E	Distance, r (Å)
SipD <sup>Δ38</sup> E230C-AF488 + SipB <sup>82-312</sup> D207C-AF647	0.91	37.7
SipD <sup>Δ100</sup> K173C-FM + SipB <sup>82-312</sup> D207C-AF647	0.71	48.2
SipD <sup>Δ38</sup> E230C-AF488 + SipB <sup>82-312</sup> N283C-AF647	0.11	79.3
SipD <sup>Δ100</sup> K173C-FM + SipB <sup>82-312</sup> N283C-AF647	0.44	58.2

Estimation of FRET efficiency and molecular FRET pair distance from FRET experiments.

#### 8.3.4. FP and FRET of SipB<sup>82-312</sup> and PrgI\*

The needle and translocon have not been reported to interact, presumably due to being separated in space by the tip protein SipD. To test whether PrgI\* interacted with SipB<sup>82-312</sup>, FP and FRET experiments were performed. No FRET signal was observed between PrgI\* L31C-AF488 and SipB<sup>82-312</sup> D207C-AF647 or SipB<sup>82-312</sup> N283C-AF647 (**Fig. 8-5A & Fig. 8-5B**). Furthermore, increasing concentrations of unlabeled SipB<sup>82-312</sup> up to 800 μM showed no significant increase in polarization with 25 nM PrgI\* L31C-AF488, suggesting a lack of interaction between PrgI\* and SipB<sup>82-312</sup> *in vitro* by FP (**Fig. 8-5C**). These results serve as control experiments for FP & FRET studies of needle, tip and translocon proteins.

### 8.3.5. Invasion Assay with SipD Mixed $\alpha/\beta$ Domain Mutants

Based on NMR, FP and FRET results, as well as the observation that the proximal end of SipD (the bottom of the coiled-coil) interacts with the needle protein PrgI (discussed in Chapter 4 and Chapter 5), I hypothesized that the distal region of SipD (the top of the coiled-coil and the mixed  $\alpha/\beta$  domain) would be the primary surface for the interaction with the N-terminal ectodomain of SipB. To test whether the distal region of SipD is important for the interaction with SipB, single, double or triple point mutations were introduced into the mixed  $\alpha/\beta$  domain of SipD (**Fig. 8-6**) and tested for their ability to effect invasion of intestinal epithelial Henle-407 cells by *Salmonella*. Removal of the *sipD* gene ( $\Delta$ SipD) completely knocked out the ability for *Salmonella* Typhimurium to invade Henle-407 cells (**Fig. 8-6**). Invasion was complemented by the addition of a plasmid containing wild-type *sipD* (SipD+) (**Fig. 8-6**). Two single mutations, L271D and L280D, had no effect on invasion (**Fig. 8-6**). In contrast, other single mutations, such as N196D and V191D, or double mutations, such as V191D/N196 and L271D/L280D, moderately decreased invasion (**Fig. 8-6**). Double and triple point mutations affecting a larger surface area of SipD drastically reduced invasion (**Fig. 8-6**). Invasion was reduced below 1% with the SipD double mutant L280D+A285D and the triple mutants N196D+L280D+A285D or N196D+V265D+L271D (**Fig. 8-6**). Western immunoblot analysis of cultured supernatants (**Fig. 8-7A**) and whole-cell lysates (**Fig. 8-7B**) showed that, other than N196+V265D+L271D (**Fig. 8-7A, B**), the SipD mutant proteins were expressed. This suggests that the drop in invasion observed (**Fig. 8-6**) was not due to failure of SipD mutant protein to express, except for N196+V265D+L271D. Together,

the results of invasion assays support the hypothesis that the distal region of SipD is essential for *Salmonella* invasion into host cells.

#### 8.4. Discussion

The data presented here show that the N-terminal ectodomain of SipB (82-312) interacts with SipD with a micromolar affinity range (**Fig. 8-3**). The slight decrease in affinity of SipB<sup>82-312</sup> D207C for SipD<sup>Δ38</sup>/SipD<sup>Δ100</sup> suggests the possibility that  $\alpha$ -helix 3 of SipB trimeric coiled-coil is at the interaction surface, if indeed the fluorophore placement inhibited the interaction (**Fig. 8-3**). However, this hypothesis has yet to be experimentally tested. The SipD/SipB affinity range of 30 to 60  $\mu$ M is in agreement with the binding affinity estimated by intermediate exchange timescale observed in NMR titrations of SipD and SipB (see Chapter 7). However, it is a factor of  $\sim$ 200 times lower than the reported value for the *Shigella* homologs IpaD/IpaB<sup>6</sup>. FRET experiments suggest that placement of the fluorophore on the SipB<sup>82-312</sup> coiled-coil (D207C) shows more efficient FRET signal than placing the fluorophore towards the C-terminus of SipB<sup>82-312</sup> (N283C) (**Fig. 8-4 & Table 8-1**). Additionally, this suggests that the SipB N-terminal domain trimeric coiled-coil is primarily involved in the interaction with SipD. In support of the initial hypothesis, mutations in the distal region of SipD decreased invasion of *Salmonella* Typhimurium with Henle-407 cells (**Fig. 8-6**). Finally, both FP and FRET showed a lack of interaction with SipB<sup>82-312</sup> and PrgI\* (**Fig. 8-5**).

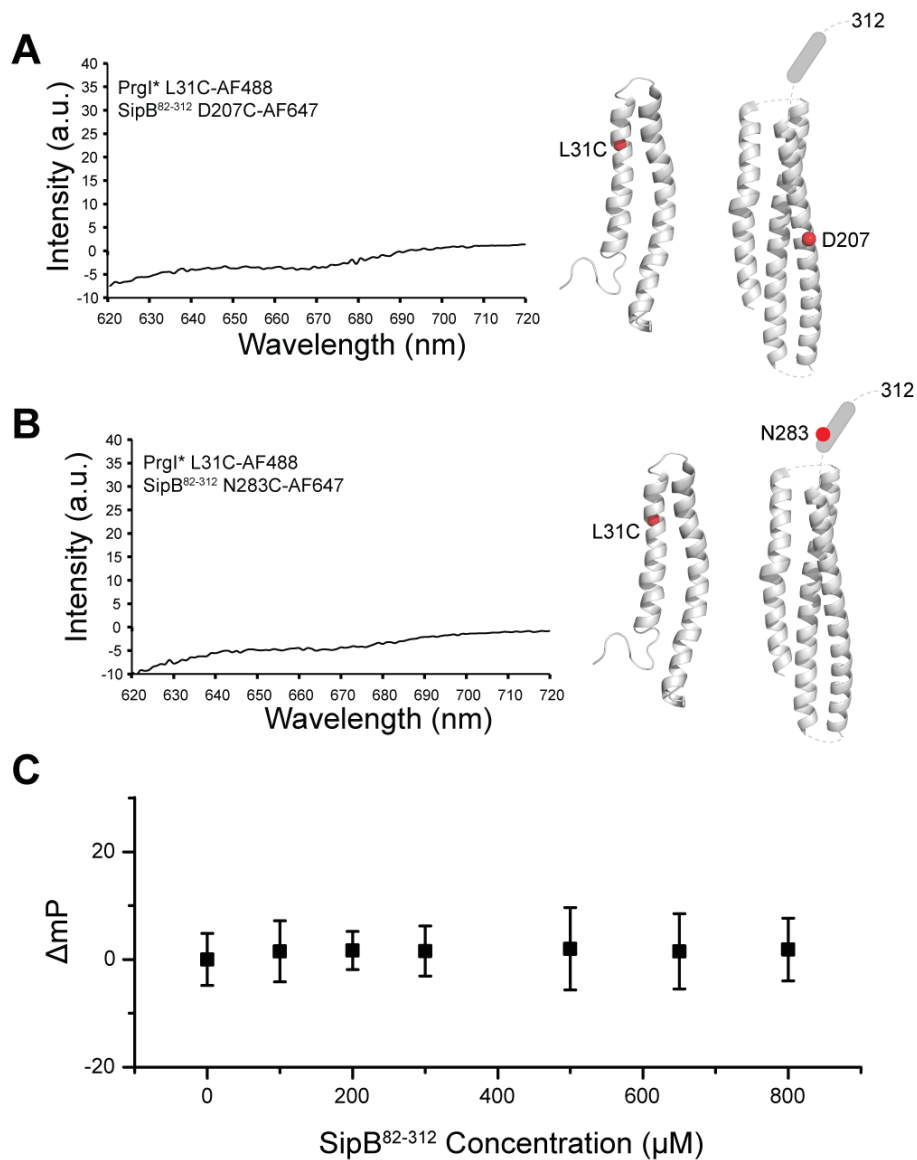


**Fig. 8-5 – FP and FRET of SipB<sup>82-312</sup> and PrgI\***  
PrgI\* L31C-AF488 does not show FRET with either **A.** SipB<sup>82-312</sup> D207C-AF647 or **B.** SipB<sup>82-312</sup> N283C-AF647. **C.** There is no change in polarization value of 25 nM PrgI\* L31C-AF488 upon the addition of unlabeled SipB<sup>82-312</sup>. The position of the fluorophore label on the structure of PrgI\* (left) and SipB<sup>82-312</sup> (right) is shown.

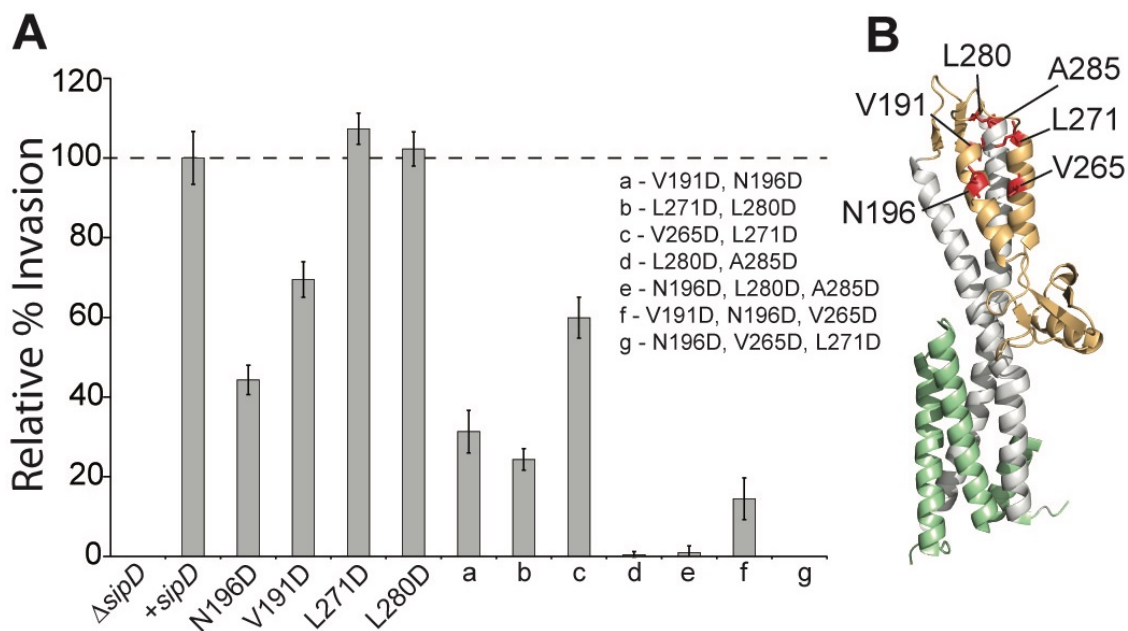


**Fig. 8-6 – *Salmonella* Invasion Assay with SipD Mixed  $\alpha/\beta$  Domain Mutants**

(A) Invasion assay between *Salmonella* Typhimurium strain SL1344 and human intestinal epithelial Henle-407 cells is shown. The *Salmonella sipD*<sup>-</sup> mutant ( $\Delta SipD$ ) was completely non-invasive. Adding back wild-type SipD (+SipD) to the *sipD*<sup>-</sup> *Salmonella* strain complemented invasion. SipD mixed  $\alpha/\beta$  mutations were tested for their ability to decrease invasion. L271D and L280D had no effect on invasion. N196D, V191D, V191D+N196D, L271D+L280D and V265D+L271D had a moderate decrease in invasion. In contrast, L280D+A285, N196D+L280D+A285 or N196D+V265D+L271D completely reduced the ability of *Salmonella* to invade Henle-407 cells. (B) The location of mutants used for invasion on SipD is shown.

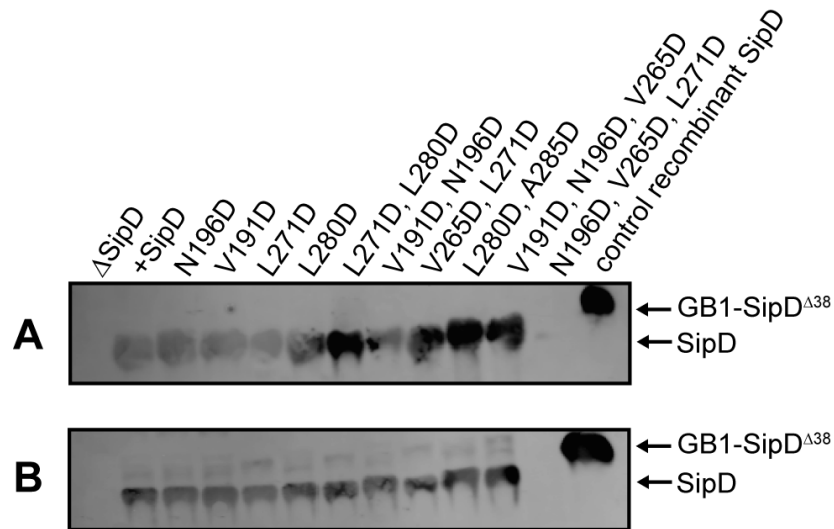


**Fig. 8-7 – Western Immunoblot Analysis of SipD Mixed  $\alpha/\beta$  Domain Mutants**  
 Western immunoblot analysis of (A) cultured supernatants and (B) whole-cell lysates of  $\Delta$ SipD, +SipD, and SipD mutant *Salmonella* Typhimurium strains. Blots were treated with a monoclonal antibody specific to SipD. Recombinant GB1-SipD<sup>Δ38</sup> was used as a positive control.

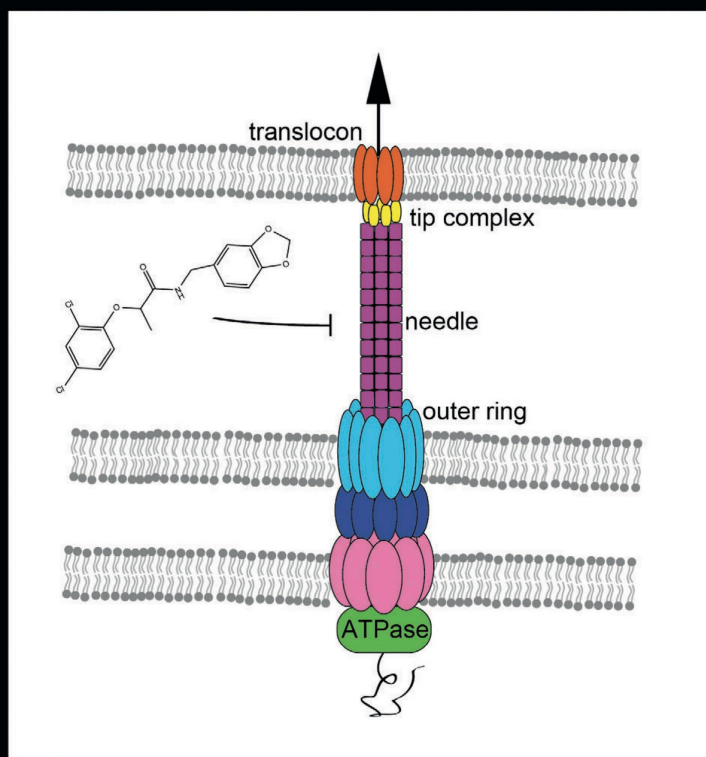
### 8.5. References

1. Lea, W. A. & Simeonov, A. (2011). Fluorescence polarization assays in small molecule screening. *Expert Opin Drug Discov* **6**, 17-32.
2. Kim, Y., Ho, S. O., Gassman, N. R., Korlann, Y., Landorf, E. V., Collart, F. R. & Weiss, S. (2008). Efficient site-specific labeling of proteins via cysteines. *Bioconjug Chem* **19**, 786-91.
3. Chatterjee, S., Zhong, D., Nordhues, B. A., Battaile, K. P., Lovell, S. & De Guzman, R. N. (2011). The crystal structures of the *Salmonella* type III secretion system tip protein SipD in complex with deoxycholate and chenodeoxycholate. *Protein Sci* **20**, 75-86.
4. Poyraz, O., Schmidt, H., Seidel, K., Delissen, F., Ader, C., Tenenboim, H., Goosmann, C., Laube, B., Thunemann, A. F., Zychlinsky, A., Baldus, M., Lange, A., Griesinger, C. & Kolbe, M. (2010). Protein refolding is required for assembly of the type three secretion needle. *Nature Structural & Molecular Biology* **17**, 788-U26.
5. Barta, M. L., Dickenson, N. E., Patil, M., Keightley, A., Wyckoff, G. J., Picking, W. D., Picking, W. L. & Geisbrecht, B. V. (2012). The Structures of Coiled-Coil Domains from Type III Secretion System Translocators Reveal Homology to Pore-Forming Toxins. *Journal of Molecular Biology* **417**, 395-405.
6. Dickenson, N. E., Arizmendi, O., Patil, M. K., Toth, R. T. t., Middaugh, C. R., Picking, W. D. & Picking, W. L. (2013). N-Terminus of IpaB Provides a Potential Anchor to the *Shigella* Type III Secretion System Tip Complex Protein IpaD. *Biochemistry*.

EDITOR-IN-CHIEF DAVID SELWOOD, UK

# CHEMICAL BIOLOGY & DRUG DESIGN

[www.cbdd.org](http://www.cbdd.org)



WILEY  
Blackwell

## Chapter 9. The Bacterial Type III Secretion System as a Target for Developing New Antibiotics

[This chapter is a review on T3SS inhibitors that has been published with the following citation: McShan AC, De Guzman RN. The Bacterial Type III Secretion System as a Target for Developing New Antibiotics. *Chem. Biol. Drug. Des.* 85, 30-42, 2015. A figure from the paper was chosen as the cover for the issue in which it was published, shown on page 173.]

### 9.1. Introduction

Pathogenic Gram-negative bacteria pose a significant global health impact with an estimated 2 million infections and 23,000 deaths per year in just the United States<sup>1</sup>. Examples of these organisms include *Pseudomonas*, *Shigella*, *Salmonella*, *Chlamydia*, enteropathogenic *E. coli* (EPEC), and *Yersinia*. The appearance and rapid evolution of multidrug resistant bacterial strains has become of great concern for public health<sup>2-4</sup>. Unfortunately, the development of new antibiotics presents a difficult challenge. Since 2009 three antibiotics targeting Gram-negative bacteria, though not exclusively, have been approved as the deadline approaches for the initiative of the Infectious Diseases Society of America's for at least 10 new antibiotics by 2020<sup>5</sup>. The rate of entry of new antibiotics into the pipeline is extremely slow<sup>6-9</sup>. This is largely due to several factors, namely, (i) the lack of novel antibiotic targets<sup>10</sup>, (ii) high throughput screens often turn up known targets or novel targets that do not make it past early stages of drug development due to toxicity or off target effects<sup>11</sup>, and (iii) the disinterest of big pharmaceutical companies to discover new antibiotics or conduct clinical trials due the problem of antibiotic resistance and poor investment return has only exacerbated the situation<sup>11,12</sup>. The rapid emergence of multidrug resistant strains coupled with the dearth of novel antibiotics suggests a need for identifying novel targets for development of antibiotics.

Traditional antibiotics often fall into two classes: bactericidal compounds that cause cell death and/or bacteriostatic compounds that inhibit cellular growth<sup>11</sup>. In either case, these drugs often induce a selection pressure on bacteria to develop drug resistance, which is usually obtained via horizontal gene transfer between bacteria or by *de novo* mutations selected by evolution<sup>11</sup>. Targeting virulence pathways of pathogenic bacteria has been suggested as an alternative strategy<sup>13,14</sup>. One current theory is that the use of antivirulence or anti-infective drugs, in contrast to antibiotics, will dampen the selection pressure for the emergence of resistant strains because these drugs do not directly harm the organism<sup>15,16</sup>. Notably, there have been documented cases of resistance to antivirulence drugs, though it has been argued that the existence of such mechanisms for resistance does not suggest it will become a problem in a clinical setting<sup>15</sup>. Another advantage is that because virulence mechanisms are used by pathogenic bacteria, antivirulence drugs are hypothesized to have less of an influence on the host commensal flora when compared to traditional broad spectrum antibiotics<sup>17</sup>.

## **9.2. The Type III Secretion System – Multiple Targeting Opportunities**

### *9.2.1. Overview of the T3SS*

The type III secretion system functions as a conduit for delivery of virulence factors by translocating proteins from the bacterial cytoplasm into the eukaryotic host cell cytoplasm to facilitate infection<sup>18</sup>. The structural component of the T3SS, the needle complex, was first visualized by Galan & coworkers in 1998<sup>19</sup> and since then the structures and functions of many T3SS proteins have been elucidated [reviewed in<sup>20-23</sup>]. T3SS proteins are highly homologous in sequence, structure and function among

different bacteria<sup>20,24,25</sup>. Therefore, protein-protein interactions within the system among different bacteria and with host cells are thought to occur through similar mechanisms. This theory is supported by the similarities observed between the assembly of the *Salmonella* and *Shigella* T3SS needles<sup>26</sup> and conserved structural motifs within the basal structure<sup>27</sup>. Importantly, disruption of many aspects of the T3SS often abolishes pathogenicity. For these reasons, the potential of using the T3SS as a pseudo-broad spectrum antivirulence target is of great interest<sup>13</sup>. As the T3SS is complex, there are many different potential targeting strategies relating to various aspects of the system, which are outlined in **9-1** and described below.

#### *9.2.2. The T3SS Needle Apparatus.*

The T3SS needle apparatus is made up of around 25 different proteins that assemble together to regulate and facilitate the secretion of effector proteins into host cells<sup>21</sup>. Together, the membrane-embedded export apparatus controls the secretion of proteins and anchors the apparatus into the bacterial membrane<sup>28</sup>. An ATPase provides recognition for chaperone/effector complexes and is thought to provide energy for insertion and unfolding of effector proteins into the apparatus<sup>29</sup>. The needle provides a ~25Å diameter extracellular channel for the secretion of partially unfolded effector proteins<sup>26,28</sup>. The tip complex regulates secretion and is a scaffold for translocon assembly<sup>30</sup>. Finally, the translocon creates a pore in host cell membrane<sup>31</sup>. Many subsections of the apparatus, such as the tip, needle, inner ring and outer ring, are assembled by oligomers of a single protein whose affinities are governed by the sum of weak protein-protein interactions<sup>32</sup>. Furthermore, the structures of T3SS proteins are

homologous between different organisms<sup>20</sup>. Two possible modes of targeting the needle apparatus directly could be protein-protein interactions within each component parts such as the needle monomer interactions or interactions between subsections such as the tip-translocon interaction (**Fig. 9-1**). *Salmonella* contains genetic loci that encode three T3SS operons with distinct functions. The *Salmonella pathogenicity island-1* (SPI-1) encoded T3SS is the most studied and functions primarily in the initial invasion of non-phagocytic cells<sup>33,34</sup>. The SPI-2 T3SS is involved in the maintenance of *Salmonella* containing vacuoles and bacterial replication within host cells, though its structure has not been as extensively characterized<sup>35</sup>. In addition, there is a flagellar T3SS (24). Other T3SS families include the Ysc and Ysa T3SS of *Yersinia* and the Sct T3SS of *Chlamydia*<sup>36</sup>.

### 9.2.3. Chaperones and Effectors

T3SS effectors have a wide range of functions within the host cell, but often involve manipulating host cell signaling, secretory trafficking, cytoskeletal dynamics, or the inflammatory response<sup>23,37</sup>. It has been shown that effectors work in concert for infection<sup>38</sup>. Regardless, deletions of many effectors attenuate virulence so they are considered potential drug targets<sup>39-41</sup>. While in the bacterial cytoplasm, effectors are often in complex with chaperone proteins that target them to the export apparatus and protect from aggregation<sup>42,43</sup>. Disrupting chaperone/effector interactions could prevent secretion of effector proteins. However, some effectors, such as YopE and SopE, have been shown to retain partial secretion even the absence of their chaperone binding domain<sup>43,44</sup>.

Therefore, disruption of the chaperone/effector interactions may not necessarily result in a decrease in infectivity.

#### 9.2.4. T3SS Gene Transcription

As stated above, the T3SS is organized into genetic loci whose gene expression is highly regulated by various transcription factors. Transcriptional regulators of both SPI-1<sup>45</sup> and SPI-2<sup>46</sup> loci have been identified in *Salmonella*. T3SS transcriptional regulators have also been characterized in other bacteria, such as *Pseudomonas*<sup>21,47</sup>, *Yersinia*<sup>48</sup> and *Shigella*<sup>49</sup>. Deletions of various T3SS transcription factors lead to the disappearance of the needle apparatuses on the bacterial surface due to essential constituents not being expressed<sup>50</sup>. For this reason, transcription factors are potential drug targets as well.

### 9.3. Literature of T3SS Inhibitors

#### 9.3.1. Salicylidene Acylhydrazides

Many different classes of structurally diverse small molecule compounds have been identified as inhibitors of the T3SS (**Fig. 9-2 & Table 9-1**). The most well studied class of T3SS inhibitors is the salicylidene acylhydrazides (SAHs). One of the first reports comes from Kauppi *et al.*<sup>51,52</sup> where they performed a whole-cell assay screen against T3SS gene expression using a reporter of the effector protein YopE fused with luciferase in *Yersinia*. Out of 9,400 compounds tested, a few compounds were identified, including SAHs. A disadvantage of the assay was that it was based on coupling between Yop effector expression and secretion of the negative regulator LcrQ, therefore it was unclear whether the compounds acted directly against the T3SS<sup>51</sup>. A follow up study

showed that their SAH compounds directly blocked effector secretion of the T3SS in a dose-dependent manner and they were suggested to act at the level of the T3SS machinery<sup>52,53</sup>. SAHs have been shown to broadly inhibit the T3SS of many bacteria genera, including *Chlamydia*<sup>54-57</sup>, *Shigella*<sup>58</sup>, *Salmonella*<sup>59-63</sup> and pathogenic *E. coli*<sup>64-66</sup>. Notably, most SAHs have been shown to have no negative affect on bacterial growth<sup>51,55,61</sup>. Interestingly, some SAHs derivatives inhibited bacterial motility by acting on the flagella<sup>51,59,60</sup>, while others did not affect bacterial motility<sup>64</sup>.

The specific targets within the T3SS itself of many SAHs remain unknown or ambiguous, though putative targets have been suggested. First, it has been suggested that these compounds target the formation or assembly of the SPI-1 needle apparatus directly<sup>58</sup>. Veenendaal *et al.*<sup>58</sup> showed by electron microscopy that *Shigella* needles were reduced in number by ~40% and the distribution of observed needle lengths was altered by one compound. Martinez-Argudo *et al.*<sup>59</sup> isolated SAH resistant *Salmonella* strains with a mutation in FlhA, a flagellar inner membrane protein, suggesting the compounds target the conserved basal body. Second, it has been suggested that SAHs target transcription factors or induce changes in cellular metabolism that affect the T3SS<sup>65,66</sup>. Wang *et al.* used affinity chromatography of conjugated beads of SAHS against *E. coli* lysate and identified three specific binding partners involved in bacterial cellular metabolism, WrbA, Tpx and FolX, and speculated targeting these proteins result in changes in T3SS gene expression by altering cellular metabolism<sup>66</sup>. Importantly, binding was observed between the SAHs and homologs of WrbA and Tpx from other T3SS containing bacterial pathogens such as *Salmonella* and *Pseudomonas*<sup>66</sup>. Since then, the crystal structure of Tpx has been solved and models of its binding to SAHs have been

described<sup>67</sup>. Finally, it has been suggested SAHs interfere with the T3SS through indirect methods, such as altering iron availability due to chelation<sup>61,63</sup>. In *Salmonella* and *Chlamydia*, the addition of exogenous iron attenuates the inhibitory effect of SAHs<sup>55,63,68</sup>. Furthermore, a mutation in *hemG*, an enzyme involved with heme synthesized, conferred resistance to SAHs in *Chlamydia*<sup>69</sup>. In addition, changes in gene expression of iron metabolism related genes has been reported in *Salmonella*, but not observed in *E. coli*, which suggests other mechanisms are at work<sup>63,65</sup>. Recently, a gallium(III)–salicylidene acylhydrazide complex has been shown to disrupt secretion and expression of T3SS proteins in addition to inhibiting biofilm formation in *Pseudomonas*<sup>70</sup>. The current data on SAHs suggest they target the T3SS through multiple mechanisms or that different SAH derivatives inhibit the system by different mechanisms.

### 9.3.2. Thiazolidinones

Another well-studied class of T3SS inhibitors is the thiazolidinones. Felise *et al.*<sup>71</sup> identified thiazolidinone from a whole-cell screen assay in *Salmonella* against protein secretion using a reporter construct of the effector SipA fused to the *Yersinia* phospholipase YplA. Cleavage of a supplied substrate, PED6, by the reporter construct resulted in measurable fluorescence, which was proportional to the amount of the secreted SipA<sup>71</sup>. Out of 92,000 screened compounds, a 2-imino-5-arylidene thiazolidinone was identified as a promising candidate, as it did not affect bacterial growth or T3SS transcription, and therefore was suggested to target formation or assembly of the needle apparatus<sup>71</sup>. The compound was additionally shown to inhibit the T3SS of *Yersinia*, as well as the type II secretion system in *Pseudomonas* and the type IV

pili secretion system of *Francisella*, though it did not target the flagellar-specific T3SS<sup>71</sup>. Because of the broad range of action, it was hypothesized that the thiazolidinones target the conserved outer membrane Secretin protein. A follow up study showed that thiazolidinone dimers inhibited the T3SS more potently and it was suggested that the compounds act along a large oligomeric protein-protein interaction surface<sup>72</sup>.

### 9.3.3. Other Classes of T3SS Inhibitors

Many other chemically and structurally diverse classes of chemical inhibitors that affect the T3SS have been identified (**Fig. 9-2**). Although the specific targets within the T3SS for most of these inhibitors have not been elucidated, the putative targets of a few compounds have been hypothesized. Yop secretion was inhibited by 2,2'-thiobis-(4-methylphenol) through an interaction with the minor translocon protein YopD of *Yersinia*<sup>76</sup>. Unfortunately, this compound was shown to be toxic to eukaryotic cells and requires structural modification to be considered a suitable drug candidate<sup>76</sup>. Mutations in the needle protein PscF of *Pseudomonas* conferred resistance against phenoxyacetamide inhibitors, suggesting PscF as their molecular target<sup>88,89</sup>. However, no biochemical binding assays showing a direct interaction between the two have been reported. Benzimidazoles have been shown to target the T3SS through inhibition of DNA binding by transcription factors such as LcrF in *Yersinia*<sup>79,80</sup> and the *Pseudomonas* homolog ExsA<sup>81</sup>. Similarly, 1-butyl-4-nitromethyl-3-quinolin-2-yl-4H-quinoline inhibited the DNA binding of the *Shigella* transcription factor VirF, which controls transcription of *Shigella* T3SS genes<sup>74</sup>. A variety of compounds have been shown to inhibit ATPases, such as YscN in *Yersinia* and its homolog BsaS in *Burkholderia*<sup>100</sup>. Further, omeprazole

inhibited the ATPase of the SPI-2 T3SS of *Salmonella*, possibly through regulation of nitric oxide production<sup>87</sup>. Pseudolipasin A inhibited phospholipase A<sub>2</sub> activity of the *Pseudomonas* effector ExoU<sup>106</sup>.

There are many small molecule inhibitors without known specific targets within the T3SS as shown in **Table 9-1**. A screen in *Yersinia* by Harmon *et al.*<sup>99</sup> identified various chemically diverse hydrophobic compounds that inhibited translocation of effectors into eukaryotic cells, but not *in vitro* secretion or expression, suggesting they disrupted the formation of a functional translocon or that they inhibited interaction with the host cell. Various compounds showing inhibition of T3SS-mediated hemolysis, such as aurodox and the gaudinomines, have also been identified<sup>78,86</sup>. Other compounds, such as salicylanilides, salicylideneanilines, sulfonylaminobenzanilides, cytosporone B, and citrus flavonoids are hypothesized to broadly inhibit T3SS gene transcription through unknown mechanisms<sup>53,64,84,85,92</sup>.

#### 9.3.4. Non-Small Molecule Inhibitors of T3SS

Non-small molecule inhibitors of T3SS have been reported. These include polymers, proteins and polypeptide mimics. Ohgita *et al.*<sup>107</sup> reported that the proton-motive force dependent rotation of the *Pseudomonas* T3SS was inhibited by the addition of the viscous polymer polyethylene glycol (PEG) 8000 and this was hypothesized to occur by the resistance of physical rotation due to solution viscosity. This hypothesis was further supported by a follow up study showing that other viscous polymers, such as alginate and mucin, inhibited T3SS rotation while low viscosity polymers such as PEG200 do not<sup>101</sup>. PEG derivatives are commonly used excipients in drug formulations

<sup>108</sup> and because these experiments showed a direct correlation between the rotation of the T3SS needle apparatus and secretion of effectors, the addition of viscous polymers such as PEG as excipients to future antivirulence drug formulations is of interest<sup>101,108</sup>.

Proteins and polypeptides have also been reported as inhibitors of T3SS. For example, the glycoprotein Lactoferrin has been shown to decrease virulence of *Salmonella*, *Shigella* and *E. coli* by targeting the T3SS<sup>109-112</sup>. In *Shigella*, Lactoferrin induced the loss and degradation of the translocon proteins IpaB and IpaC at the bacterial surface<sup>111</sup>. Similarly, Lactoferrin caused the loss and degradation of the *E. coli* tip and translocon proteins (EspA, EspB and EspD) at the bacterial surface<sup>109,110,113</sup>. Lactoferrin-mediated inhibition of the T3SS is thought to occur through two mechanisms. First, its ability to bind lipopolysaccharide on the bacterial surface is thought to cause instability of virulence proteins at the bacterial surface by disrupting essential protein-protein interactions<sup>102</sup>. Second, the degradation of T3SS proteins occurs via the intrinsic serine protease activity of Lactoferrins<sup>102</sup>. Additionally, Lactoferrin inhibits infection and has a bacteriostatic effect due to its ability to sequester iron, which is an essential micronutrient needed by many bacterial pathogens<sup>102</sup>.

Polypeptide mimics targeting T3SS components have also been described. In *Chlamydia*, a 28 amino acid polypeptide mimic targeting the CdsN ATPase via its interaction with the putative inner membrane-tethering protein CdsL inhibited bacterial invasion of eukaryotic host cells<sup>104</sup>. In *Salmonella*, Hayward *et al.*<sup>114</sup> showed that a polypeptide derived from the C-terminus of the translocon protein SipB was shown to be a potent inhibitor of the membrane fusion activity of both wild-type SipB and the *Shigella* homolog IpaB *in vitro*. This polypeptide mimic also blocked the entry of

*Salmonella* and *Shigella* into cultured eukaryotic cells<sup>114</sup>. Finally, coiled-coiled peptides designed against the *EPEC* tip protein EspA inhibited T3SS-mediated hemolysis, EspA polymerization and secretion of effector proteins<sup>105</sup>.

### 9.3.5. Small Molecules That Bind T3SS Proteins

Biologically relevant small molecules interact with structural and effector proteins of the T3SS and could potentially be used as scaffolds for drug design. These small molecules include sterols and lipids. Bile salts in the intestines of hosts are thought to act as environmental sensors for infection by *Salmonella* and *Shigella*<sup>115</sup>. In *Shigella*, bile salts increase invasiveness to epithelial cells<sup>116</sup>, while in *Salmonella* bile salts decrease invasiveness<sup>117</sup>. Because the tip protein is present on top of the needle at the bacterial surface prior to host cell contact, it has been suggested to function as a sensor for the host environment by interacting with bile salts<sup>115</sup>. NMR titrations suggested different interaction sites for bile salts such as deoxycholate and chenodeoxycholate on the *Salmonella* SipD and the *Shigella* IpaD tip proteins<sup>118,119</sup>. This is further supported by differences in the binding of deoxycholate in co-crystal structures with SipD<sup>120</sup> or IpaD<sup>121</sup>. Interestingly, binding of bile salts was reported to induce a conformation change in IpaD, but not SipD<sup>121</sup>, which possibly explains the difference in the responses observed between *Salmonella* and *Shigella* in the presence of bile salts.

The translocon proteins interact with sterols, for example, the *Shigella* IpaB translocon protein interacts with cholesterol and sphingolipids on host cell lipid rafts to mediate infection<sup>122,123</sup>. Binding of IpaB to sterol was proposed to cause the disorganization of the Golgi and other recycling networks by altering the distribution of

cholesterol on the cell membrane and the sorting of the eukaryotic cell surface that promoted bacterial uptake<sup>124</sup>. Interaction of cholesterol with homologous translocon proteins in other bacteria such as the *Salmonella* SipB and the *Pseudomonas* PopB/PopD proteins is required for infection<sup>125,126</sup>. Data also suggests interaction of translocon proteins with cholesterol is essential after initial infection. For example, the T3SS effectors IcsB from *Shigella* and BopA from *Burkholderia* bound to cholesterol leading to evasion of autophagy in host cells<sup>127</sup>. In *Salmonella*, the SPI-2 effector SseJ caused esterification of cholesterol to maintain the *Salmonella* containing vacuole<sup>128</sup>. Currently, a detailed mechanism of the molecular interactions of T3SS proteins with cholesterol or sphingolipids and their role in pathogenesis remain to be worked out.

## **9.4. Future Directions**

### *9.4.1. Identification of T3SS Targets*

Drug discovery and development of small molecule inhibitors is lengthy and costly, with a potential drug candidate taking an average of over 10 years and costing millions of dollars to reach the market as an approved drug. The process often begins with a high throughput screen to identify potential hits. This is followed by target identification and validation, often in parallel with structure activity relationships to identify the most potent lead compound. Next, *in vivo* animal models are tested. If successful, pharmacokinetics and dynamics are analyzed and product is formulated as needed. Finally, clinical trials are performed.

The most pressing concern in the field is the identification and characterization of specific targets within the many protein components of the T3SS. Even with the most

well studied classes of inhibitors, SAHs and thiazolidinones, the specific T3SS targets remain unknown or ambiguous. This is likely due to the fact that most high throughput screens utilized assays that broadly monitored the secretion of effectors or gene transcription rather than using a targeted approach, such as a specific protein-protein interaction involved in the assembly of the T3SS needle apparatus. In addition, derivatives within a class of T3SS inhibitors have unique chemical structure that could potentially interact with non-T3SS targets in other organisms leading to differences in potency or mechanisms of action. This could explain the complex nature of the results observed in the literature of SAHs. A targeted and more specific approach for future high throughput screens could help solve this problem. Many binding assays have been developed to monitor protein-protein interactions of the structural proteins of the T3SS needle apparatus that could be adapted for drug screening. For example, fluorescence polarization and FRET assays show binding of the tip and translocon protein in *Shigella*<sup>129</sup> and NMR spectroscopy showed binding of the tip and needle protein in *Salmonella*<sup>130</sup>.

#### 9.4.2. SAR Design

Structure-activity relationships (SAR) provide a direct link between the chemical structure of a molecule and its observed activity to create a potent lead compound. The identification of a target facilitates SAR studies especially when the mechanism of interaction is known, although they can be performed in the absence of a target<sup>131</sup>. SAR studies have been initiated for a few T3SS inhibitor classes and extensively with SAHs. The data from SAR analysis of SAHs is complex and difficult to interpret. The salicylic

phenol group is necessary for inhibiting activity, but substitutions in other positions are generally tolerable<sup>52,132</sup>. SAR based optimization of future SAHs compounds could be complicated if they target T3SS through multiple mechanisms as suggested in the literature<sup>52,132</sup>. SAR data on other classes of small molecule inhibitors of T3SS are available as well. Thiazolidinone analogs show sensitivity against substitutions at the imino N-2, amido N-3, and 5-arylidene groups and SAR analysis led to the identification of a more soluble derivative<sup>71</sup>. Hydrophobicity and lipophilicity were shown to be important factors for inhibition of the T3SS by sulfonylaminobenzanilides<sup>53</sup>. Cytosporone derivatives with extensive carbon chains containing a phenyl acetic acetate ester group were most potent<sup>85</sup>. Derivatives of 8-hydroxyquinoline required a fused pyridine ring and an aromatic hydroxyl group for inhibition of T3SS function<sup>77</sup>. Benzimidazoles are sensitive to substitutions in the linker ring and the middle phenyl ring<sup>79</sup>. Finally, phenoxyacetamides were sensitive to changes on the A ring (where 2,4-dichlorophenyl is preferred) and their stereocenter was critical for T3SS inhibition and SAR analysis led to the identification of an 8-fold more potent compound than found in initial screens<sup>88,89</sup>.

#### 9.4.3. Animal Models, Pharmacokinetics and Formulation

Preliminary studies using animal models have shown the effectiveness of different T3SS inhibitors against infection *in vivo* and validated the approach of targeting T3SS<sup>61,78,80,95</sup>. However, evaluation of pharmacokinetic parameters and formulation of potential drug molecule for delivery into host organisms is an essential step of drug discovery. Challenges with small molecule drug development include efflux, metabolism

and membrane permeability. Notably, most of the literature describes relatively small and hydrophobic compounds that were identified through whole-cell screening, and therefore these compounds are likely to be able to pass through cellular membranes. A study examined the pharmacokinetics of SAHs in a mouse model<sup>95</sup>. Many compounds were shown to have a short half-life, suggesting rapid metabolism or clearance, as well as problems with compound stability and solubility<sup>95</sup>. Attempts at formulation with the non-ionic surfactant Poloxamer 407 and the polysaccharide (2-hydroxypropyl)- $\beta$ -cyclodextrin<sup>95,133</sup> were unsuccessful in improving efficacy. The ability of academia and the pharmaceutical industry to work together will speed the entry of new drugs into the pipeline by allowing for more extensive SAR optimization, pharmacokinetic analysis, formulation and *in vivo* testing of small molecule compounds<sup>134</sup>.

## 9.5. Conclusion

The clinical application of small molecule inhibitors of bacterial virulence as anti-infectives remains to be exploited. Small molecule T3SS inhibitors that have been identified could be used to treat bacterial infection on their own because most of them are non-toxic to eukaryotic cells while still preventing secretion of effector proteins. A drawback of virulence drugs is that they will not inhibit bacterial proliferation and therefore the bacteria must be cleared by other means such as the host immune system. In contrast, these drugs may lead to increased immune cell memory. It is also possible that antivirulence drugs will need to be used in combination with other antibiotics for clearance. The discovery and validity of many classes of small molecule inhibitors targeting different aspects of the type III secretion systems of Gram-negative bacteria

suggest that it is a promising approach that will be applicable to clinical settings in the future.

Compound	Structure # (Figure 2)	Organism	T3SS Target	Reference
(-)-Hopeaphenol	4	<i>Yersinia, Pseudomonas, Chlamydia</i>	?	73
1-butyl-4-nitromethyl-3-quinolin-2-yl-4H-quinoline [SE-1]	10	<i>Shigella</i>	VirF / transcription factor	74
2-imino-5-arylidene thiazolidinone	13	<i>Yersinia, Salmonella</i>  also inhibits T2S of <i>Pseudomonas</i> and T4-Pilli Secretion of <i>Francisella</i>	Secretin?	71,72,75
2,2'-thiobis-(4-methylphenol)	14	<i>Yersinia Pseudomonas</i>	YopD / translocon	76
8-hydroxyquinolines [INP1750]	1	<i>Yersinia, Chlamydia</i>	?	77
Aurodox	5	<i>EPEC, Citrobacter</i>	?	78
Benzimidazole		<i>Yersinia Pseudomonas</i>	LcrF / transcription factor  ExsA / transcription factor	79  80,81
Caminoside A-D	7	<i>EPEC</i>	?	82,83
Citrus Flavonoids	11	<i>Vibrio</i>	?	84
Cytosporone B	8	<i>Salmonella</i>	?	85
Gaudinomine A-D	12	<i>EPEC</i>	?	86
Omeprazole	15	<i>Salmonella</i>	ATPase inhibitor, effects through nitric oxide production	62,87
Phenoxyacetamide	16	<i>Pseudomonas</i>	PscF / needle protein	88,89
Piericidin A1	3	<i>Yersinia</i>	?	90
Pseudoceramine	18	<i>Yersinia</i>	?	91
Pseudolipasin A	9	<i>Pseudomonas</i>	ExoU / effector	10
Salicylanilide	20	<i>Yersinia</i>	?	51,92,93
Salicylidene Acylhydrazide	2	<i>Chlamydia</i>  <i>Yersinia</i>  <i>Shigella</i>  <i>Salmonella</i>  <i>EPEC</i>	<i>HemG</i> / heme metabolism  ?  needle assembly?  FlhA / flagellar inner membrane protein  ?, possibly due to non-T3SS cell metabolism enzymes, such as WrbA/Tpx/FolX	54-57,94,95  51,52  58  59-63  64-66
Salicylideneaniline	19	<i>Yersinia, EPEC</i>	?	64
Sulfonylaminobenzanilide	17	<i>Yersinia</i>	?	51,53
Thiohydrazones of Thiohydrazide	6	<i>Chlamydia</i>	?	96
Various Compounds	not shown	<i>Yersinia, EPEC</i>	?	97,98
Various Compounds	not shown	<i>Yersinia</i>	?	99
Various Compounds	not shown	<i>Yersinia Burkholderia</i>	YscN / ATPase BsaS / ATPase	100
Viscous Polymers [PEG8000 / Alginate / Mucin]	not shown	<i>Pseudomonas</i>	inhibits T3SS apparatus rotation	101
Lactoferrin	not shown	<i>Shigella, EPEC, Salmonella</i>	Degradation of tip and translocon proteins	102
Polypeptide Mimics	not shown	<i>Salmonella/Shigella EPEC</i>	SipB, IpaB / Translocon CdsN ATPase EspA / tip	103 104 105

**Table 9-1 – T3SS Inhibitors and Their Putative Targets**

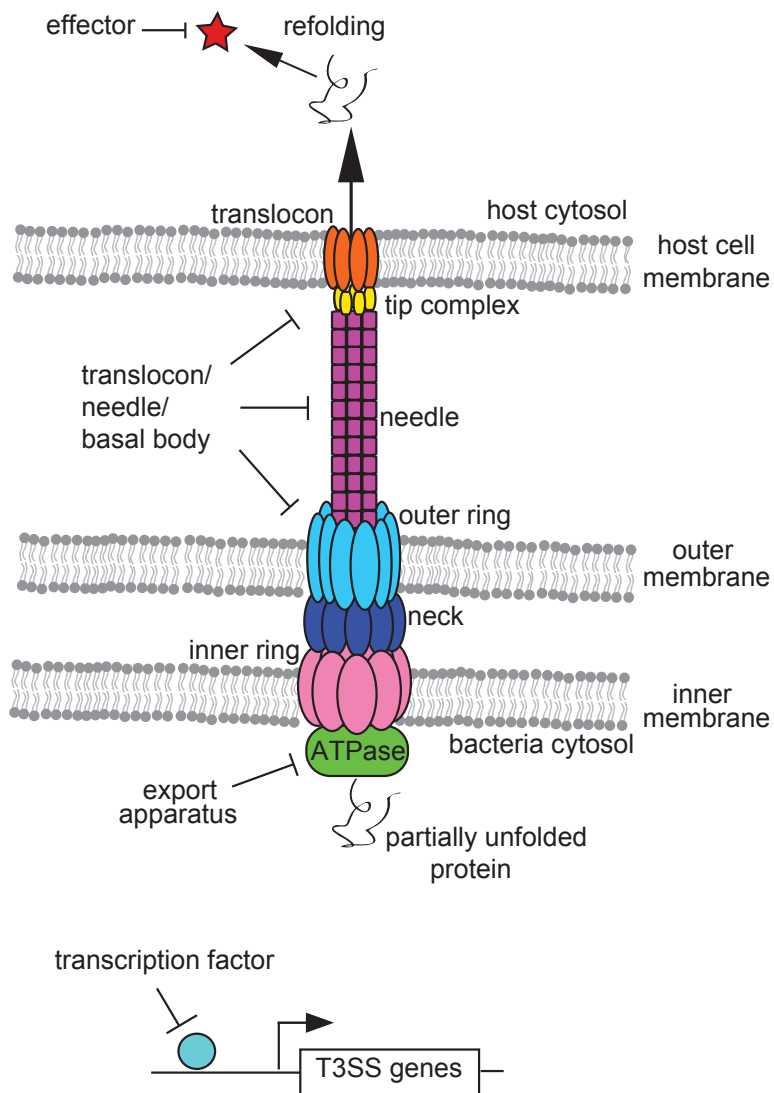


**Fig. 9-1 – Strategies for Inhibiting the T3SS**

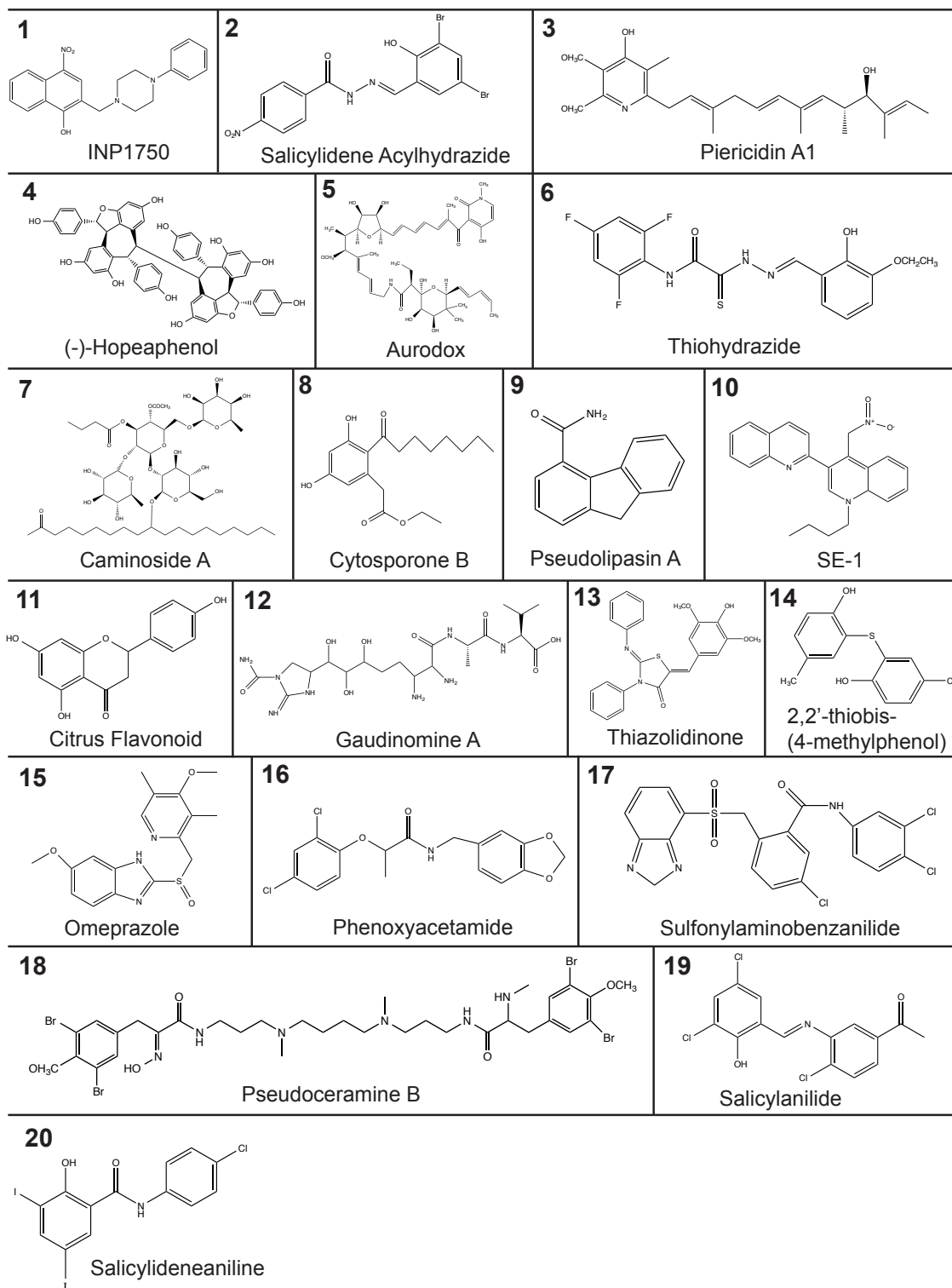


Fig. 9-2 – T3SS Inhibitor Structures

## 9.6. References

1. CDC. Antibiotic Resistance Threats in the United States, 2013. ed.
2. Allen HK, Donato J, Wang HH, Cloud-Hansen KA, Davies J, Handelsman J 2010. Call of the wild: antibiotic resistance genes in natural environments. *Nat Rev Microbiol* 8(4):251-259.
3. Wellington EMH, Boxall ABA, Cross P, Feil EJ, Gaze WH, Hawkey PM, Johnson-Rollings AS, Jones DL, Lee NM, Otten W, Thomas CM, Williams AP 2013. The role of the natural environment in the emergence of antibiotic resistance in Gram-negative bacteria. *Lancet Infectious Diseases* 13(2):155-165.
4. Davies J, Davies D 2010. Origins and Evolution of Antibiotic Resistance. *Microbiology and Molecular Biology Reviews* 74(3):417-+.
5. Gilbert DN, Guidos RJ, Boucher HW, Talbot GH, Spellberg B, Edwards JE, Scheld WM, Bradley JS, Bartlett JG, Amer IDS 2010. The 10 x '20 Initiative: Pursuing a Global Commitment to Develop 10 New Antibacterial Drugs by 2020. *Clinical Infectious Diseases* 50(8):1081-1083.
6. Payne DJ, Gwynn MN, Holmes DJ, Pompliano DL 2007. Drugs for bad bugs: confronting the challenges of antibacterial discovery. *Nat Rev Drug Discov* 6(1):29-40.
7. Butler MS, Blaskovich MA, Cooper MA 2013. Antibiotics in the clinical pipeline in 2013. *J Antibiot (Tokyo)* 66(10):571-591.
8. Schaberle TF, Hack IM 2014. Overcoming the current deadlock in antibiotic research. *Trends Microbiol* 22(4):165-167.
9. Bassetti M, Merelli M, Temperoni C, Astilean A 2013. New antibiotics for bad bugs: where are we? *Annals of Clinical Microbiology and Antimicrobials* 12.
10. Lee JH, Jeong SH, Cha SS, Lee SH 2007. A lack of drugs for antibiotic-resistant gram-negative bacteria. *Nature Reviews Drug Discovery* 6(11):938-939.
11. Coates ARM, Halls G, Hu YM 2011. Novel classes of antibiotics or more of the same? *British Journal of Pharmacology* 163(1):184-194.
12. Projan SJ 2003. Why is big Pharma getting out of antibacterial drug discovery? *Current Opinion in Microbiology* 6(5):427-430.
13. Baron C 2010. Antivirulence drugs to target bacterial secretion systems. *Current Opinion in Microbiology* 13(1):100-105.
14. Keyser P, Elofsson M, Rosell S, Wolf-Watz H 2008. Virulence blockers as alternatives to antibiotics: type III secretion inhibitors against Gram-negative bacteria. *Journal of Internal Medicine* 264(1):17-29.
15. Allen RC, Popat R, Diggle SP, Brown SP 2014. Targeting virulence: can we make evolution-proof drugs? *Nature Reviews Microbiology* 12(4):300-308.
16. Clatworthy AE, Pierson E, Hung DT 2007. Targeting virulence: a new paradigm for antimicrobial therapy. *Nature Chemical Biology* 3(9):541-548.
17. Duncan MC, Linington RG, Auerbuch V 2012. Chemical Inhibitors of the Type Three Secretion System: Disarming Bacterial Pathogens. *Antimicrobial Agents and Chemotherapy* 56(11):5433-5441.
18. Cornelis GR 2006. The type III secretion injectisome. *Nature Reviews Microbiology* 4(11):811-825.

19. Kubori T, Matsushima Y, Nakamura D, Uralil J, Lara-Tejero M, Sukhan A, Galan JE, Aizawa S 1998. Supramolecular structure of the Salmonella typhimurium type III protein secretion system. *Science* 280(5363):602-605.
20. Chatterjee S, Chaudhury S, McShan AC, Kaur K, De Guzman RN 2013. Structure and Biophysics of Type III Secretion in Bacteria. *Biochemistry* 52(15):2508-2517.
21. Izore T, Job V, Dessen A 2011. Biogenesis, Regulation, and Targeting of the Type III Secretion System. *Structure* 19(5):603-612.
22. Abrusci P, McDowell MA, Lea SM, Johnson S 2014. Building a secreting nanomachine: a structural overview of the T3SS. *Curr Opin Struct Biol* 25C:111-117.
23. Dean P 2011. Functional domains and motifs of bacterial type III effector proteins and their roles in infection. *Fems Microbiology Reviews* 35(6):1100-1125.
24. Rosqvist R, Hakansson S, Forsberg A, Wolf-Watz H 1995. Functional conservation of the secretion and translocation machinery for virulence proteins of yersiniae, salmonellae and shigellae. *EMBO J* 14(17):4187-4195.
25. Hermant D, Menard R, Arricau N, Parsot C, Popoff MY 1995. Functional Conservation of the Salmonella and Shigella Effectors of Entry into Epithelial-Cells. *Molecular Microbiology* 17(4):781-789.
26. Demers JP, Sgourakis NG, Gupta R, Loquet A, Giller K, Riedel D, Laube B, Kolbe M, Baker D, Becker S, Lange A 2013. The Common Structural Architecture of Shigella flexneri and Salmonella typhimurium Type Three Secretion Needles. *Plos Pathogens* 9(3).
27. Spreter T, Yip CK, Sanowar S, Andre I, Kimbrough TG, Vuckovic M, Pfuetzner RA, Deng WY, Yu AC, Finlay BB, Baker D, Miller SI, Strynadka NCJ 2009. A conserved structural motif mediates formation of the periplasmic rings in the type III secretion system. *Nature Structural & Molecular Biology* 16(5):468-476.
28. Abrusci P, Vergara-Irigaray M, Johnson S, Beeby MD, Hendrixson DR, Roversi P, Friede ME, Deane JE, Jensen GJ, Tang CM, Lea SM 2013. Architecture of the major component of the type III secretion system export apparatus. *Nat Struct Mol Biol* 20(1):99-104.
29. Zarivach R, Vuckovic M, Deng WY, Finlay BB, Strynadka NCJ 2007. Structural analysis of a prototypical ATPase from the type III secretion system. *Nature Structural & Molecular Biology* 14(2):131-137.
30. Veenendaal AKJ, Hodgkinson JL, Schwarzer L, Stabat D, Zenk SF, Blocker AJ 2007. The type III secretion system needle tip complex mediates host cell sensing and translocon insertion. *Molecular Microbiology* 63(6):1719-1730.
31. Mattei PJ, Faudry E, Job V, Izore T, Attree I, Dessen A 2011. Membrane targeting and pore formation by the type III secretion system translocon. *Febs Journal* 278(3):414-426.
32. Deeds EJ, Bachman JA, Fontana W 2012. Optimizing ring assembly reveals the strength of weak interactions. *Proceedings of the National Academy of Sciences of the United States of America* 109(7):2348-2353.
33. Galan JE, Curtiss R 1989. Cloning and Molecular Characterization of Genes Whose Products Allow Salmonella-Typhimurium to Penetrate Tissue-Culture Cells. *Proceedings of the National Academy of Sciences of the United States of America* 86(16):6383-6387.

34. Egan F, Barret M, O'Gara F 2014. The SPI-1-like Type III secretion system: more roles than you think. *Frontiers in Plant Science* 5.
35. Figueira R, Holden DW 2012. Functions of the Salmonella pathogenicity island 2 (SPI-2) type III secretion system effectors. *Microbiology-Sgm* 158:1147-1161.
36. Barret M, Egan F, O'Gara F 2013. Distribution and diversity of bacterial secretion systems across metagenomic datasets. *Environmental Microbiology Reports* 5(1):117-126.
37. Galan JE 2007. SnapShot: Effector proteins of type III secretion systems. *Cell* 130(1):192-U195.
38. Zhou DG, Galan J 2001. Salmonella entry into host cells: the work in concert of type III secreted effector proteins. *Microbes and Infection* 3(14-15):1293-1298.
39. Figueira R, Watson KG, Holden DW, Helaine S 2013. Identification of Salmonella Pathogenicity Island-2 Type III Secretion System Effectors Involved in Intramacrophage Replication of *S. enterica* Serovar Typhimurium: Implications for Rational Vaccine Design. *Mbio* 4(2).
40. Kidwai AS, Mushamiri I, Niemann GS, Brown RN, Adkins JN, Heffron F 2013. Diverse Secreted Effectors Are Required for Salmonella Persistence in a Mouse Infection Model. *Plos One* 8(8).
41. Coburn B, Sekirov I, Finlay BB 2007. Type III secretion systems and disease. *Clinical Microbiology Reviews* 20(4):535-+.
42. Akeda Y, Galan JE 2005. Chaperone release and unfolding of substrates in type III secretion. *Nature* 437(7060):911-915.
43. Lee SH, Galan JE 2004. Salmonella type III secretion-associated chaperones confer secretion-pathway specificity. *Molecular Microbiology* 51(2):483-495.
44. Boyd AP, Lambermont I, Cornelis GR 2000. Competition between the Yops of *Yersinia enterocolitica* for delivery into eukaryotic cells: Role of the SycE chaperone binding domain of YopE. *Journal of Bacteriology* 182(17):4811-4821.
45. Ellermeier JR, Slauch JM 2007. Adaptation to the host environment: regulation of the SPI1 type III secretion system in *Salmonella enterica* serovar Typhimurium. *Current Opinion in Microbiology* 10(1):24-29.
46. Osborne SE, Coombes BK 2011. Transcriptional Priming of Salmonella Pathogenicity Island-2 Precedes Cellular Invasion. *Plos One* 6(6).
47. Yahr TL, Wolfgang MC 2006. Transcriptional regulation of the *Pseudomonas aeruginosa* type III secretion system. *Molecular Microbiology* 62(3):631-640.
48. Li LM, Yan H, Feng LP, Li YL, Lu P, Hu YB, Chen SY 2014. LcrQ Blocks the Role of LcrF in Regulating the Ysc-Yop Type III Secretion Genes in *Yersinia pseudotuberculosis*. *Plos One* 9(3).
49. Dorman CJ, Porter ME 1998. The *Shigella* virulence gene regulatory cascade: a paradigm of bacterial gene control mechanisms. *Molecular Microbiology* 29(3):677-684.
50. Sukhan A, Kubori T, Wilson J, Galan JE 2001. Genetic analysis of assembly of the *Salmonella enterica* serovar typhimurium type III secretion-associated needle complex. *Journal of Bacteriology* 183(4):1159-1167.
51. Kauppi AM, Nordfelth R, Uvell H, Wolf-Watz H, Elofsson M 2003. Targeting bacterial virulence: inhibitors of type III secretion in *Yersinia*. *Chem Biol* 10(3):241-249.

52. Nordfelth R, Kauppi AM, Norberg HA, Wolf-Watz H, Elofsson M 2005. Small-molecule inhibitors specifically targeting type III secretion. *Infect Immun* 73(5):3104-3114.
53. Kauppi AM, Andersson CD, Norberg HA, Sundin C, Linusson A, Elofsson M 2007. Inhibitors of type III secretion in *Yersinia*: design, synthesis and multivariate QSAR of 2-arylsulfonylamino-benzanilides. *Bioorg Med Chem* 15(22):6994-7011.
54. Muschiol S, Normark S, Henriques-Normark B, Subtil A 2009. Small molecule inhibitors of the *Yersinia* type III secretion system impair the development of *Chlamydia* after entry into host cells. *Bmc Microbiology* 9.
55. Slepentin A, Chu H, Elofsson M, Keyser P, Peterson EM 2011. Protection of Mice From a *Chlamydia trachomatis* Vaginal Infection Using a Salicylidene Acylhydrazide, a Potential Microbicide. *Journal of Infectious Diseases* 204(9):1313-1320.
56. Bailey L, Gylfe A, Sundin C, Muschiol S, Elofsson M, Nordstrom P, Henriques-Normark B, Lugert R, Waldenstrom A, Wolf-Watz H, Bergstrom S 2007. Small molecule inhibitors of type III secretion in *Yersinia* block the *Chlamydia pneumoniae* infection cycle. *Febs Letters* 581(4):587-595.
57. Muschiol S, Bailey L, Gylfe A, Sundin C, Hultenby K, Bergstrom S, Elofsson M, Wolf-Watz H, Normark S, Henriques-Normark B 2006. A small-molecule inhibitor of type III secretion inhibits different stages of the infectious cycle of *Chlamydia trachomatis*. *Proc Natl Acad Sci U S A* 103(39):14566-14571.
58. Veenendaal AKJ, Sundin C, Blocker AJ 2009. Small-Molecule Type III Secretion System Inhibitors Block Assembly of the *Shigella* Type III Secretion. *Journal of Bacteriology* 191(2):563-570.
59. Martinez-Argudo I, Veenendaal AK, Liu X, Roehrich AD, Ronessen MC, Franzoni G, van Rietschoten KN, Morimoto YV, Saijo-Hamano Y, Avison MB, Studholme DJ, Namba K, Minamino T, Blocker AJ 2013. Isolation of *Salmonella* Mutants Resistant to the Inhibitory Effect of Salicylidene acylhydrazides on Flagella-Mediated Motility. *PLoS One* 8(1):e52179.
60. Negrea A, Bjur E, Ygberg SE, Elofsson M, Wolf-Watz H, Rhen M 2007. Salicylidene acylhydrazides that affect type III protein secretion in *Salmonella enterica* serovar Typhimurium. *Antimicrobial Agents and Chemotherapy* 51(8):2867-2876.
61. Hudson DL, Layton AN, Field TR, Bowen AJ, Wolf-Watz H, Elofsson M, Stevens MP, Galyov EE 2007. Inhibition of type III secretion in *Salmonella enterica* serovar typhimurium by small-molecule inhibitors. *Antimicrobial Agents and Chemotherapy* 51(7):2631-2635.
62. Puiac S, Sem XH, Negrea A, Rhen M 2011. Small-molecular virulence inhibitors show divergent and immunomodulatory effects in infection models of *Salmonella enterica* serovar Typhimurium. *International Journal of Antimicrobial Agents* 38(5):409-416.
63. Layton AN, Hudson DL, Thompson A, Hinton JC, Stevens JM, Galyov EE, Stevens MP 2010. Salicylidene acylhydrazide-mediated inhibition of type III secretion system-1 in *Salmonella enterica* serovar Typhimurium is associated with iron restriction and can be reversed by free iron. *FEMS Microbiol Lett* 302(2):114-122.

64. Gauthier A, Robertson ML, Lowden M, Ibarra JA, Puente JL, Finlay BB 2005. Transcriptional inhibitor of virulence factors in enteropathogenic *Escherichia coli*. *Antimicrobial Agents and Chemotherapy* 49(10):4101-4109.
65. Tree JJ, Wang D, McNally C, Mahajan A, Layton A, Houghton I, Elofsson M, Stevens MP, Gally DL, Roe AJ 2009. Characterization of the effects of salicylidene acylhydrazide compounds on type III secretion in *Escherichia coli* O157:H7. *Infect Immun* 77(10):4209-4220.
66. Wang D, Zetterstrom CE, Gabrielsen M, Beckham KSH, Tree JJ, Macdonald SE, Byron O, Mitchell TJ, Gally DL, Herzyk P, Mahajan A, Uvell H, Burchmore R, Smith BO, Elofsson M, Roe AJ 2011. Identification of Bacterial Target Proteins for the Salicylidene Acylhydrazide Class of Virulence-blocking Compounds. *Journal of Biological Chemistry* 286(34):29922-29931.
67. Gabrielsen M, Beckham KS, Feher VA, Zetterstrom CE, Wang D, Muller S, Elofsson M, Amaro RE, Byron O, Roe AJ 2012. Structural characterisation of Tpx from *Yersinia pseudotuberculosis* reveals insights into the binding of salicylidene acylhydrazide compounds. *PLoS One* 7(2):e32217.
68. Slepentin A, Enquist PA, Hagglund U, de la Maza LM, Elofsson M, Peterson EM 2007. Reversal of the antichlamydial activity of putative type III secretion inhibitors by iron. *Infect Immun* 75(7):3478-3489.
69. Engstrom P, Nguyen BD, Normark J, Nilsson I, Bastidas RJ, Gylfe A, Elofsson M, Fields KA, Valdivia RH, Wolf-Watz H, Bergstrom S 2013. Mutations in hemG Mediate Resistance to Salicylidene Acylhydrazides, Demonstrating a Novel Link between Protoporphyrinogen Oxidase (HemG) and *Chlamydia trachomatis* Infectivity. *Journal of Bacteriology* 195(18):4221-4230.
70. Rzhepishevskaya O, Hakobyan S, Ekstrand-Hammarstrom B, Nygren Y, Karlsson T, Bucht A, Elofsson M, Boily JF, Ramstedt M 2014. The gallium(III)-salicylidene acylhydrazide complex shows synergistic anti-biofilm effect and inhibits toxin production by *Pseudomonas aeruginosa*. *J Inorg Biochem* 138C:1-8.
71. Felise HB, Nguyen HV, Pfuetzner RA, Barry KC, Jackson SR, Blanc MP, Bronstein PA, Kline T, Miller SI 2008. An Inhibitor of Gram-Negative Bacterial Virulence Protein Secretion. *Cell Host & Microbe* 4(4):325-336.
72. Kline T, Barry KC, Jackson SR, Felise HB, Nguyen HV, Miller SI 2009. Tethered thiazolidinone dimers as inhibitors of the bacterial type III secretion system. *Bioorganic & Medicinal Chemistry Letters* 19(5):1340-1343.
73. Zetterstrom CE, Hasselgren J, Salin O, Davis RA, Quinn RJ, Sundin C, Elofsson M 2013. The Resveratrol Tetramer (-)-Hopeaphenol Inhibits Type III Secretion in the Gram-Negative Pathogens *Yersinia pseudotuberculosis* and *Pseudomonas aeruginosa*. *PLoS One* 8(12):e81969.
74. Koppolu V, Osaka I, Skredenske JM, Kettle B, Hefty PS, Li JQ, Egan SM 2013. Small-Molecule Inhibitor of the *Shigella flexneri* Master Virulence Regulator VirF. *Infection and Immunity* 81(11):4220-4231.
75. Kline T, Felise HB, Barry KC, Jackson SR, Nguyen HV, Miller SI 2008. Substituted 2-Imino-5-arylidenethiazolidin-4-one Inhibitors of Bacterial Type III Secretion. *Journal of Medicinal Chemistry* 51(22):7065-7074.

76. Jessen DL, Bradley DS, Nilles ML 2014. A Type III Secretion System Inhibitor Targets YopD while Revealing Differential Regulation of Secretion in Calcium-Blind Mutants of *Yersinia pestis*. *Antimicrobial Agents and Chemotherapy* 58(2):839-850.
77. Enquist PA, Gylfe A, Hagglund U, Lindstrom P, Norberg-Scherman H, Sundin C, Elofsson M 2012. Derivatives of 8-hydroxyquinoline-antibacterial agents that target intra- and extracellular Gram-negative pathogens. *Bioorganic & Medicinal Chemistry Letters* 22(10):3550-3553.
78. Kimura K, Iwatsuki M, Nagai T, Matsumoto A, Takahashi Y, Shiomi K, Omura S, Abe A 2011. A small-molecule inhibitor of the bacterial type III secretion system protects against in vivo infection with *Citrobacter rodentium*. *J Antibiot (Tokyo)* 64(2):197-203.
79. Kim OK, Garrity-Ryan LK, Bartlett VJ, Grier MC, Verma AK, Medjanis G, Donatelli JE, Macone AB, Tanaka SK, Levy SB, Alekshun MN 2009. N-hydroxybenzimidazole inhibitors of the transcription factor LcrF in *Yersinia*: novel antivirulence agents. *J Med Chem* 52(18):5626-5634.
80. Garrity-Ryan LK, Kim OK, Balada-Llasat JM, Bartlett VJ, Verma AK, Fisher ML, Castillo C, Songsungthong W, Tanaka SK, Levy SB, Mecsas J, Alekshun MN 2010. Small molecule inhibitors of LcrF, a *Yersinia pseudotuberculosis* transcription factor, attenuate virulence and limit infection in a murine pneumonia model. *Infect Immun* 78(11):4683-4690.
81. Grier MC, Garrity-Ryan LK, Bartlett VJ, Klausner KA, Donovan PJ, Dudley C, Alekshun MN, Tanaka SK, Draper MP, Levy SB, Kim OK 2010. N-Hydroxybenzimidazole inhibitors of ExsA MAR transcription factor in *Pseudomonas aeruginosa*: In vitro anti-virulence activity and metabolic stability. *Bioorganic & Medicinal Chemistry Letters* 20(11):3380-3383.
82. Linington RG, Robertson M, Gauthier A, Finlay BB, van Soes R, Andersen RJ 2002. Caminoside A, an antimicrobial glycolipid isolated from the marine sponge *Caminus sphaeroconia*. *Organic Letters* 4(23):4089-4092.
83. Linington RG, Robertson M, Gauthier A, Finlay BB, MacMillan JB, Molinski TF, van Soest R, Andersen RJ 2006. Caminosides B-D, antimicrobial glycolipids isolated from the marine sponge *Caminus sphaeroconia*. *J Nat Prod* 69(2):173-177.
84. Vikram A, Jayaprakasha GK, Jesudhasan PR, Pillai SD, Patil BS 2010. Suppression of bacterial cell-cell signalling, biofilm formation and type III secretion system by citrus flavonoids. *Journal of Applied Microbiology* 109(2):515-527.
85. Li JF, Lv C, Sun WY, Li ZY, Han XW, Li YY, Shen YM 2013. Cytosporone B, an Inhibitor of the Type III Secretion System of *Salmonella enterica* Serovar Typhimurium. *Antimicrobial Agents and Chemotherapy* 57(5):2191-2198.
86. Iwatsuki M, Uchida R, Yoshijima H, Ui H, Shiomi K, Kim YP, Hirose T, Sunazuka T, Abe A, Tomoda H, Omura S 2008. Guadinomines, Type III secretion system inhibitors, produced by *Streptomyces* sp K01-0509. *Journal of Antibiotics* 61(4):230-236.
87. Puiac S, Negrea A, Richter-Dahlfors A, Plant L, Rhen M 2009. Omeprazole antagonizes virulence and inflammation in *Salmonella enterica*-infected RAW264.7 cells. *Antimicrob Agents Chemother* 53(6):2402-2409.
88. Aiello D, Williams JD, Majgier-Baranowska H, Patel I, Peet NP, Huang J, Lory S, Bowlin TL, Moir DT 2010. Discovery and Characterization of Inhibitors of

- Pseudomonas aeruginosa* Type III Secretion. *Antimicrobial Agents and Chemotherapy* 54(5):1988-1999.
89. Bowlin NO, Williams JD, Knoten CA, Torhan MC, Tashjian TF, Li B, Aiello D, Mecsas J, Hauser AR, Peet NP, Bowlin TL, Moir DT 2014. Mutations in the *Pseudomonas aeruginosa* needle protein gene *pscF* confer resistance to phenoxyacetamide inhibitors of the type III secretion system. *Antimicrob Agents Chemother* 58(4):2211-2220.
90. Duncan MC, Wong WR, Dupzyk AJ, Bray WM, Linington RG, Auerbuch V 2014. An NF-kappa B-Based High-Throughput Screen Identifies Piericidins as Inhibitors of the *Yersinia pseudotuberculosis* Type III Secretion System. *Antimicrobial Agents and Chemotherapy* 58(2):1118-1126.
91. Yin S, Davis RA, Shelper T, Sykes ML, Avery VM, Elofsson M, Sundin C, Quinn RJ 2011. Pseudoceramines A-D, new antibacterial bromotyrosine alkaloids from the marine sponge *Pseudoceratina* sp. *Org Biomol Chem* 9(19):6755-6760.
92. Kauppi AM, Nordfelth R, Hagglund U, Wolf-Watz H, Elofsson M 2003. Salicylanilides are potent inhibitors of type III secretion in *Yersinia*. *Genus Yersinia: Entering the Functional Genomic Era* 529:97-100.
93. Dahlgren MK, Kauppi AM, Olsson IM, Linusson A, Elofsson M 2007. Design, synthesis, and multivariate quantitative structure-activity relationship of salicylanilides--potent inhibitors of type III secretion in *Yersinia*. *J Med Chem* 50(24):6177-6188.
94. Wolf K, Betts HJ, Chellas-Gery B, Hower S, Linton CN, Fields KA 2006. Treatment of *Chlamydia trachomatis* with a small molecule inhibitor of the *Yersinia* type III secretion system disrupts progression of the chlamydial developmental cycle. *Molecular Microbiology* 61(6):1543-1555.
95. Ur-Rehman T, Slepkin A, Chu H, Blomgren A, Dahlgren MK, Zetterstrom CE, Peterson EM, Elofsson M, Gylfe A 2012. Pre-clinical pharmacokinetics and anti-chlamydial activity of salicylidene acylhydrazide inhibitors of bacterial type III secretion. *J Antibiot (Tokyo)* 65(8):397-404.
96. Zigangirova NA, Zayakin ES, Kapotina LN, Kost EA, Didenko LV, Davydova DY, Rumyancheva JP, Gintsburg AL 2012. Development of Chlamydial Type III Secretion System Inhibitors for Suppression of Acute and Chronic Forms of Chlamydial Infection. *Acta Naturae* 4(2):87-97.
97. Pan N, Lee C, Goguen J 2007. High throughput screening for small-molecule inhibitors of type III secretion in *Yersinia pestis*. *Genus Yersinia: From Genomics to Function* 603:367-375.
98. Pan NJ, Brady MJ, Leong JM, Goguen JD 2009. Targeting Type III Secretion in *Yersinia pestis*. *Antimicrobial Agents and Chemotherapy* 53(2):385-392.
99. Harmon DE, Davis AJ, Castillo C, Mecsas J 2010. Identification and Characterization of Small-Molecule Inhibitors of Yop Translocation in *Yersinia pseudotuberculosis*. *Antimicrobial Agents and Chemotherapy* 54(8):3241-3254.
100. Swietnicki W, Carmany D, Retford M, Guelta M, Dorsey R, Bozue J, Lee MS, Olson MA 2011. Identification of Small-Molecule Inhibitors of *Yersinia pestis* Type III Secretion System YscN ATPase. *Plos One* 6(5).
101. Ohgita T, Hayashi N, Gotoh N, Kogure K 2013. Suppression of type III effector secretion by polymers. *Open Biol* 3(12):130133.

102. Ochoa TJ, Cleary TG 2009. Effect of lactoferrin on enteric pathogens. *Biochimie* 91(1):30-34.
103. Hayward RD, Hume PJ, McGhie EJ, Koronakis V 2002. A Salmonella SipB-derived polypeptide blocks the 'trigger' mechanism of bacterial entry into eukaryotic cells. *Molecular Microbiology* 45(6):1715-1727.
104. Stone CB, Bulir DC, Emdin CA, Pirie RM, Porfilio EA, Slootstra JW, Mahony JB 2011. Chlamydia Pneumoniae CdsL Regulates CdsN ATPase Activity, and Disruption with a Peptide Mimetic Prevents Bacterial Invasion. *Front Microbiol* 2:21.
105. Larzabal M, Mercado EC, Vilte DA, Salazar-Gonzalez H, Cataldi A, Navarro-Garcia F 2010. Designed coiled-coil peptides inhibit the type three secretion system of enteropathogenic Escherichia coli. *PLoS One* 5(2):e9046.
106. Lee VT, Pukatzki S, Sato H, Kikawada E, Kazimirova AA, Huang J, Li XH, Arm JP, Frank DW, Lory S 2007. Pseudolipasin A is a specific inhibitor for phospholipase A(2) activity of Pseudomonas aeruginosa cytotoxin ExoU. *Infection and Immunity* 75(3):1089-1098.
107. Ohgita T, Hayashi N, Hama S, Tsuchiya H, Gotoh N, Kogure K 2013. A novel effector secretion mechanism based on proton-motive force-dependent type III secretion apparatus rotation. *FASEB J* 27(7):2862-2872.
108. Strickley RG 2004. Solubilizing excipients in oral and injectable formulations. *Pharm Res* 21(2):201-230.
109. Ochoa TJ, Cleary TG 2004. Lactoferrin disruption of bacterial type III secretion systems. *Biometals* 17(3):257-260.
110. Ochoa TJ, Noguera-Obenza M, Ebel F, Guzman CA, Gomez HF, Cleary TG 2003. Lactoferrin impairs type III secretory system function in enteropathogenic Escherichia coli. *Infect Immun* 71(9):5149-5155.
111. Gomez HF, Ochoa TJ, Carlin LG, Cleary TG 2003. Human lactoferrin impairs virulence of Shigella flexneri. *J Infect Dis* 187(1):87-95.
112. Mosquito S, Ochoa TJ, Cok J, Cleary TG 2010. Effect of bovine lactoferrin in Salmonella ser. Typhimurium infection in mice. *Biometals* 23(3):515-521.
113. Yekta MA, Verdonck F, Van Den Broeck W, Goddeeris BM, Cox E, Vanrompay D 2010. Lactoferrin inhibits E. coli O157:H7 growth and attachment to intestinal epithelial cells. *Veterinarni Medicina* 55(8):359-368.
114. Hayward RD, Hume PJ, McGhie EJ, Koronakis V 2002. A Salmonella SipB-derived polypeptide blocks the 'trigger' mechanism of bacterial entry into eukaryotic cells. *Mol Microbiol* 45(6):1715-1727.
115. Olive AJ, Kenjale R, Espina M, Moore DS, Picking WL, Picking WD 2007. Bile salts stimulate recruitment of IpaB to the Shigella flexneri surface, where it colocalizes with IpaD at the tip of the type III secretion needle. *Infection and Immunity* 75(5):2626-2629.
116. Pope LM, Reed KE, Payne SM 1995. Increased protein secretion and adherence to HeLa cells by Shigella spp. following growth in the presence of bile salts. *Infect Immun* 63(9):3642-3648.
117. Prouty AM, Gunn JS 2000. Salmonella enterica serovar typhimurium invasion is repressed in the presence of bile. *Infection and Immunity* 68(12):6763-6769.

118. Wang Y, Nordhues BA, Zhong D, De Guzman RN 2010. NMR characterization of the interaction of the Salmonella type III secretion system protein SipD and bile salts. *Biochemistry* 49(19):4220-4226.
119. Dickenson NE, Zhang L, Epler CR, Adam PR, Picking WL, Picking WD 2011. Conformational changes in IpaD from *Shigella flexneri* upon binding bile salts provide insight into the second step of type III secretion. *Biochemistry* 50(2):172-180.
120. Chatterjee S, Zhong D, Nordhues BA, Battaile KP, Lovell S, De Guzman RN 2011. The crystal structures of the Salmonella type III secretion system tip protein SipD in complex with deoxycholate and chenodeoxycholate. *Protein Sci* 20(1):75-86.
121. Barta ML, Guragain M, Adam P, Dickenson NE, Patil M, Geisbrecht BV, Picking WL, Picking WD 2012. Identification of the bile salt binding site on IpaD from *Shigella flexneri* and the influence of ligand binding on IpaD structure. *Proteins* 80(3):935-945.
122. Lafont F, Tran Van Nhieu G, Hanada K, Sansonetti P, van der Goot FG 2002. Initial steps of *Shigella* infection depend on the cholesterol/sphingolipid raft-mediated CD44-IpaB interaction. *EMBO J* 21(17):4449-4457.
123. Epler CR, Dickenson NE, Olive AJ, Picking WL, Picking WD 2009. Liposomes Recruit IpaC to the *Shigella flexneri* Type III Secretion Apparatus Needle as a Final Step in Secretion Induction. *Infection and Immunity* 77(7):2754-2761.
124. Mounier J, Boncompain G, Senerovic L, Lagache T, Chretien F, Perez F, Kolbe M, Olivo-Marin JC, Sansonetti PJ, Sauvonnet N 2012. *Shigella* effector IpaB-induced cholesterol relocation disrupts the Golgi complex and recycling network to inhibit host cell secretion. *Cell Host Microbe* 12(3):381-389.
125. Hayward RD, Cain RJ, McGhie EJ, Phillips N, Garner MJ, Koronakis V 2005. Cholesterol binding by the bacterial type III translocon is essential for virulence effector delivery into mammalian cells. *Molecular Microbiology* 56(3):590-603.
126. Schoehn G, Di Guilmi AM, Lemaire D, Attree I, Weissenhorn W, Dessen A 2003. Oligomerization of type III secretion proteins PopB and PopD precedes pore formation in *Pseudomonas*. *Embo Journal* 22(19):4957-4967.
127. Kayath CA, Hussey S, El Hajjami N, Nagra K, Philpott D, Allaoui A 2010. Escape of intracellular *Shigella* from autophagy requires binding to cholesterol through the type III effector, IcsB. *Microbes and Infection* 12(12-13):956-966.
128. Nawabi P, Catron DM, Haldar K 2008. Esterification of cholesterol by a type III secretion effector during intracellular *Salmonella* infection. *Mol Microbiol* 68(1):173-185.
129. Dickenson NE, Arizmendi O, Patil MK, Toth RTt, Middaugh CR, Picking WD, Picking WL 2013. N-Terminus of IpaB Provides a Potential Anchor to the *Shigella* Type III Secretion System Tip Complex Protein IpaD. *Biochemistry*.
130. Rathinavelan T, Tang C, De Guzman RN 2011. Characterization of the Interaction between the Salmonella Type III Secretion System Tip Protein SipD and the Needle Protein PrgI by Paramagnetic Relaxation Enhancement. *Journal of Biological Chemistry* 286(6):4922-4930.
131. Andricopulo AD, Montanari CA 2005. Structure-activity relationships for the design of small-molecule inhibitors. *Mini-Reviews in Medicinal Chemistry* 5(6):585-593.
132. Dahlgren MK, Zetterstrom CE, Gylfe S, Linusson A, Elofsson M 2010. Statistical molecular design of a focused salicylidene acylhydrazide library and multivariate QSAR

of inhibition of type III secretion in the Gram-negative bacterium *Yersinia*. *Bioorg Med Chem* 18(7):2686-2703.

133. Ur-Rehman T, Nordfelth R, Blomgren A, Zetterstrom CE, Elofsson M, Gylfe A 2012. Preliminary Pharmacokinetics of the Bacterial Virulence Inhibitor N'-(3,5-Dibromo-2-HydroxyBenzylidenene)-Nicotinic Acid Hydrazide. *Advances in Yersinia Research* 954:349-356.

134. Hughes JP, Rees S, Kalindjian SB, Philpott KL 2011. Principles of early drug discovery. *British Journal of Pharmacology* 162(6):1239-1249.

## **Chapter 10. Characterization of the Binding of Hydroxyindole, Indoleacetic acid and Morpholinoaniline to the *Salmonella* Type III Secretion System Proteins SipD and SipB**

[Some data in this chapter has been published with the following citation: McShan AC, Anbanandam A, Patnaik S, De Guzman RN. Characterization of the Binding of Hydroxyindole, Indoleacetic acid and Morpholinoaniline to the *Salmonella* Type III Secretion System Proteins SipD and SipB. *ChemMedChem*. 2016]

### **10.1. Introduction**

*Salmonella*, a causative agent of food borne illness and typhoid fever that is responsible for millions of infections each year worldwide<sup>1</sup>, and other Gram-negative bacteria belonging to the *Pseudomonas*, *Shigella*, *Chlamydia* and *Yersinia* genera assemble the type III secretion system (T3SS) to initiate infectious diseases in humans<sup>2</sup>. The rise of antibiotic resistance among these pathogens coupled with the dearth of new antibiotics necessitates the development of new anti-bacterials<sup>3</sup>. The T3SS is an attractive target for developing new anti-bacterials because of its essential role in virulence, its exposure on the bacterial surface, and its presence only among pathogens<sup>3</sup>.

The function of the T3SS is to inject effector proteins into the host cytoplasm to manipulate host-signaling pathways for the benefit and survival of bacteria<sup>2</sup>. The structure component of the T3SS is a mega-Dalton assemblage of over 20 proteins that form the needle apparatus, which consists of a base, an extracellular needle, a tip complex and a translocon<sup>4</sup>. In *Salmonella*, the tip protein is SipD and the translocon proteins are the membrane proteins SipB and SipC. The tip protein SipD is exposed to the extracellular environment prior to contact with host cells<sup>5</sup>. Upon contact with the host cell, the translocon assembles on the tip complex to form a pore on the host cell membrane to

allow the passage of effectors into the host cell cytoplasm<sup>5</sup>. The crystal structure of SipD<sup>6</sup> and other tip proteins<sup>7</sup> are known. SipD contains an N-terminal  $\alpha$ -helical hairpin, an elongated central coiled-coil and a domain of mixed  $\alpha$ -helices and  $\beta$ -strands<sup>6</sup>. The crystal structures of the N-terminal ectodomains of the *Shigella* IpaB<sup>74-224</sup> and *Salmonella* SipB<sup>82-226</sup> translocon proteins show coiled-coils of three anti-parallel  $\alpha$ -helices<sup>8</sup>, and the IpaB and SipB ectodomains interact directly with their tip proteins<sup>9</sup>.

Currently, the only known small molecules that bind to the tip protein and translocon proteins are bile salts (to SipD and its *Shigella* homolog, IpaD)<sup>10</sup> and sphingolipids and cholesterol (to SipB)<sup>11</sup>. To identify other molecular fragments that could bind to SipD and SipB that could potentially be used as potential scaffolds for development of novel T3SS inhibitors, we screened a library of 288 compounds from a Zenobia library. We identified that 5-hydroxyindole (**Structure 1, Fig. 10-1**) binds to both SipD <sup>$\Delta$ 38</sup> and SipB<sup>82-240</sup>, 3-indole acetic acid (**2, Fig. 10-1**) binds to SipB<sup>82-240</sup> and 4-morpholinoaniline (**10, Fig. 10-1**) binds to SipD <sup>$\Delta$ 38</sup>. Our results revealed new small scaffolds based on indole and morpholinoaniline that can bind to SipD and SipB.

## 10.2. Materials and Methods

### 10.2.1. Protein Expression and Purification

Isotopically labeled <sup>15</sup>N/ILV SipD <sup>$\Delta$ 38</sup> and <sup>15</sup>N/ILV SipB<sup>82-240</sup> were expressed and purified as previously described (Chapter 4 for SipD and Chapter 6 for SipB).

### 10.2.2. Surface Plasmon Resonance (SPR) Screening

Surface Plasmon Resonance (SPR) was used for screening using a BIACORE 3000

instrument (GE Healthcare Life Science). The amine coupling kit (#BR-110633) and CM5 sensor chip (#BR-100399) were purchased from GE Healthcare. The target proteins SipD<sup>Δ38</sup> and SipB<sup>82-240</sup> were covalently immobilized to the sensor chip surface by standard amine coupling chemistry with 1.05× PBS buffer as the running buffer. There were four flow cells available for immobilization of the target protein per CM5 chip. Flow cell 1 was kept as a reference flow cell without immobilized protein. The remaining 3 flow cells were loaded with target proteins. All four flow cells were activated for 7 minutes with a mixture of N-hydroxysuccinimide (NHS) and 1-ethyl-3-(3-dimethylaminopropyl)-carbodiimide (EDC) at 1:1 ratio and at a flow rate of 15 μL/min at 25°C. Proteins at a concentration of 50 μg/mL in 10 mM sodium acetate pH 4.3 were injected for 7 minutes resulting in 2,727 response units (RU) for SipB82-240 and 10,110 RU for SipD. All four flow cell surfaces were treated with a 7 minute injection of 1M ethanolamine pH 8.0 to eliminate all the unbound proteins and unreacted esters of NHS/EDC from the flow cells.

A library of 288 compounds (Fragment Library 2, Zenobia, San Diego) was obtained in three 96-well microplates with each compound at a concentration of 100 mM stock in 100% DMSO. Compounds were diluted to a final concentration of 1 mM in 5% DMSO and 1.05× PBS. Biacore 3000 allowed the automate injection of compounds from 96-well plates. The compounds were injected over the chip surface for 60 sec at a flow rate of 60 μL/min and the dissociation was monitored for 60 sec. Running buffer (1.05× PBS) was used as negative control. The surface was not regenerated between sample injections. The flow system, except sensor surface, was washed with 1:1 mixture of DMSO and water to remove any unbound compound from the flow system. Running

buffer was injected between each compound run to monitor carryover effects. Eight DMSO calibration solutions with varying concentrations (4-6%) were injected sequentially at the beginning and end of the experiments, using the same slow rate as the compounds.

### *10.2.3. NMR Spectroscopy and Data Analysis*

NMR data were acquired using a Bruker Avance 800 MHz spectrometer equipped with a cryogenic triple resonance probe and were processed using NMRpipe<sup>12</sup> and analyzed using NMRview<sup>13</sup>. Saturation transfer difference (STD) NMR data were acquired using Bruker Avance 600 MHz spectrometer equipped with a TXI-RT probe and processed using Topspin. Two-dimensional <sup>1</sup>H-<sup>15</sup>N TROSY and <sup>1</sup>H-<sup>13</sup>C HSQC spectra were acquired at 30°C using 0.3 mM of <sup>15</sup>N/ILV SipD<sup>Δ38</sup> or 0.5 mM of <sup>15</sup>N/ILV SipB<sup>82-240</sup> dissolved in buffer (10% D<sub>2</sub>O, 20 mM NaCl, 10 mM sodium phosphate, pH 7.4). For NMR titrations, the compounds were dissolved in d<sub>6</sub>-DMSO (Cambridge Isotope Laboratories, Inc., Andover, MA). All titration samples contained 1.5% (v/v) d<sub>6</sub>-DMSO for SipD<sup>Δ38</sup> or 2.5% (v/v) d<sub>6</sub>-DMSO for SipB<sup>82-240</sup>. Typical 2D <sup>1</sup>H-<sup>15</sup>N TROSY acquisition parameters were 16 scans with 2048 complex points (<sup>1</sup>H) and 400 complex points (<sup>15</sup>N) with sweep width 17.9 ppm for <sup>1</sup>H centered at 4.7 ppm and 30 ppm for <sup>15</sup>N centered at 118 ppm. For 2D <sup>1</sup>H-<sup>13</sup>C HSQC experiments acquisition parameters were 8 scans with 1024 complex points (<sup>1</sup>H) and 256 complex points (<sup>13</sup>C) with sweep width 10.01 ppm for <sup>1</sup>H centered at 4.69 ppm and 18 ppm for <sup>13</sup>C centered at 18 ppm. Chemical shift deviations (CSD, Δδ) were calculated using the following equations<sup>14</sup>:

$$\Delta\delta_{\text{HN}} = \sqrt{\frac{\Delta\delta_{\text{H}}^2 + \frac{\Delta\delta_{\text{N}}^2}{25}}{2}}$$

or

$$\Delta\delta_{\text{ILV}} = \sqrt{\frac{\Delta\delta_{\text{H}}^2 + \frac{\Delta\delta_{\text{C}}^2}{4}}{2}}$$

where  $\delta$  is the chemical shift in ppm

Dissociation constants were estimated from plots of chemical shift deviation vs. compound concentration for multiple residues and curve fitting using GraphPad Prism Version 5 (GraphPad Software, Inc., USA). The R2 values for the fits were  $\geq 0.99$ .

One-dimensional  $^1\text{H}$  saturation transfer difference (STD) NMR experiments NMR<sup>15</sup> data were acquired at 30°C on samples that contained protein plus compound at a 1:100 ratio (40  $\mu\text{M}$  protein, 4000  $\mu\text{M}$  compound, 10% D<sub>2</sub>O, 0.4% d<sub>6</sub>-DMSO) or compound only (4000  $\mu\text{M}$  compound in 100% d<sub>6</sub>-DMSO). The protein saturation pulse (Gaussian) was 50 ms over a period of 2 sec with the center of the on-resonance pulse varied from -0.2 to 0.1 ppm to give an optimal STD signal, where the off-resonance center was kept at 40 ppm. Typical acquisition parameters were 128 scans, 16 ppm  $^1\text{H}$  sweep width centered at 4.70 and 2 sec recycle delay.

### 10.3. Results

#### 10.3.1. SPR screening

The expression and purification of SipD <sup>$\Delta 38$</sup>  and SipB<sup>82-240</sup> yielded milligram amounts of proteins and their solubility allowed for SPR screening followed by NMR

characterization. SPR is a label free method of screening for small molecule fragments that bind to proteins<sup>16</sup>. The SPR screen of 288 compounds from a structurally diverse library of fragment-like compounds (Zenobia Library 2) identified the binding of 5-hydroxyindole (**1, Fig. 10-1**) to both SipD<sup>Δ38</sup> and SipB<sup>82-240</sup>; 3-indoleacetic acid (**2, Fig. 10-1**) to SipB<sup>82-240</sup>; and 4-morpholinoaniline (**10, Fig. 10-1**) to SipD<sup>Δ38</sup> (**Fig. 10-2**). Results of the SPR screen also identified the important functional groups within the scaffolds in binding to SipD<sup>Δ38</sup> and SipB<sup>82-240</sup>. Regarding the binding of the indole scaffold to SipD<sup>Δ38</sup> and SipB<sup>82-240</sup>, other functional groups, such as hydroxyl and acetyl groups, were needed for binding, as the indole ring compounds containing other modifications were incapable of binding (**Fig. 10-3**). Replacing the 5-hydroxy group with a 5-cyano group (**4, Fig. 10-1**) abrogated the interaction suggesting that the 5'-hydroxy group in might be needed for hydrogen bonding with SipD<sup>Δ38</sup> and SipB<sup>82-240</sup> (**Fig. 10-3**). The acetate methylene group (**2, Fig. 10-1**) was needed for binding SipB<sup>82-240</sup> as its removal (**5 & 6, Fig. 10-1**) resulted in loss of binding (**Fig. 10-3**). Likewise, the acetate carbonyl group (**2, Fig. 10-1**) was important for binding as its removal (**7, 8, 9, Fig. 10-1**) resulted in loss of binding (**Fig. 10-3**). Regarding the binding of the morpholinoaniline (**10, Fig. 10-1**) scaffold to SipD<sup>Δ38</sup>, hydroxylation or removal of the amino group (**11, Fig. 10-1**) or introducing a methylene group between the two rings (**12, Fig. 10-1**) resulted in loss of binding (**Fig. 10-3**).

### 10.3.2. NMR titrations of SipD<sup>Δ38</sup> with 5-hydroxyindole

NMR was used to characterize the interaction of SipD<sup>Δ38</sup> with 5-hydroxyindole. SipD<sup>Δ38</sup> uniformly labeled with both <sup>15</sup>N and ILV was titrated with 5-hydroxyindole at

increasing molar ratios of 1:0, 1:25, 1:50 and 1:100 and the titration was monitored by acquiring 2D  $^1\text{H}$ - $^{15}\text{N}$  TROSY and 2D  $^1\text{H}$ - $^{13}\text{C}$  HSQC datasets. Titration of SipD $^{\Delta 38}$  with 5-hydroxyindole resulted in chemical shift perturbations of specific SipD $^{\Delta 38}$  amide peaks in a concentration dependent manner (**Fig. 10-4**). SipD $^{\Delta 38}$  residues that were affected by binding (e.g. E133, M174, G175, L179, N211 and W234ε) showed progressive changes in their peak positions indicating interaction in fast exchange NMR time scale. In addition to the  $^{15}\text{N}$  resonances of SipD $^{\Delta 38}$ , the ILV  $^{13}\text{C}$  methyl groups of SipD $^{\Delta 38}$  were also used as probes of the interaction. Like the results of the  $^{15}\text{N}$  titrations, titration with 5-hydroxyindole resulted in chemical shift perturbations of specific SipD $^{\Delta 38}$  ILV peaks in a concentration dependent manner (**Fig. 10-5**). Based on the chemical shift deviations of  $^{15}\text{N}$  data (for E133, M174, G175 and L179, **Fig. 10-4B**) and ILV data (for L48, L178 and V187, **Fig. 10-5B**), the dissociation constant for the binding of 5-hydroxyindole to SipD $^{\Delta 38}$  was estimated to be  $32 \pm 8$  mM.

The chemical shift deviation for each non-overlapped amide (**Fig. 10-6A**) and ILV (**Fig. 10-6B**) peak of SipD $^{\Delta 38}$  identified that residues were strongly affected by binding of 5-hydroxyindole. Results of the  $^{15}\text{N}$  titration showed that the SipD $^{\Delta 38}$  residues affected by 5-hydroxyindole ranged from hydrophobic (L97, A115, I134, L171, G175, L179, V187) to polar (R106, R126, E133, K188, K302) residues (**Fig. 10-6A**). The ILV titration confirmed the results of the  $^{15}\text{N}$  titration as many residues, such as I134, L171 and V187 identified in the  $^{15}\text{N}$  titration also showed significant chemical shift deviations in the ILV titration with 5-hydroxyindole. Additionally, the ILV titrations identified other residues (I45, V253, V323, **Fig. 10-6B**) that were not previously identified in the  $^{15}\text{N}$  titration that showed significant chemical shift deviation upon binding to 5-

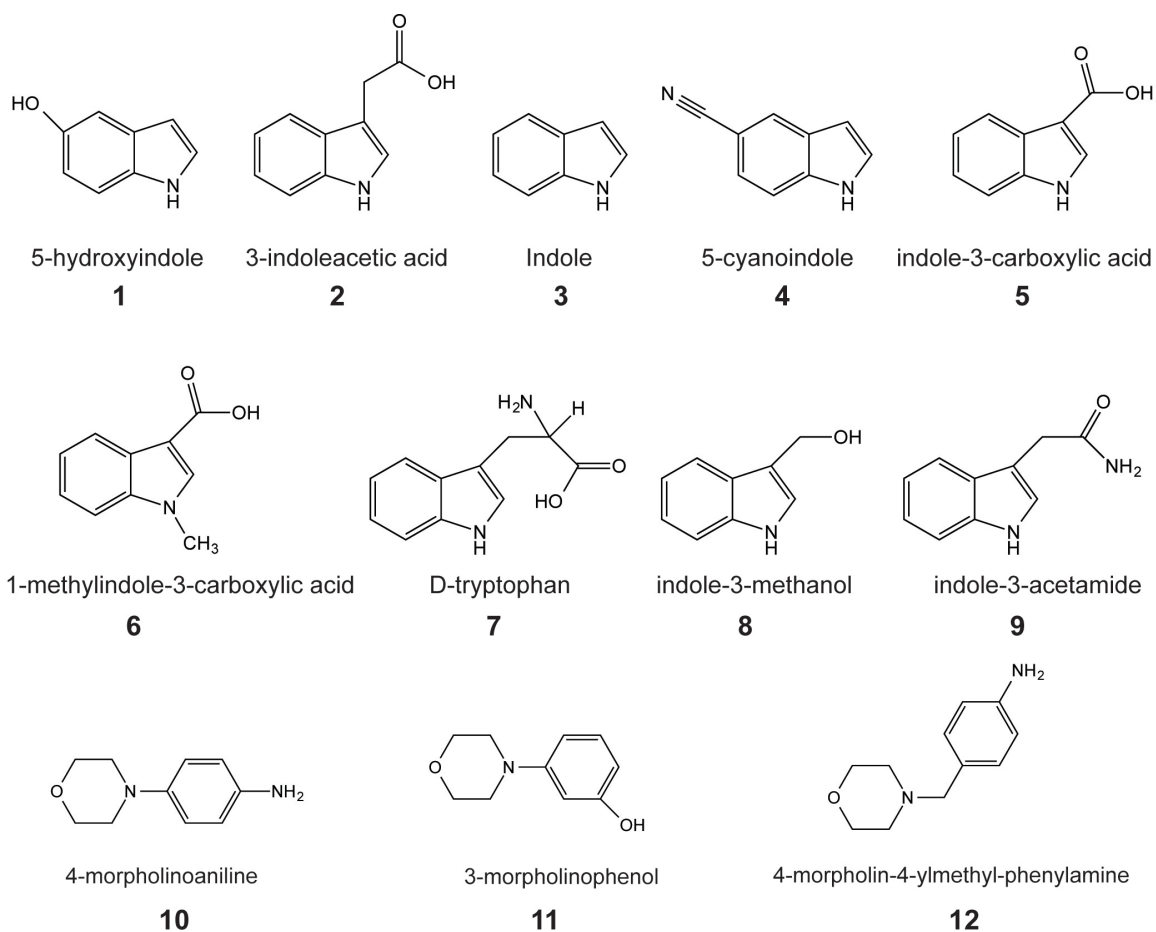
hydroxyindole. The methyl side chains of I45, V253 and V323 were likely involved in the hydrophobic contacts with 5-hydroxyindole.

The residues that showed significant chemical shift deviations clustered on two surfaces on SipD. One surface maps to the mixed  $\alpha/\beta$  domain (involving residues G175, L178 and V187) (**Fig. 10-7**). The second largest surface maps near the bottom of the coiled-coil and is formed by S110, S114, R126 in the 23-residue loop spanning residues 110-132 that connects the  $\alpha$ -helical hairpin to the coiled-coil (**Fig. 10-7**). I45 in the  $\alpha$ -helical hairpin and I134 in the coiled-coil also showed strong chemical shifted deviations. Our results suggest that 5-hydroxyindole binds at the bottom of the coiled-coil and the loop 110-132 because most of the residues affected by interaction are in this region. The other site that showed chemical shift deviations perhaps indicate transient, weaker interactions with 5-hydroxyindole.

### 10.3.3. STD NMR of 5-hydroxyindole with SipD <sup>$\Delta$ 38</sup>

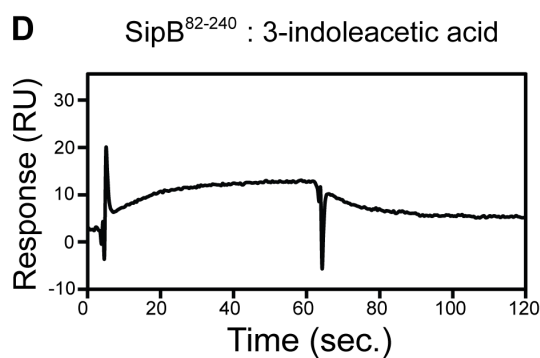
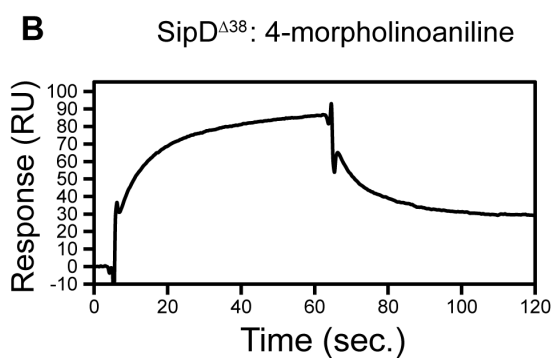
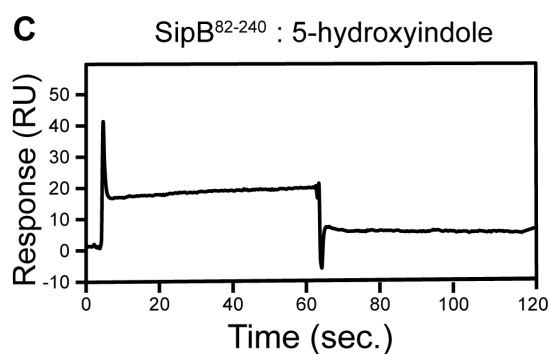
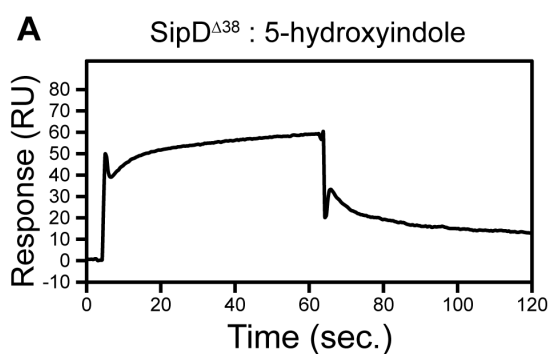
Results of <sup>1</sup>H STD NMR experiments identified which parts of 5-hydroxyindole were needed for binding to SipD <sup>$\Delta$ 38</sup>. As expected, the off-resonance reference spectrum showed NMR peaks from both SipD <sup>$\Delta$ 38</sup> and 5-hydroxyindole (**Fig. 10-8A**). The resulting <sup>1</sup>H STD NMR spectrum showed all the NMR peaks corresponding to 5-hydroxyindole remained above noise level (**Fig. 10-8B**). This indicated that, with the exception of the OH group for which there was no NMR peak in the STD NMR, all the protons in 5-hydroxyindole were affected by the interaction with SipD <sup>$\Delta$ 38</sup>. This suggested that the entire molecule of 5-hydroxyindole was embedded in SipD <sup>$\Delta$ 38</sup> upon binding. As a control experiment, irradiation of 5-hydroxyindole using the same conditions in the absence of

SipD<sup>Δ38</sup> did not result in STD peaks, indicating that the observed STD peaks were not due to indirect saturation of 5-hydroxyindole (**Fig. 10-8C**).



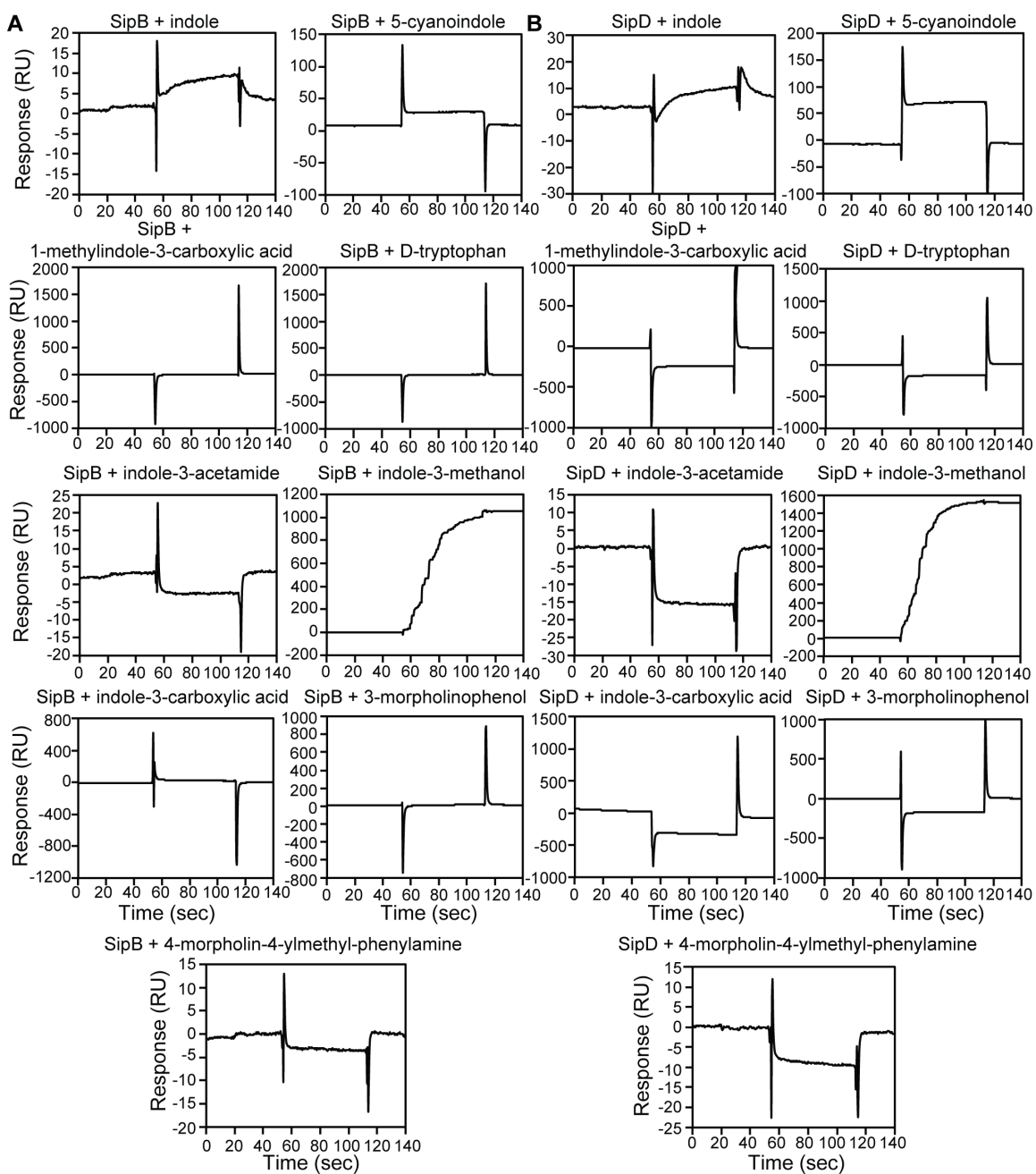
### 10-1 – Structure of Small Molecule Scaffolds

SPR identified the binding of 5-hydroxyindole (**1**) to SipD<sup>Δ38</sup> and SipB<sup>82-240</sup>, 3-indoleacetic acid (**2**) to SipB<sup>82-240</sup>, and 4-morpholinoaniline (**10**) to SipB<sup>82-240</sup>. The non-binding or relatively weaker binding of other similar scaffolds revealed the important functional groups needed for binding to SipD<sup>Δ38</sup> or SipB<sup>82-240</sup>.



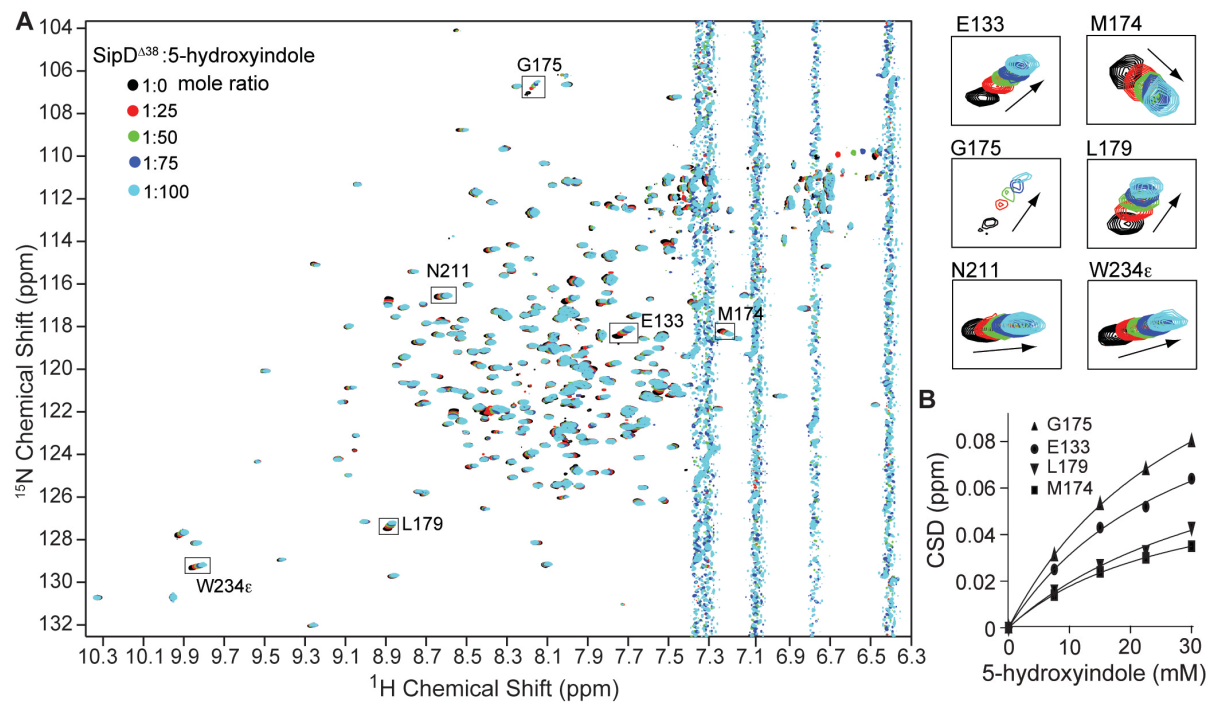
### 10-2 – SPR Screening of SipD<sup>Δ38</sup> and SipB<sup>82-240</sup>

SPR sensorgrams showing the binding of (A) 5-hydroxyindole to SipD<sup>Δ38</sup>, (B) 4-morpholinoaniline to SipD, (C) 5-hydroxyindole to SipB<sup>82-240</sup>, and (D) 3-indoleacetic acid to SipB<sup>82-240</sup>.



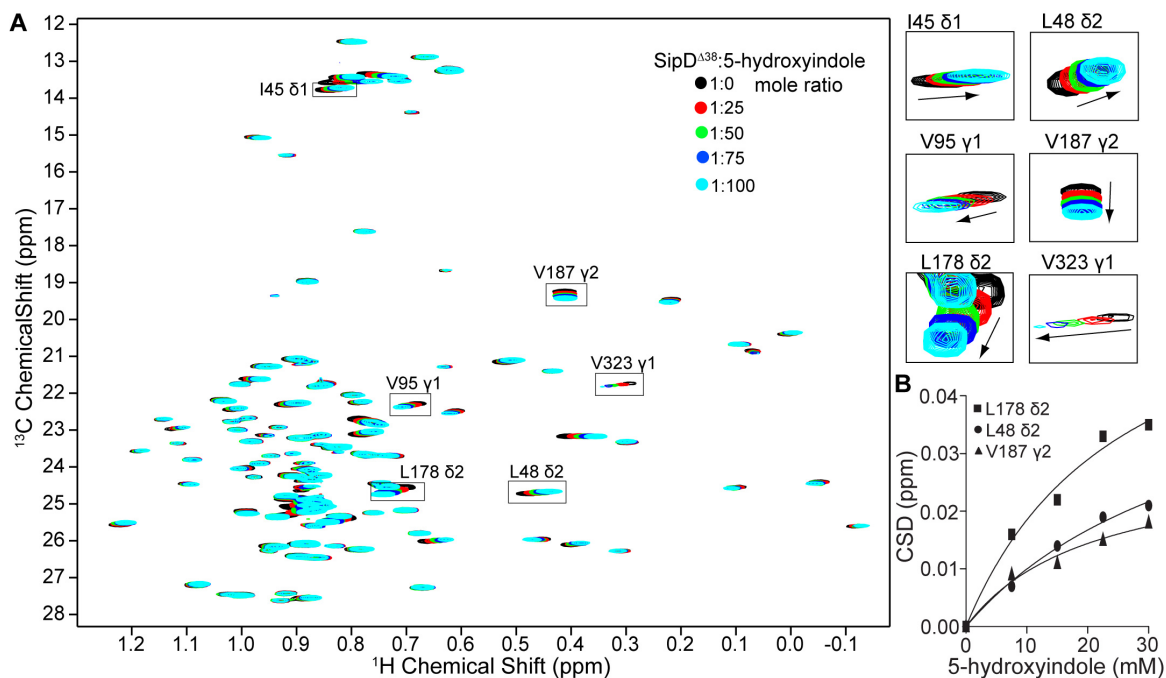
### 10-3 – Further SPR Screening of SipD<sup>A38</sup> and SipB<sup>82-240</sup>

SPR sensorgrams from the screening of small molecules against (A) SipB<sup>82-240</sup> and (B) SipD<sup>A38</sup>. The structure of some of these compounds are shown in Fig. 10-1.



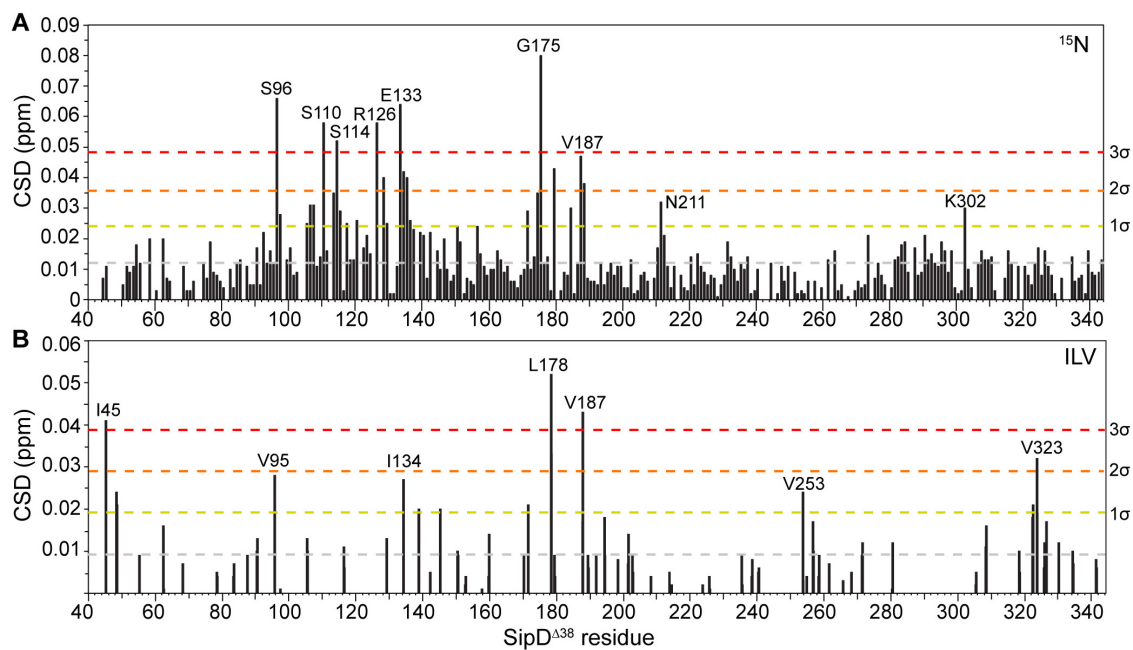
#### 10-4 – $^{15}\text{N}$ NMR Titration of SipD $\Delta$ 38 with 5-hydroxyindole

(A) Overlay of five 2D  $^1\text{H}$ - $^{15}\text{N}$  TROSY spectra of  $^{15}\text{N}$ /ILV labeled SipD $\Delta$ 38 titrated with increasing molar ratios of 5-hydroxyindole, with expanded sections for selected SipD $\Delta$ 38 residues affected by the interaction with 5-hydroxyindole. (B) Plot of chemical shift deviation (CSD) vs concentration of 5-hydroxyindole for selected residues.



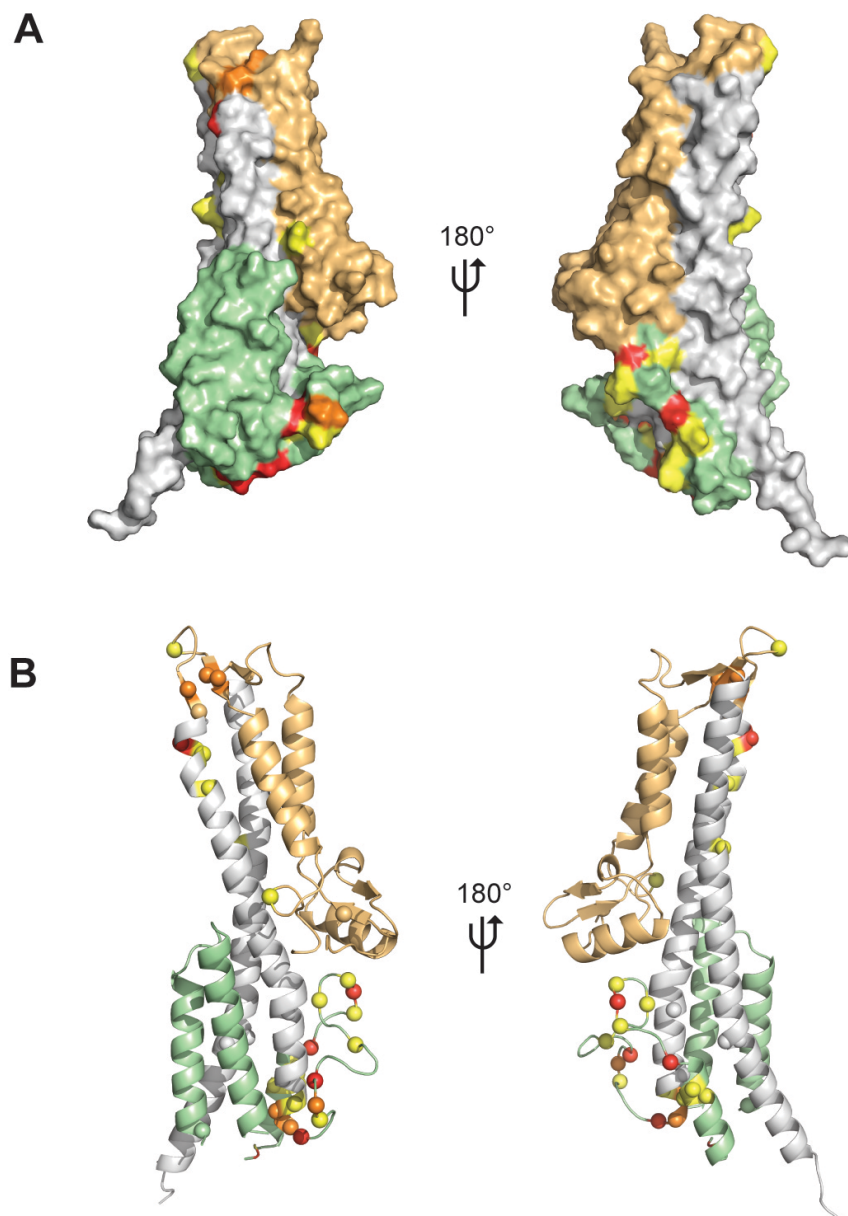
### 10-5 – ILV Methyl Titration of SipD $\Delta^{38}$ with 5-hydroxyindole

(A) Overlay of five 2D  $^1\text{H}$ - $^{13}\text{C}$  HSQC spectra of  $^{15}\text{N}$ /ILV labeled SipD $\Delta^{38}$  titrated with increasing mole ratios of 5-hydroxyindole. (B) Plots of chemical shift deviation (CSD) vs concentration of 5-hydroxyindole for selected  $^{13}\text{C}$  methyl peaks.



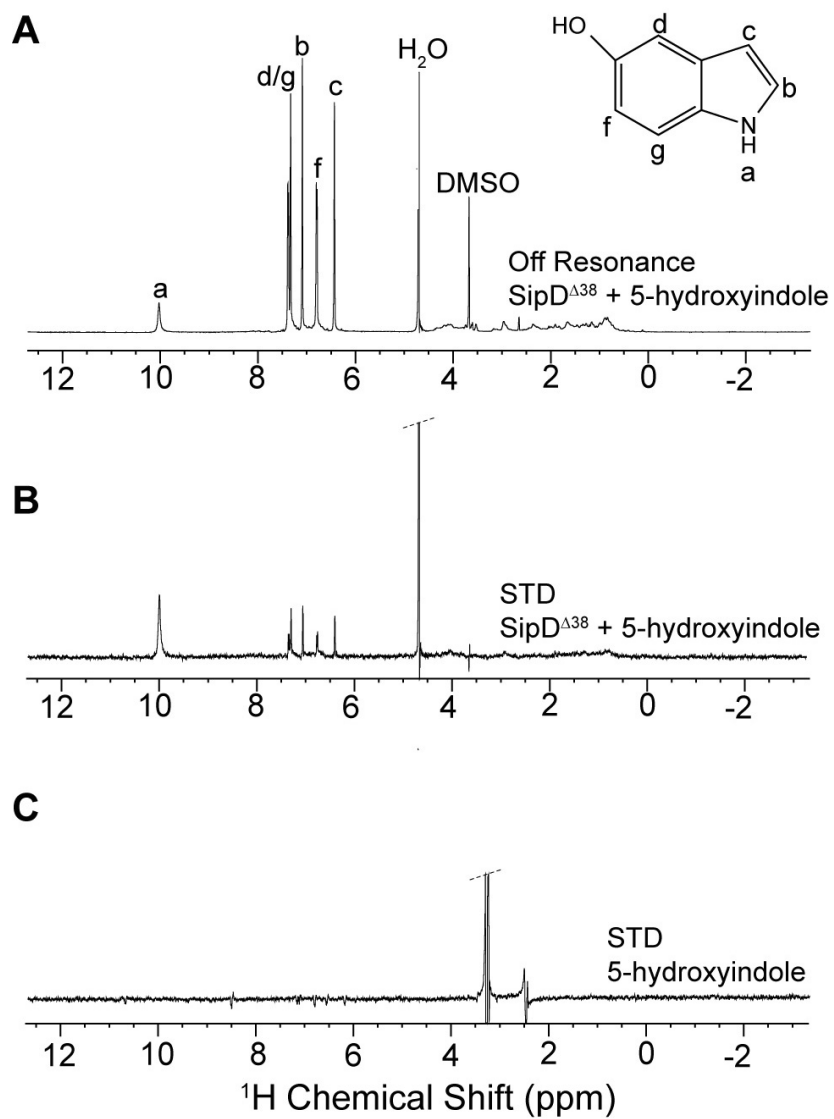
### 10-6 – Plots of Chemical Shift Deviations of SipD $\Delta^{38}$ with 5-hydroxyindole

Chemical shift deviations for (A)  $^{15}\text{N}$  and (B) ILV titrations of SipD $\Delta^{38}$  with 5-hydroxyindole ( $\sigma$ , or average CSD).



### 10-7 – SipD Surfaces Affected by Binding of 5-hydroxyindole

$C\alpha$  of SipD colored according to  $^{15}\text{N}$  and ILV chemical shift deviations as follows:  $1\sigma$  (yellow),  $2\sigma$  (orange),  $3\sigma$  (red); where  $\sigma$  is the standard deviation from the average CSD Fig. 10-5. [SipD N-terminal domain (green), coiled-coil (gray), mixed  $\alpha/\beta$  domain (light orange)]



### 10-8 – STD NMR of 5-hydroxyindole with SipD<sup>Δ38</sup>

(A) Off-resonance, (B) on-resonance STD NMR spectra of 5-hydroxyindole with SipD<sup>Δ38</sup>, and (C) STD NMR spectrum of 5-hydroxyindole in the absence of SipD<sup>Δ38</sup>.

#### 10.3.4. SipD<sup>Δ38</sup> binds to 4-morpholinoaniline

In addition to 5-hydroxyindole, SPR identified the binding of another scaffold, 4-morpholinoaniline, to SipD<sup>Δ38</sup> (**Fig. 10-2B**). Titration of <sup>15</sup>N/ILV labeled SipD<sup>Δ38</sup> with 4-morpholinoaniline at molar ratios of 1:0, 1:25, 1:50 and 1:100 resulted in distinct chemical shift deviations of specific SipD<sup>Δ38</sup> amide peaks in a concentration dependent manner as monitored by <sup>15</sup>N TROSY and <sup>13</sup>C HSQC (**Fig. 10-9 & Fig. 10-10**). Representative panels from the <sup>15</sup>N titration (S110, A111, F117, E133, V187 and K188, **Fig. 10-9A**) and ILV titrations (L138, L171, L178, V187 and L194, **Fig. 10-10A**) showed peaks in fast exchange NMR time scale. Plots of the weighted chemical shift deviations (**Fig. 10-11A, B**) identified SipD<sup>Δ38</sup> residues that were strongly affected by 4-morpholinoaniline. These residues ranged from hydrophobic (G94, A111, F117, V138, L150, V156, L179, V213) to polar (D131, E133, K188, K279) residues (**Fig. 10-11A, B**). The dissociation constant, however, could not be estimated, as plots of the chemical shift deviations vs concentrations of 4-morpholinoaniline did not reach saturation (**Fig. 10-9B, Fig. 10-10B**). STD NMR signals were not observed because SipD<sup>Δ38</sup> could not be selectively saturated, as there are proton resonances of 4-morpholinoaniline near the STD NMR irradiation frequency. Nevertheless, mapping the SipD<sup>Δ38</sup> residues affected by 4-morpholinoaniline showed two distinct surfaces: the top of the mixed  $\alpha/\beta$  domain and near the bottom of the coiled-coil (**Fig. 10-12**), similar to the surface maps of SipD<sup>Δ38</sup> interaction with 5-hydroxyindole (**Fig. 10-7**). Results with 5-hydroxyindole and 4-morpholinoaniline suggest that these surfaces in SipD could be hotspots for binding small molecule fragments.

### 10.3.5. SipB<sup>82-240</sup> binds to 5-hydroxyindole and 3-indoleacetic acid

We also screened for small molecules that will bind to the major translocon protein SipB using the N-terminal soluble domain, SipB<sup>82-240</sup>. SPR identified the binding of 5-hydroxyindole (**Fig. 10-2C**) and 3-indoleacetic acid (**Fig. 10-2D**) to SipB<sup>82-240</sup>. NMR titrations of SipB<sup>82-240</sup> with 5-hydroxyindole at protein to compound ratios of 1:0, 1:25 and 1:50 monitored by 2D <sup>1</sup>H-<sup>15</sup>N TROSY resulted in distinct chemical shift perturbations of specific SipB<sup>82-240</sup> amide peaks in a concentration dependent manner (**Fig. 10-13A**). Likewise, stepwise titration of SipB<sup>82-240</sup> with 3-indoleacetic acid at protein to compound ratios of 1:0, 1:4 and 1:8 resulted in distinct chemical shift perturbations of specific SipB<sup>82-240</sup> amide peaks in a concentration dependent manner (**Fig. 10-13B**). In addition, the ILV methyl resonances of SipB<sup>82-240</sup> were affected by titration with 5-hydroxyindole (**Fig. 10-14A**) and 3-indoleacetic acid (**Fig. 10-13B**). There are currently no NMR assignments available for SipB<sup>82-240</sup>, thus, it is not possible to use NMR chemical shift perturbation methods to identify which parts of SipB<sup>82-240</sup> are involved in the interaction with 5-hydroxyindole and 3-indoleacetic acid. NMR assignments of SipB<sup>82-240</sup> would have been challenging and not carried out because only ~50% of the expected amide resonances were observed.

STD NMR confirmed the binding of 5-hydroxyindole and 3-indoleacetic acid to SipB<sup>82-240</sup>. Further, STD NMR identified how 5-hydroxyindole and 3-indoleacetic acid bound to SipB<sup>82-240</sup>. The off-resonance reference spectra show both compound and SipB<sup>82-240</sup> signals present (**Fig. 10-15A, B**). The resulting <sup>1</sup>H STD NMR spectra show many of the signals corresponding to 3-indoleacetic acid (**Fig 10-15B**) and 5-hydroxyindole (**Fig. 10-15E**) remained above noise level. This suggests that most of 5-

hydroxyindole or 3-indoleacetic acid are interacting with or in close proximity to SipB<sup>82-240</sup>. In contrast, irradiation of compounds using the same conditions in the absence of SipB<sup>82-240</sup> resulted in no observable STD signals, indicating that SipB<sup>82-240</sup> must be present to observe the STD signals of the compound (**Fig. 10-15C, F**).

#### 10.4. Discussion

There are currently only a few small molecules that are known to bind to the T3SS tip and translocon proteins. Bile salts, such as deoxycholate, are sterol-like compounds that bind to SipD and its Shigella homolog IpaD<sup>6; 10; 17</sup>. Cholesterol and sphingolipids bind to the translocon protein SipB and its homolog IpaB<sup>11; 18</sup>. Finally, 2,2'-thiobis-(4-methylphenol) binds to the translocon protein YopD of *Yersinia pestis*<sup>19</sup>. Here, we identified new small molecule scaffolds (**Fig. 10-1**) that bind to SipD<sup>Δ38</sup> (5-hydroxyindole and 4-morpholinoaniline) and SipB<sup>82-240</sup> (5-hydroxyindole and 3-indoleacetic acid).

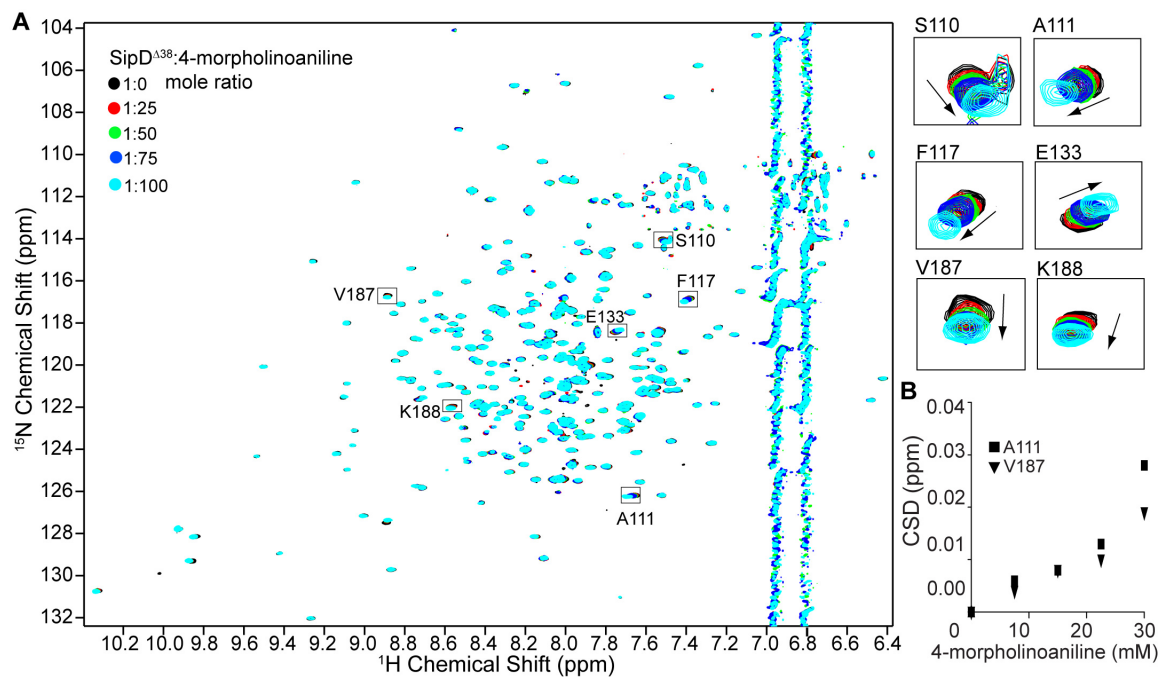
Comparison of the results of NMR titrations suggest that 5-hydroxyindole and 4-morpholinoaniline perturbed similar surfaces on SipD. Both compounds affected SipD residues near the mixed  $\alpha/\beta$  domain and the bottom region of the coiled-coil (**Fig. 10-7 & Fig 10-12**). The bottom of the coiled-coil of SipD has been previously identified as an important surface for the interaction with the needle protein PrgI<sup>20</sup>. Therefore, it may be possible to block the SipD:PrgI interaction by developing a compound that will bind to SipD with higher affinity. Our efforts at co-crystallization of SipD<sup>Δ38</sup> or SipB<sup>82-240</sup> with their interacting compounds has so far failed. Development of tighter binding compounds should allow for co-crystallization for the characterization of binding by X-ray diffraction.

The observation that two surfaces on SipD were affected by the compounds could be because both compounds have weak affinity to SipD (~30 mM for 5-hydroxyindole) and are therefore not very selective for a specific binding surface. The perturbation of ILV methyl resonances of SipD<sup>Δ38</sup> with both 5-hydroxyindole (**Fig. 10-5A**) and 4-morpholinoaniline (**Fig. 10-10A**) suggests that the protein-small molecule interaction included hydrophobic contacts. However, the small molecules also bound to SipD<sup>Δ38</sup> by polar interactions (perhaps by hydrogen bonding or ionic contacts) because many charged SipD<sup>Δ38</sup> residues were affected as well (**Fig. 10-4A & Fig. 10-9A**). This interaction with hydrophobic and hydrophilic surfaces is possible because the compounds contain hydrophobic rings as well as hydrophilic groups that are available for hydrogen bonding, such as OH and NH (**Fig. 10-1**).

Indole-like chemical scaffolds have not been identified as inhibitors of T3SS<sup>3</sup>. In contrast, molecules that are somewhat chemically related to the aniline scaffold have been previously shown to inhibit type III secretion, such as salicylideneaniline and the 8-hydroxyquinoline derivative INP1750<sup>3</sup>. Salicylideneanilines (salicylidene + aniline like scaffold) have been suggested to function as a transcriptional inhibitor of the *E. coli* T3SS<sup>21</sup>, although the specific molecular target has not been identified, while the mechanism of INP1750 (quinoline + piperazine + aniline like scaffold) is currently unknown<sup>22</sup>. Because the tip and translocon proteins are conserved in many bacterial pathogens, it may be possible that more potent binding versions of indole and morpholinoaniline scaffolds might interact with homologs of SipD, such as IpaD from *Shigella*, BipD from *Burkholderia*, LcrV from *Yersinia* and PcrV from *Pseudomonas*. Indeed, some T3SS inhibitors, such as thiazolidinones and salicylidene acylhydrazides,

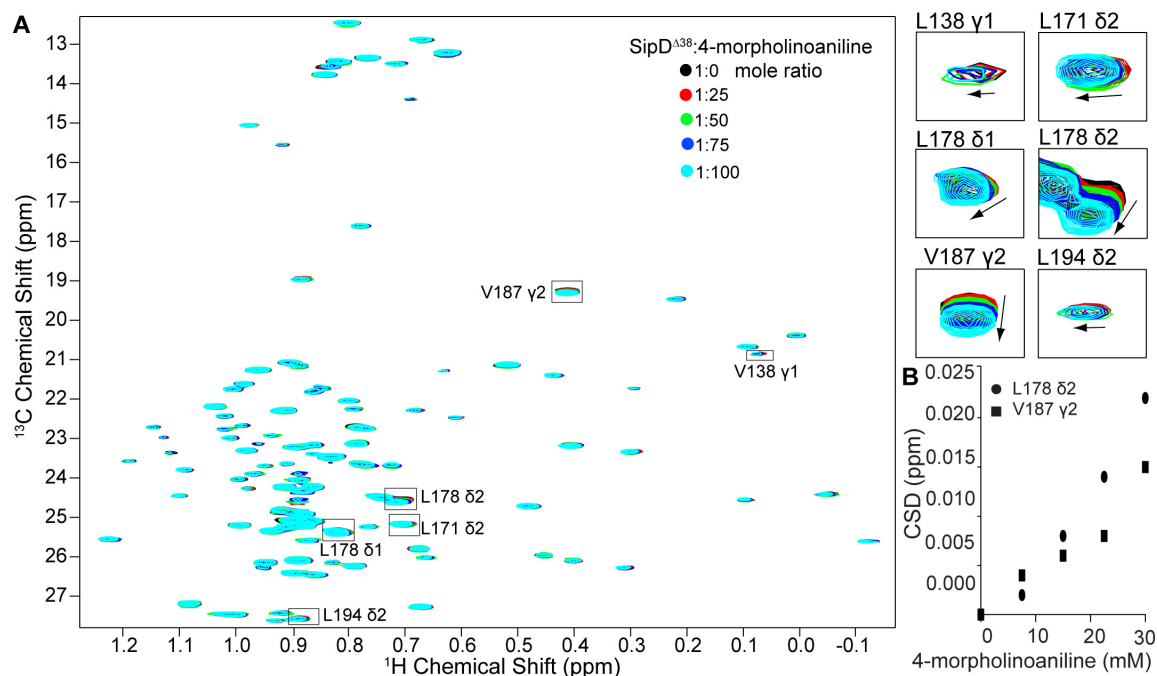
have been shown to be active against a broad range of bacteria, suggesting their target is a conserved T3SS protein<sup>3</sup>. Efforts are currently underway to determine if 5-hydroxyindole, 3-indoleacetic acid or 4-morpholinoaniline interact with proteins from other bacterial T3S systems.

To summarize, the significance of this work is that we have identified new small molecules based on the indole and morpholinoaniline scaffolds that interact with the *Salmonella* translocon protein SipB and the tip protein SipD. These scaffolds could be used as potential starting structures in the rational design of inhibitors of type III secretion.



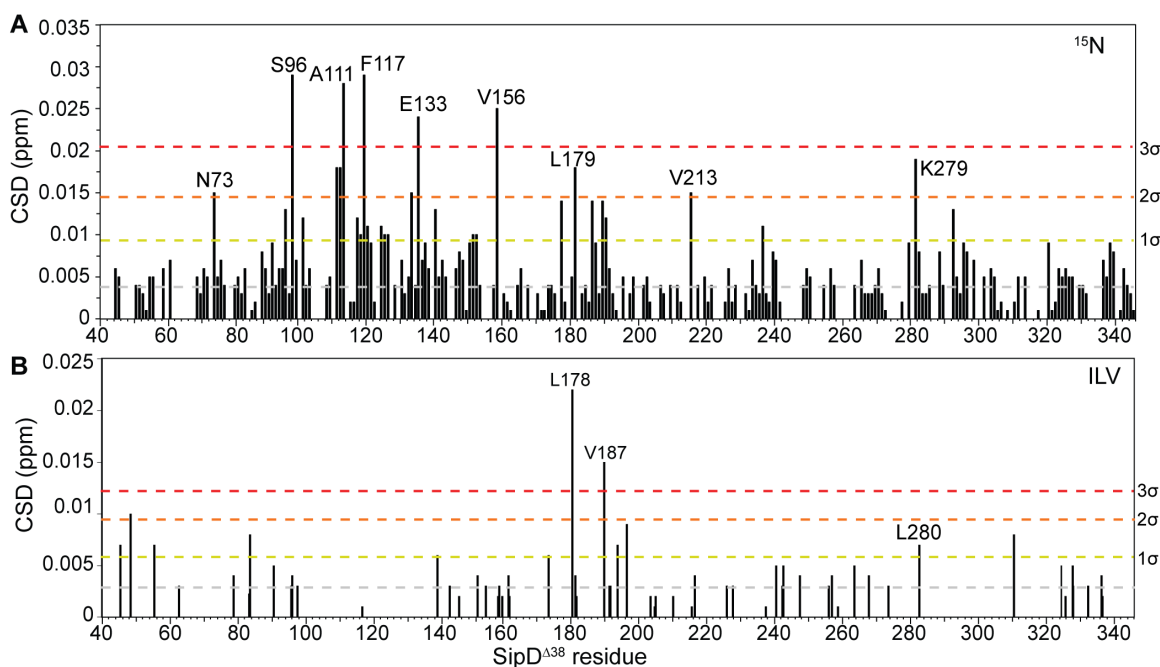
### 10-9 – <sup>15</sup>N Titration of SipD<sup>Δ38</sup> with 4-morpholinoaniline

Titration of <sup>15</sup>N/ILV labeled SipD<sup>Δ38</sup> with 4-morpholinoaniline monitored by 2D <sup>1</sup>H-<sup>15</sup>N TROSY and The two vertical ridges in are from 4-morpholinoaniline.



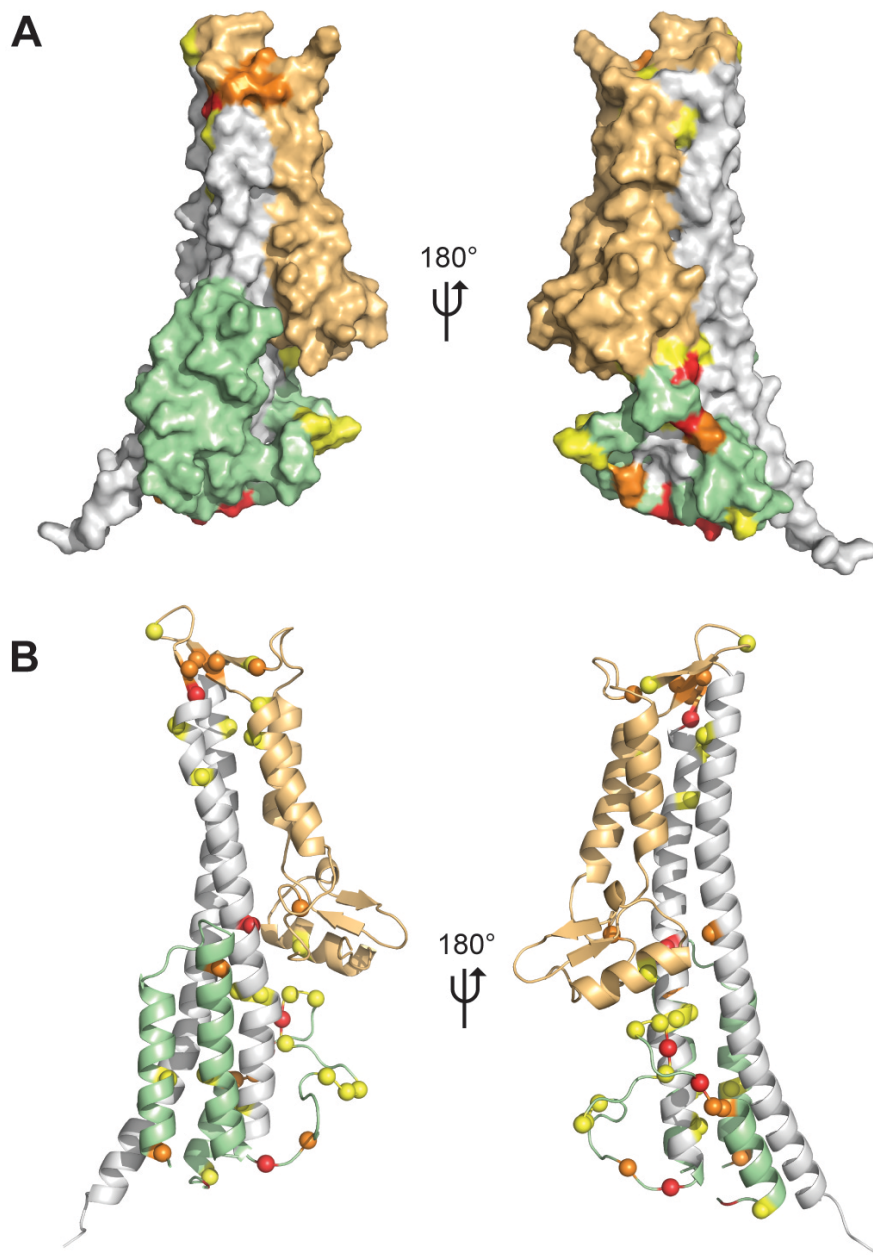
### 10-10 – ILV Titration of SipD<sup>Δ38</sup> with 4-morpholinoaniline

Titration of <sup>15</sup>N/ILV labeled SipD<sup>Δ38</sup> with 4-morpholinoaniline monitored by 2D <sup>1</sup>H-<sup>13</sup>C HSQC.



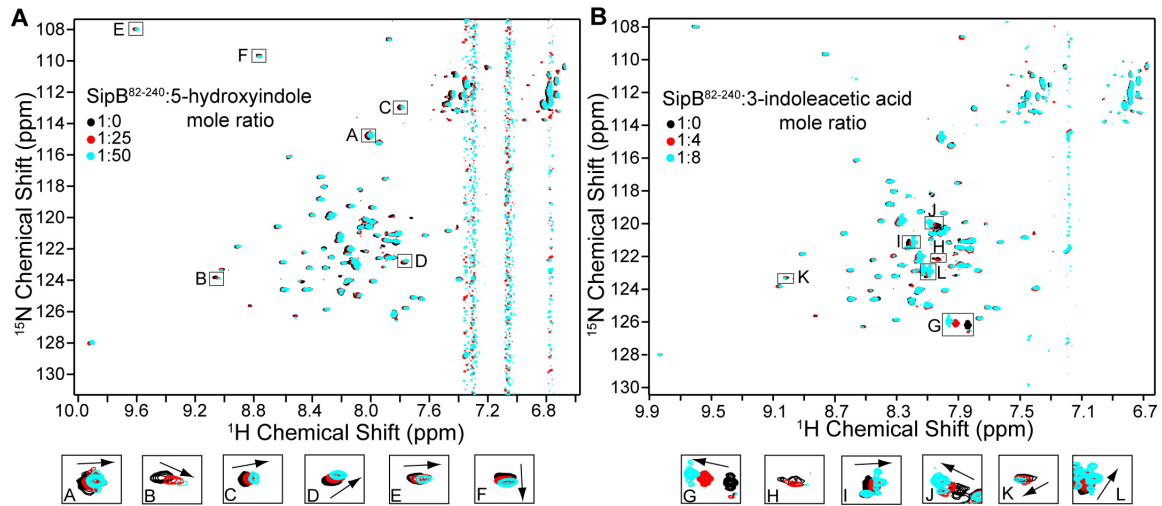
### 10-11 –NMR Titration Analysis of SipD<sup>Δ38</sup> with 4-morpholinoaniline

Plots of chemical shift deviations (CSD) of SipD<sup>Δ38</sup> with 4-morpholinoaniline based on (A) <sup>15</sup>N and (B) ILV titrations ( $\sigma$ , average CSD).

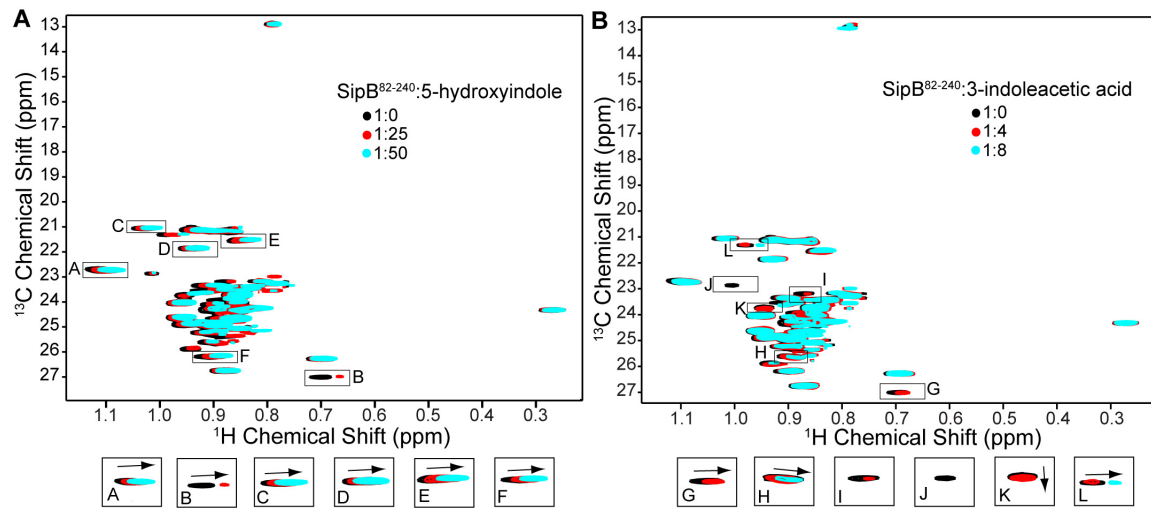


**10-12 –SipD Surfaces Affected by Binding with 4-morpholinoaniline**

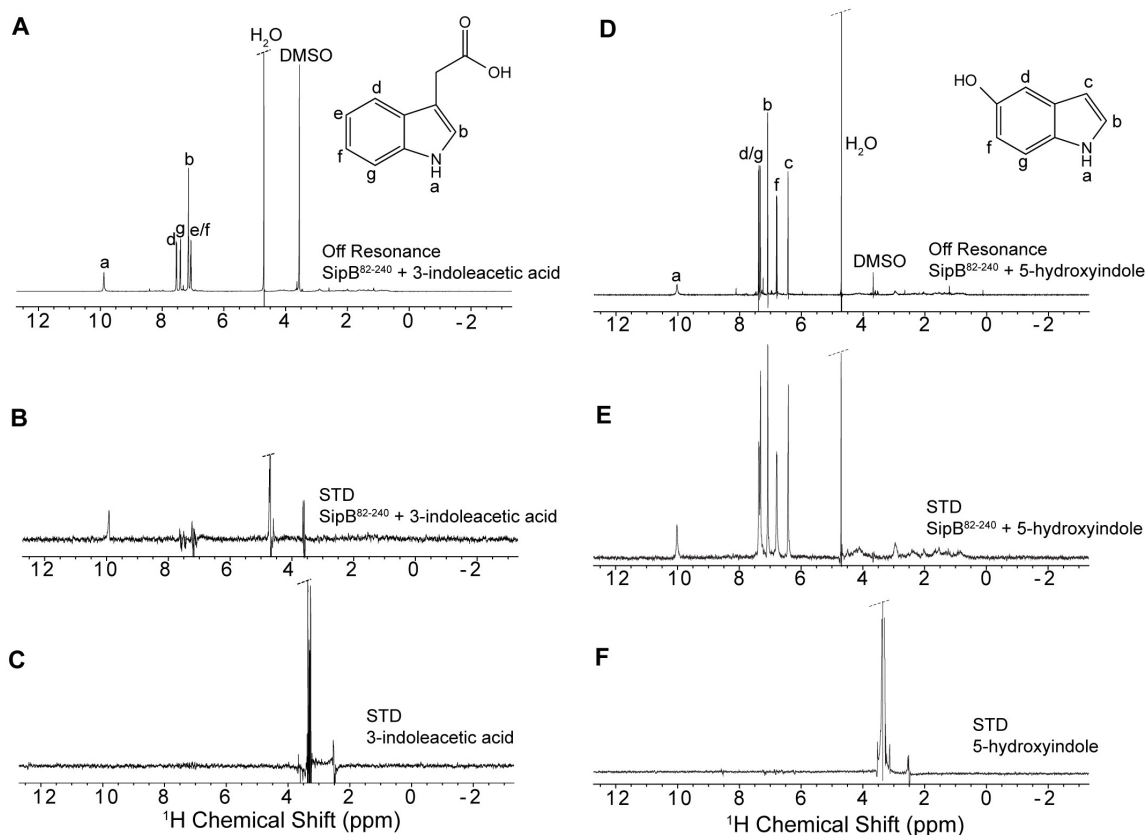
$C\alpha$  of SipD colored according to  $^{15}\text{N}$  and ILV chemical shift deviations as follows:  $1\sigma$  (yellow),  $2\sigma$  (orange),  $3\sigma$  (red); where  $\sigma$  is the standard deviation from the average CSD in Fig. 10-8.



10-13 –  $^{15}\text{N}$  Titration of SipB<sup>82-240</sup> with (A) 5-hydroxyindole and (B) 3-indoleacetic acid



10-14 – ILV Titration of SipB<sup>82-240</sup> with (A) 5-hydroxyindole and (B) 3-indoleacetic acid



### 10-15 – STD NMR of SipB<sup>82-240</sup> with (A-C) 3-indoleacetic acid and (D-F) 5-hydroxyindole

(A, D) Off-resonance and (B, E) on-resonance STD NMR spectra of SipB<sup>82-240</sup> with the small molecules. (C, F) STD NMR spectra of the small molecules in the absence of SipB<sup>82-240</sup>.

### 10.5. References

1. Majowicz, S. E., Musto, J., Scallan, E., Angulo, F. J., Kirk, M., O'Brien, S. J., Jones, T. F., Fazil, A., Hoekstra, R. M. & International Collaboration on Enteric Disease 'Burden of Illness, S. (2010). The global burden of nontyphoidal *Salmonella* gastroenteritis. *Clin Infect Dis* **50**, 882-9.
2. Galan, J. E., Lara-Tejero, M., Marlovits, T. C. & Wagner, S. (2014). Bacterial Type III Secretion Systems: Specialized Nanomachines for Protein Delivery into Target Cells. *Annual Review of Microbiology, Vol 68* **68**, 415-438.
3. McShan, A. C. & De Guzman, R. N. (2015). The Bacterial Type III Secretion System as a Target for Developing New Antibiotics. *Chemical Biology & Drug Design* **85**, 30-42.

4. Chatterjee, S., Chaudhury, S., McShan, A. C., Kaur, K. & De Guzman, R. N. (2013). Structure and Biophysics of Type III Secretion in Bacteria. *Biochemistry* **52**, 2508-2517.
5. Lara-Tejero, M. & Galan, J. E. (2009). Salmonella enterica Serovar Typhimurium Pathogenicity Island 1-Encoded Type III Secretion System Translocases Mediate Intimate Attachment to Nonphagocytic Cells. *Infection and Immunity* **77**, 2635-2642.
6. Chatterjee, S., Zhong, D., Nordhues, B. A., Battaile, K. P., Lovell, S. & De Guzman, R. N. (2011). The crystal structures of the Salmonella type III secretion system tip protein SipD in complex with deoxycholate and chenodeoxycholate. *Protein Sci* **20**, 75-86.
7. Chaudhury, S., Battaile, K. P., Lovell, S., Plano, G. V. & De Guzman, R. N. (2013). Structure of the Yersinia pestis tip protein LcrV refined to 1.65 Å resolution. *Acta Crystallogr Sect F Struct Biol Cryst Commun* **69**, 477-81.
8. Barta, M. L., Dickenson, N. E., Patil, M., Keightley, A., Wyckoff, G. J., Picking, W. D., Picking, W. L. & Geisbrecht, B. V. (2012). The Structures of Coiled-Coil Domains from Type III Secretion System Translocators Reveal Homology to Pore-Forming Toxins. *Journal of Molecular Biology* **417**, 395-405.
9. Dickenson, N. E., Arizmendi, O., Patil, M. K., Toth, R. T. t., Middaugh, C. R., Picking, W. D. & Picking, W. L. (2013). N-Terminus of IpaB Provides a Potential Anchor to the Shigella Type III Secretion System Tip Complex Protein IpaD. *Biochemistry*.
10. Wang, Y., Nordhues, B. A., Zhong, D. & De Guzman, R. N. (2010). NMR characterization of the interaction of the Salmonella type III secretion system protein SipD and bile salts. *Biochemistry* **49**, 4220-6.
11. Hayward, R. D., Cain, R. J., McGhie, E. J., Phillips, N., Garner, M. J. & Koronakis, V. (2005). Cholesterol binding by the bacterial type III translocon is essential for virulence effector delivery into mammalian cells. *Molecular Microbiology* **56**, 590-603.
12. Delaglio, F., Grzesiek, S., Vuister, G. W., Zhu, G., Pfeifer, J. & Bax, A. (1995). NMRPipe: a multidimensional spectral processing system based on UNIX pipes. *J Biomol NMR* **6**, 277-93.
13. Johnson, B. A. (2004). Using NMRView to visualize and analyze the NMR spectra of macromolecules. *Methods Mol Biol* **278**, 313-52.
14. Grzesiek, S., Stahl, S. J., Wingfield, P. T. & Bax, A. (1996). The CD4 determinant for downregulation by HIV-1 Nef directly binds to Nef. Mapping of the Nef binding surface by NMR. *Biochemistry* **35**, 10256-61.
15. Mayer, M. & Meyer, B. (1999). Characterization of ligand binding by saturation transfer difference NMR spectroscopy. *Angewandte Chemie-International Edition* **38**, 1784-1788.
16. Arkin, M. R. & Wells, J. A. (2004). Small-molecule inhibitors of protein-protein interactions: Progressing towards the dream. *Nature Reviews Drug Discovery* **3**, 301-317.
17. Barta, M. L., Guragain, M., Adam, P., Dickenson, N. E., Patil, M., Geisbrecht, B. V., Picking, W. L. & Picking, W. D. (2012). Identification of the bile salt binding

- site on IpaD from *Shigella flexneri* and the influence of ligand binding on IpaD structure. *Proteins-Structure Function and Bioinformatics* **80**, 935-945.
18. Lafont, F., Tran Van Nhieu, G., Hanada, K., Sansonetti, P. & van der Goot, F. G. (2002). Initial steps of *Shigella* infection depend on the cholesterol/sphingolipid raft-mediated CD44-IpaB interaction. *EMBO J* **21**, 4449-57.
  19. Jessen, D. L., Bradley, D. S. & Nilles, M. L. (2014). A Type III Secretion System Inhibitor Targets YopD while Revealing Differential Regulation of Secretion in Calcium-Blind Mutants of *Yersinia pestis*. *Antimicrobial Agents and Chemotherapy* **58**, 839-850.
  20. Rathinavelan, T., Lara-Tejero, M., Lefebvre, M., Chatterjee, S., McShan, A. C., Guo, D. C., Tang, C., Galan, J. E. & De Guzman, R. N. (2014). NMR model of PrgI-SipD interaction and its implications in the needle-tip assembly of the *Salmonella* type III secretion system. *J Mol Biol* **426**, 2958-69.
  21. Gauthier, A., Robertson, M. L., Lowden, M., Ibarra, J. A., Puente, J. L. & Finlay, B. B. (2005). Transcriptional inhibitor of virulence factors in enteropathogenic *Escherichia coli*. *Antimicrobial Agents and Chemotherapy* **49**, 4101-4109.
  22. Enquist, P. A., Gylfe, A., Hagglund, U., Lindstrom, P., Norberg-Scherman, H., Sundin, C. & Elofsson, M. (2012). Derivatives of 8-hydroxyquinoline-antibacterial agents that target intra- and extracellular Gram-negative pathogens. *Bioorganic & Medicinal Chemistry Letters* **22**, 3550-3553.

## Chapter 11. CD and NMR Characterization of Chaperone/Translocon Complexes

### 11.1. Introduction

Currently, the only known atomic structure of T3SS translocon proteins have been restricted to small domains (SipB<sup>82-226</sup>, IpaB<sup>74-224</sup>, YopD<sup>278-300</sup>, AcrH+AopB<sup>40-264</sup>)<sup>1; 2; 3</sup> and peptides with their cognate chaperones (YopD<sup>56-65</sup>+SycD, PopB<sup>51-59</sup>+PcrH, PopD<sup>47-55</sup>+PcrH)<sup>4; 5</sup>. This is presumably because the translocon proteins are stable and properly folded only upon insertion into the host membrane environment, or in complex with their cognate chaperone. Two proteins, a major and a minor translocon, form the T3SS translocon complex. Here, full-length translocon proteins from *Salmonella* and *Pseudomonas* were subcloned, expressed and purified with their cognate chaperone for the purpose of structural characterization and use in studies of protein-protein interaction. Preliminary structural and biophysical analyses were performed, including size exclusion chromatography, circular dichroism and NMR spectroscopy. Data suggest that the full-length translocon-chaperone complexes are not ideal candidates for NMR studies, and in the future should be separated from their chaperone for insertion into membrane or membrane-like environments to determine their structure or used in studies of protein-protein interaction.

### 11.2. Materials and Methods

#### 11.2.1. Subcloning, Protein Expression and Purification

PCR primers were designed to amplify the genes for SicA, SipC and SipB from *Salmonella* Typhimurium strain SL1344. Full-length SicA and SipC were subcloned into

cloning site 1 (using EcoRI/HindIII restriction sites for SicA) and cloning site 2 (using NdeI/XhoI restriction sites for SipC) of the vector pET-DUET1 and confirmed by DNA sequencing. Similarly, full-length SicA and SipB were subcloned into cloning site 1 (using EcoRI/HindIII restriction sites for SicA) and cloning site 2 (using NdeI/XhoI restriction sites for SipB) of pET-DUET1 and confirmed by DNA sequencing.

PCR primers were designed to amplify the genes for PcrH, PopD and PopB from *Pseudomonas aeruginosa* strain PAO1. Full-length PcrH and PopD were subcloned into cloning site 1 (using BamHI/HindIII restriction sites for PcrH) and cloning site 2 (using NdeI/XhoI restriction sites for PopD) of the vector pET-DUET1 and confirmed by DNA sequencing. Similarly, full-length PcrH and PopB were subcloned into cloning site 1 (using BamHI/HindIII restriction sites for PcrH) and cloning site 2 (using NdeI/XhoI restriction sites for PopB) of pET-DUET1 and confirmed by DNA sequencing.

All unlabeled proteins were expressed in *E. coli* BL21(DE3) DNAY cells in 1L of LB media with 100 µg/mL carbenicillin at 37°C. Protein expression was induced at an OD<sub>600</sub> of ~0.8 with 0.5 mM IPTG and expressed at 15°C overnight. Isotopically labeled co-expression of chaperone/translocon constructs were expressed in *E. coli* BL21(DE3) DNAY cells in 1L of 1× M9 minimal media with antibiotics at 37°C containing 1 g/L <sup>15</sup>N<sub>4</sub>Cl (Sigma-Aldrich, St. Louis, MO) and 2 g/L D-glucose. At an OD<sub>600</sub> of ~ 0.4 the growth medium was supplemented with 60 mg of α-ketobutyric acid, sodium salt (methyl-<sup>13</sup>C) (δ methyl group of Ile) (Cambridge Isotope Laboratories, Inc., Andover, MA) dissolved in 1 mL autoclaved water. Protein expression was induced with 0.5 mM IPTG at an OD<sub>600</sub> of 0.8 and cell growth was continued overnight at 15°C. Bacterial cells were harvested by centrifugation at 4000 r.p.m. for 10 minutes, resuspended with binding

buffer (500 mM NaCl, 20 mM Tris-HCl, 5 mM imidazole, pH 8.0, 1 mM phenylmethanesulfonyl fluoride) at 4°C and sonicated while keeping the lysate ice-cold. Cells were sonicated using a Branson Digital Sonifier for 5 minutes and 20 seconds at amplitude 32% with 2 second on pulses and 6 second off pulses. The cell lysate was centrifuged for 10 mins at 13,000 r.p.m. Next, 700 µL of 5% polyethyleneimine was added to the supernatant, which was centrifuged again to remove further cellular debris. The supernatant was loaded onto a 10 mL Ni<sup>2+</sup>-affinity chromatography column (Gold Biotechnology), and the column was washed with 150 mL binding buffer (500 mM NaCl, 20 mM Tris-HCl, 5 mM imidazole, pH 8.0) and bound protein was eluted with 40 mL elution buffer (500 mM NaCl, 20 mM Tris-HCl, 250 mM imidazole, pH 8.0). All purified proteins were dialyzed into NMR buffer and concentrated using Amicon Ultra 3K (Millipore) filtration columns. Protein concentrations were measured by the absorbance at A<sub>280</sub>.

#### *11.2.2. Size Exclusion Chromatography (SEC)*

Purified chaperone/translocon complexes containing 1 mM EDTA and 0.5 mM DTT were loaded onto a Superdex 75 SEC column (column height 51 cm and bed volume 300 mL) (GE Healthcare) to determine their oligomeric state(s) and to separate chaperone/translocon complexes from unbound chaperone. The SEC column was equilibrated with 1 column volume of 150 mM NaCl, 0.5 mM DTT, 10 mM Tris-HCl, pH 8.0. Typical parameters used for SEC runs were 1 mL/min flow rate, 0.3 MPa pressure and 6 mL elution fraction size. The SEC column was calibrated using protein standards of known molecular weights, including Blue Dextran (200 kDa), Albumin (66

kDa), Carbonic Anhydrase (29 kDa), Cytochrome C (12.4 kDa) and Aprotinin (6.5 kDa). To calculate the partition coefficient ( $K_{av}$ ) values for the protein standards, the equation  $K_{av} = (V_e - V_0) / (V_c - V_0)$  was used, where  $V_e$  = elution volume,  $V_0$  = void volume,  $V_c$  = column volume, and  $K_{av}$  = partition coefficient. The logarithm of the molecular weight (y-axis) vs  $K_{av}$  (x-axis) for each protein standard was then plotted to obtain the standard curve,  $y = -0.4207x + 2.118$ , where  $y = K_{av}$  and  $x = \log$  molecular weight in Daltons. The  $K_{av}$  obtained from the SEC run for each peak could then be used to determine the estimated molecular weight using the standard curve.

### 11.2.3. Circular Dichroism (CD)

Far-UV CD experiments were acquired using a JASCO J-815 Spectropolarimeter. The chaperone/translocon complexes for CD were prepared with 0.05 mg/mL protein in 2 mL sterile water in a quartz cuvette. A water blank was acquired and subtracted from each protein spectra. CD spectra were acquired from 190 to 260 nm in triplicate at 20°C with a scan rate of 50 nm/minute. Thermal denaturation experiments were performed by measuring ellipticity at 222 nm over a temperature range of 20°C to 90°C and a ramp rate of 2°C/minute. The experimental CD values of ellipticity (mdeg) were converted to molar ellipticity ( $\theta = \text{deg cm}^2/\text{dmol}$ ). The melting temperature ( $T_m$ ) was calculated using JASCO J-815 software.

### 11.2.3. NMR Spectroscopy

All data was collected using a Bruker Avance 800 MHz spectrometer equipped with a cryogenic triple resonance probe and were processed using NMR pipe<sup>6</sup> and

analyzed using NMRview<sup>7</sup>. Two-dimensional 2D <sup>1</sup>H-<sup>15</sup>N TROSY spectra were acquired at 40°C using 0.5 mM of <sup>15</sup>N/<sup>13</sup>C-Ile (isoleucine <sup>13</sup>C-methyl side-chain) labeled chaperone/translocon complex in NMR buffer (100 mM NaCl, 1 mM DTT, 10 mM sodium phosphate, pH 7.4, 10% D<sub>2</sub>O). Typical acquisition parameters were 200 scans with 2048 complex points (<sup>1</sup>H) and 256 complex points (<sup>15</sup>N) with sweep width 10.01 ppm for <sup>1</sup>H centered at 4.69 ppm and 17.9 ppm for <sup>15</sup>N centered at 119 ppm. Two-dimensional <sup>1</sup>H-<sup>13</sup>C HSQC spectra were acquired at 40°C using 0.5 mM <sup>15</sup>N/<sup>13</sup>C-Ile labeled chaperone/translocon complex in NMR buffer. Typical acquisition parameters were 128 scans with 1024 complex points (<sup>1</sup>H) and 100 complex points (<sup>13</sup>C) with sweep width 10.01 ppm for <sup>1</sup>H centered at 4.69 ppm and 20 ppm for <sup>13</sup>C centered at 19 ppm.

### 11.3. Results

#### 11.3.1. Purification of hisSicA/SipC

Originally, the chaperone/translocon constructs were subcloned in a dual expression system<sup>8</sup> where the chaperone was inserted into multiple cloning site 1 (MCS1) of pET-DUET1 and the translocon was inserted into MCS2 of pACYC- DUET1. However, this dual expression system resulted in significant overexpression of the chaperone protein relative to minor expression of the translocon proteins. Therefore, the chaperones were kept in MCS1 of pET-DUET1, while the translocon was inserted into MCS2 of the pET-DUET1 vector containing the chaperone. This single vector system resulted in much better expression of the translocon relative to the chaperone.

HisSicA/SipC complex was expressed and purified by affinity chromatography. The elution from the Ni<sup>2+</sup> column was loaded onto an SEC column to separate any free

chaperone from the sample. SEC results showed two primary peaks: one corresponding to the hisSicA/SipC complex and one corresponding to monomeric hisSicA (**Fig. 11-1A**). An SDS-PAGE gel of the SEC column sample elutions resulted in two bands representing purified hisSicA (20.9 kDa) and SipC (42.9 kDa), suggesting that the hisSicA/SipC complex was successfully isolated (**Fig. 11-1B**). CD of the hisSicA/SipC complex showed minima at 208 and 222 nm with a  $\theta_{222/208}$  ratio of 1.02, indicating highly  $\alpha$ -helical content (**Fig. 11-2A**). Thermal denaturation experiments showed that the hisSicA/SipC complex had a single thermal melt at 55°C (**Fig. 11-2B**).

Unfortunately, although hisSicA/SipB was subcloned and verified by DNA sequencing, experiments showed that the plasmid containing hisSicA/SipB resulted only in expression of hisSicA, but never SipB (data not shown). Many expression experiments were performed with varying parameters (growth temperature, IPTG concentration), but full-length SipB did not express under any attempted condition. Therefore, our biophysical characterization of the *Salmonella* translocon proteins was limited to the HisSicA/SipC complex.

### 11.3.2. NMR Spectroscopy of hisSicA/SipC

Isotopically  $^{15}\text{N}/^{13}\text{C}$ -Ile labeled HisA/SipC complex was prepared to observe whether amide or isoleucine methyl resonances of HisA/SipC complex good quality NMR data. Unfortunately, two-dimensional  $^1\text{H}$ - $^{15}\text{N}$  TROSY and  $^1\text{H}$ - $^{13}\text{C}$  HSQC experiments showed that hisSicA/SipC NMR peaks were broad and not well-resolved (**Fig. 11-3A, B**). The 2D  $^1\text{H}$ - $^{15}\text{N}$  TROSY spectrum showed < 20% of expected amide peaks and the  $^1\text{H}$  resonance dispersion was < 1 ppm, indicating the presence of many

disordered regions (**Fig. 11-3A**). Similarly, the 2D  $^1\text{H}$ - $^{13}\text{C}$  HSQC spectrum showed 8 out of 29 expected isoleucine peaks for the complex (**Fig. 11-3B, 12 to 15 ppm  $^{13}\text{C}$  range**). Together, these data suggest that the hisSicA/SipC is not an optimal complex for TROSY/HSQC experiments.

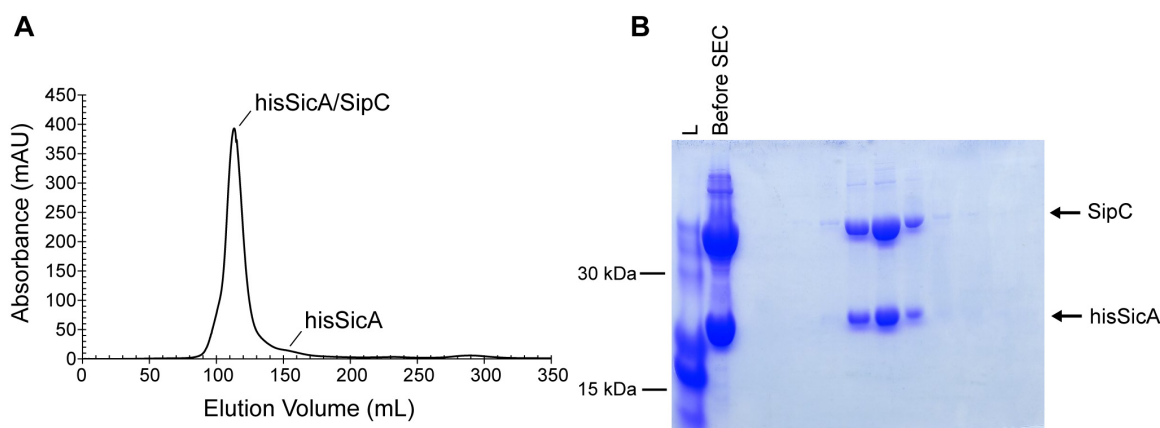


**Fig. 11-1 – Purification of hisSicA/SipC**

(**A**) SEC of hisSicA shows two peaks; one for the hisSicA/SipC complex at a 1:1 protein ratio and one for monomeric hisSicA. (**B**) SDS-PAGE gel of sample elutions from the SEC column shows the purified hisSicA/SipC complex. L is the protein ladder.

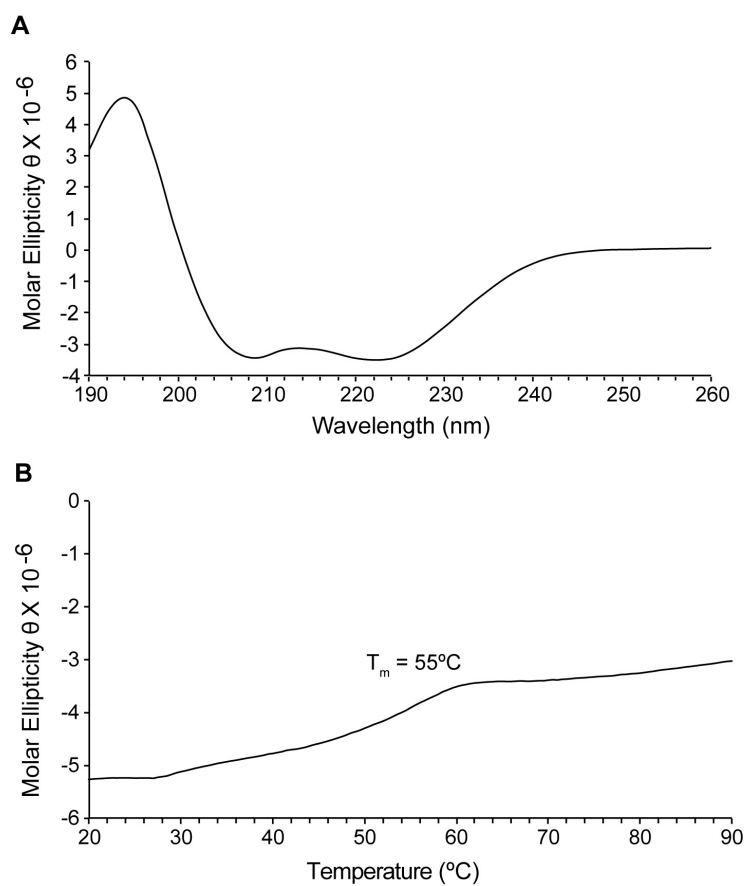


**Fig. 11-2 – Circular Dichroism of hisSicA/SipC**

(A) Far-UV CD of hisSicA/SipC shows minima at 208 and 222 nm, indicating the presence of  $\alpha$ -helical character. (B) Thermal denaturation of the hisSicA/SipC complex estimates a single thermal melt at 55 $^{\circ}\text{C}$ .

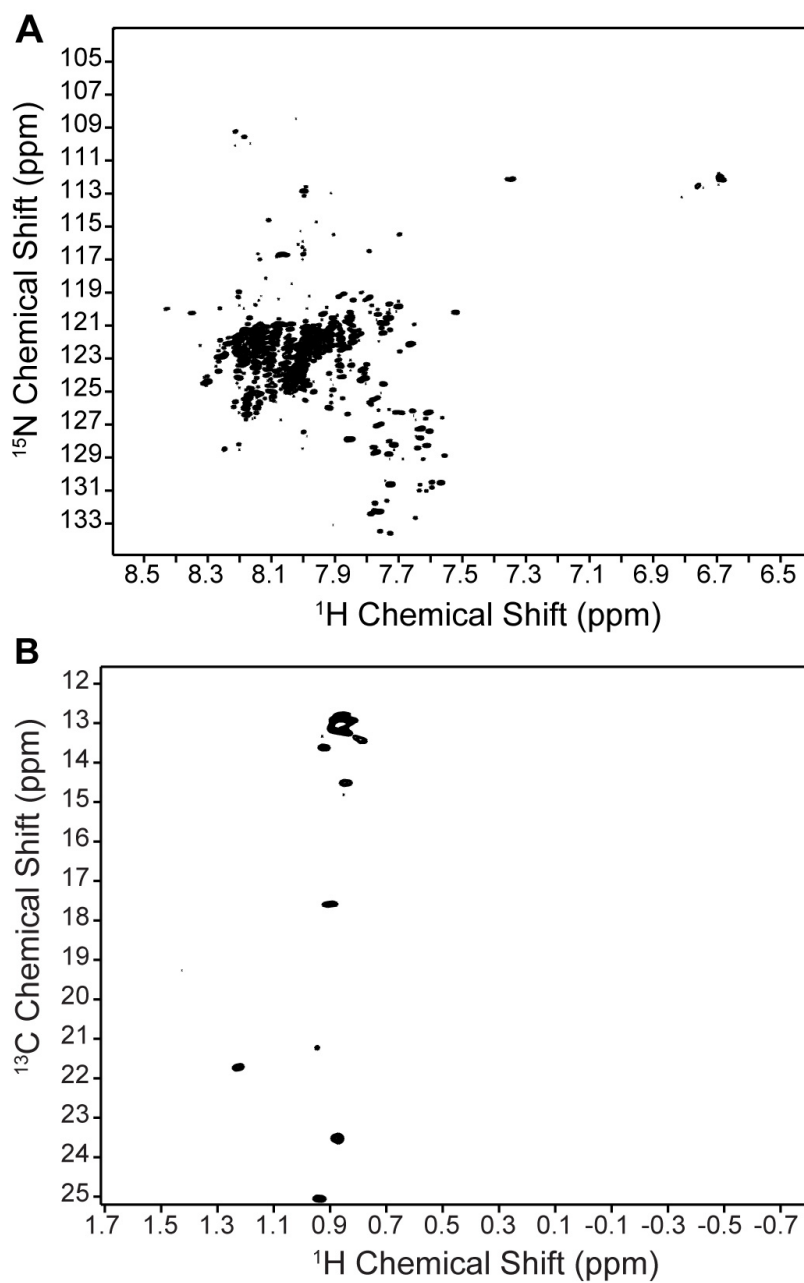


**Fig. 11-3 – NMR Spectroscopy of hisSicA/SipC**

**(A)** 2D  $^1\text{H}$ - $^{15}\text{N}$  TROSY of the  $^{15}\text{N}/^{13}\text{C}$ -Ile labeled hisSicA/SipC complex shows  $<1$  ppm  $^1\text{H}$  dispersion, broad resonances and less than 40% of expected amide resonances. **(B)** The 2D  $^1\text{H}$ - $^{13}\text{C}$  HSQC of the  $^{15}\text{N}/^{13}\text{C}$ -Ile labeled hisSicA/SipC complex shows  $\sim 8$  out of 29 expected Ile methyl resonances.

### 11.3.3. Purification of hisPcrH/PopD and hisPcrH/PopB

HisPcrH/PopD expressed and was purified by affinity chromatography. The elution from the Ni<sup>2+</sup> column was loaded onto an SEC column to separate free chaperone hisPcrH from the sample. The SEC column showed two peaks; one corresponding to the hisPcrH/PopD complex and one corresponding to monomeric hisPcrH (**Fig. 11-4A**). An SDS-PAGE gel of the SEC column elutions showed two bands representing purified hisPcrH (19.5 kDa) and PopD (31.3 kDa) (**Fig. 11-4B**). In contrast to hisSicA/SipB, which didn't express, hisPcrH/PopB expressed and was purified by affinity chromatography. SEC showed two primary peaks; one corresponding to the hisPcrH/PopB complex and one corresponding to monomeric hisPcrH (**Fig. 11-5A**). Furthermore, SEC of hisPcrH/PopB resulted in much more free hisPcrH (**Fig. 11-5A**) compared to SEC of hisPcrH/PopD (**Fig. 11-4A**). An SDS-PAGE of the SEC elutions showed bands representing purified hisPcrH (19.5 kDa) and PopB (62.4 kDa) (**Fig. 11-5B**). CD of the hisPcrH/PopD and hisPcrH/PopB complexes resulted in minima at 208 and 222 nm with a  $\theta_{222/208}$  ratio of 1.00, indicating highly  $\alpha$ -helical content (**Fig. 11-6A**). Thermal denaturation experiments estimated that the hisPcrH/PopD and hisPcrH/PopB complexes had a single thermal melt around 55°C (**Fig. 11-6B**).

### 11.3.4. NMR of Free hisPcrH, hisPcrH/PopB and hisPcrH/PopD

NMR experiments were performed on the isotopically <sup>15</sup>N/<sup>13</sup>C-Ile labeled hisPcrH/PopD complex. Two-dimensional <sup>1</sup>H-<sup>15</sup>N TROSY and <sup>1</sup>H-<sup>13</sup>C HSQC experiments showed that hisPcrH/PopD NMR peaks were very broad and not well resolved (**Fig. 11-7A, B**). The 2D <sup>1</sup>H-<sup>15</sup>N TROSY spectrum showed < 20% of expected

amide resonances and the  $^1\text{H}$  resonance dispersion was  $< 1$  ppm, indicating the presence of many disordered regions (**Fig. 11-7A**). Likewise, the 2D  $^1\text{H}$ - $^{13}\text{C}$  HSQC spectrum showed 5 out of 18 expected isoleucine methyl peaks (**Fig. 11-7B, 11 to 15 ppm  $^{13}\text{C}$  range**). Together, these data suggest that the hisPcrH/PopD complex is not ideal for typical TROSY/HSQC NMR experiments. Similarly, NMR experiments were performed on  $^{15}\text{N}/^{13}\text{C}$ -Ile labeled hisPcrH/PopB complex. As with other the chaperone/translocon constructs, the 2D  $^1\text{H}$ - $^{15}\text{N}$  TROSY spectrum of hisPcrH/PopB showed NMR peaks that were broad and not well resolved (**Fig. 11-8B**). In contrast, the 2D  $^1\text{H}$ - $^{15}\text{N}$  TROSY spectrum of free hisPcrH showed  $^1\text{H}$  resonance dispersion of  $>3$  ppm and the resonances were well resolved (**Fig. 11-8B**), unlike the broad amide peaks of hisPcrH/PopB or hisPcrH/PopD. Together, these data suggest that the hisPcrH/PopB complex is not ideal for typical TROSY/HSQC experiments and that the presence of the translocon, not the chaperone, reduces the quality of the chaperone/translocon NMR spectra.

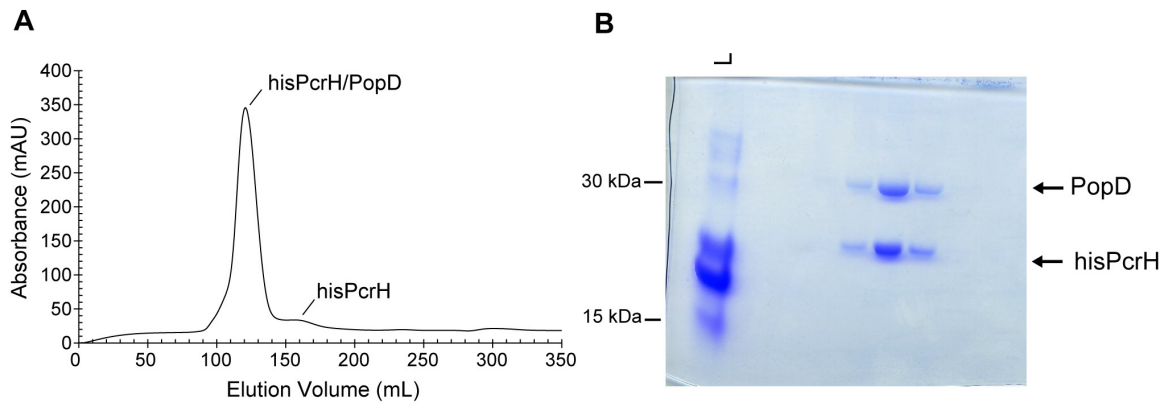


**Fig. 11-4 – Purification of hisPcrH/PopD**

(A) SEC of hisPcrH/PopD shows two peaks; one is the hisPcrH/PopD complex and one is free hisPcrH. (B) SDS-PAGE gel SEC column elutions showing purified hisPcrH/PopD complex. L is the protein ladder.

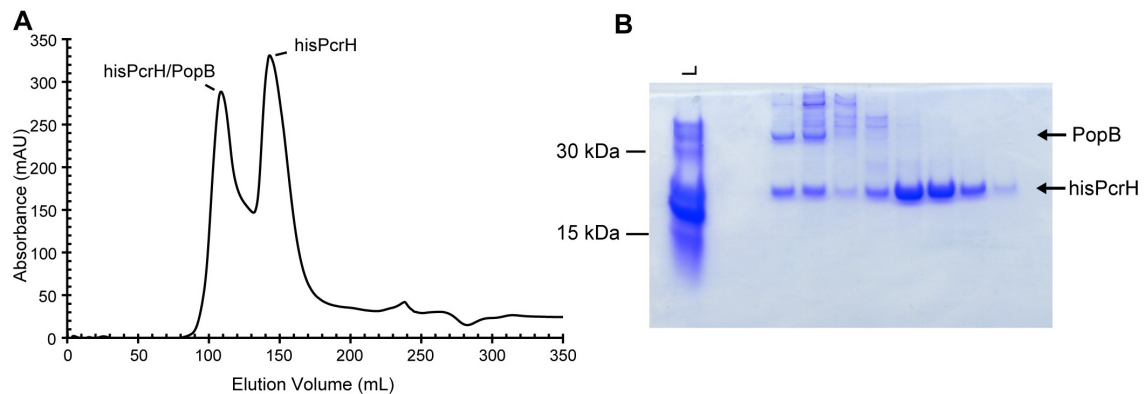


**Fig. 11-5 – Purification of Free hisPcrH and hisPcrH/PopB**

(A) SEC of hisPcrH/PopB shows two peaks; one is the hisPcrH/PopB complex and one is free hisPcrH. (B) SDS-PAGE gel of SEC column elutions showing purified hisPcrH/PopB complex and purified free hisPcrH. L is the protein ladder.

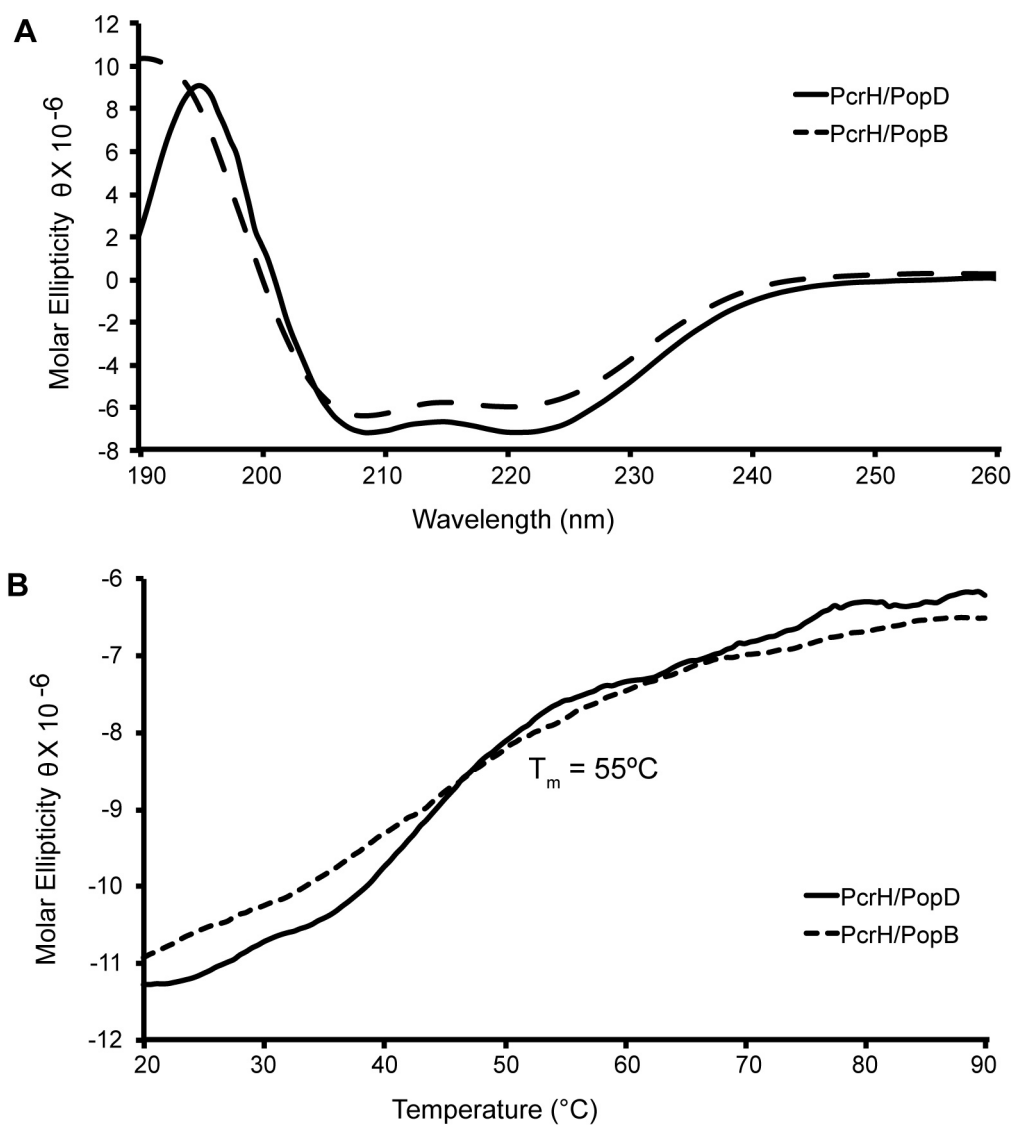


**Fig. 11-6 – Circular Dichroism of hisPcrH/PopD and hisPcrH/PopB**

(A) Far-UV circular dichroism of hisPcrH/PopD and hisPcrH/PopB shows minima at 208 and 222 nm. (B) Thermal denaturation of hisPcrH/PopD and hisPcrH/PopB estimates a single thermal melt at 55°C.

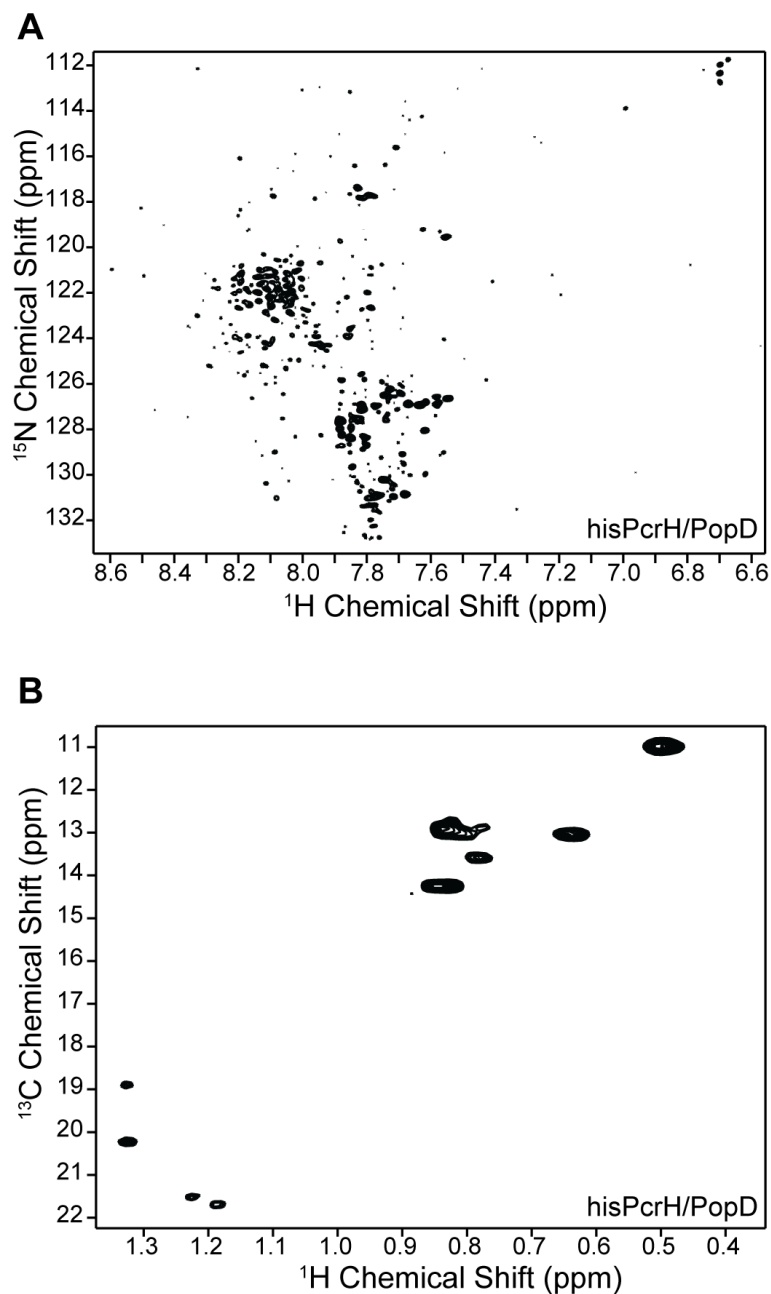


**Fig. 11-7 – NMR Spectroscopy of hisPcrH/PopD**

(A) 2D  $^1\text{H}$ - $^{15}\text{N}$  TROSY of the  $^{15}\text{N}/^{13}\text{C}$ -Ile labeled hisPcrH/PopD complex shows  $<1$  ppm  $^1\text{H}$  dispersion, broad resonances and less than 40% of expected amide peaks. (B) 2D  $^1\text{H}$ - $^{13}\text{C}$  HSQC of the  $^{15}\text{N}/^{13}\text{C}$ -Ile labeled hisPcrH/PopD complex shows 5 out of 18 expected Ile methyl peaks.

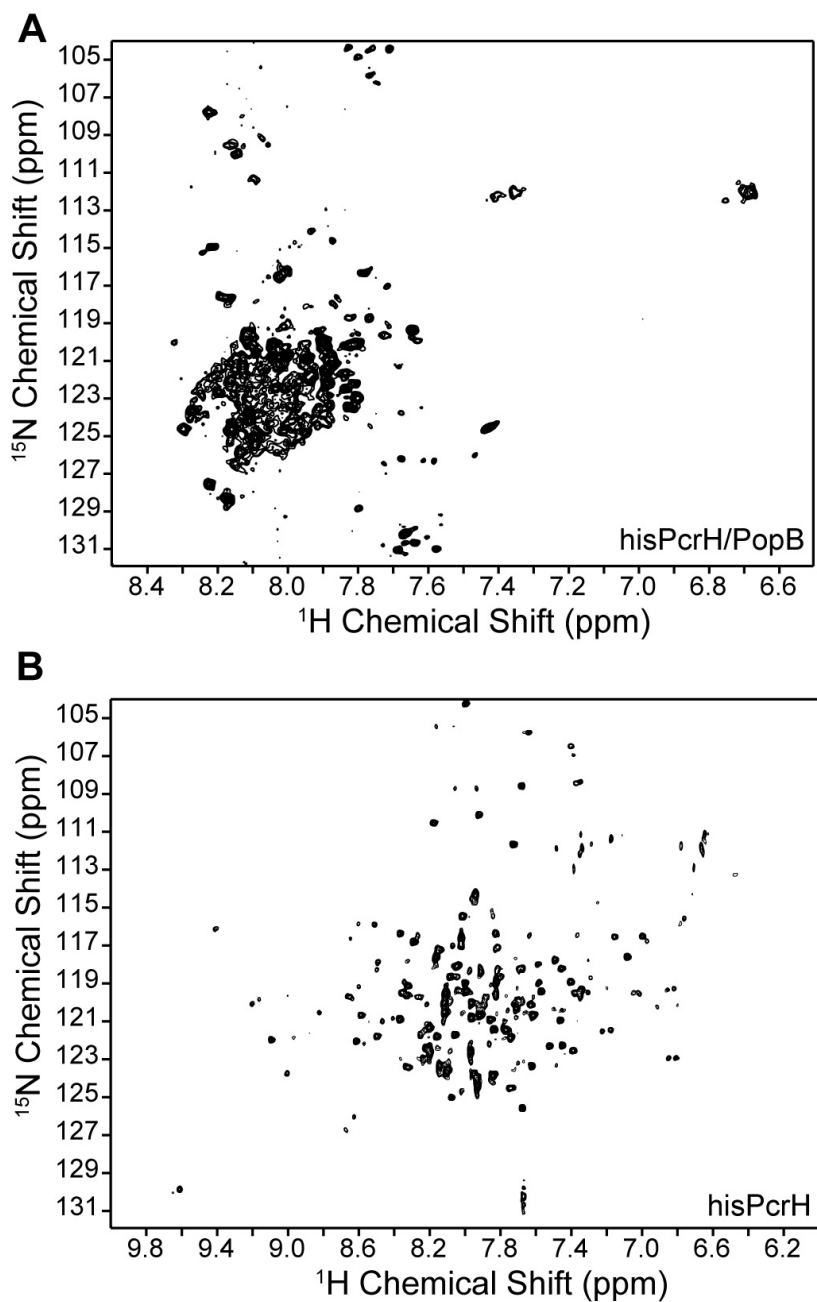


**Fig. 11-8 – NMR Spectroscopy of Free hisPcrH and hisPcrH/PopB**

**(A)** 2D  $^1\text{H}$ - $^{15}\text{N}$  TROSY of the  $^{15}\text{N}/^{13}\text{C}$ -Ile labeled hisPcrH/PopB complex shows  $<1$  ppm  $^1\text{H}$  dispersion, broad resonances and less than 40% of expected amide peaks. **(B)** 2D  $^1\text{H}$ - $^{15}\text{N}$  TROSY of the  $^{15}\text{N}/^{13}\text{C}$ -Ile labeled free hisPcrH shows  $>3$  ppm  $^1\text{H}$  dispersion and well resolved amide peaks.

## 11.4. Discussion

In the chapter, chaperone/translocon complexes were successfully co-expressed and co-purified, including hisSicA/SipC (**Fig. 11-1**) from *Salmonella* Typhimurium and hisPcrH/PopD (**Fig. 11-4**) and hisPcrH/PopB (**Fig. 11-5**) from *Pseudomonas aeruginosa*. CD experiments of hisSicA/SipC (**Fig. 11-2A**) and hisPcrH/PopD or hisPcrH/PopB (**Fig. 11-6A**) showed that the chaperone/minor translocon complexes contained  $\alpha$ -helical coiled-coils due to their  $\theta_{222/208}$  nm ratio near 1.0. Furthermore, both had a single melting point of 55°C (**Fig. 11-2B & Fig. 11-6B**). Unfortunately, all of the chaperone/translocon complexes tested here gave poor NMR spectrum in both 2D  $^1\text{H}$ - $^{15}\text{N}$  TROSY and 2D  $^1\text{H}$ - $^{13}\text{C}$  HSQC experiments. HisSicA/SipC (**Fig. 11-3**), hisPcrH/PopD (**Fig. 11-7**) and hisPcrH/PopB (**Fig. 11-8A**) resonances were broad and not well resolved, and many of the expected amide or isoleucine methyl peaks were not observed. First, the poor quality NMR spectra observed could be due to the high molecular weight of the chaperone/translocon complexes; HisSicA/SipC is 64 kDa, hisPcrH/PopD is 50.8 kDa and hisPcrH/PopB is 59.5 kDa. It is not surprising to see broad resonances for large protein complexes<sup>9</sup>. However, with some experimental optimization and perdeuteration it is likely that the resolution may be increased somewhat. Second, poor quality NMR data could be due to the presence of disordered regions in the translocon protein. Interestingly, free hisPcrH gave excellent 2D  $^1\text{H}$ - $^{15}\text{N}$  TROSY data with >3 ppm  $^1\text{H}$  dispersion and well resolved resonances, unlike hisPcrH/PopD and hisPcrH/PopB (**Fig. 11-8B**). Therefore, it is likely the presence of disordered regions in the translocon protein, not the chaperone, which dictates the poor quality of the chaperone/translocon complexes. The chaperones bind to only a small region of the translocon, leaving the rest of the

translocon mobile in solution and hydrophobic translocon proteins that are not in their native conformation likely harbor unfolded regions. Together, these data suggest that chaperone/translocon complexes are not ideal for NMR experiments. Instead, the chaperone and translocon proteins should be separated by use of detergents<sup>8</sup> or changes in pH<sup>10</sup>. In all constructs, the chaperone contains a His tag while the translocon doesn't, making affinity purification following separation plausible. Following separation and isolation from the chaperones, the translocon proteins should then be put into a membrane, such as a nanodisc, or membrane-like environments, such as micelles, for structure analysis or protein interaction experiments.

## 11.5. References

1. Barta, M. L., Dickenson, N. E., Patil, M., Keightley, A., Wyckoff, G. J., Picking, W. D., Picking, W. L. & Geisbrecht, B. V. (2012). The Structures of Coiled-Coil Domains from Type III Secretion System Translocators Reveal Homology to Pore-Forming Toxins. *Journal of Molecular Biology* **417**, 395-405.
2. Tengel, T., Sethson, I. & Francis, M. S. (2002). Conformational analysis by CD and NMR spectroscopy of a peptide encompassing the amphipathic domain of YopD from *Yersinia*. *European Journal of Biochemistry* **269**, 3659-3668.
3. Nguyen, V. S., Jobichen, C., Tan, K. W., Tan, Y. W., Chan, S. L., Ramesh, K., Yuan, Y., Hong, Y., Seetharaman, J., Leung, K. Y., Sivaraman, J. & Mok, Y. K. (2015). Structure of AcrH-AopB Chaperone-Translocator Complex Reveals a Role for Membrane Hairpins in Type III Secretion System Translocon Assembly. *Structure* **23**, 2022-31.
4. Schreiner, M. & Niemann, H. H. (2012). Crystal structure of the *Yersinia enterocolitica* type III secretion chaperone SycD in complex with a peptide of the minor translocator YopD. *Bmc Structural Biology* **12**.
5. Banerjee, A., Dey, S., Chakraborty, A., Datta, A., Basu, A., Chakrabarti, S. & Datta, S. (2014). Binding mode analysis of a major T3SS translocator protein PopB with its chaperone PcrH from *Pseudomonas aeruginosa*. *Proteins* **82**, 3273-85.
6. Delaglio, F., Grzesiek, S., Vuister, G. W., Zhu, G., Pfeifer, J. & Bax, A. (1995). NMRPipe: a multidimensional spectral processing system based on UNIX pipes. *J Biomol NMR* **6**, 277-93.
7. Johnson, B. A. (2004). Using NMRView to visualize and analyze the NMR spectra of macromolecules. *Methods Mol Biol* **278**, 313-52.

8. Romano, F. B., Rossi, K. C., Savva, C. G., Holzenburg, A., Clerico, E. M. & Heuck, A. P. (2011). Efficient Isolation of *Pseudomonas aeruginosa* Type III Secretion Translocators and Assembly of Heteromeric Transmembrane Pores in Model Membranes. *Biochemistry* **50**, 7117-7131.
9. Fernandez, C. & Wider, G. (2003). TROSY in NMR studies of the structure and function of large biological macromolecules. *Current Opinion in Structural Biology* **13**, 570-580.
10. Schoehn, G., Di Guilmi, A. M., Lemaire, D., Attree, I., Weissenhorn, W. & Dessen, A. (2003). Oligomerization of type III secretion proteins PopB and PopD precedes pore formation in *Pseudomonas*. *Embo Journal* **22**, 4957-4967.

## Chapter 12. Overall Discussion and Future Directions

### 12.1. Overall Discussion and Future Directions

The T3SS is an essential virulence factor used by many Gram-negative bacterial pathogens, including the causative agents of food poisoning/typhoid (*Salmonella* Typhimurium /Typhi), dysentery (*Shigella flexneri*), pneumonia (*Pseudomonas aeruginosa*), bubonic plague (*Yersinia pestis*), and trachoma/sexually-transmitted disease (*Chlamydia trachomatis*) (**Table 1-1**). Since the visualization of the needle apparatus in 1998 by Galan and co-workers<sup>1</sup>, extensive effort has gone into characterizing the structure and function of the more than 20 proteins that assemble to form the structural component of the T3SS. The needle apparatus is composed of a bacterial membrane spanning base, an extracellular needle, a tip complex, and a translocon that creates a pore in the host cell membrane. The protein-protein interactions involved at the needle-tip and tip-translocon interfaces of the needle apparatus are poorly understood. Therefore, work described in this dissertation was directed towards characterizing the interactions of the *Salmonella* needle protein PrgI and the tip protein SipD; as well as the interaction between SipD and the major translocon protein SipB. In addition, because the T3SS is utilized among pathogenic bacteria and parts of the needle apparatus are exposed to the extracellular environment, the T3SS represents an attractive target for the development of new antibiotics<sup>2</sup>. Therefore, work described in this dissertation was additionally directed at discovering small molecule fragments that bound to T3SS proteins that could serve as scaffolds for the development of inhibitors of T3SS protein-protein interactions.

### 12.1.1. Isotopic $^{13}\text{C}$ Labeling of ILV Side-Chain Methyls in T3SS Proteins

Many proteins needed for the assembly of the T3SS apparatus, such as the tip and translocon, are large molecules in the range of 40 kDa or more, especially when they form complexes with their binding partners. Therefore, structural and biophysical studies of large molecular weight T3SS proteins and characterizing T3SS protein-protein interactions by NMR spectroscopy require unique experimental strategies. One such strategy is the isoleucine, leucine and valine (ILV) side-chain  $^{13}\text{C}$ -methyl isotopic labeling scheme developed by Lewis Kay and co-workers<sup>3</sup>. In this method,  $\alpha$ -ketoacids, such as  $\alpha$ -ketobutyrate and  $\alpha$ -ketoisovalerate, serve as biosynthetic precursors for specifically labeled Ile and Leu/Val side-chain methyl carbons, respectively<sup>4</sup>. Compared to amide labeling, ILV  $^{13}\text{C}$ -methyl labels are useful probes because they contain favorable relaxation properties for high molecular weight systems, are more sensitive due to averaging of three proton signals, and they reduce complexity of protein NMR spectra<sup>5; 6; 7</sup>.

In Chapter 2, the ILV methyl resonances of the *Salmonella* Typhimurium T3SS SPI-1 tip protein SipD $^{\Delta 38}$  were completely assigned (**Fig. 2-6**). This represents the first report of ILV methyl resonance assignments for a T3SS protein. The 2D  $^1\text{H}$ - $^{13}\text{C}$  HSQC spectrum (**Fig. 2-6**) of SipD $^{\Delta 38}$  is far less complex than the 2D  $^1\text{H}$ - $^{15}\text{N}$  TROSY spectrum (**Fig. 3-2**) of SipD $^{\Delta 38}$ . This allowed for simpler analysis of NMR titration experiments. The ILV methyl assignments of SipD $^{\Delta 38}$  were useful in elucidating the interaction of SipD with both the needle protein PrgI (**Chapter 4**) and the N-terminal ectodomain of the major translocon protein SipB (**Chapter 7**). Simultaneous labeling of T3SS proteins with  $^{15}\text{N}$  and ILV probes allowed for comparison between affected amide and ILV methyl

resonances. Importantly, the protein interaction surfaces identified from  $^{15}\text{N}$  titrations were in agreement with the surfaces identified from ILV methyl titrations.

Two-dimensional  $^1\text{H}$ - $^{13}\text{C}$  HSQC spectra of ILV labeled PrgI\* (**Fig. 4-8**) and SipB<sup>82-240</sup> (**Fig. 10-14**) helped either confirm or deny the presence of a molecular interaction with other molecules, even in the absence of NMR assignments. ILV methyl peaks of PrgI\* could plausibly be assigned in the future due to the high quality spectra and observation of the expected number of resonances (**Fig. 4-8**). In contrast, many expected ILV methyl peaks of SipB<sup>82-240</sup>, SipB<sup>11-232</sup>, and SipB<sup>11-312</sup> were absent from the 2D  $^1\text{H}$ - $^{13}\text{C}$  HSQC spectra (**Fig. 6-5**) so their complete assignment is currently not plausible. Likewise, 2D  $^1\text{H}$ - $^{13}\text{C}$  HSQC spectra of ILV labeled of chaperone/translocon complexes, such as SicA/SipC, PcrH/PopB and PcrH/PopD, resulted in poor quality data with broad resonances,  $<1$  ppm  $^1\text{H}$  dispersion and less than the expected number of resonances, likely due to presence of disordered or unfolded regions in the translocon (**Chapter 11**).

In summary, ILV labeling of T3SS proteins is a robust and useful strategy to aid in the elucidation of T3SS protein structure and protein-protein interactions.

### 12.1.2. Comparison of SipD<sup>Δ38</sup> and SipD<sup>Δ132</sup>

The N-terminal  $\alpha$ -helical domain of the *Salmonella* tip protein SipD is known to be a self-chaperone domain<sup>8</sup>, but is also hypothesized to regulate the interaction of SipD with other T3SS proteins<sup>9</sup>. To determine the role of the N-terminal domain of SipD in the context of its interactions with other T3SS proteins, a SipD construct lacking its N-terminal  $\alpha$ -helical domain, SipD<sup>Δ132</sup>, was compared to a construct of SipD containing its

N-terminal  $\alpha$ -helical domain, SipD $^{\Delta 38}$ . Circular dichroism showed that SipD $^{\Delta 38}$  and SipD $^{\Delta 132}$  had similar secondary structure characteristics (**Fig. 3-1A**), but slightly different thermal denaturation profiles (**Fig. 3-1B**). Data suggested that the  $T_m$  at 61°C was due to the N-terminal domain and the  $T_m$  at 75°C was due to the other domains of SipD (**Fig. 3-1**). The 2D  $^1\text{H}$ - $^{15}\text{N}$  TROSY spectra and  $^1\text{H}$ - $^{13}\text{C}$  HSQC spectra of SipD $^{\Delta 38}$  and SipD $^{\Delta 132}$  were similar to each other with many peaks overlapping (**Fig. 3-4 & Fig. 3-7**). This allowed for transfer of both amide (**Fig. 3-5**) and ILV methyl (**Fig. 3-8**) resonance assignments from SipD $^{\Delta 38}$  to SipD $^{\Delta 132}$ . I was able to assign 82% of amide and 76% of ILV methyl resonances for SipD $^{\Delta 132}$ . The amide and ILV methyl assignments were useful in elucidating the interaction of SipD $^{\Delta 132}$  with PrgI (**Chapter 4**) and SipB (**Chapter 7**).

### *12.1.3. Summary of the needle-tip and tip-translocon interactions*

The N-terminal  $\alpha$ -helical hairpin of SipD is hypothesized to regulate the interaction of SipD with other T3SS proteins, such as the needle protein PrgI<sup>9</sup>. In support of this hypothesis, PrgI was shown by NMR spectroscopy and fluorescence spectroscopy to bind tighter to SipD $^{\Delta 132}$  or SipD $^{\Delta 100}$  (both lack the N-terminal  $\alpha$ -helical domain) than to SipD $^{\Delta 38}$  (contains N-terminal domain). PrgI did not show signs of interaction with SipD $^{\Delta 38}$  by solution NMR (**Fig. 4-1 & Fig 4-2**). Results of FP and FRET detected a very weak interaction between PrgI and SipD $^{\Delta 38}$  (**Fig 5-3A & Fig. 5-4B**), but the binding of PrgI to SipD $^{\Delta 100}$  was much stronger (**Fig. 5-3A & Fig. 5-4A**). Results of NMR titrations between PrgI and SipD $^{\Delta 132}$  in Chapter 4 elucidated the following: *i*) a cluster of affected residues near the bottom of the SipD $^{\Delta 132}$  coiled-coil (**Fig. 4-6A, B**) and *ii*) a cluster of affected residues near the middle of the  $\alpha$ -helical hairpin and both the N- and C-termini

of PrgI\* (**Fig. 4-7B**). The PrgI\*/SipD<sup>Δ100</sup> interaction was estimated to be  $108 \pm 11 \mu\text{M}$  in FP experiments (**Fig. 5-3A**) and removal of the SipD N-terminal domain resulted in higher FRET signal with PrgI\* (**Fig. 5-4A**). SipD mutations along the bottom of the coiled-coil domain decreased the ability of *Salmonella* Typhimurium to invade intestinal epithelial Henle-407 cells (**Fig 5-6**). Importantly, this observed decrease in invasion correlated well with a decrease in binding affinity between PrgI\* and SipD<sup>Δ100</sup> (**Fig 5-3A, B**).

Because the proximal end of SipD (defined as the bottom of coiled-coil, Fig 7-1C) interacted with PrgI, it was hypothesized that the distal end of SipD (defined as top of coiled-coil and mixed  $\alpha/\beta$  domain, Fig 7-1C) would interact with the N-terminal ectodomain of SipB, which is modeled to extend into the extracellular environment upon insertion into the host cell membrane<sup>10; 11; 12</sup>. Results of NMR titrations between <sup>15</sup>N/ILV labeled SipD<sup>Δ38</sup> or SipD<sup>Δ132</sup> and unlabeled SipB<sup>11-232</sup> or SipB<sup>11-312</sup> are shown in Chapter 7. In support of this hypothesis, results of NMR titration between <sup>15</sup>N/ILV labeled SipD<sup>Δ38</sup> with SipB<sup>11-232</sup> showed a cluster of affected residues in the distal region of SipD (**Fig. 7-1C & Fig. 7-2C**). Unlike the results of NMR titrations between PrgI and SipD, removal of the N-terminal domain of SipD was not expected to affect the tip-translocon interaction. To test this hypothesis, NMR titrations were performed between <sup>15</sup>N/ILV SipD<sup>Δ132</sup> and unlabeled SipB N-terminal domain. As expected, removal of the N-terminal  $\alpha$ -helical hairpin of SipD did not significantly affect the surface of the interaction of SipD with the N-terminal domain of SipB in <sup>15</sup>N titrations (**Fig. 7-6C & Fig 7-7C**) or ILV titrations (**Fig. 7-8C & Fig. 7-9C**). There were no major differences in the interaction between SipB<sup>11-232</sup> and SipB<sup>11-312</sup> with SipD<sup>Δ38</sup> as observed by solution NMR (**Fig. 7-6C**

**& Fig 7-7C).** This suggested that residues 232-312, which contain a predicted  $\alpha$ -helix, did not result in higher affinity binding with SipD. Overall, titration data suggests the distal region of SipD is the primary interaction surface with the N-terminal ectodomain of SipB.

Fluorescence polarization was used to estimate the binding affinity of SipB<sup>82-312</sup> to SipD <sup>$\Delta$ 38</sup>/SipD <sup>$\Delta$ 100</sup> and was determined to be in the range of 30 to 60  $\mu$ M (**Fig. 8-3A, B**). Furthermore, FRET experiments estimated that the coiled-coil of SipB<sup>82-312</sup> is closer in space to the distal end of SipD than the C-terminus of SipB<sup>82-312</sup> (**Table 8-1 & Fig. 8-4**). In agreement with these results, mutations along the mixed  $\alpha/\beta$  domain of SipD reduced the ability of *Salmonella* Typhimurium to invade intestinal epithelial Henle-407 cells (**Fig. 8-6A**). In both FP and FRET experiments, SipB<sup>82-312</sup> did not interact with the needle PrgI (**Fig. 8-5**). The FP and FRET data are in agreement with the results from solution NMR.

#### 12.1.4. Model of the T3SS Needle/Tip/Translocon Interface

Together, the results from solution NMR and FP/FRET allowed for a model of the *Salmonella* SPI-1 T3SS needle-tip and tip-translocon interactions (**Fig. 12-1**). First, the needle protein PrgI interacts with the proximal end of the SipD coiled-coil, which is oriented as pointed down towards the needle (**Fig. 12-1**). In this model, the N-terminal domain of SipD is proposed to swing away from the assembled tip and needle to allow for binding of PrgI to the SipD coiled-coil (**Fig. 12-1**). However, there is no current experimental evidence to support this theory, except for a lack of electron density observed for the N-terminal domain of IpaD (SipD homolog) in electron microscopy

experiments of the T3SS tip complex in *Shigella flexneri*<sup>13</sup>. A current hypothesis in the literature is that the tip complex exists as a tetramer<sup>13; 14</sup> with five copies of SipD that each interact with two copies of PrgI. Therefore, each SipD molecule is expected to insert between two PrgI molecules in the needle-tip model (**Fig. 12-1**). Second, the N-terminal ectodomain of SipB interacts with the distal region of the SipD, the mixed  $\alpha/\beta$  domain, which is oriented as pointed away from the needle and towards the host cell membrane (**Fig. 12-1**). Six to eight total translocon subunits have been estimated to compose the T3SS translocon from results of atomic force microscopy in *E. coli*<sup>15</sup>. Therefore, the model presented here estimates five copies of SipB could be present in the host cell membrane to interact with five copies of SipD at a 1:1 stoichiometry (**Fig. 12-1**). However, there is no current consensus on the *in vivo* stoichiometry of the SipD-SipB interaction. The minor translocon, SipC, is not included in the model because it has not been reported to interact with SipD. Because SipB and PrgI are separated in space by the presence of SipD, they do not interact, as was confirmed here by FP/FRET experiments.

#### 12.1.5. Fluorescence based binding assays of T3SS proteins

FP and FRET are binding assays that can be used to probe protein-protein interactions and can be adapted for high-throughput screening to discover inhibitors of protein-protein interactions<sup>16; 17</sup>. Here, FP and FRET based protein-protein binding assays were reported for both the SipD/PrgI interaction (**Fig. 5-3 & Fig. 5-4**) and the SipD/SipB interaction (**Fig. 8-3 & Fig. 8-4**). In the FP assays, 25 nM of labeled protein was not saturated until around 400  $\mu$ M of unlabeled protein. Therefore, high-throughput screening of such a weak interaction would likely require milligram quantities of unlabeled protein.

Likewise, FRET experiments required  $\mu\text{M}$  amounts of proteins for each FRET experiments. FP and FRET as high-throughput screens have a drawback of required labeling protein and leading to a high-amount of false positives<sup>16, 17</sup>. For these reasons, a more direct approach was used in Chapter 10 where surface plasmon resonance was used in a fragment based screen to identify small molecules that bound directly to T3SS proteins. Regardless of their potential use for high-throughput screening, FP and FRET assays developed in this dissertation were used as quick and efficient protein binding assays, especially for the testing of mutant proteins to identify important protein interaction surfaces. The FP and FRET assays presented here would be easily adaptable for other T3SS protein interaction systems as well.

#### *12.1.6. Comparison of SipB<sup>82-240</sup>, SipB<sup>11-232</sup> and SipB<sup>11-312</sup> Constructs*

Three constructs of the N-terminal ectodomain of SipB were prepared to determine an optimal SipB construct for NMR experiments. SipB lacking its extreme N-terminal residues, SipB<sup>82-240</sup>, was compared to two SipB constructs containing the extreme N-terminal residues, SipB<sup>11-232</sup> and SipB<sup>11-312</sup>. SEC experiments showed SipB<sup>11-232</sup> and SipB<sup>11-312</sup> were primarily populations of dimers or trimers in solution (**Fig. 6-2**). CD spectra showed that SipB<sup>11-232</sup> and SipB<sup>11-312</sup> had similar secondary structure characteristics (**Fig. 6-3A**) and a single thermal melt between 57 and 59°C (**Fig. 6-3B**). However, SipB<sup>82-240</sup> gave much higher quality NMR data compared to SipB<sup>11-232</sup> and SipB<sup>11-312</sup> (**Fig. 6-4 & Fig. 6-5**). Up to 70% of amide resonances were observed with SipB<sup>82-240</sup> in 2D <sup>1</sup>H-<sup>15</sup>N TROSY experiments (**Fig. 6-4C**), while less than half of expected resonances were observed in 2D <sup>1</sup>H-<sup>15</sup>N TROSY experiments with SipB<sup>11-232</sup> and SipB<sup>11-</sup>

<sup>312</sup> (**Fig. 6-4A, B**). Similar conclusions were observed with 2D <sup>1</sup>H-<sup>13</sup>C HSQC spectra of ILV methyl labeled proteins (**Fig. 6-5**). The most likely explanation is that the residues 11-81 are disordered or contain random coiled character, as suggested by secondary structure prediction servers, resulting in small <sup>1</sup>H dispersion and broad resonances. For these reasons, SipB<sup>82-240</sup> was used in validation of small molecule binding hits from surface plasmon resonance screens.

#### *12.1.7. Small Molecule Binders of SipD<sup>Δ38</sup> and SipB<sup>82-240</sup>*

A surface plasmon resonance (SPR) screen identified small molecule fragments that bound to SipD<sup>Δ38</sup> and SipB<sup>82-240</sup> (**Chapter 10**). SPR identified that 5-hydroxyindole bound to both SipD<sup>Δ38</sup> and SipB<sup>82-240</sup>, 3-indoleacetic acid bound to SipB<sup>82-240</sup>, and 4-morpholinoaniline bound to SipD<sup>Δ38</sup> (**Fig. 10-2**). Titration and <sup>1</sup>H saturation transfer difference (STD) NMR experiments validated the hits from the SPR screen. These indole and morpholinoaniline scaffolds are the first small molecules (other than bile salts<sup>18</sup> and host cell lipids<sup>19</sup>) to be reported to interact with the T3SS tip or major translocon protein. NMR titration showed an interaction between SipD<sup>Δ38</sup> or SipB<sup>82-240</sup> with the small molecule fragments in the mM range; 32 ± 8 mM for the binding of 5-hydroxyindole to SipD<sup>Δ38</sup>. The <sup>15</sup>N and ILV assignments of SipD<sup>Δ38</sup> were utilized to characterize the interaction between SipD<sup>Δ38</sup> and small molecules by chemical shift mapping. Both 5-hydroxyindole and 4-morpholinoaniline affected similar SipD surfaces – the bottom of the coiled-coil and portions of the distal region (**Fig. 12-2**), suggesting these SipD surfaces are potential hotspots for drug interaction. Together, these data suggest that indole and morpholinoaniline may be suitable scaffolds for the development of higher

affinity small molecule binders for the tip and translocon. In the future, a chemically diverse library of indole or morpholinoaniline based small molecules should be developed and tested for binding to SipD<sup>Δ38</sup> or SipB<sup>82-240</sup> by SPR and then subsequently validated by NMR experiments. Ideally, binding in the nM or low μM range should be achieved to test for biological inhibition activity. These tighter binding molecules can be tested for T3SS inhibition by either in vitro *Salmonella* invasion assay or protein-protein binding assays, such as the FP or FRET experiments described in this dissertation.

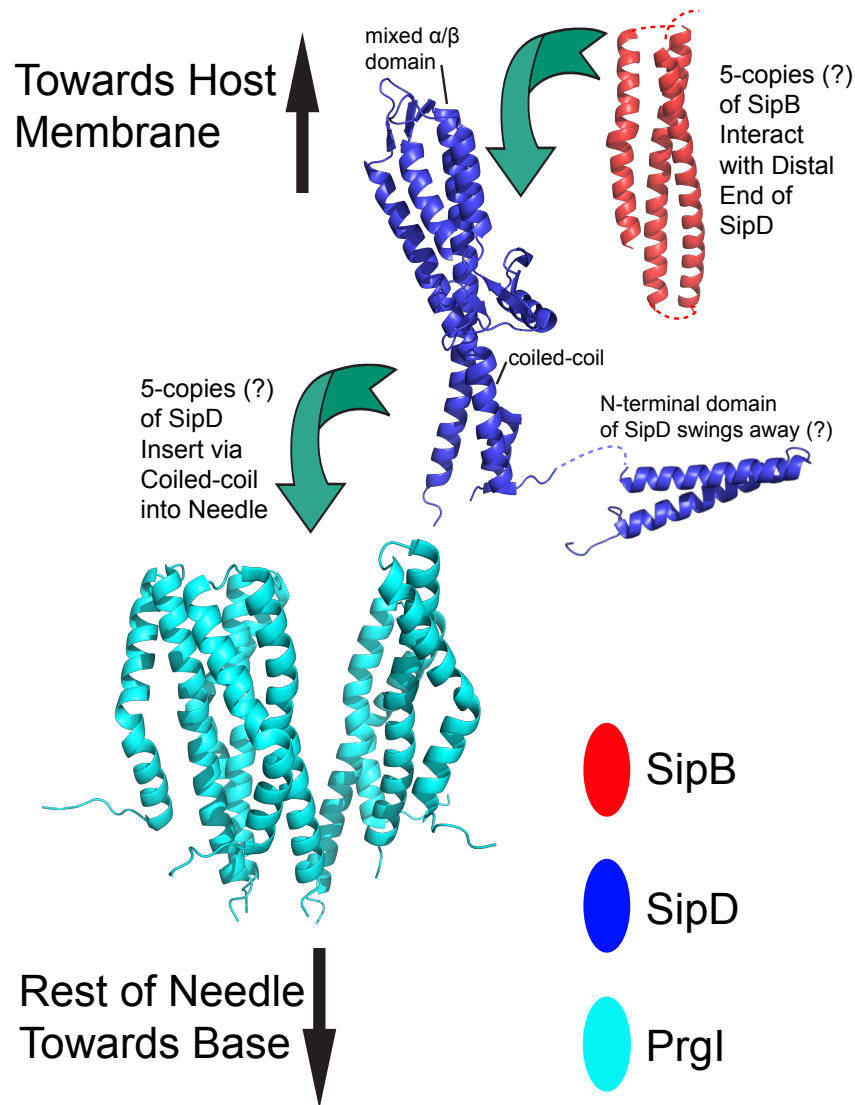


### Fig. 12-1 – Proposed Model of the PrgI, SipD and SipB Interface

Five copies of SipD (blue) are expected to insert between PrgI (cyan). Data presented in this dissertation suggests the proximal end of SipD (i.e. the bottom of the coiled-coil) interacts with PrgI. The N-terminal domain of SipD is modeled to swing away following assemble of the needle/tip, but that requires experimental testing. The distal end of SipD (mixed  $\alpha/\beta$ ) interacts with five copies of the N-terminal domain of SipB (red). The C-terminus of SipB<sup>82-226</sup> extends upwards towards the host membrane. Proteins not to scale.

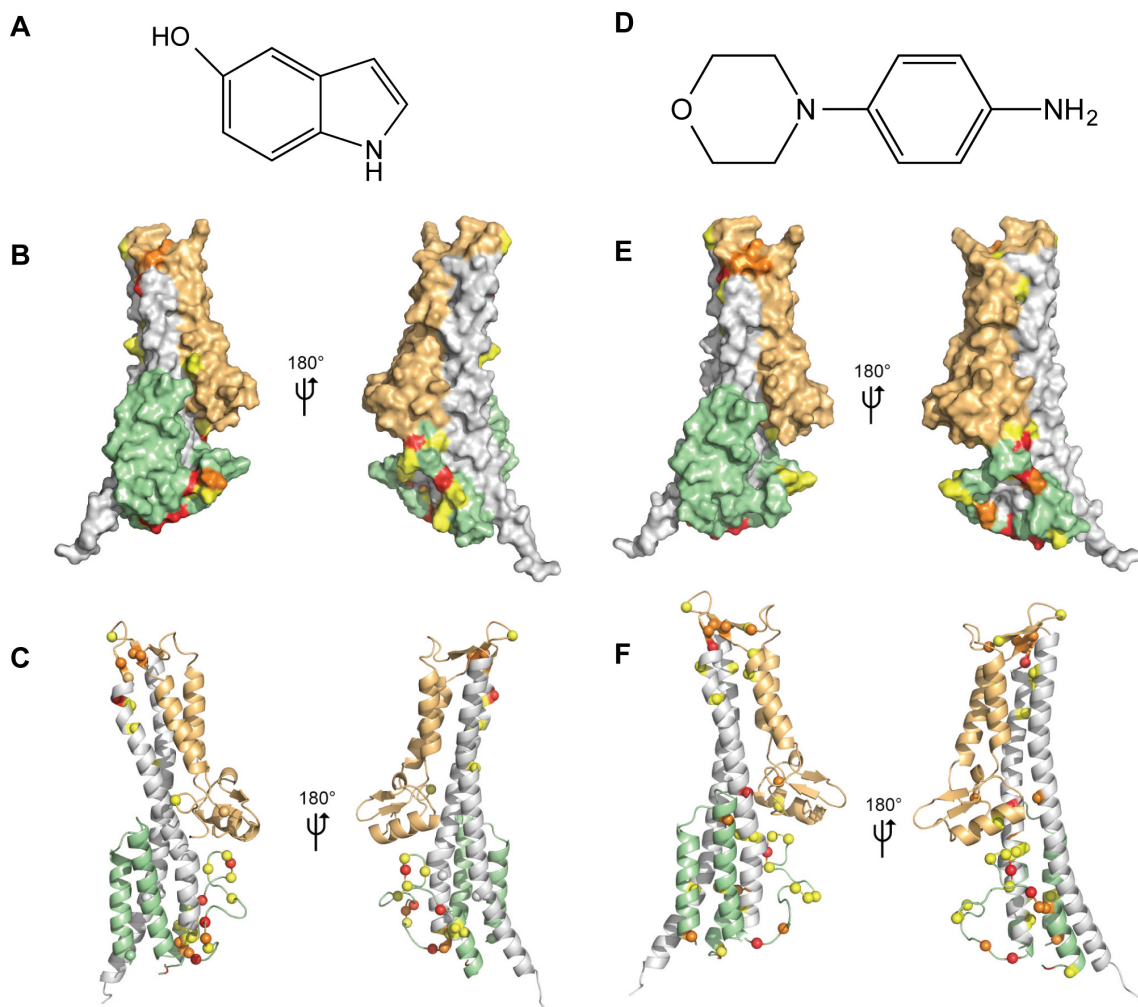


### Fig. 12-2 – Comparison of the SipD Surface Affected by Small Molecules

The chemical structure of (A) 5-hydroxyindole and (D) 4-morpholinoaniline. The SipD residues affected by interaction with 5-hydroxyindole are shown on the atomic structure of SipD as (B) a surface representation and (C) a cartoon representation. The SipD residues affected by interaction with 4-morpholinoaniline are shown on the atomic structure of SipD as (E) a surface representation and (F) a cartoon representation. SipD structure is colored with the N-terminal domain in green, the coiled-coil in gray and the mixed  $\alpha/\beta$  domain in light orange. Residues are colored as strongly affected (red), moderately affected (orange) or weakly affected (yellow).

### 12.1.8. Characterization of Chaperone/Translocon Complexes

To date, a full-length atomic structure of any of the T3SS translocon proteins has not yet been reported. Further, atomic resolution information on the interaction of the translocon proteins with other T3SS proteins is lacking. To perform biophysical and biochemical characterization on T3SS translocon proteins, full-length major and minor translocon proteins were prepared in complex with their cognate chaperone.

Chaperone/translocon complexes were successfully expressed and purified in a single vector system, including hisSicA/SipC (**Fig. 11-1**) from *Salmonella* Typhimurium and hisPcrH/PopD (**Fig. 11-4**) or hisPcrH/PopB (**Fig. 11-5**) from *Pseudomonas aeruginosa*. CD experiments on hisSicA/SipC (**Fig. 11-2**) and hisPcrH/PopD (**Fig. 11-7**) showed that the chaperone/minor translocon protein complexes were contained  $\alpha$ -helical content due to their  $\theta_{222/208}$  nm ratio near 1.0, and both had a single melting point of 55°C.

Unfortunately, all of the chaperone/translocon complexes tested gave poor NMR data in both 2D  $^1\text{H}$ - $^{15}\text{N}$  TROSY and  $^1\text{H}$ - $^{13}\text{C}$  HSQC experiments. HisSicA/SipC (**Fig. 11-3**), hisPcrH/PopD (**Fig. 11-7**) and hisPcrH/PopB (**Fig. 11-8**) NMR peaks were broad and many of the expected amide or isoleucine methyl resonances were not observed.

Experiments comparing free HisPcrH vs. HisPcrH/PopB suggested the presence of the translocon, not the chaperone, dictates the poor quality of the chaperone/translocon complexes (**Fig 11-8A, B**). The chaperones bind to only a small portion of the translocon, leaving the rest of the translocon free to undergo dynamic motions solution. Furthermore, the translocon proteins are likely not in their native folded conformation because the lack of a membrane or membrane-like environment in our experiments. Together, these data suggest that chaperone/translocon complexes are not ideal for NMR experiments and

instead that the chaperone and translocon proteins should be separated, likely by methods utilizing detergents or pH change. In all constructs, the chaperone contains a His tag while the translocon doesn't, making affinity purification following separation plausible. Following separation and isolation from the chaperones, the translocon proteins should then be put into membranes (nanodiscs) or membrane-like environments (detergents) for structure analysis or protein interaction experiments.

### 12.3. References

1. Kubori, T., Matsushima, Y., Nakamura, D., Uralil, J., Lara-Tejero, M., Sukhan, A., Galan, J. E. & Aizawa, S. (1998). Supramolecular structure of the Salmonella typhimurium type III protein secretion system. *Science* **280**, 602-605.
2. McShan, A. C. & De Guzman, R. N. (2015). The Bacterial Type III Secretion System as a Target for Developing New Antibiotics. *Chemical Biology & Drug Design* **85**, 30-42.
3. Goto, N. K., Gardner, K. H., Mueller, G. A., Willis, R. C. & Kay, L. E. (1999). A robust and cost-effective method for the production of Val, Leu, Ile ( $\delta$  1) methyl-protonated  $^{15}\text{N}$ -,  $^{13}\text{C}$ -,  $^2\text{H}$ -labeled proteins. *J Biomol NMR* **13**, 369-74.
4. Tugarinov, V., Kanelis, V. & Kay, L. E. (2006). Isotope labeling strategies for the study of high-molecular-weight proteins by solution NMR spectroscopy. *Nat Protoc* **1**, 749-54.
5. Gardner, K. H., Rosen, M. K. & Kay, L. E. (1997). Global folds of highly deuterated, methyl-protonated proteins by multidimensional NMR. *Biochemistry* **36**, 1389-401.
6. Hajduk, P. J., Meadows, R. P. & Fesik, S. W. (1999). NMR-based screening in drug discovery. *Quarterly Reviews of Biophysics* **32**, 211-240.
7. Tugarinov, V. & Kay, L. E. (2005). Methyl groups as probes of structure and dynamics in NMR studies of high-molecular-weight proteins. *ChemBiochem* **6**, 1567-+.
8. Johnson, S., Roversi, P., Espina, M., Olive, A., Deane, J. E., Birket, S., Field, T., Picking, W. D., Blocker, A. J., Galyov, E. E., Picking, W. L. & Lea, S. M. (2007). Self-chaperoning of the type III secretion system needle tip proteins IpaD and BipD. *Journal of Biological Chemistry* **282**, 4035-4044.
9. Rathinavelan, T., Lara-Tejero, M., Lefebvre, M., Chatterjee, S., McShan, A. C., Guo, D. C., Tang, C., Galan, J. E. & De Guzman, R. N. (2014). NMR model of PrgI-SipD interaction and its implications in the needle-tip assembly of the Salmonella type III secretion system. *J Mol Biol* **426**, 2958-69.

10. McGhie, E. J., Hume, P. J., Hayward, R. D., Torres, J. & Koronakis, V. (2002). Topology of the Salmonella invasion protein SipB in a model bilayer. *Molecular Microbiology* **44**, 1309-1321.
11. Dickenson, N. E., Arizmendi, O., Patil, M. K., Toth, R. T. t., Middaugh, C. R., Picking, W. D. & Picking, W. L. (2013). N-Terminus of IpaB Provides a Potential Anchor to the Shigella Type III Secretion System Tip Complex Protein IpaD. *Biochemistry*.
12. Nguyen, V. S., Jobichen, C., Tan, K. W., Tan, Y. W., Chan, S. L., Ramesh, K., Yuan, Y., Hong, Y., Seetharaman, J., Leung, K. Y., Sivaraman, J. & Mok, Y. K. (2015). Structure of AcrH-AopB Chaperone-Translocator Complex Reveals a Role for Membrane Hairpins in Type III Secretion System Translocon Assembly. *Structure* **23**, 2022-31.
13. Cheung, M., Shen, D. K., Makino, F., Kato, T., Roehrich, A. D., Martinez-Argudo, I., Walker, M. L., Murillo, I., Liu, X., Pain, M., Brown, J., Frazer, G., Mantell, J., Mina, P., Todd, T., Sessions, R. B., Namba, K. & Blocker, A. J. (2015). Three-dimensional electron microscopy reconstruction and cysteine-mediated crosslinking provide a model of the type III secretion system needle tip complex. *Mol Microbiol* **95**, 31-50.
14. Lunelli, M., Hurwitz, R., Lambers, J. & Kolbe, M. (2011). Crystal Structure of PrgI-SipD: Insight into a Secretion Competent State of the Type Three Secretion System Needle Tip and its Interaction with Host Ligands. *Plos Pathogens* **7**.
15. Ide, T., Laarmann, S., Greune, L., Schillers, H., Oberleithner, H. & Schmidt, M. A. (2001). Characterization of translocation pores inserted into plasma membranes by type III-secreted Esp proteins of enteropathogenic Escherichia coli. *Cellular Microbiology* **3**, 669-679.
16. Lea, W. A. & Simeonov, A. (2011). Fluorescence polarization assays in small molecule screening. *Expert Opin Drug Discov* **6**, 17-32.
17. Song, Y., Madahar, V. & Liao, J. Y. (2011). Development of FRET Assay into Quantitative and High-throughput Screening Technology Platforms for Protein-Protein Interactions. *Annals of Biomedical Engineering* **39**, 1224-1234.
18. Wang, Y., Nordhues, B. A., Zhong, D. & De Guzman, R. N. (2010). NMR characterization of the interaction of the Salmonella type III secretion system protein SipD and bile salts. *Biochemistry* **49**, 4220-6.
19. Hayward, R. D., Cain, R. J., McGhie, E. J., Phillips, N., Garner, M. J. & Koronakis, V. (2005). Cholesterol binding by the bacterial type III translocon is essential for virulence effector delivery into mammalian cells. *Molecular Microbiology* **56**, 590-603.

## Addendum. Interaction of PcrV and PcrG by Fluorescence

### Spectroscopy

#### A1.1. Introduction

*Pseudomonas aeruginosa* is an opportunistic Gram-negative bacterial pathogen that is a common cause of nosocomial infections in immunocompromised patients, such as those with AIDS, cystic fibrosis and cancer<sup>1</sup>. *P. aeruginosa* harbors a protein nanoinjector, the type-three secretion system (T3SS), that translocates virulence factors into host cells to initiate and maintain infection<sup>2</sup>. The structural T3SS component, the needle apparatus, is comprised of a bacterial membrane spanning base, a needle-like structure, a tip and a host membrane embedded translocon. In *P. aeruginosa*, PcrV is the tip protein and PcrG is its chaperone<sup>3;4</sup>. These proteins have sequence homology to LcrV and LcrG in *Yersinia pestis*. Together, PcrV and PcrG are responsible for proper assembly and regulation of effector secretion through the T3SS and are therefore essential for bacterial virulence<sup>5;6</sup>.

In *P. aeruginosa*, effector secretion is host cell contact and calcium dependent<sup>7</sup>. Deletion of *pcrv* or *pcrg* results in constitutive effector secretion, even in the absence of calcium depletion or cell contact<sup>5</sup>. In addition, PcrG is required for proper PcrV secretion to the needle tip, but also regulates effector secretion independent of PcrV through unknown mechanisms. This model of secretion is different from *Yersinia* model in which deletion of the LcrV tip inhibits effector secretion due to negative T3SS regulation by LcrG<sup>8</sup>. Recently, PcrV and LcrV have been examined as targets for vaccine development. Preliminary results from a small phase II trial showed that an anti-PcrV vaccine reduced

ventilator-associated pneumonia by 50% in the treated group<sup>9</sup>. These results, though promising, have yet to be corroborated with larger scale trials.

A large gap in knowledge that remains to be understood is determination of the atomic structure of PcrV and PcrG, and the characterization of the PcrV-PcrG interaction. Here, fluorescence polarization (FP) and Förster resonance energy transfer (FRET) are utilized as protein binding assays for PcrV and PcrG. The objective of this research was to i) develop a method that could be combined with mutagenesis to determine essential interacting residues and protein binding surfaces, and ii) develop binding assays for high-throughput screening of small molecular inhibitors of the tip-chaperone interaction.

## **A1.2. Materials and Methods**

### *A1.2.1. Protein Expression and Purification*

PcrV<sup>25-294</sup> and PcrG<sup>9-76</sup> constructs were made as fusion proteins in pET-21a with His<sub>6</sub>-tagged GB1 (N-terminal for PcrV and C-terminal for PcrG) that included a tobacco etch virus (TEV) protease cleavage site. GB1, the  $\beta$ 1 immunoglobulin binding domain of *Streptococcus* protein G, was used as a solubility enhancer to improve product yield. Truncations of PcrV and PcrG improved their NMR spectra<sup>10</sup>, and therefore PcrV<sup>25-294</sup> and PcrG<sup>9-76</sup> were used here to complement NMR experiments. Proteins were expressed in *E. coli* BL21(DE3) DNAY cells in 1L of LB media containing 30  $\mu$ g/mL kanamycin and 100  $\mu$ g/mL carbenicillin. Cells were grown at 37°C until an OD<sub>600</sub> of 0.8 then induced with 1 mM isopropyl- $\beta$ -D-thiogalactopyrandoside (IPTG) and grown overnight at 15°C to a final OD<sub>600</sub> of 2.6. Bacterial cells were harvested by centrifugation at 4000 rpm for 10 minutes, resuspended with binding buffer (500 mM NaCl, 20 mM Tris-HCl, 5

mM imidazole, pH 8.0, 2 mM phenylmethanesulfonyl fluoride, PMSF) at 4°C and sonicated while keeping the lysate ice-cold. The cell lysate was centrifuged for 10 minutes at 13000 rpm. Next, 700 µL of 5% polyethyleneimine (P.E.I.) was added to the supernatant, which was centrifuged again to remove cellular debris. The supernatant was loaded onto a Ni<sup>2+</sup>-affinity chromatography column (Sigma), the column was washed with 150 mL binding buffer (500 mM NaCl, 20 mM Tris-HCl, 5 mM imidazole, pH 8.0) and bound protein was eluted with 40 mL elution buffer (500 mM NaCl, 20 mM Tris-HCl, 250 mM imidazole, pH 8.0). The column elutions were then incubated at 25°C overnight with 250 µL of 0.04 mM recombinant TEV protease in TEV protease buffer (50 mM Tris-HCl, pH 8.0, 0.5 mM EDTA, pH 8.5, 1 mM DTT, 20 mM NaCl) and further purified by Ni<sup>2+</sup>-affinity chromatography to separate protein from the His<sub>6</sub>-GB1 tag. Purified proteins were dialyzed in 1× PBS, pH 7.4 overnight and concentrated using Amicon Ultra 3K (Millipore) filtration columns. Protein concentrations were determined by the absorbance at A<sub>280</sub>.

#### *41.2.2. Secondary Structure Prediction*

Primary amino acid sequences were aligned using Clustal Omega<sup>11</sup> and edited with ESPrpt 2.2 (<http://esprpt.ibcp.fr>)<sup>12</sup>. Secondary structure prediction was performed on PcrG with I-TASSER<sup>13</sup>, DSC, MLRC and PHD<sup>14</sup>. The 3D atomic structure of PcrV was predicted using I-TASSER<sup>13</sup>, based on sequence homology with the previously solved structure of LcrV<sup>15</sup>. The C-score of the PcrV model was 1.3, while TM-score was 0.9 and R.M.S.D. was 3.3 ± 2.3Å. Unfortunately, I-TASSER did not produce a reliable model for PcrG (C-scores in the range of -3.5 and TM-score of 0.33 ± 0.11).

### *A1.2.3. Circular Dichroism (CD)*

CD spectra were acquired in triplicate using a JASCO J-815 Spectropolarimeter. Scans were collected from 195 nm to 260 nm at 25°C at a scan rate of 50 nm/min to assess the secondary structure and foldedness of PcrV and PcrG. Thermal stability was monitored between 25°C and 80°C at 222 nm at temperature ramp rate of 30°C/hr. All spectra were subtracted from a 1×, PBS pH 7.4 blank.

### *A1.2.4. Fluorophore Conjugation*

A single cysteine mutation was introduced into PcrV<sup>25-294</sup> and PcrG<sup>9-76</sup> by site-directed mutagenesis using a Qiagen Kit (Stratagene). Maleimide conjugated fluorophores were used to label PcrV and PcrG constructs. First, proteins were dialyzed into 1× PBS, pH 7.4 overnight prior to labeling. A 10 fold excess of tris(2-carboxyethyl)phosphine (TCEP) to protein was used to reduce disulfide bonds for 30 minutes at 25°C. A 20 fold excess of dye to protein was resuspended in 100% (v/v) DMSO for Fluorescein-C<sub>5</sub>-maleimide (Invitrogen) or 1× PBS, pH 7.4 for Alexa Fluor 647-C<sub>2</sub>-Maleimide (Invitrogen). Dye was added drop wise to the reduced protein solution while mixing and allowed to react for 3 hours in the dark at 25°C. Unreacted dye was removed by dialysis in 1× PBS, pH 7.4 followed by passage through an Amicon Ultra 3K (Millipore) filtration column. The concentrations of labeled proteins were assessed using UV-vis spectra. Herein, dyes are denoted as FM (Fluorescein-C<sub>5</sub>-maleimide) and AF647 (Alexa Fluor 647-C<sub>2</sub>-Maleimide).

#### *A1.2.5. Fluorescence Polarization (FP)*

FP experiments were performed by titrating 25 nM of PcrG<sup>9-76</sup> E28C-FM with increasing concentrations of unlabeled PcrV<sup>25-294</sup>. The fluorometer was zeroed to 1× PBS, pH 7.4. The average of measured data points (n=5) was subtracted from a base polarization value of PcrG<sup>9-76</sup> E28C-FM without any PcrV<sup>25-294</sup> added. The difference in millipolarization ( $\Delta mP$ ) was plotted against increasing concentrations of PcrV<sup>25-294</sup> to obtain a saturated binding curve. The FP binding curve was fitted with Origin (OriginLab, Northampton, MA). All FP data was collected using a Varian Cary Eclipse Fluorescence Spectrophotometer at 25°C.

#### *A1.2.6. Förster Resonance Energy Transfer (FRET)*

Fluorescence emission spectra were examined for 1  $\mu$ M PcrG<sup>9-76</sup> E28C-FM (donor only), 1  $\mu$ M PcrV<sup>25-294</sup> D133C-AF647 (acceptor only), and 1  $\mu$ M PcrG<sup>9-76</sup> E28C-FM in the presence of 1  $\mu$ M PcrV<sup>25-294</sup> D133C-AF647 (donor + acceptor). Spectra were collected between 500 nm and 800 nm using an excitation wavelength of 480 nm, excitation and emission slit widths of 5 nm and an integration time of 0.1 seconds. All data was collected on a Varian Cary Eclipse Fluorescence Spectrophotometer at 25°C.

FRET efficiency,  $E$ , can be calculated from emission spectra as follows:

$$E = 1 - \frac{F_{DA}}{F_D}$$

Once FRET efficiency is known, the distance between the FRET dye pairs,  $r$ , can be calculated from the following formula:

$$r = R_0 \left( \frac{1}{E} - 1 \right)^{1/6}$$

Here,  $R_0$  is the Förster distance between two FRET pairs at which  $E = 50\%$ , which is  $56\text{\AA}$  for the FRET pairs used in this study (Invitrogen).

### A1.3. Results

#### A1.3.1. CD of Fluorophore Labeled PcrG<sup>9-76</sup> E28C and PcrV<sup>25-294</sup> D133C

A cysteine mutation was introduced into PcrV and PcrG for the attachment of fluorophore. Sites chosen were based on minimal sequence conservation (**Fig. A1-1A, B**), likelihood to be surface exposed and likelihood to be present on an  $\alpha$ -helix. For PcrG, this was estimated based on secondary structure prediction from the primary amino acid sequence (**Fig. A1-1C**). For PcrV, these parameters were partially estimated from the I-TASSER 3D structure predicted based on homology to the *Yersinia* homolog, LcrV (**Fig. A1-1D**). Following purification, PcrG<sup>9-76</sup> E28C was labeled with FM and PcrV<sup>25-294</sup> D133C was labeled with AF647. CD spectra taken between 190 and 260 nm showed that fluorophore and non-fluorophore conjugated PcrV<sup>25-294</sup> D133C is a highly  $\alpha$ -helical (**A1-2A**), while fluorophore and non-fluorophore conjugated PcrG<sup>9-76</sup> E28C is partially  $\alpha$ -helical and partially random-coil (**A1-2B**). The secondary structure characteristics of PcrV<sup>25-294</sup> D133C-AF647 resembled PcrV<sup>25-294</sup> D133C (**Fig. A1-2A**). Similarly, the secondary structure characteristics of PcrG<sup>9-76</sup> E28C-FM resembled PcrG<sup>9-76</sup> E28C (**Fig. A1-2B**). PcrV<sup>25-294</sup> D133C and PcrV<sup>25-294</sup> D133C-AF647 showed a single melting point at  $65^\circ\text{C}$ , while none of the PcrG constructs showed a distinct melting point (data not shown). The CD data of PcrV<sup>25-294</sup> and PcrG<sup>9-76</sup> presented here are in agreement with previously reported spectra<sup>16</sup> and show that fluorophore conjugation did not have a drastic effect on overall protein fold or stability.

### *A1.3.2. FP of PcrG<sup>9-76</sup> E28C-FM and Unlabeled PcrV<sup>25-294</sup>*

FP was used to determine the binding affinity between PcrG<sup>9-76</sup> and PcrV<sup>25-294</sup>. FP of 25 nM PcrG<sup>9-76</sup> E28C-FM titrated with increasing concentrations of unlabeled PcrV<sup>25-294</sup> resulted in a saturated binding curve with an estimated dissociation constant of  $1.0 \pm 0.1 \mu\text{M}$  (**Fig. A1-3**).

### *A1.3.3. FRET of PcrG<sup>9-76</sup> E28C-FM and PcrV<sup>25-294</sup> D133C-AF647*

To determine distance specific information on the PcrG<sup>9-76</sup> and PcrV<sup>25-294</sup> interaction, FRET was performed on PcrG<sup>9-76</sup> E28C-FM and PcrV<sup>25-294</sup> D133C-AF647 to estimate the intermolecular distance between the FRET dye pairs. Donor only (PcrG<sup>9-76</sup> E28C-FM) and acceptor only (PcrV<sup>25-294</sup> D133C-AF647) spectra were combined to exclude fluorophore emission due to cross talk and bleed through (**Fig. A1-4, solid line**). When PcrG<sup>9-76</sup> E28C-FM and PcrV<sup>25-294</sup> D133C-AF647 were added together in a 1:1 ratio, there was a noticeable decrease in donor emission and increase in acceptor emission indicating FRET had occurred (**Fig. A1-4, dotted line**). The estimated FRET efficiency,  $E$ , between PcrG<sup>9-76</sup> E28C-FM and PcrV<sup>25-294</sup> D133C-AF647 was 5.1%, which suggests the FRET pairs were 91 Å apart. This suggests the possibility that the N-terminus of PcrG<sup>9-76</sup> E28C-FM is extended and far away from the PcrV coiled-coil during interaction (**Fig. A1-5**).



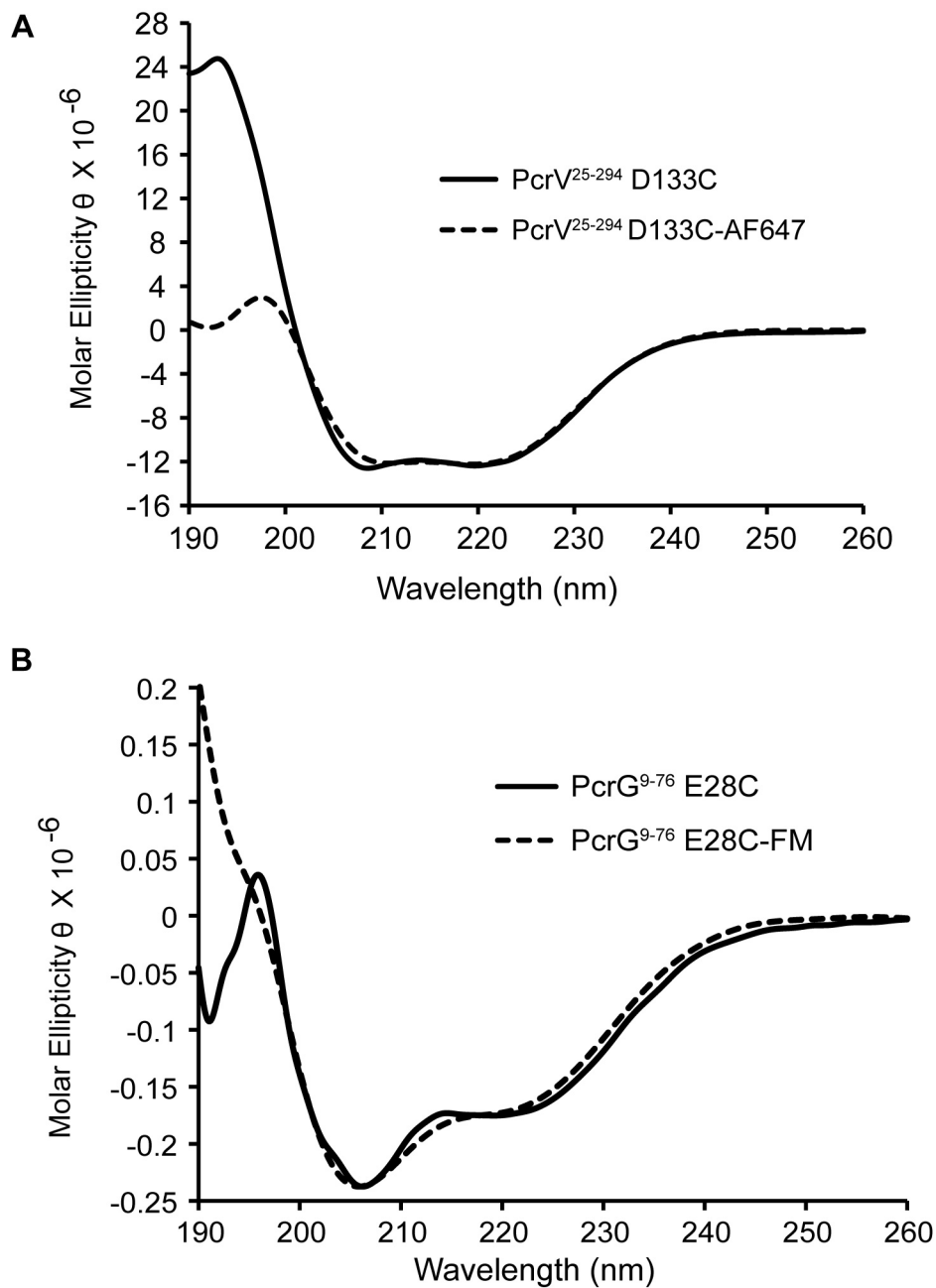


**Fig. A1-2 – CD of Fluorophore Labeled PcrG<sup>9-76</sup> E28C and PcrV<sup>25-294</sup> D133C**  
 Far UV circular dichroism spectra of protein without fluorophore (solid line) and with conjugated fluorophore (dotted line) for (A) PcrV<sup>25-294</sup> D133C and (B) PcrG<sup>9-76</sup> E28C.

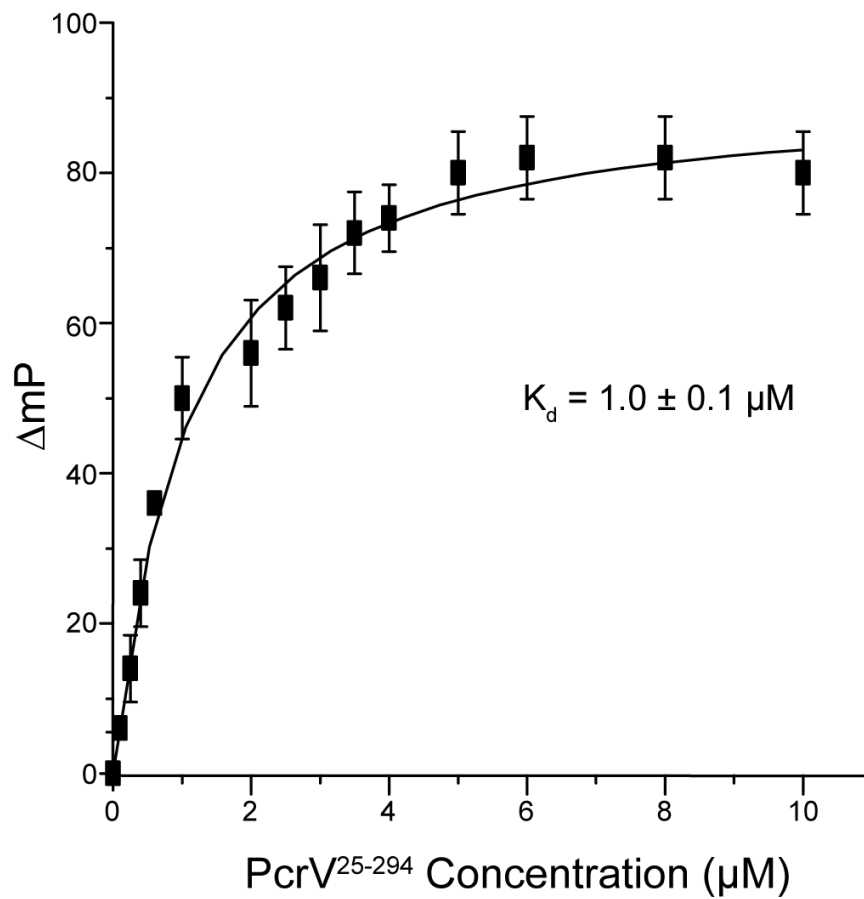


**Fig. A1-3 – Fluorescence Polarization of PcrG<sup>9-76</sup> E28C-FM with PcrV<sup>25-294</sup>**  
FP of 25 nM PcrG<sup>9-76</sup> E28C-FM titrated with increasing concentration of unlabeled PcrV<sup>25-294</sup>. The dissociation constant was estimated to be  $\sim 1 \mu M$ .

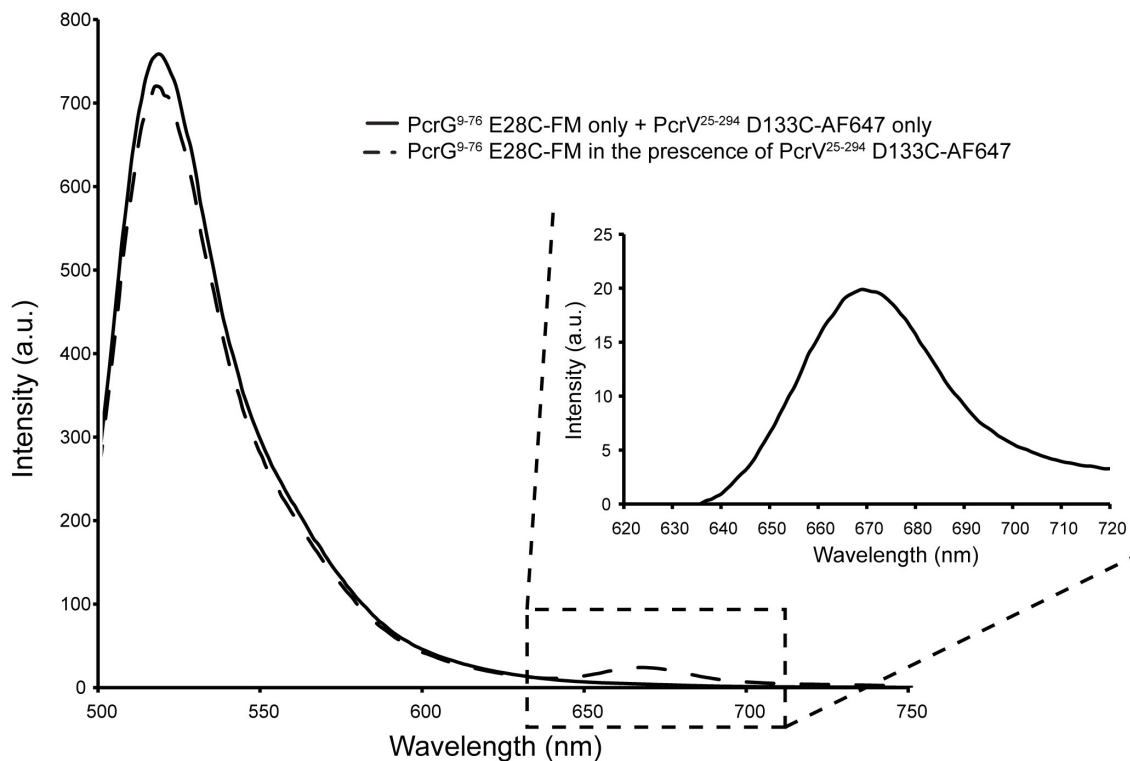


**Fig. A1-4 – FRET of PcrG<sup>9-76</sup> E28C-FM and PcrV<sup>25-294</sup> D133C-AF647**

The fluorescence emission spectrum of donor only (PcrG<sup>9-76</sup> E28C-FM) plus the emission spectrum of the acceptor only (PcrV<sup>25-294</sup> D133C-AF647) is shown as a solid line. The fluorescence emission spectra of PcrG<sup>9-76</sup> E28C-FM in the presence of PcrV<sup>25-294</sup> D133C-AF647 at a 1:1 ratio is shown as a dotted line. FRET is observed as seen by the donor emission decrease and the acceptor emission increase. An expanded view of the acceptor emission is shown.

#### A1.4. Discussion

The protein-protein interaction data reported here are the first report of an interaction between PcrG and PcrV by fluorescence spectroscopy. FP experiments estimated the dissociation constant between FM labeled PcrG<sup>9-76</sup> E28C and unlabeled PcrV<sup>25-294</sup> to be 1  $\mu$ M (**Fig. A1-3**). This value is similar to a recent publication by Basu and co-workers<sup>17</sup> that estimated the dissociation constant by surface plasmon resonance experiments between PcrG<sup>13-72</sup> and PcrV<sup>128-294</sup> to be 0.6  $\mu$ M; although the  $K_d$  between full-length proteins was reported to be 15.6 nM. These results suggest that PcrG and PcrV truncations interact weaker than wild-type proteins by around 65 fold. FRET signal was also observed between FM labeled PcrG<sup>9-76</sup> E28C and AF647 labeled PcrV<sup>25-294</sup> D133C (**Fig. A1-4**). However, the FRET efficiency was low and the distance between the between the FRET pairs was estimated to be 91 Å. First, it is possible that the location of the fluorophore at D133C on PcrV<sup>25-294</sup> inhibited the interaction with PcrG<sup>9-76</sup> E28C because the PcrV coiled-coil is suspected to be an interaction site with PcrG<sup>10</sup>. This possibility could be tested by creating cysteine point mutations in the distal region of PcrV, labeling with fluorophore and then tested for interaction with PcrG. Another possibility is that the N-terminus of PcrG<sup>9-76</sup> that contains E28C fluorophore is oriented away from the coiled-coil of PcrV<sup>25-294</sup> during interaction (**Fig. A1-5**).

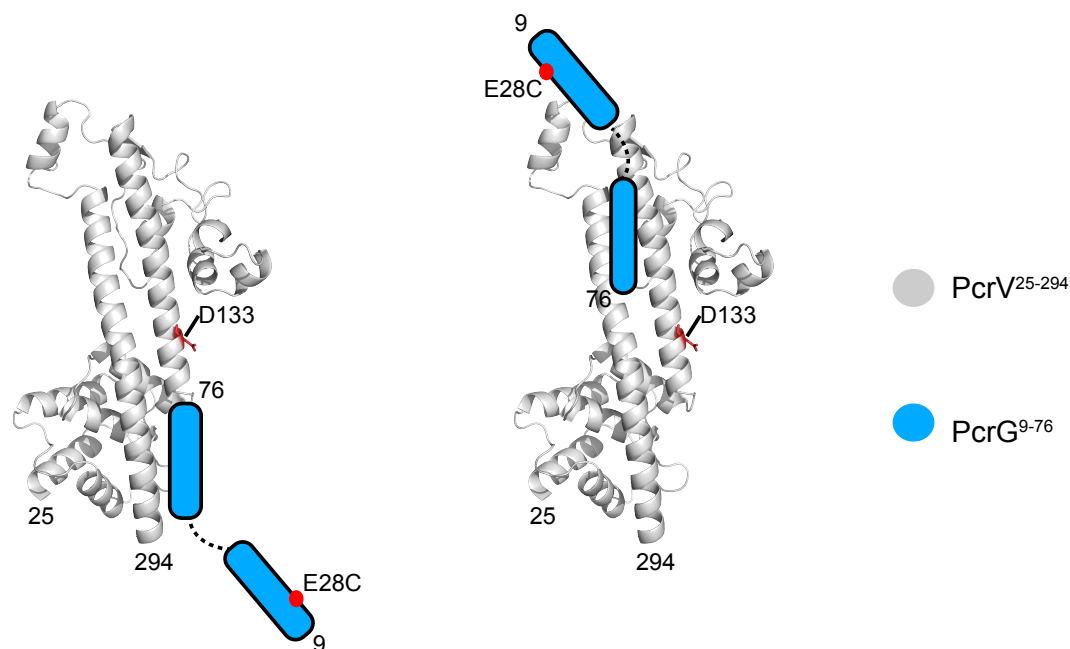


**Fig. A1-5 – Possible Model of the PcrG and PcrV Interaction**

PcrV<sup>25-294</sup> (simulated 3D structure from I-TASSER) is shown in gray and PcrG<sup>9-76</sup> (no known atomic structure) is shown in blue with two predicted  $\alpha$ -helices. The model shows the N-terminus of PcrG<sup>9-76</sup> with the label E28C (red sphere) pointing away from the coiled-coil of PcrV<sup>25-294</sup> with the label D133C (red stick) based on the estimate of the two fluorophore labeled residues by FRET in Fig. A1-4.

### A1.5. References

1. Lyczak, J. B., Cannon, C. L. & Pier, G. B. (2000). Establishment of *Pseudomonas aeruginosa* infection: lessons from a versatile opportunist. *Microbes Infect* **2**, 1051-60.
2. Hauser, A. R. (2009). The type III secretion system of *Pseudomonas aeruginosa*: infection by injection. *Nature Reviews Microbiology* **7**, 654-665.
3. Allmond, L. R., Karaca, T. J., Nguyen, V. N., Nguyen, T., Wiener-Kronish, J. P. & Sawa, T. (2003). Protein binding between PcrG-PcrV and PcrH-PopB/PopD encoded by the pcrGVH-popBD operon of the *Pseudomonas aeruginosa* type III secretion system. *Infection and Immunity* **71**, 2230-2233.
4. Goure, J., Pastor, A., Faudry, E., Chabert, J., Dessen, A. & Attree, I. (2004). The V antigen of *Pseudomonas aeruginosa* is required for assembly of the functional PopB/PopD translocation pore in host cell membranes. *Infect Immun* **72**, 4741-50.
5. Lee, P. C., Stopford, C. M., Svenson, A. G. & Rietsch, A. (2010). Control of effector export by the *Pseudomonas aeruginosa* type III secretion proteins PcrG and PcrV. *Molecular Microbiology* **75**, 924-941.

6. Sundin, C., Thelaus, J., Broms, J. E. & Forsberg, A. (2004). Polarisation of type III translocation by *Pseudomonas aeruginosa* requires PcrG, PcrV and PopN. *Microbial Pathogenesis* **37**, 313-322.
7. Kim, J., Ahn, K., Min, S., Jia, J., Ha, U., Wu, D. & Jin, S. (2005). Factors triggering type III secretion in *Pseudomonas aeruginosa*. *Microbiology* **151**, 3575-87.
8. Lawton, D. G., Longstaff, C., Wallace, B. A., Hill, J., Leary, S. E. C., Titball, R. W. & Brown, K. A. (2002). Interactions of the type III secretion pathway proteins LcrV and LcrG from *Yersinia pestis* are mediated by coiled-coil domains. *Journal of Biological Chemistry* **277**, 38714-38722.
9. Francois, B., Luyt, C. E., Dugard, A., Wolff, M., Diehl, J. L., Jaber, S., Forel, J. M., Garot, D., Kipnis, E., Mebazaa, A., Misset, B., Andremont, A., Ploy, M. C., Jacobs, A., Yarranton, G., Pearce, T., Fagon, J. Y. & Chastre, J. (2012). Safety and pharmacokinetics of an anti-PcrV PEGylated monoclonal antibody fragment in mechanically ventilated patients colonized with *Pseudomonas aeruginosa*: a randomized, double-blind, placebo-controlled trial. *Crit Care Med* **40**, 2320-6.
10. Chaudhury, S., Nordhues, B. A., Kaur, K., Zhang, N. & De Guzman, R. N. (2015). NMR Characterization of the Type III Secretion System Tip Chaperone Protein PcrG of *Pseudomonas aeruginosa*. *Biochemistry*.
11. Sievers, F., Wilm, A., Dineen, D., Gibson, T. J., Karplus, K., Li, W. Z., Lopez, R., McWilliam, H., Remmert, M., Soding, J., Thompson, J. D. & Higgins, D. G. (2011). Fast, scalable generation of high-quality protein multiple sequence alignments using Clustal Omega. *Molecular Systems Biology* **7**.
12. Robert, X. & Gouet, P. (2014). Deciphering key features in protein structures with the new ENDscript server. *Nucleic Acids Research* **42**, W320-W324.
13. Zhang, Y. (2008). I-TASSER server for protein 3D structure prediction. *BMC Bioinformatics* **9**, 40.
14. Combet, C., Blanchet, C., Geourjon, C. & Deleage, G. (2000). NPS@: network protein sequence analysis. *Trends Biochem Sci* **25**, 147-50.
15. Derewenda, U., Mateja, A., Devedjiev, Y., Routzahn, K. M., Evdokimov, A. G., Derewenda, Z. S. & Waugh, D. S. (2004). The structure of *Yersinia pestis* V-antigen, an essential virulence factor and mediator of immunity against plague. *Structure* **12**, 301-6.
16. Nanao, M., Ricard-Blum, S., Di Guilmi, A. M., Lemaire, D., Lascoux, D., Chabert, J., I, A. & Dessen, A. (2003). Type III secretion proteins PcrV and PcrG from *Pseudomonas aeruginosa* form a 1 : 1 complex through high affinity interactions. *Bmc Microbiology* **3**.
17. Basu, A., Das, U., Dey, S. & Datta, S. (2014). PcrG protects the two long helical oligomerization domains of PcrV, by an interaction mediated by the intramolecular coiled-coil region of PcrG. *BMC Struct Biol* **14**, 5.